University
of Southampton

A Study of Recombination Centres in Electron Irradiated Silicon Solar Cells

Doctor of Philosophy Thesis

University of Southampton, SO17 1BJ, UK.

Researcher:	Robert Roland Smith
Supervisor:	Dr Tomas Markvart
Sponsor:	Engineering and Physical Sciences Research Council

Solar Energy Research

Materials Research Group

School of Engineering Sciences

Report No. TM/SE/RS/00/01/323

UNIVERSITY OF SOUTHAMPTON

ABSTRACT

SCHOOL OF ENGINEERING SCIENCES

MATERIALS RESEARCH GROUP

Doctor of Philosophy Thesis

A STUDY OF RECOMBINATION CENTRES IN SILICON SOLAR CELLS

by Robert Roland Smith

Solar cells in space are subject to a harsh radiation environment that reduces the efficiency of these cells by introducing point defects with energy levels in the forbidden bandgap. The lifetime of minority-carriers is reduced by these deep level defects that can act as recombination centres and annihilate electron-hole pairs. These recombination centres are investigated in this report using a variety of characterisation techniques.

Firstly the basic principles involved in the generation and recombination of electron-hole pairs is reviewed and the physics of particle irradiation is discussed. The properties of shallow and deep levels are also discussed and these deep level defects are then examined in detail. The characterisation technique known as Deep Level Transient Spectroscopy (DLTS) and some related techniques are then reviewed and the silicon solar cells used for this investigation are described.

The electrical properties of silicon solar cells doped with either boron, gallium, indium, aluminium or phosphorus formed on a variety of substrates are then determined before and after electron irradiation. The reduction in minority-carrier diffusion length caused by particle irradiation is deduced from these results by fitting the experimental data to a theoretical model. DLTS is then used to identify and categorise the deep levels present in these samples after particle irradiation. A new version of the forward bias DLTS technique is then defined and used to determine that the minority-carrier capture cross-section of the positive charge state of the divacancy ($VV^{+/0}$) is between 1 and 5×10^{-13} cm^2.

The Shockley-Read-Hall (SRH) model is then used to determine the minority-carrier lifetime of each of the observed defects in the gallium-doped cells. This model is then extended to show that the $VV^{+/0}$ defect is mainly responsible for the lifetime degradation observed in irradiated czochralski silicon solar cells. The damage coefficients are then determined for all of the cells examined in this study and they were compared to the literature data. Finally it is shown that the commonly observed relationship between the doping density and damage coefficient in silicon solar cells can be explained simply in terms of the divacancies ($VV^{+/0}$) capture cross-section, introduction rate, and its probability of occupation.

CHAPTER EIGHT – DISCUSSION OF RESULTS 201

CHAPTER NINE – CONCLUSIONS AND FUTURE WORK 259

CHAPTER TWO – THE PHYSICS OF SILICON SOLAR CELLS

CHAPTER THREE – RADIATION DAMAGE AND DEFECTS IN SILICON

CHAPTER FOUR – DEEP LEVEL TRANSIENT SPECTROSCOPY

CHAPTER FIVE – EXPERIMENTAL

CHAPTER SIX – PRESENTATION OF RESULTS

CHAPTER SEVEN – MODELLING OF SOLAR CELLS

CHAPTER EIGHT – DISCUSSION OF RESULTS

REFERENCES TO FIGURES

---

[1] Green, M.A., Solar Cells (Operating Principles, Technology and System Applications), Prentice Hall Inc., p.3, (1982).

[2] Anspaugh, B.E., GaAs Solar cell radiation handbook, NASA Publication, Jet Propulsion Laboratory (JPL96-9), p3-3, (1996).

[3] Sze, S.M., Physics of Semiconductor Devices, Second Edition, John Wiley and Sons Inc., p.8, (1981).

[4] Sze, S.M., Physics of Semiconductor Devices, Second Edition, John Wiley and Sons Inc., p.74, (1981).

[5] Sze, S.M., Physics of Semiconductor Devices, Second Edition, John Wiley and Sons Inc., p.801, (1981).

[6] Sze, S.M., Physics of Semiconductor Devices, Second Edition, John Wiley and Sons Inc., p.794, (1981).

[7] Goetzberger, A., Knobloch, J., and Voss, B., Crystalline Silicon Solar Cells, John Wiley and Sons Ltd., p.35, (1998).

---

[8] Green, M.A., Solar Cells (Operating Principles, Technology and System Applications), Prentice Hall Inc., p.53, (1982).

[9] Green, M.A., Solar Cells (Operating Principles, Technology and System Applications), Prentice Hall Inc., p.54, (1982).

[10] Watkins, G.D., EPR and ENDOR studies of defects in semiconductors, in Identification of defects in semiconductors: Semiconductors and semimetals, Volume 51A, Volume editor Stavlova, M., Academic Press, p.20, (1998).

[11] Watkins, G.D., EPR and ENDOR studies of defects in semiconductors, in Identification of defects in semiconductors: Semiconductors and semimetals, Volume 51A, Volume editor Stavlova, M., Academic Press, p.23, (1998).

[12] Kimerling, L.C., Asom, M.T. and Benton, J.L., Interstitial Defect Reactions in Silicon, Materials Science Forum, 38-41, p.141, (1989).

[13] Blood, P. and Orton, J.W.: The electrical characterisation of semiconductors: majority carriers and electron states, Techniques of Physics, Vols. 13 & 14, Academic Press, London, p.357, (1992).

[14] Blood, P. and Orton, J.W.: The electrical characterisation of semiconductors: majority carriers and electron states, Techniques of Physics, Vols. 13 & 14, Academic Press, London, p.348, (1992).

[15] Blood, P. and Orton, J.W.: The electrical characterisation of semiconductors: majority carriers and electron states, Techniques of Physics, Vols. 13 & 14, Academic Press, London, p.358, (1992).

[16] Lang, D.V., Space charge spectroscopy in semiconductors, Thermally stimulated relaxation of solids, (Ed. Braunlich, P.), Springer-Verlag, p.93-113, (1979).

[17] Blood, P. and Orton, J.W.: The electrical characterisation of semiconductors: majority carriers and electron states, Techniques of Physics, Vols. 13 & 14, Academic Press, London, p.555, (1992).

[18] Blood, P. and Orton, J.W.: The electrical characterisation of semiconductors: majority carriers and electron states, Techniques of Physics, Vols. 13 & 14, Academic Press, London, p.562, (1992).

[19] J. Zhao, A. Wang and M.A. Green, 16th Photov. Solar Energy Conf., Glasgow, UK, B1/53, (2000).

[20] Anspaugh, B.E., GaAs Solar cell radiation handbook, NASA Publication, Jet Propulsion Laboratory (JPL96-9), p2-1, (1996).

---

[21] Goetzberger, A., Knobloch, J., and Voss, B., Crystalline Silicon Solar Cells, John Wiley and Sons Ltd., p.115, (1998).

[22] Sze, S.M., Physics of Semiconductor Devices, Second Edition, John Wiley and Sons Inc., p.811, (1981).

[23] Goetzberger, A., Knobloch, J., and Voss, B., Crystalline Silicon Solar Cells, John Wiley and Sons Ltd., p.120, (1998).

CHAPTER THREE – RADIATION DAMAGE AND DEFECTS IN SILICON

CHAPTER FIVE - EXPERIMENTAL

CHAPTER SIX – PRESENTATION OF RESULTS

CHAPTER SEVEN – MODELLING OF SOLAR CELLS

CHAPTER EIGHT – DISCUSSION OF RESULTS

I would like to firstly thank my supervisor Dr Tomas Markvart for his endless support, understanding and patience. I would also like to say thanks to my family especially my mum and dad who have always supported me without question and thanks to the EPSRC for providing the funds for this project. I am also eternally indebted to Dr Jianhua Zhao of the University of New South Wales in Australia for his help, and for his generosity in supplying over 100 PERL/PERT high efficiency silicon solar cells used in this study.

Many thanks also to Chris Goodbody at DERA in Farnborough for his advice and the use his excellent AM0 solar simulator and spectral response equipment. Thanks should also go to the staff at BioRad, Steve Mclachlan and Dale Page who provided endless support with the DLTS equipment. Many thanks to Graham King for carrying out numerous repairs to the various equipment used in this study and thanks to Dr Graham Ensell for the preparation of the samples and help with the dark IV curves.

I am also indebted to Bill Williams of TS Space Systems for his help with the commissioning of the solar simulator, and Tim Bruton of BP Solar for supplying the p-on-n cells used in this study. Thanks must also go to Dr Marinus Hom at the University of Delft for carrying out the irradiations and last but not least I would like to thank all the laboratory and administration staff who have always provided excellent support, especially Dave, Big Eric, Little Eric, Gwyneth and Sue.

CHAPTER ONE

INTRODUCTION

1.1 Introduction

The problem of radiation damage to solar cells has been of major importance since the first solar powered satellite was launched in the 1950's. This problem continues to evolve with an increasing demand for satellites to operate in orbits in which they will be exposed to very high levels of radiation[1]. Silicon was the first material to be used in space and it has remained the most popular choice ever since due to it's history of reliable performance. A greater understanding of the mechanisms involved in silicon solar cell degradation is therefore crucial to optimise cell performance and design cells that can withstand the harsh radiation environment of space.

The introduction of deep level defects into silicon solar cells has been investigated for many years[2,3,4] although the research has often focussed on boron-doped czochralski (CZB) silicon[5,6]. The charge-carrier lifetimes in these cells severely degrade when exposed to space radiation and recently they have even been shown to fail under high fluences of electrons or protons[7,8,9]. Alternatives to boron are also being considered for silicon cells because large performance degradations have been observed when the standard CZB cells are exposed to sunlight[10,11].

The identity of the recombination centre responsible for the observed reduction in lifetime in irradiated silicon is still subject to much debate. It has been suggested that in FZ silicon the divacancy level ($VV^{+/0}$) may be responsible[12,13] although it has also been suggested[14] that the A centre (VO) is the dominant centre. In another study both the A centre and the divacancy were assumed to act in parallel controlling the lifetime[15]. More recently the Shockley-Read-Hall (SRH) carrier lifetime model has been used to conclude that the divacancy in its neutral charge state ($VV^{0/-}$) is responsible under low injection conditions. Under higher injection conditions the A centre becomes responsible in low doped n- and p-type silicon[16,17]. The carbon complex (H(0.36)) is also thought to act as a recombination centre[7] in space solar cells.

In this study high efficiency passivated-emitter rear locally-diffused (PERL)[18] and passivated-emitter rear totally-diffused (PERT)[19] silicon solar cells kindly supplied by the

University of New South Wales (UNSW) and doped with either boron, gallium, aluminium, indium or phosphorus formed on a variety of substrates are compared to standard back surface field (BSF) back surface reflector (BSR) silicon space solar cells. The current-voltage (IV) characteristics and spectral response are determined for these silicon solar cells before and after three different fluence levels of 1MeV electron irradiation.

The defects created by the radiation damage are observed using deep level transient spectroscopy (DLTS), forward bias DLTS (FBDLTS) and minority-carrier trap spectroscopy (MCTS) and are then identified by comparing their energy levels and capture cross-sections with published data. A new technique is then invented to determine the minority-carrier capture cross-section of the positively charged divacancy level ($VV^{+/0}$). This data is then used to model the shockley-read-hall (SRH) lifetime of each of the observed defects to identify the dominant recombination centre in these cells.

1.2 Structure of Thesis

Firstly in chapter two some of the basic solar cell equations are derived. The solar spectrum is examined and the AM0 and AM1.5 spectral distributions are defined. The next section examines the physics of p-n junction solar cells and considers their behaviour in the dark and when illuminated by the solar spectrum. A short review of recombination in solar cells is then given and this analysis is expanded in the next chapter. Finally in chapter two the photocurrent generated by an abrupt p-n junction solar cell is examined and this leads to a definition of quantum efficiency and spectral response.

Chapter three examines the damage caused by irradiation and summarises the defects produced. Firstly the principles of radiation damage in solar cells are outlined and then the theoretical calculations used to describe shallow and deep level defects are briefly discussed. The primary defects produced by high-energy particle irradiation are then examined in more detail and the subsequent defect complexes that form by annealing are tabulated.

Chapter four examines the capture and emission of charge carriers at defects states and defines the DLTS technique. The capacitance of a p-n junction under reverse bias is then defined and it is then explained how a capacitance transient is formed by the emission of charge carriers. The analysis of this transient by the DLTS method is then defined and this section also shows how the concentration, activation energy and capture cross-section of each deep level trap can be determined. The FBDLTS experiment is also analysed together with several other measurement techniques, such as the analysis of the minority-carrier capture cross-section and the MCTS technique.

All of the cells used in this study are described in chapter five that also describes the experimental equipment used to determine the IV characteristics, spectral response and the concentration and composition of the defect states. Chapter six then gives all of the experimental results. The DLTS results are given for each cell type and the spectral response is determined together with the dark and illuminated IV characteristics before and after the electron irradiations.

To analyse the spectral response data a computer model has been built in chapter seven that determines the spectral response of an ideal solar cell from first principles using the equations given in chapter two. This model is then extended to calculate the theoretical spectral response of the silicon solar cells described in chapter five. The results from this simple model are also compared to the results obtained using a one-dimensional finite element program known as PC1D. This comparison shows that for the silicon based cells described in chapter five there is an almost exact agreement between these two models. The experimentally determined values of spectral response are then compared to the theoretical models to determine the diffusion length of minority-carriers in the p-type region.

Chapter eight firstly examines the IV characteristics of the PERL/PERT silicon solar cells after three fluence levels of electron irradiation. The defects observed using DLTS in all of the cells studied are then examined and identified, and the published data on recombination centres is discussed. A new variety of the FBDLTS technique is then developed and the electron concentration at the edge of the depletion region during this experiment is calculated. This then enables the minority-carrier capture cross-section of the positive charge state of the divacancy defect level to be determined.

The SRH model is then used to study the defects observed in the gallium doped czochralski PERL/PERT silicon cells (CZG) and it is shown that the positive charge state of the divacancy ($VV^{+/0}$) is the dominant defect. This model is then extended to consider various doping levels to show that the $VV^{+/0}$ defect level may be responsible for the relationship between doping density and radiation tolerance commonly observed in irradiated silicon solar cells. Finally the damage coefficients are calculated for all of the cells used in this study and it is shown that the relationship between the damage coefficient and doping density can be described in terms of the divacancies ($VV^{+/0}$) capture cross-section, introduction rate and probability of occupation.

1.3 References

---

[1] Iles, P.A., Future of Photovoltaics for Space Applications, Prog. in Photov.: Res. Appl. 8, 39, (2000).

[2] Watkins, G.D., An EPR study of the lattice vacancy in silicon., J. Phys. Soc. Japan, 18, Supp.2, 22, (1963).

[3] Watkins, G.D., and Corbett, J.W., Defects in Electron Irradiated Silicon: EPR of the divacancy, Physical Review B, 138, 2A, p.543, (1964).

[4] Watkins, G.D., and Corbett, J.W., Defects in irradiated silicon: Electron spin resonance of the silicon A centre, Physical Review, 121, 4, (1961).

[5] Kimerling, L.C., Asom, M.T. and Benton, J.L., Interstitial Defect Reactions in Silicon, Materials Science Forum, 38-41, 141, (1989).

[6] Mooney, P.M., Cheng, L.J., Suli, M., Gerson, J.D., and Corbett, J.W.: Defect energy levels in boron doped silicon irradiated with 1MeV electrons, Physics Review B, 15, 8, p.3836, (1977).

[7] A. Khan et al, Proc. 16th Europ. Photov. Solar Energy Conf., Glasgow, UK, VA3.7., (2000).

[8] T. Yamaguchi et al, Appl. Phys. Lett. 72, 1226, (1998).

[9] A. Khan et al, J. Appl. Phys. 38, 2679, (1999).

[10] J. Knobloch et al, Proc. 25th IEEE Photov. Spec. Conf., IEEE Publication, 405, (1996).

---

[11] J. Schmidt, A.G. Aberle and R. Hezel, Proc. 26th IEEE Photov. Spec. Conf., IEEE Publication, 13, (1997).

[12] A.O. Evyware and B.J. Baliga, J. Electrochem. Soc. 124, 193, (1977).

[13] B.J. Baliga and A.O. Evwaraye, J. Electrochem. Soc. 130, 1916, (1983).

[14] J.W. Corbett, and G.D. Watkins, Phys.Rev. 138, 555, (1965).

[15] S.D. Brotherton, and P. Bradley, J. Appl. Phys. 53, 5720, (1982).

[16] N. Keskitalo et al, J. Appl. Phys. 83, 4206, (1998).

[17] H. Bleichner et al, J. Appl. Phys. 79, 9142, (1996).

[18] J. Zhao, A. Wang and M.A. Green, Progress in Photovoltaics 7, 471, (1999).

[19] J. Zhao, A. Wang and M.A. Green, 16th Photov. Solar Energy Conf., Glasgow, UK, B1/53, (2000).

CHAPTER TWO

THE PHYSICS OF SILICON SOLAR CELLS

2.1 Introduction

The photovoltaic effect was first observed in 1839 when Edmund Bequerel noted that "electric currents arose from certain light-induced chemical reactions." Several decades later a similar effect was observed in the solid element selenium. Quantum theory paved the way for the first solid-state devices in the late forties and this lead to the announcement that the first silicon solar cell with a 6% efficiency had been produced in 1954[1]. Similar cells were then first used to power satellites in 1958[2] and this was their main application until the late seventies when the terrestrial use of solar cells became popular.

Since the first silicon solar cell was produced research has been carried out all over the world and vast improvements have been made to reduce the cost and improve the efficiency of these cells. Silicon monocrystalline solar cells now hold the largest share of the terrestrial market and a number of measures have been implemented to increase the lifetime and efficiency of these cells. When they are illuminated by the AM1.5 solar spectrum in the laboratory efficiencies of $23-24\%$ are now possible[3,4].

This chapter reviews the equations and theories that have been developed to explain the photovoltaic effect. The theories developed in this chapter form the backbone of this report and will be reviewed and expanded in the later chapters. A great deal of this chapter is based upon books by Sze[5], Markvart[6], Green[7,8] and others[9, 10,11,12,13] which give a more detailed picture.

Firstly the solar spectrum is examined and some of the basic equations for intrinsic semiconductors are given. This leads to the section on p-n junctions where the dark and illuminated characteristics are discussed and recombination in solar cells is then briefly examined. The photocurrents generated by illumination of a solar cell are then examined and a cells quantum efficiency and spectral response is then defined. These equations are then used in chapter seven to determine the ideal characteristics of a solar cell.

2.2 The Solar Spectrum

The radiative energy output from the sun derives from a nuclear fusion reaction. Every second around 6×10^{11}kg of hydrogen is converted to helium with a net mass loss of around 4×10^{3} kg which, using the Einstein relation, equates to 4×10^{20} J/s. This energy is emitted primarily as electromagnetic radiation in the ultraviolet to infrared and radio spectral regions. The total mass of the sun in now around 2×10^{30} kg and a reasonably stable life of over 10 billion years is predicted with a nearly constant radiative energy output. For a perfectly absorbing or "black-body" *Planck's radiation law* gives the spectral distribution of the emitted radiation (Figure 2.1.).

Intense radiation (2×10^{7} K) from the sun's centre is absorbed by a layer of negative hydrogen ions near the sun surface. These ions act as continuous absorbers over a great range of wavelengths. The accumulation of heat in this layer sets up convective currents that transport the excess energy through the optical barrier. Once through most of this layer, the energy is re-radiated into the relatively transparent gases above. This sharply defined layer where convective transport gives way to radiation is known as the photosphere and radiates an essentially continuous spectrum of electro-magnetic radiation.

The spectral irradiance of the sun just outside the Earth's atmosphere (1 astronomical unit from the sun) is known as air mass zero (AM0). This is of primary importance for solar cell applications in outer space and closely approximates the irradiance of a 6000K black-body[14]. The slight difference is due to effects such as the differing transmissivity of the sun's atmosphere at different wavelengths. High altitude spectral measurements have led to an accurate solar irradiance spectrum which was published in 1971[15]. This has been further improved by Willson[16] in 1985 and these results are shown in Figure 2.2.. The total irradiance or solar constant at AM0 is around 136.8 mW/cm^2 and varies very slightly with sunspot activity[17].

Sunlight is attenuated by around 30% during its passage through the atmosphere by Rayleigh scattering or scattering by the molecules in the atmosphere. This attenuates sunlight at all wavelengths but is most effective at short wavelengths. Scattering by aerosols and dust particles is another reason and some light is also absorbed by the atmosphere and its constituent gases, notably oxygen, ozone, water vapour, and carbon dioxide. The degree of attenuation is highly variable and the most important parameter determining the total incident power under clear conditions is the length of the light path through the atmosphere.

When the sun is directly overhead at the equator at sea level, the optical air mass is unity and the radiation is described as *air mass one radiation* (AM1). When the sun is at an angle θ, the air mass is approximated by air mass = 1/Cos θ. AM1.5 is therefore defined as sunlight radiating through an air mass 1.5 times greater than the vertical case and Figure 2.3. shows both the AM0 and the AM1.5 solar spectra. The AM1.5 spectrum is used with a total irradiance of 1kW/m^2 for the calibration of solar cells and modules and some of these tests are even covered by the British Standards[18].

2.3 Intrinsic Semiconductors

Semiconducting crystals such as silicon (Si) and gallium arsenide (GaAs) are atomically arranged in the diamond face-centred-cubic lattice or, for compound semiconductors, the zincblende lattice (Figure 2.4.). The four outer or valence electrons of each silicon atom covalently bond with the four nearest neighbours and this results in a four-fold tetrahedral co-ordination. This is a very stable structure at low temperatures but at higher temperatures some electrons in the covalent bond can obtain enough energy to break free and are therefore promoted from the valence band to the conduction. The electrons released are free to move through the crystal and contribute to the current flow.

Electron energy levels in a crystal occupy well defined bands separated by forbidden energy regions or gaps band (see Figure 2.5.). At low temperatures electrons in a crystal occupy the lowest possible energy states. The *Pauli exclusion principle* implies that only two electrons of opposite spin can occupy each energy state so at low temperatures two electrons, up to a certain energy level known as the *Fermi level*, occupy all the available energy states. As the temperature increases some electrons gain energy in excess of the Fermi level and the probability that a level at energy E is occupied by an electron can then be calculated using the *Fermi-Dirac distribution function*[19]

$$F(E) = \frac{1}{1 + \exp\left(\frac{E - E_F}{kT}\right)} \qquad \textbf{(2.1)}$$

where F(E) = Density of free electrons

E_F = Fermi energy level

k = Boltzmann constant

T = Absolute temperature

$F(E) = 1$ between absolute zero and the Fermi level, E_F, and $F(E) = 0$ above E_F.
The minimum energy required to release an electron is equal to the width of the semiconductor's forbidden band gap (E_G). This value varies with temperature and can be found above 250K by using the expression[20]

$$E_G(T) = 1.206 - 2.73 \times 10^{-4} T (eV) \tag{2.2}$$

In silicon at 300K this forbidden energy gap is around 1.12eV.

Now consider an intrinsic semiconductor which is very pure and contains a negligibly small amount of impurities. The number of occupied conduction band levels is given by[5]

$$n = N_C \frac{2}{\sqrt{\pi}} F_{1/2}\left(\frac{E_F - E_C}{kT}\right) \tag{2.3}$$

where n = Density of free electrons
k = Boltzmann constant
T = Absolute temperature
E_F = Fermi energy level
E_C = Bottom of the conduction band
N_C = Effective density of states in the conduction band
$F_{1/2}$ = Fermi-Dirac integral[21]

N_C is given by

$$N_C \equiv 2\left(\frac{2\pi m_{de} kT}{h^2}\right)^{\frac{3}{2}} \tag{2.4}$$

where m_{de} = Density of state effective mass for electrons[22]
h = Planck constant

The Fermi-Dirac integral $F_{1/2}(\eta_f)$ (see Blackmore[21]) approaches $\sqrt{(\pi e^{\eta_f}/2)}$ for the Boltzmann statistics case (that is when the Fermi level is several kT below E_C in non-degenerate semiconductors) therefore Equation 2.3 becomes

$$n = N_C \exp\left(-\frac{E_C - E_F}{kT} \right) \tag{2.5}$$

Similarly the hole density near the top of the valence band equals

$$p = N_V \exp\left(-\frac{E_F - E_V}{kT} \right) \tag{2.6}$$

where the effective density of states in the valence band N_V is given by

$$N_V \equiv 2\left(\frac{2\pi m_{dh} kT}{h^2} \right)^{\frac{3}{2}} \tag{2.7}$$

where N_V = Effective density of states in the valence band

m_{dh} = Density of state effective mass for holes[22]

For intrinsic semiconductors $n=p=n_i$ where n_i is the intrinsic carrier concentration. Combining Equations 2.5 and 2.6 gives the Intrinsic Fermi level E_i

$$E_F - E_i = \frac{E_C + E_V}{2} + \frac{kT}{2}\ln\left(\frac{N_V}{N_C} \right) = \frac{E_C + E_V}{2} + \frac{3kT}{4}\ln\left(\frac{m_{dh}}{m_{de} M_C^{\frac{2}{3}}} \right) \tag{2.8}$$

Hence the Fermi level of an intrinsic semiconductor generally lies very close to the middle of the bandgap. The intrinsic carrier density n_i is obtained from Equations 2.5, 2.6 and 2.8 where $E_g=E_C-E_V$

$$np = n_i^2 = N_C N_V \exp\left(\frac{E_G}{kT} \right) \tag{2.9}$$

$$n_i = \sqrt{N_C N_V e^{\frac{E_G}{2kT}}} \tag{2.10}$$

2.4 The Physics of P-n Junctions

If isolated pieces of n-type and p-type semiconducting material are brought together electrons flow from regions of high concentration (n-type side) to regions of low concentration (p-type side) and the opposite can be said for holes. However electrons leaving the n-type side will create a charge imbalance by exposing ionised donors (positive charge) and holes leaving the p-type side will expose negative charge. These exposed charges set up an electric field that opposes the natural diffusion tendencies of the electrons and holes and an equilibrium situation is obtained.

2.4.1 Dark Characteristics

The characteristics of the equilibrium situation can be found by considering Fermi levels because a system in thermal equilibrium can have only one Fermi level. Far away from the metallurgical junction conditions could be expected to remain identical to those in isolated material. Hence there must be a transition or depletion region near the junction in which a potential change, V_{bi}, occurs.

When impurity atoms are added to an intrinsic semiconductor the np product is still given by Equation 2.9 and the product is independent of the added impurities. At elevated temperatures most of the donors, N_D and acceptors, N_A are ionised so the neutrality condition can be approximated by

$$n + N_A = p + N_D \tag{2.11}$$

Equations 2.9 and 2.11 can now be combined to give the concentration of electrons and holes in an n-type semiconductor

$$n_{no} = \frac{1}{2}\left[(N_D - N_A) + \sqrt{(N_D - N_A)^2 + 4n_i^2}\right] \tag{2.12}$$

If $(N_D\text{-}N_A) \gg n_i$ and $N_D \gg N_A$ then

$$n_{no} \approx N_D \tag{2.13}$$

$$p_{no} = \frac{n_i^2}{n_{no}} \approx \frac{n_i^2}{N_D} \tag{2.14}$$

where n_{no} = Density of holes in n-type material

p_{no} = Density of electrons in n-type material

and the position of the Fermi level in n-type material can now be found using

$$E_C - E_F = kT\ln\left(\frac{N_C}{N_D}\right) \tag{2.15}$$

The concentration of holes (p_{po}) and electrons (n_{po}) in p-type material can now also be obtained by interchanging the symbols n and p. This leads to an expression for the position of the Fermi level in p-type material

$$E_F - E_V = kT\ln\left(\frac{N_V}{N_A}\right) \tag{2.16}$$

Figure 2.6. shows the space charge distribution (a) of an abrupt p-n junction in thermal equilibrium, as well as the electric field distribution (b), the potential variation (c) and the energy band diagram (d)[5]. The diffusion or built-in potential V_{bi} is therefore equal to

$$\mathrm{qV_{bi}} = \mathrm{E_G} - \left(q\mathrm{V_n} + qV_p\right) \tag{2.17}$$

$$\mathrm{qV_{bi}} = \mathrm{kT}\ln\left(\frac{N_C N_V}{n_i^2}\right) - \left[\mathrm{kT}\ln\left(\frac{N_C}{n_{no}}\right) + \mathrm{kT}\ln\left(\frac{N_V}{p_{po}}\right)\right] \tag{2.18}$$

Therefore

$$\mathrm{qV_{bi}} = \mathrm{kT}\ln\left(\frac{n_{no}p_{po}}{n_i^2}\right) \approx \mathrm{kT}\ln\left(\frac{N_A N_D}{n_i^2}\right) \tag{2.19}$$

Since at equilibrium $n_{no}p_{no} = n_{po}p_{po} = n_i^2$

$$\mathrm{V_{bi}} = \frac{\mathrm{kT}}{q}\ln\left(\frac{p_{po}}{p_{no}}\right) = \frac{\mathrm{kT}}{q}\ln\left(\frac{n_{no}}{n_{po}}\right) \tag{2.20}$$

The space charge distribution (Figure 2.6.(a)) of the junction shows two distinct regions: quasi-neutral regions where the space-charge density is assumed zero throughout, and a depletion region where the carrier concentrations are assumed so small that the only contribution to space-charge density comes from the ionised dopants. The width of the depletion region (W) for a two-sided junction equals[5]

$$W = \sqrt{\frac{2\varepsilon_S}{q}\left(\frac{N_A + N_D}{N_A N_D}\right)V_{bi}} \tag{2.21}$$

where ε_S = Semiconductor permittivity

For a one-sided abrupt junction where $N_B=N_D$ or N_A depending whether $N_A >> N_D$ or vice versa

$$W = \sqrt{\frac{2\varepsilon_S V_{bi}}{qN_B}} \qquad \textbf{(2.22)}$$

Consider the p-n junction shown in Figure 2.7.. The depletion width in the n-type region W_n can be determined using

$$W_n = \frac{WN_A}{N_A + N_D} \qquad \textbf{(2.23)}$$

and in the p-type region

$$W_p = \frac{WN_D}{N_A + N_D} \qquad \textbf{(2.24)}$$

A more accurate result for the depletion layer width can be obtained by considering the majority carrier distribution in addition to the impurity concentration. The depletion width is essentially the same as Equation 2.21 except V_{bi} is replaced by (V_{bi} – 2kT/q). This correction factor comes about because of the two majority carrier distribution or Debye tails[23] (electrons in n side and holes in p side as shown by the dashed lines in Figure 2.6.(a)) which each contribute a correction factor of kT/q. The depletion layer width at thermal equilibrium for a two sided abrupt junction becomes

$$W = \sqrt{\frac{2\varepsilon_S}{q}\left(\frac{N_A + N_D}{N_A N_D}\right)\left(V_{bi} - \frac{2kT}{q}\right)} \qquad \textbf{(2.25)}$$

When a voltage V is applied to the junction, the total electrostatic potential variation across the junction is given by V_{bi} + V for reverse bias and by V_{bi} – V for forward bias. Substituting these voltage values into Equation 2.25 yields the depletion layer width as a function of the applied voltage.

2.4.2 Illuminated Characteristics

A standard solar cell consists of a shallow n-type layer diffused into the p-type base layer to form a p-n junction near the surface of the cell (Figure 2.8.). When the cell is exposed to the solar spectrum photons generate electron-hole pairs in the bulk of the semiconductor. The minority carriers then diffuse towards and across the junction creating a potential difference and therefore a current can be extracted from the cell.

The built in voltage (V_{bi}) is shown in Figure 2.6.(d) and Figure 2.9. shows the idealised circuit that describes the power generation characteristics of the cell. The ideal IV characteristic of a solar cell, differs from the diode equation only by the presence of a light generated current, and is described by the equation

$$I = I_S\left(e^{\frac{qV}{kT}} - 1\right) - I_L \qquad \textbf{(2.26)}$$

where I_S = Dark saturation current
I_L = Light generated current

and

$$J_S = \frac{I_S}{A} = qN_C N_V\left(\frac{1}{N_A}\sqrt{\frac{D_n}{\tau_n}} + \frac{1}{N_D}\sqrt{\frac{D_p}{\tau_p}}\right)e^{\frac{-E_g}{kT}} \qquad \textbf{(2.27)}$$

where J_S = Dark saturation current density
I_S = Dark saturation current
A = Area
D_n, D_p = Diffusion coefficient in n and p-type
τ_n, τ_p = Lifetime in n and p-type material

The IV curve passes through the fourth quadrant (Figure 2.10.) and therefore power can be extracted from the device. The maximum power (P_m) is generated when $V = V_m$ and $I = I_m$. The open-circuit voltage (V_{oc}) and the short-circuit current (I_{sc}) are given by

$$I_{SC} = -I_L \qquad \textbf{(2.28)}$$

$$V_{OC} = \frac{kT}{q}\ln\left(\frac{I_L}{I_S}+1\right) \approx \frac{kT}{q}\ln\left(\frac{I_L}{I_S}\right) \tag{2.29}$$

Hence for a given I_L the open-circuit voltage increases logarithmically with decreasing saturation current. The output power is given by

$$P = IV = I_S V\left(e^{\frac{qV}{kT}}-1\right)-I_L V \tag{2.30}$$

The condition for maximum power can be obtained when dP/dV=0, or

$$I_m = I_S \beta V_m e^{\beta V_m} \approx I_L\left(1-\frac{1}{\beta V_m}\right) \tag{2.31}$$

$$V_m = \frac{1}{\beta}\ln\left(\frac{I_L/I_S+1}{1+\beta V_m}\right) \approx V_{OC}-\frac{1}{\beta}\ln(1+\beta V_m) \tag{2.32}$$

where β=q/kT. The maximum power output is then

$$P_m = I_m V_m \approx I_L\left(V_{OC}-\frac{1}{\beta}\ln(1+\beta V_m)-\frac{1}{\beta}\right) = I_L\left(\frac{E_m}{q}\right) \tag{2.33}$$

E_m corresponds to the energy per photon delivered to the load at the maximum power point and is given by

$$E_m = q\left(V_{OC}-\frac{1}{\beta}\ln(1+\beta V_m)-\frac{1}{\beta}\right) \tag{2.34}$$

Under the AM1.5 condition the short-circuit current density, J_L can be obtained graphically from Figure 2.3.

$$J_L(E_g) = q\int_{h\nu=E_g}^{\infty}\left(\frac{dn_{ph}}{dh\nu}\right)d(h\nu) \tag{2.35}$$

Once J_S and J_L are known E_m can be obtained by the numerical solution of the Equations 2.29, 2.32 and 2.34. Because J_S and hence E_m depends on material properties such as lifetime, diffusion length and doping levels then these properties should be optimised to obtain the ideal efficiency. The ideal conversion efficiency is the ratio of the maximum power output, P_m to the incident power P_{in}. The power conversion efficiency is given by

$$\eta = \frac{I_m V_m}{P_{IN}} = \frac{FF I_L V_{OC}}{P_{IN}} \tag{2.36}$$

where P_{IN} is the incident power and FF is the fill factor defined by

$$FF = \frac{I_m V_m}{I_L V_{OC}} \tag{2.37}$$

2.5 Recombination in Solar Cells

Light of appropriate wavelength shining on a semiconductor creates electron-hole pairs. When the light is switched off the excess concentration of carriers will decay back to equilibrium values. This process is known as recombination and there are several different mechanisms by which this can occur. The main processes of recombination can occur in parallel in which case the recombination rate is just the sum of the individual components described in the following sections.

2.5.1 Radiative recombination

Radiative recombination is just the reverse of the absorption process. An electron occupying a higher energy state makes a transition to an empty lower energy state with all or most of the energy difference between states emitted as light. All of the mechanisms considered for absorption have inverse radiative recombination processes. Radiative recombination occurs more rapidly in direct-band-gap semiconductors because of the two-steps involved in the indirect-band-gap process (Figure 2.11.).

The total radiative recombination rate R_R is proportional to the concentration of electrons in the conduction band and holes in the valence band therefore $R_R = Bnp$ where B is a semiconductor material constant. Because of the relationship between optical absorption and this recombination process B can be calculated from the semiconductors absorption coefficient. In thermal equilibrium when $np = ni^2$ this recombination rate is balanced by an equal and opposite generation rate. The net recombination rate, U_R, is therefore given by the total recombination rate minus the equilibrium generation rate

$$U_R = B\left(np - ni^2\right) \tag{2.38}$$

The associated carrier lifetimes for electrons (τ_e) and holes (τ_h) are therefore

$$\tau_e = \frac{\Delta n}{U} \tag{2.39}$$

$$\tau_h = \frac{\Delta p}{U} \tag{2.40}$$

where U is the net recombination rate and Δn and Δp are the disturbances of the respective carriers from their equilibrium values, n_0 and p_0. For the radiative recombination mechanism with Δn = Δp the characteristic lifetime is[24]

$$\tau = \frac{n_0 p_0}{B n_i^2 \left(n_0 + p_0\right)} \tag{2.41}$$

This process forms the basis of commercial semiconductor lasers and light-emitting diodes using GaAs and its alloys. The lifetime of charge carriers for this recombination process was first calculated at around 0.75s[25] and this result contradicted all the experimental observations. A very short carrier lifetime had been measured[33] which showed a relationship with the dopant concentration. It was therefore obvious that radiative recombination must play a very secondary role and the other mechanisms must primarily influence the lifetime of charge carriers.

2.5.2 Auger Recombination

In Auger recombination the electron recombining with the hole gives the excess energy to a second electron in either band instead of emitting light (Figure 2.12.). This second electron then relaxes back to its original energy by emitting phonons. Auger recombination is the inverse of the impact ionisation effect, where a high energy electron collides with an atom, breaking a bond and creating an electron-hole pair. Landsberg[26,27] and others have explained this three particle process. For the electron-hole-hole process the reaction mechanism will be proportional to p^2n and for an the electron-electron-hole process the reaction mechanism will be proportional to n^2p. This means that the recombination rate R_A for electrons is

$$R_A = Bn^2 p \tag{2.42}$$

thus the Auger lifetime τ_A is

$$\tau_A = \frac{p}{R_A} = \frac{1}{Bn^2} \tag{2.43}$$

The value of the Auger coefficient B for silicon[28,29] works out as 4×10^{-31} $cm^6 s^{-1}$. This means that Auger recombination only becomes noticeable at dopant concentrations higher than 10^{18} cm^{-3} and is therefore not the most significant process in most semiconductor devices.

2.5.3 Recombination through Traps

The recombination of electron-hole pairs at defect levels in the band-gap was first discussed by Shockley and Read,[30] and by Hall[31]. Later work by Sah, Noyce and Shockley[32] added to the understanding of the role of such defects. Usually this type of recombination is non-radiative, however sometimes sub-bandgap photoluminescence is produced by this process. This process is therefore commonly called Shockley Read Hall (SRH) or non-radiative recombination.

Impurities and defects give rise to allowed energy levels within the otherwise forbidden band gap. These defect levels create a very efficient two-step recombination process whereby electrons relax to the valence band, annihilating a hole (Figure 2.13.(a)). The net recombination generation rate by traps, U_T, can be written

$$U_T = \frac{np - n_i^2}{\tau_{ho}(n + n_1) + \tau_{eo}(p + p_1)} \tag{2.44}$$

where τ_{ho} and τ_{eo} are lifetime parameters which depend on the type of traps and the volume density of trapping defects and parameters n_1 and p_1 introduce a dependency of the recombination rate upon the energy of the trapping level, Et

$$n_1 = N_C \exp\left(E_t - \frac{E_C}{kT}\right) \tag{2.45}$$

$$n_1 p_1 = n_i^2 \tag{2.46}$$

If τ_{ho} and τ_{eo} are of the same magnitude U will have its peak value when $n_1 \approx p_1$. This occurs if the defect level lies near the middle of the forbidden band gap hence impurities that introduce energy levels near mid-gap are very effective recombination centres. The formation of these defects is discussed in detail in Chapter Three.

2.5.4 Recombination at Surfaces

Surfaces represent rather severe defects in the crystal structure and are the site of many allowed states within the band gap (Figure 2.13.(b)). Recombination can therefore occur very efficiently at surfaces by recombination through traps. The net recombination rate per unit area U_A for a single level surface state takes the form

$$U_A = \frac{S_{eo}S_{ho}\left(np - ni^2\right)}{S_{eo}\left(n + n_1\right) + S_{ho}\left(p + p_1\right)} \qquad \textbf{(2.47)}$$

where S_{eo} and S_{ho} are surface recombination velocities. Again surface-state levels lying near mid-gap are the most effective recombination centres.

2.6 Light Generated Photocurrents

In a modern p-n junction silicon solar cells the base material is usually p-type and the emitter n-type. The n-type material is nearly always more highly doped than the base by several orders of magnitude therefore the space charge or depletion region extends mainly into the p-type region. To calculate photocurrents we assume that the light enters on the emitter side and the calculation is first made for monochromatic light. In the case of illumination by a spectrum we must integrate over all the wavelengths in this spectrum. The integration limits are the smallest occurring wavelength λ_{min} and the wavelength corresponding to the semiconductor band gap λ_{max}, as longer wavelengths are not absorbed. For sunlight λ_{min} is around 0.3 μm and for silicon λ_{max} is 1.14 μm.

The generation rate G, of electron-hole pairs at a distance x from the semiconductor surface, when illuminated by incident monochromatic light of wavelength λ, is given by[33]

$$G(\lambda, x) = \alpha(\lambda)F(\lambda)\left(1 - R(\lambda)\right)\exp\left(-\alpha(\lambda)x\right) \qquad \textbf{(2.48)}$$

where $\alpha(\lambda)$ = Absorption coefficient

$F(\lambda)$ = No. of incident photons/cm^2/s per unit bandwidth
$R(\lambda)$ = The fraction of incident photons reflected from the surface

For an abrupt p-n junction solar cell with constant doping on each side of the junction there are no electric fields outside the depletion region. In the case of a standard p^+n junction, equation 2.48 can be combined with the continuity equations and the current density equations to yield an expression for the top side of the junction. Applying boundary conditions for surface recombination and the excess carrier density at the depletion edge gives, after some manipulation, the resulting hole photocurrent density at the depletion edge

$$J_P(\lambda) = \frac{qF(1-R)\alpha L_P}{(\alpha^2 L_P{}^2 - 1)} \times \left[\frac{\left(\frac{S_P L_P}{D_P} + \alpha L_P\right) - e^{-\alpha xj}\left(\frac{S_P L_P}{D_P}\cosh\frac{xj}{L_P}\sinh\frac{xj}{L_P}\right)}{\left(\frac{S_P L_P}{D_P}\right)\sinh\frac{xj}{L_P} + \cosh\frac{xj}{L_P}} - \alpha L_P e^{-\alpha xj} \right] \quad \textbf{(2.49)}$$

where α = Absorption coefficient
F = No. of incident photons/cm^2/s per unit bandwidth
R = The fraction of incident photons reflected from the surface
L_p = Hole diffusion length = $(D_p\tau_p)^{1/2}$
S_p = Surface recombination velocity of holes
xj = Depth of the depletion edge in n-type layer (See Figure 2.7.)

This photocurrent would be collected from the front side of a p^+n junction solar cell at a given wavelength assuming this region to be uniform in lifetime, mobility, and doping level.

In addition to the hole photocurrent collected from the emitter there is an electron photocurrent collected from the base which is derived in a similar way[5]. The photocurrent due to electrons $J_n(\lambda)$ is therefore

$$J_n(\lambda) = \frac{qF(1-R)\alpha L_n}{(\alpha^2 L_n{}^2 - 1)} e^{(-\alpha(xj+W))} \times \left[\alpha L_n - \frac{\left(\frac{S_n L_n}{D_n}\right)\left[\left(\cosh\frac{H'}{L_n}\right) - \left(e^{-\alpha H'}\right)\right] + \left(\sinh\frac{H'}{L_n}\right) + \left(\alpha L_n\left(e^{-\alpha H'}\right)\right)}{\left(\frac{S_n L_n}{D_n}\right)\sinh\frac{H'}{L_n} + \cosh\frac{H'}{L_n}} \right] \quad \textbf{(2.50)}$$

where L_n = Electron diffusion length = $(D_n\tau_n)^{1/2}$

S_n = Surface recombination velocity of electrons

W = Depletion width (See Figure 2.7.)

H' = Depth of the depletion edge in p-type layer (See Figure 2.7.)

This photocurrent would be collected from the back side of a p^+n junction solar cell at a given wavelength again assuming this region to be uniform in lifetime, mobility, and doping level. If any of these quantities are a function of distance numerical analysis must be used.

Some photocurrent is also generated within the depletion region and because the electric field in this region is generally high, the photogenerated carriers are accelerated out of this region before they can recombine. The photocurrent per unit bandwidth $J_d(\lambda)$ is therefore equal to the number of photons absorbed

$$J_d(\lambda) = qF(1-R)(e^{-\alpha x_j})\left[1 - e^{-\alpha W}\right] \quad \textbf{(2.51)}$$

The total photocurrent at a given wavelength is then the sum of equations 2.49, 2.50 and 2.51

$$J_t(\lambda) = J_p(\lambda) + J_n(\lambda) + J_d(\lambda) \quad \textbf{(2.52)}$$

2.7 Quantum Efficiency and Spectral Response

The quantum efficiency (QE) is the number of electron-hole pairs collected, at a given wavelength, under short circuit conditions relative to the number of photons which enter the cell. The quantum efficiency is therefore the total photocurrent divided by the photon density, qF for external quantum efficiency, or qF(1-R) for internal quantum efficiency

$$QE_{\text{int}}(\lambda) = \frac{J_t(\lambda)}{qF(\lambda)(1 - R(\lambda))} \tag{2.53}$$

$$QE_{ext}(\lambda) = \frac{J_t(\lambda)}{qF(\lambda)} \tag{2.54}$$

The ideal internal quantum efficiency of a semiconductor with an energy band gap E_g is a step function that equals zero for $h\nu<E_g$ and unity for $h\nu \geq E_g$.

The spectral response is the ratio of the short-circuit current to the incident light power as a function of the wavelength. Both spectral response (Amps/Watt) and quantum efficiency express the solar cells ability to convert light into electrical current. Both quantities are related by the equation

$$SR(\lambda) = \frac{QE_{ext}(\lambda)}{E_{ph}} \tag{2.55}$$

where E_{ph} = Photon energy in eV

2.8 References

---

[1] Chapin, D.M., Fuller, C.S., and Pearson, G.L.: A new p-n junction photocell for converting solar radiation into electrical power, Journal of Applied Physics, 25, p.676-677, (1954).

[2] Wolf, M., Historical development of solar cells, Solar Cells (ed. Backus, C.E.), New York, IEEE Press, (1976).

[3] Green, M.A., Proc. 10th EC PV Solar Energy Conf., Lissabon, Portugal, p.250, (1991).

[4] Knoblocch, J., et al, Proc. 25th IEEE PV Spec. Conf., Washington DC, USA, p.405, (1996).

[5] Sze, S.M., Physics of Semiconductor Devices, Second Edition, John Wiley and Sons Inc., (1981).

[6] Markvart, T. (*Ed*), Solar Electricity, John Wiley and Sons Ltd., (1994).

[7] Green, M.A., Solar Cells (Operating Principles, Technology and System Applications), Prentice Hall Inc., (1982).

[8] Green, M.A., Silicon Solar Cells, Centre of Photovoltaic devices and systems, University of New South Wales, (1995).

[9] Goetzberger, A., Knobloch, J., and Voss, B., Crystalline Silicon Solar Cells, John Wiley and Sons Ltd., (1998).

[10] Blood, P. and Orton, J.W.: The electrical characterisation of semiconductors: majority carriers and electron states, Techniques of Physics, Vols. 13 & 14, Academic Press, London, (1992).

---

[11] Orton, J.W., and Blood, P.: The electrical characterisation of semiconductors: minority carriers, Techniques of Physics, Vols. 13 & 14, Academic Press, London, (1992).

[12] Lannoo, M. and Bourgoin, J.: Point Defects in Semiconductors I: Theoretical Aspects, Springer Verlag, (1981).

[13] Bourgoin, J., and Lannoo, M.: Point Defects in Semiconductors II: Experimental Aspects, Springer Verlag, (1981).

[14] Johnson, F.S., Journal of Meteorology, 11, 6, p.431, (1954).

[15] Thekackara, M.P., et al, Solar electromagnetic radiation, NASA SP 8005, Revised, May (1971).

[16] Willson, R.C., Solar total irradiance and its spectral distribution, Encyclopaedia of Physics, 3rd Ed., Editor: Besancon, R.M., Van Nostrand Reinhold, p.1135, (1985).

[17] Willson, R.C., and Hudson, H.S., The sun's luminosity over a complete solar cycle, Nature, 351, p.42, (1991).

[18] BS EN 60891 : Procedures for temperature and irradiance corrections to measure I-V characteristics of crystalline silicon photovoltaic devices, (1994).
BS EN 60904-1 : Photovoltaic devices part 1 : Measurement of photo-voltaic current voltage devices, (1993).
BS EN 60904-2 : Photovoltaic devices part 2 : Requirements for reference solar cells, (1993).
BS EN 60904-3 : Photovoltaic devices part 3 : Measurement principles for terrestrial photovoltaic solar devices with reference spectral irradiance data, (1993).

BS EN 60904-5 : Photovoltaic devices part 5 : Determination of the equivalent cell temperature (ECT) of photovoltaic (PV) devices by the open-circuit voltage method, (1995).

BS EN 60904-6 : Photovoltaic devices part 6 : Requirements for reference solar modules, (1994).

BS EN 61215 : Crystalline silicon terrestrial photovoltaic (PV) modules – Design qualification and type approval, (1995).

[19] Kittel, C., Introduction to Solid State Physics, Sixth Edition, John Wiley and Sons Inc., (1986).

[20] Green, M.A., Intrinsic Concentration, Effective Densities of States, and Effective Mass in Silicon, J. Appl. Phys., 67, p.6, (1990).

[21] Blackmore, J.S., Carrier concentrations and Fermi levels in semiconductors, Electron. Commun., 29, p.131, (1952).

[22] Smith, R.A., Semiconductors, 2nd Ed., Cambridge University Press, London, (1979).

[23] Garrett, C.G.B., and Brattain, W.H., Physical theory of semiconductor surfaces, Phys. Rev., 99, p.376, (1955).

[24] Pankove, J.I., Optical processes in semiconductors, Prentice Hall, (1971).

[25] Van Roosbroek, W., and Shockley, W., Phys. Rev. 94, p.1558, (1954).

[26] Landsberg, P.T., Solid State Elect., 30, p.1107, (1987).

[27] Landsberg, P.T., Appl. Phys. Lett., 50, p.745, (1987).

---

[28] Beck, S.D, Solid State Commun.,13, p.93, (1973).

[29] Rohatgi, A., IEEE-TED 31, p.597, (1984).

[30] Shockley, W. and Read, W.T.: Phys. Rev., 87, p.335, (1952).

[31] Hall, R.N.: Phys. Rev., 87, p.387, (1952).

[32] Sah, C.T., Noyce, R.N. and Shockley, W.: Proc. IRE, 45, p.1228, (1957).

[33] Hovel, H.J., Solar cells in Willardson and Beer (Eds.), Semiconductors and Semimetals, Vol.11, Academic New York, (1975).

FIGURE 2.1. PLANCKS BLACK-BODY RADIATION DISTRIBUTIONS FOR DIFFERENT BLACK-BODY TEMPERATURES

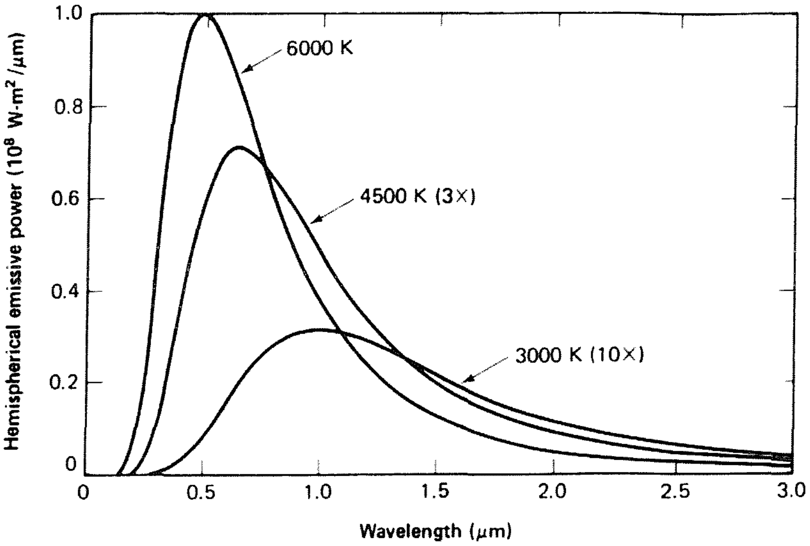

FIGURE 2.2. COMPARISON OF DIFFERENT AM0 SOLAR SPECTRA, THEKAEKARA (1971) AND WILLSON (1985)

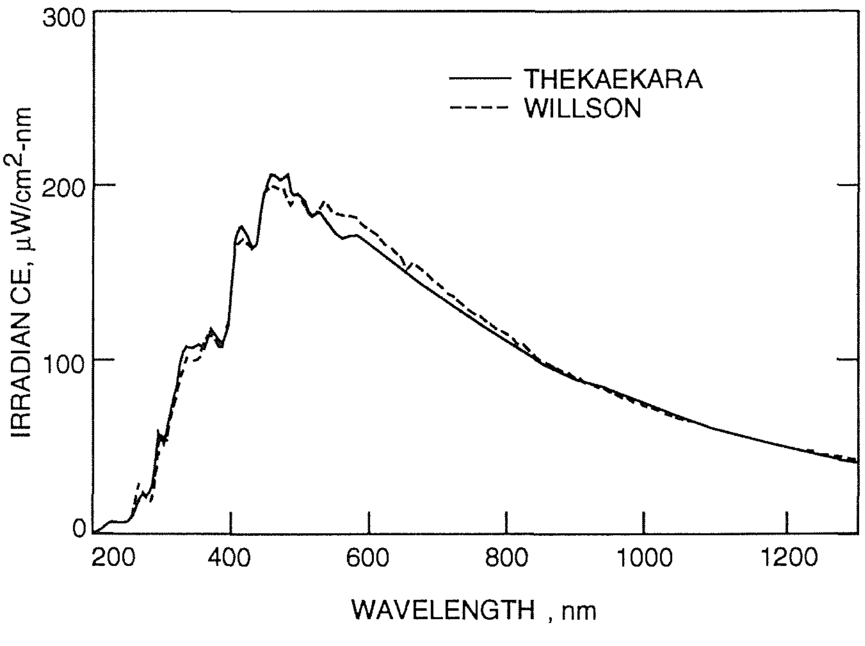

FIGURE 2.3. THE AM0 AND AM1.5 SOLAR SPECTRA

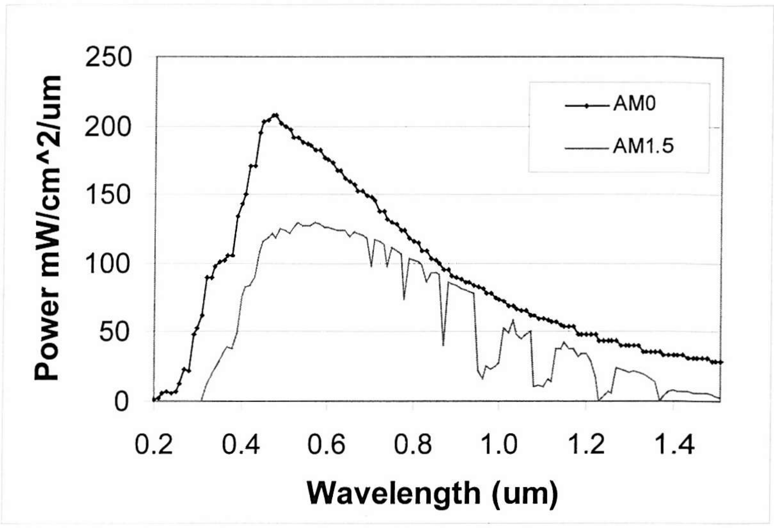

FIGURE 2.4. ATOMIC ARRANGEMENT IN THE DIAMOND AND ZINCBLENDE F.C.C. BRAVAIS LATTICES

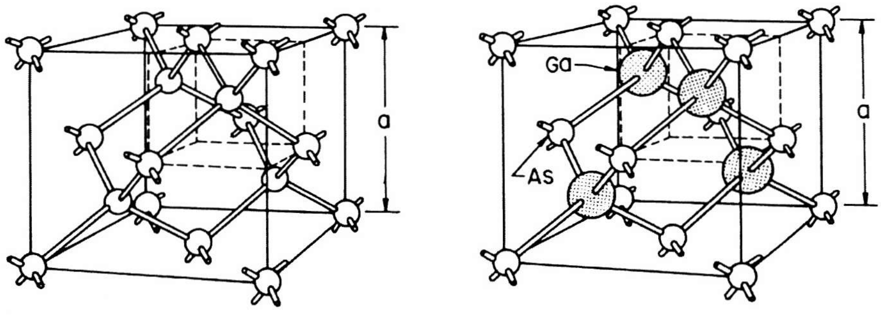

FIGURE 2.5. SIMPLIFIED ENERGY BAND DIAGRAM OF A SEMICONDUCTOR

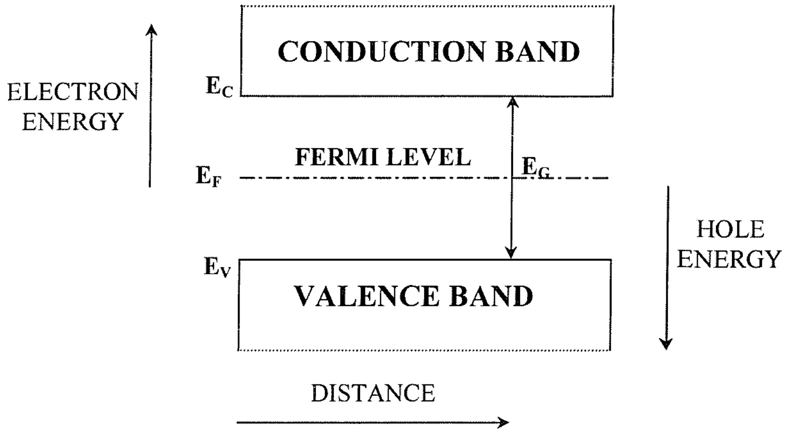

FIGURE 2.6. (a) *SPACE-CHARGE DISTRIBUTION OF AN ABRUPT P-N JUNCTION IN THERMAL EQUILIBRIUM. THE DASHED LINES INDICATE THE MAJORITY CARRIER DISTRIBUTION TAILS*
(b) *ELECTRIC FIELD DISTRIBUTION*
(c) *POTENTIAL VARIATION WITH DISTANCE*
(d) *ENERGY BAND DIAGRAM*

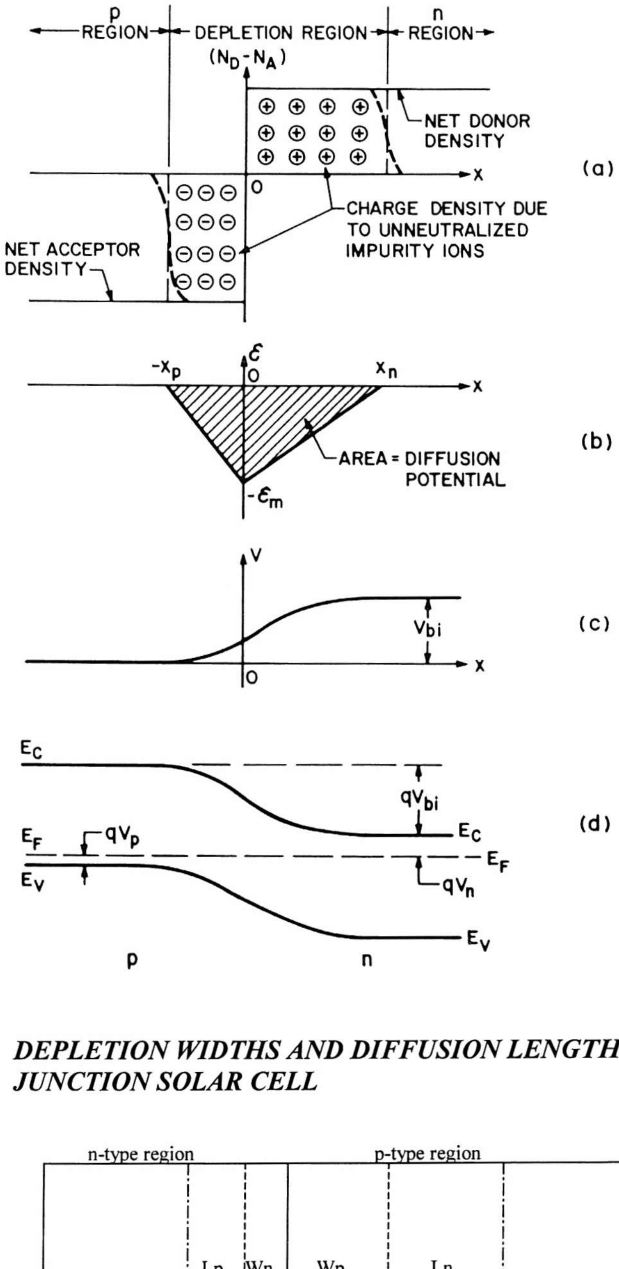

FIGURE 2.7. *DEPLETION WIDTHS AND DIFFUSION LENGTHS IN AN IDEALISED P-N JUNCTION SOLAR CELL*

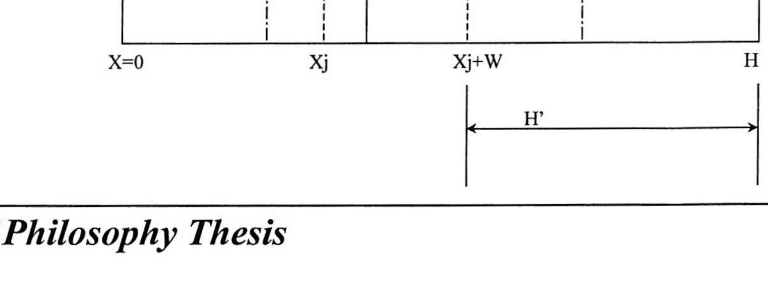

FIGURE 2.8. SCHEMATIC REPRESENTATION OF A SILICON P-N JUNCTION SOLAR CELL

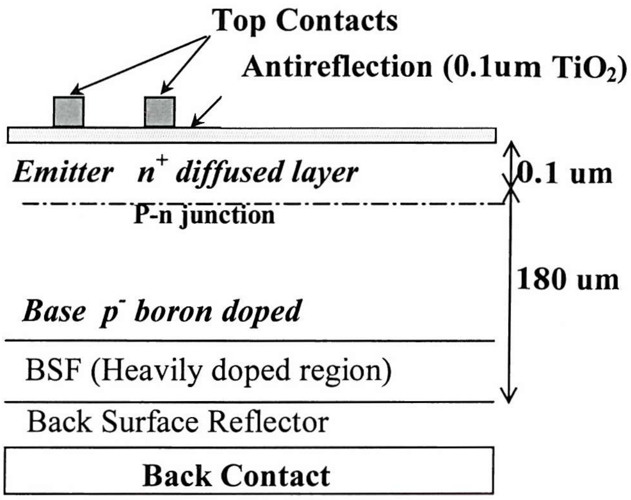

FIGURE 2.9. IDEALISED EQUIVALENT CIRCUIT OF A SOLAR CELL

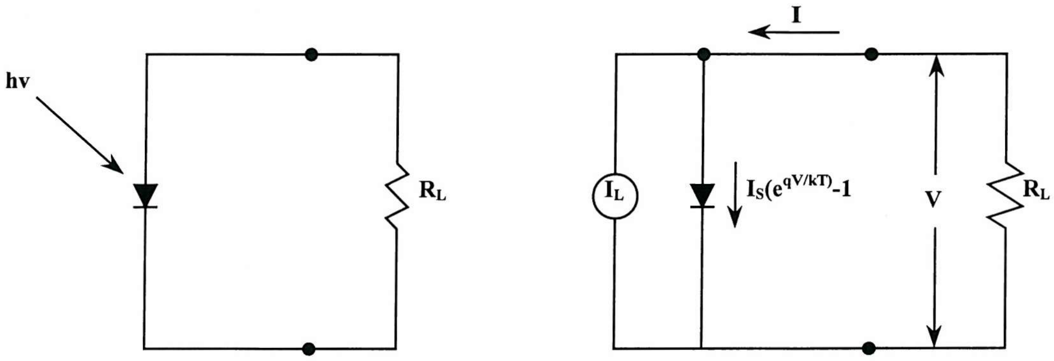

FIGURE 2.10. CURRENT-VOLTAGE CHARACTERISTICS OF AN ILLUMINATED SOLAR CELL

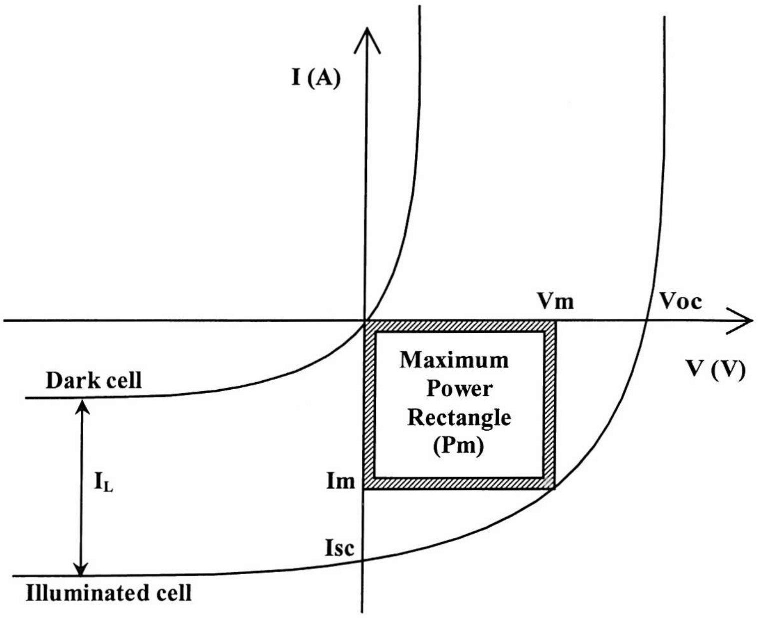

FIGURE 2.11. (a) RADIATIVE RECOMBINATION IN DIRECT BAND GAP SEMICONDUCTORS
(b) RADIATIVE RECOMBINATION IN INDIRECT BAND GAP SEMICONDUCTORS

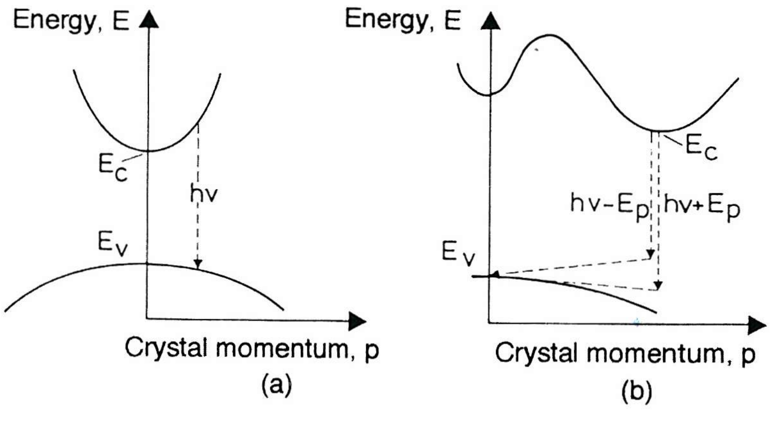

FIGURE 2.12. (a) AUGER RECOMBINATION IN THE CONDUCTION BAND
(b) AUGER RECOMBINATION IN THE VALENCE BAND

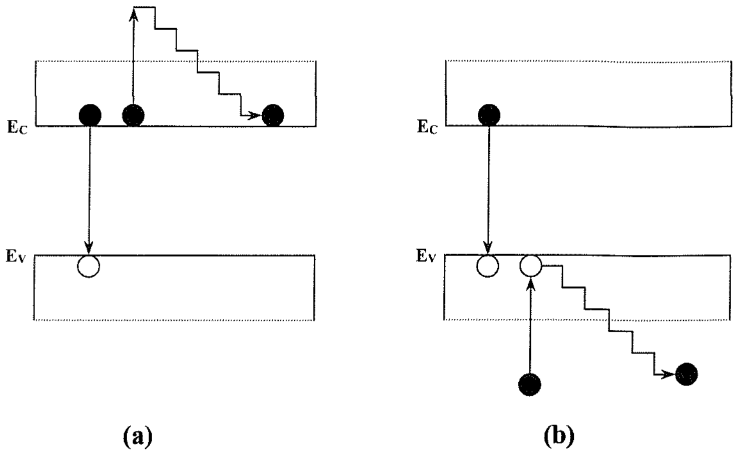

FIGURE 2.13. (a) TWO STEP RECOMBINATION PROCESS VIA A TRAPPING LEVEL WITHIN THE FORBIDDEN GAP OF A SEMICONDUCTOR
(b) SURFACE STATES LYING WITHIN THE FORBIDDEN GAP AT THE SURFACE OF A SEMICONDUCTOR

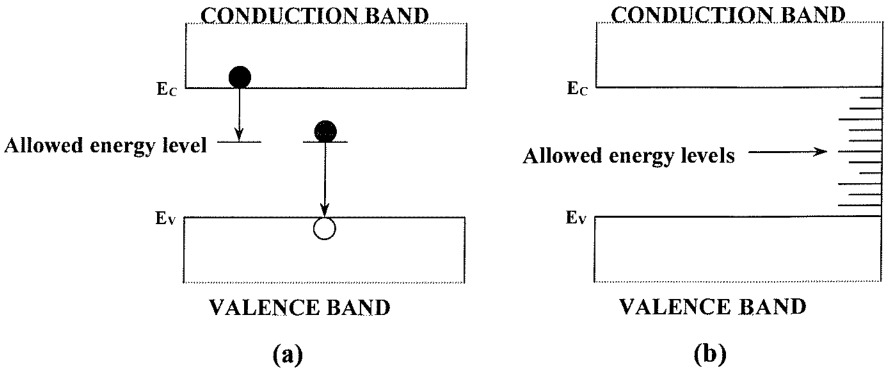

CHAPTER THREE

RADIATION DAMAGE AND DEFECTS IN SILICON

3.1 Introduction

Solar cells operating on a satellite are exposed to fluxes of energetic or fast massive particles. These may include electrons, protons, neutrons, or ions trapped in the van Allen belts. These particles can cause atomic displacements which disrupt the periodic structure of the lattice and interfere with the movement of minority carriers within the semiconductor. These particles have mass, energy and usually charge so they can interact with the material in several ways. As an energetic charged particle enters the surface of a material it slows down more or less continuously by interactions with the electrons and nuclei in the material and the type of interactions vary with the speed of the projectile.

Collisions with the nuclei can displace these atoms from their lattice sites, forming interstitials and vacancies. Thermally activated diffusion processes then cause the defects produced to interact with each other, the dopant, and impurities, to form defect pairs, clusters, and complexes. The nature of semiconductors means that the addition of a small amount of impurities can modify the electrical properties of the material and a small amount of deep levels will have a similar effect. The minority carrier lifetime for example is controlled by very small concentrations of deep centres, and determines device properties such as storage and switching times, luminescent efficiency of light emitting diodes, threshold current of lasers, and excess currents in junctions and photodiodes.

Luminescence[1] has been widely used with great success in the study of shallow centres, because of its sensitivity, speed and spectroscopic nature. Measurement techniques such as Electron Paramagnetic Resonance (EPR)[2,3,4], Local Vibrational Mode (LVM) and infrared absorption[5] have been used to identify the chemical composition and structure of deep levels. Transient techniques such as Deep Level Transient Spectroscopy (DLTS)[6] have provided information about the electrical properties of deep levels and this has helped considerably to further the understanding of deep levels and their effect on devices. The complete understanding of deep level defects and their effects on device performance can therefore only be attained through a combination of characterisation techniques. This chapter is based upon several references which describe the concepts of radiation damage[7,8,9,10] and the defects produced[11,12,13,14] (see also[15,16,17,18]).

3.2 The Principles of Radiation Damage in Solar Cells

There are two principle forms of interaction of charged particles with matter, inelastic and elastic collisions. In an inelastic collision, the projectile loses energy and the target particle gains energy, but the sum total of kinetic energies after the collision is generally less than the kinetic energies the particles had before collision. The energy difference goes into excitation of the electrons in the material, mostly by ionisation. Inelastic collisions are primarily between the incident particle and the electron cloud of the target material.

Inelastic collisions are the most probable process in the interaction between space radiation and semiconductor materials and are the primary mechanism for energy loss in the target[7,10]. Once the velocity of the moving ion is much less than the velocities of the electrons at the top of the Fermi distribution, it is improbable that electrons can be excited. To within a factor of approximately two the incident particle reaches this velocity at an energy, in keV, which is equal to its atomic weight. This estimate is independent of the target material. The limiting energy for ionisation E_I is therefore around 1keV for protons, 2keV for deuterons, 28keV for Si and 70keV for a Ga atom. Below these incident energies the collisions are primarily elastic so ionisation losses may be neglected.

An elastic collision occurs when an incoming particle collides with a target atom giving it a certain amount of energy and losing the same amount of energy in the process. The total kinetic energy of the projectile-target system is conserved in elastic collisions, and no energy is dissipated in electron excitation. Elastic collisions are the interactions that cause displacement damage which is responsible for the degradation of solar cell performance.

3.2.1 Displacement Damage

Elastic collisions are commonly classified according to the energies of the incident particles. At higher energies the incident particle can partially penetrate the electron cloud surrounding the target atom and this is known as a Rutherford collision. At lower energies where the electron cloud is not penetrated the collisions are treated as though the particles were hard elastic spheres, and these interactions are known as hard sphere collisions. The displacements caused by the interaction of the incident charged-particle beam with the target atom are known as primary displacements. It is quite probable that these “primaries” will have enough kinetic energy to produce additional or secondary displacements. The secondary displacements will almost always be of the hard sphere type.

In an elastic collision the moving and stationary atoms interact with a screened Coulomb potential energy of the form

$$V(r) = \frac{\left(Z_1 Z_2 q^2\right)}{r} \exp\left(\frac{-r}{a}\right) \qquad \textbf{(3.1)}$$

The screening radius (a) is given by the approximate relation

$$a \cong \frac{a_0}{\sqrt{\left(Z_1^{\frac{2}{3}} + Z_2^{\frac{2}{3}}\right)}} \qquad \textbf{(3.2)}$$

where r = Atomic separation
Z_1 = Atomic number of moving particle
Z_2 = Atomic number of stationary particle
a_0 = Bohr radius of hydrogen ($\approx 5.3*10^{-9}$ cm)

If the energy of the incoming particle is high enough r will be quite small and equation 3.1 reduces two the classical Coulomb repulsion between the two charged particles. If the incident particle has sufficient energy to come closer than distance a, to the target particle, the collision will be of the Rutherford type but if it has less than this energy the collision will be of the hard sphere type. This critical energy, E_A, can be calculated using[19]

$$E_A = 2E_R \frac{\left(M_1 + M_2\right)}{M_2} Z_1 Z_2 \sqrt{Z_1^{\frac{2}{3}} + Z_2^{\frac{2}{3}}} \qquad \textbf{(3.3)}$$

where E_R = Rydberg energy ($= q^2/2a_0 \approx 13.6$ eV)
M_1 = Mass of the incident particle
M_2 = Mass of the struck particle
a_0 = Bohr radius of hydrogen ($\approx 5.3*10^{-9}$ cm)

The collisions will therefore become hard-sphere like when the energy of the incident particle becomes << E_A. For protons incident on Si the collisions will be hard-sphere like if the incident energies are less than $E_A \approx 1.03$keV.

One of the most important considerations is the transfer of energy to an atom in the target. The maximum energy transfer, T_m, will occur in a head-on collision and the maximum kinetic energy transfer to the target atom in the non-relativistic case (where the incoming particle has a kinetic energy E and mass M_1) can be shown to be

$$T_m = \frac{4M_1M_2}{(M_1+M_2)^2}E \tag{3.4}$$

When electrons are the incident particles they must have high velocities because of their small mass in order to dislodge lattice atoms. A relativistic version of equation 3.4 must therefore be used for T_m

$$T_m = \frac{2mE}{M_2}\left(\frac{E}{mc^2}+2\right)\cos^2\theta \tag{3.5}$$

where m = Electron mass (1/1823 in atomic mass units)
M_2 = Atomic weight of target atoms (69.72 for Ga, 28 for Si)
mc^2 = Mass-energy equivalence of the electron (0.511 MeV)
θ = Scattering angle of the displaced atom with respect to the incident direction of the electrons (θ is related to the deflection angle ϕ of the scattered electron by $\phi = \pi - 2\theta$)

The maximum energy transfer will occur when $\theta = 0$. For example the maximum energy a 1MeV electron can transfer to a Si atom is 155 eV.

3.2.2 Atomic Displacements

Energetic electrons or protons entering an absorber lose almost all of their energy by collision with the electron cloud in the absorber. Only rarely does the energetic particle come close enough to a nucleus for an energy transfer to occur because an atom has a diameter of around 10^{-8} cm, while the nucleus has a much smaller diameter of around 10^{-13} cm. Nevertheless interactions with the nucleus do occur and when the incident particles come close enough to a nucleus they can give it enough energy to permanently displace it from its lattice site. These displaced atoms and their associated vacancies undergo other reactions which often involve dopant atoms, and finally form stable defects which produce significant changes in the equilibrium carrier concentrations and the minority carrier lifetime.

An energetic particle must have more than a specific threshold energy to be able to displace an atom from its lattice site. The atom itself must receive a certain energy, known as the displacement energy, for it to be removed sufficiently far from its lattice site that it does not return there. In silicon displacement energies ranging between 11.0 and 12.9 eV have been measured[20,21,22]. The threshold energy, E_t and the displacement energy E_d may be calculated from equation 3.4 for protons

$$E_d = \left(\frac{4M_p M_2}{(M_p + M_2)^2} \right) E_t \qquad \textbf{(3.6)}$$

Similarly the threshold energy for electrons can be calculated from equation 3.5

$$E_d = \frac{2mE_t}{M_2} \left(\frac{E_t}{mc^2} + 2 \right) \cos^2 \theta \qquad \textbf{(3.7)}$$

3.2.3 Secondary Displacements

When an atom is knocked out of its lattice site it may have considerable kinetic energy and become a projectile itself. For particles above the threshold energy the probability of an atomic displacement can be described in terms of a displacement cross-section along with an average number of secondary displacements induced by the primary displacement. Using this concept the number of displacements can be estimated from the relationship

$$N_d = n_a \sigma_d \bar{\nu} \Phi \qquad \textbf{(3.8)}$$

where N_d = Number of displacements per unit volume

n_a = Number of atoms per unit volume of absorber

σ_d = Displacement cross-section (see[9] for derivation)

$\bar{\nu}$ = Average number of displacements per primary displacement including the primary, averaged over the energy spectrum of primary knock-ons

Φ = Radiation fluence (particles/cm^2)

The number of displacements produced by a knock on of energy T, assuming the secondary collisions occur by hard-sphere collisions, has been calculated as[23]

$$\begin{aligned} \nu(T) &= 1 && 0 < T < 2E_d \\ \nu(T) &= \frac{T}{2E_d} && 2E_d < T < E_i \\ \nu(T) &= \frac{E_i}{2E_d} && T > E_i \end{aligned} \tag{3.9}$$

The average number of displacements, $\bar{\nu}$, is calculated by averaging v over the energy spectrum of the knock-on atoms[8]

$$\bar{\nu} = \frac{1}{2}\left(\frac{T_m}{T_m - E_d}\right)\left(1 + \ln\frac{T_m}{2E_d}\right) \tag{3.10}$$

The rate of displacement production of an incident particle of energy E can now be computed and this is shown for electrons in silicon in Figure 3.1. and for protons in silicon in Figure 3.2.[10].

If these displacement rates are multiplied by the incident particle fluence then the rates will be displacements per unit volume. The total number of displacements produced by an incident particle is an integral of the displacement rates over the energy range E to 0 if the particle stops in the material, and over E to E_0 if the particle emerges from the target with energy E_0. Values for the stopping power and range for electrons have been calculated in various materials[24,25] and they have also been determined for protons in various materials[26]. It should be noted that a beam of 1MeV electrons will travel 0.23 cm through silicon before losing all its energy but 1MeV protons will only penetrate 15.6 μm and will therefore come to rest inside a standard silicon solar cell. It can also be shown that the damage distribution produced by electrons and protons is very different. As the energy of the electron decreases it produces a slowly decreasing rate of displacements/cm (Figure 3.1.) and most of these particles will pass through the cell. On the other hand as the energy of a proton decreases, it produces a very rapidly increasing displacement rate, so that most of the displacements are produced near the end of its trajectory which are in a very active region of a silicon solar cell.

3.2.4 Minority Carrier Lifetime

The main effect of the displacements produced by radiation is a disruption of the periodic lattice structure, resulting in a decrease of the minority carrier lifetime. This lifetime is inversely proportional to the recombination rate therefore the lifetime contributions caused by the various sets of recombination centres can be summarised as

$$\frac{1}{\tau}=\frac{1}{\tau_0}+\frac{1}{\tau_e}+\frac{1}{\tau_p} \qquad \textbf{(3.11)}$$

where τ = Final minority carrier lifetime
τ_0 = Minority carrier lifetime before irradiation
τ_e = Minority carrier lifetime due to electron irradiation
τ_p Minority carrier lifetime due to proton irradiation

The behaviour of lifetime upon each type of irradiation is classically described by the equation[27]

$$\frac{1}{\tau}=\frac{1}{\tau_0}+K_\tau\Phi \qquad \textbf{(3.12)}$$

where τ = Final minority carrier lifetime
τ_0 = Minority carrier lifetime before irradiation
K_τ = Damage Coefficient
Φ = Radiation Fluence

When analysing solar cells however, minority carrier diffusion length is more applicable and is related to the lifetime by

$$L=\sqrt{D\tau} \qquad \textbf{(3.13)}$$

where L = Diffusion length
D = Diffusion constant

The diffusion constant (cm^2s^{-1}) is related to the carrier mobility ($cm^2V^{-1}s^{-1}$) by the *Einstein relations*

$$D_n = \mu_n\left(\frac{kT}{q}\right) \tag{3.14}$$

$$D_p = \mu_p\left(\frac{kT}{q}\right) \tag{3.15}$$

and the carrier mobility's can be calculated from the doping densities in silicon using the empirical relationships[28]

$$\mu_n = 65 + \left(\frac{1265}{1+\left(\frac{N}{8.5*10^{16}}\right)^{0.72}}\right) \tag{3.16}$$

$$\mu_p = 47.7 + \left(\frac{447.3}{1+\left(\frac{N}{6.3*10^{16}}\right)^{0.76}}\right) \tag{3.17}$$

The behaviour of lifetime can now be given in terms of the diffusion length and also the minority-carrier capture cross-section

$$\Delta\left(\frac{1}{L^2}\right) = \frac{1}{L_0^{\,2}} - \frac{1}{L_\phi^{\,2}} = K_L\phi = \sum\frac{I_{ri}\sigma_i v\phi}{D} \tag{3.18}$$

where L_ϕ = Final minority carrier diffusion length

L_0 = Initial minority carrier diffusion length

K_L = Diffusion length damage coefficient ($K_L=K_\tau/D$)

I_{ri} = Introduction rate of the ith recombination centre by irradiation

σ_i = Minority-carrier capture cross-section of ith recombination centre

v = Thermal velocity of minority-carriers

D = Diffusion coefficient

3.3 Shallow and Deep Levels

Defect and impurity states in semiconductors are usually divided into two classes known as shallow and deep states. The term shallow states is taken to be synonymous with simple substitutional hydrogenic impurities at which the electron is weakly bound by a Coulomb potential in an extended state with the effective mass of the appropriate band edge. In a deep state the impurity potential is more strongly localised, causing the electrons to be tightly bound and resulting in an energy level which is deeper in the bandgap than that of the hydrogenic impurities. In Si and GaAs the deep levels are more than around 0.05eV from the band edges and are not thermally ionised at room temperature[11,12].

The properties of defect energy levels have been thoroughly described in References 13,14,15 and 16 that form the basis of section 3.3. In a neutral semiconductor an electron trap can be defined as a defect for which the electron capture rate c_n is much larger than the hole capture rate c_p. In contrast a recombination centre is one for which both c_n and c_p are large. The defect has capture cross-sections σ_n and σ_p for electrons and holes respectively. The electron and hole capture rates are given by

$$c_n = \sigma_n v_n n \tag{3.19}$$

$$c_p = \sigma_p v_p p \tag{3.20}$$

where n and p are the electron and hole concentrations and v_n and v_p are the thermal velocities.

3.3.1 Carrier Capture by Neutral Donors and Acceptors

Impurities that have one valence electron more than the lattice atom they replace are usually shallow donors. For example when substituting a silicon atom by a phosphorus atom, four of the five valence electrons are consumed by covalent bonding with neighbouring silicon atoms, while the fifth remains weakly bound. The binding of this "spare" electron with the positively charged phosphorus ion takes place due to the Coulomb forces. Since in semiconductors the Coulomb interaction is weakened by the large dielectric constant, the spare electron binding energy appears to be very small, and consequently the effective Bohr radius is very large. Small values of the electron effective mass in many semiconductors may also aid in decreasing the binding energy and increasing the Bohr radius[29].

A hydrogen-like model known as the effective mass theory[30,31,32] describes well the shallow donor in the simplest case of an isotropic square-energy spectrum of electrons. The energy required for ionising a donor in this case is given by

$$E_D = \frac{e^4 m}{2\kappa^2\hbar^2} \tag{3.21}$$

where E_D = Ionisation energy
m = Electron effective mass (usually smaller than m_0)
κ = Dielectric constant
e = Magnitude of electronic charge
= Normalised Plank's constant =h/2π

This equation gives excellent agreement with experimental results obtained for excited states but has had limited success for the ground state. Better agreement between calculated and measured values for ground state energies is obtained using the pseudo-impurity model developed by Pantelides[33]. Nevertheless adapting this equation to obtain an estimate of ground state energies in silicon gives 10^{-2} to 10^{-3}eV which is far less than the forbidden gap value therefore the effective mass approximation in calculating E_D is justified. The dimension of a shallow neutral donor is characterised by its Bohr radius a_B

$$a_B = \frac{\hbar^2\kappa}{me^2} = 0.53\times10^{-8}\left(\frac{\kappa m_0}{m}\right)(cm) \tag{3.22}$$

The magnitude of a_B is of the order of tens of lattice spacings, which makes it possible to use the dielectric constant when describing the Coulomb electron-ion interaction in a crystal.

Shallow acceptors usually have one less electron than the atoms in the crystal lattice. Boron for example is a shallow acceptor in silicon. While substituting a silicon atom, a dangling bond appears which is saturated by an electron belonging to a neighbouring silicon atom. The boron ion therefore acquires a negative charge while a free hole appears in its proximity. Negatively charged remainders can bind holes due to weak Coulomb forces. Equations 3.21 and 3.22 therefore still apply in the simplest case for the binding energy of acceptor holes and the bound state radii assuming m is regarded as the effective mass of a hole.

Other impurity atoms produce deep energy levels in the forbidden bandgap, the radii of these impurity atoms being small. They cannot be described in the framework of the effective mass approximation. Positions of the energy levels depend upon the chemical nature of impurities. Deep centres can usually be formed in different charge states and the same impurity atom may be both an acceptor and a donor.

The large ionisation energy of deep levels implies a strong potential that localises the wave function of the electron or hole near the site of the defect. A consequence of localisation in real space is a delocalization in k-space, which results in two important properties. First the deep states tend to be non-radiative rather than radiative recombination centres, because the large extent in k-space allows the defect to couple strongly with a variety of phonons. Second the entire band structure must be involved in a theoretical description of the defect, making calculations of the energies of deep states much more complicated than calculations of the shallow states of the substitutional impurities typically used as dopants in semiconductors.

The tight binding approximation can be used to describe the main physical properties of the bulk semiconductor but any quantitative theory of deep levels in semiconductors must incorporate the electron-electron interactions. The Hartree approximation for example assumes any point defect will create a disturbance such that the electron density will be modified from its perfect crystal repartitions. Regions with accumulation or depletion of charge induce an electrostatic potential which must be included in the treatment in a self-consistent manner. The same conclusions hold for the more refined techniques such as the Hartree-Fock or the "local density" formalism. For deep levels that arise from neutral defects the self-consistent potential is practically identical to what would occur in a metal of the same density and is well approximated by a linearized Thomas-Fermi treatment. To approximate the self-consistent potential for the neutral vacancy for example the Thomas-Fermi method can be used and shows that this potential is very efficiently screened in space (i.e. in a radius of 2.07Å which is smaller than the nearest neighbour distance of 2.3Å)[14].

3.3.2 Carrier Capture by Isolated Attractive Centres

Thomson[34] was the first to consider the problem of capture by attractive ions. The capture cross-section is the product of a cross-sectional area of a sphere or radius r_T and the probability that an ion loses its kinetic energy due to collision during the time it spends inside this sphere. This cross-section is therefore

$$\sigma = \frac{4}{3}\pi r_T^{\,2}\frac{r_T}{l} \tag{3.23}$$

where l is the mean free path. The probability of collision during the passage of an ion through a sphere of radius r_T is given by the factor r_T/l.

To explain the enormous cross-sections of the capture by attractive centres in semiconductors Lax[35] employed the idea that the capture occurred with a higher probability not in the ground state but in highly excited states. Abakumov[36] refined this idea and obtained a formula for the capture cross-section similar to Thomson's formula, the main difference being that the factor r_T/l is replaced by $r_T/v\tau_\varepsilon$, where v is the electron velocity and τ_ε is the relaxation time of the electron energy

$$\sigma = \frac{4}{3}\frac{\pi}{l_0}\left(\frac{e^2Z}{\kappa kT}\right) \tag{3.24}$$

where eZ is the centre charge. Therefore the capture cross-section is inversely proportional to the cube of the temperature. The length l_0 does not depend on the electron energy or on the temperature and is related to the mean free path l by

$$l_0 = v\tau_\varepsilon = l\frac{kT}{2ms^2} \tag{3.25}$$

These formulas give a precise solution to the problem of the cross-section of the cascade capture by an isolated attractive centre under the condition $kT>>ms^2$ when electron-phonon collisions are quasi-eleastic.

At low temperatures ($kt<<ms^2$) electron-phonon collisions are essentially inelastic and in the case of the Coulomb potential $V(r)==e^2Z/\kappa r$ the capture cross-section is[29]

$$\sigma = \frac{8\pi}{45 l_0}\left(\frac{e^2 Z}{\kappa kT}\right)\left(\frac{e^2 Z}{\kappa m s^2}\right)^2 \tag{3.26}$$

This result differs from the expression 3.24 by the factor $2(kT)^2/15(ms^2)^2$. Therefore as the temperature decreases below ms^2, the capture cross-section growth slows down and σ becomes inversely proportional to the temperature. Thus for $kT \ll ms^2$, $\sigma \propto T^{-1}$ and for $kT \gg ms^2$, $\sigma \propto T^{-3}$.

3.3.3 Carrier Capture by Repulsive Centres

The binding energy of a carrier at a deep centre is determined by the short-range part of the potential, thus in a number of cases a carrier can be bound to the centre even if the long-range Coulomb field of the centre is repulsive. The principle factor in this case is the existence of a Coulomb potential barrier to be overcome by an electron so that it can reach the centre. This potential barrier under real conditions is overcome by tunnelling. Tunnelling probability grows as the electron energy rises and this results in an exponential dependence of the cross-section on the electron temperature T_e in the form[29]

$$\sigma \alpha \exp\left(\frac{-T_0}{T_e}\right)^{\frac{1}{3}} \tag{3.27}$$

where kT_0 is the characteristic energy equal to

$$kT_0 = 27\pi^2 E_B = \frac{27\pi^2 m Z^2 e^4}{2\hbar\kappa^2} \tag{3.28}$$

E_B is the Bohr energy for shallow donors (acceptors). This dependence has been observed many times in the study of capture by deep repulsive centres as a function of temperature. An electron that has tunnelled through the Coulomb barrier loses a large portion of its energy in the transition to a bound state. This energy might be given to the lattice via the emission of a large number of phonons simultaneously. In such a many-phonon process, the excess energy loss probability also depends exponentially on the initial energy of an electron. This results in a modification of equation 3.28 replacing T_e by T_e^* where

$$\frac{1}{kT_e^*} = \frac{1}{kT_e} + \frac{1}{\varepsilon_{ph}} \tag{3.29}$$

3.4 Defects in Silicon Solar Cells

The removal of an atom from its lattice site to a crystal surface creates a vacancy which is referred to as a Schottky defect. When an atom is removed from the lattice site to an interstitial position and therefore remains proximate to the vacancy the defect is referred to as a Frenkel pair. Individual point defects however are often attracted to each other and form clusters with the other defects and impurities present in the material. Dopant atoms are not normally considered to be defects because their presence is required in certain concentrations but they may combine with self-interstitials or impurity atoms to form complexes[37].

Irradiation with high energy electrons or other energetic particles has frequently been used to introduce controlled densities of defects into semiconductors[15,38,39]. Annealing of the samples allows the thermal stability of the defects and the evolution of the defect complexes to be determined. The defect introduction rate and annealing behaviour determined from the DLTS spectra can then be tentatively correlated with the EPR spectra to determine a defects' composition. External perturbations have then been applied to obtain additional information about deep levels and can be used to confirm the identification of the defect in question. Uniaxial stress has been used for example in conjunction with EPR measurements to confirm the identity of the divacancy and the oxygen-vacancy pair[3,4].

Low temperature measurements have identified the native vacancy in silicon[40] however the interstitial has been inferred but never directly observed. Kimerling[41] has proposed a reaction sequence for interstitial defects, initiating from the self-interstitial, which summarises the defect reactions as a hierarchical scheme. Watkins[2,3,4] and Corbett[5] contributed much of the original work on point defects in silicon and concluded that the vacancy and the interstitial can exist in many charge states which manifest themselves as levels within the forbidden gap.

3.4.1 The Vacancy

The formation of vacancies in silicon has been reviewed[42] and some of the main concepts are given here. The damage process which forms isolated vacancies has been deduced from experimental studies[43,44] using high energy electrons at 4.2 and 20.4K. The primary process is the formation of a Frenkel pair but because the interstitial silicon atom is mobile even at 4.2K, the Frenkel pair either annihilates itself or the interstitial escapes and is trapped at some impurity, leaving the isolated vacancy.

The presence of the vacancy lowers the symmetry of the crystal which results in a distortion of the local region as a result of the Jahn-Teller effect. The Jahn-Teller effect is the splitting of the degenerate states under low symmetry distortions and Bourgoin and Lannoo[13,14] provide a detailed review of the lattice distortion and the Jahn-Teller effect and include theoretically and experimentally observed distortions caused by the vacancy in silicon.

The vacancy is only observed during low temperature studies. After irradiation at 300K it complexes with other vacancies or impurities which results in a further series of defects such as the divacancy or the A centre. The isolated vacancy has been observed in the single positive V^+ and single negative V^- charge states by EPR and although no EPR spectrum is observed for charge states where there is no resultant spin, two further levels V^0 and $V^=$ have been deduced[44]. All the charge states result in a distortion of the lattice to differing degrees, depending on the number of electrons trapped.

The EPR results suggest a simple linear combination of atomic orbital-molecular orbital (LCAO-MO) model for the various charge states of the vacancy. Figure 3.3. shows this model and the atomic orbitals are the broken bonds (a,b,c,d) of the four atoms surrounding the vacancy. For V^{++} (Figure 3.3.(a)) two electrons go into the a_1 orbital paired off, the defect is diamagnetic and no EPR is observed. For V^+ (Figure 3.3.(b)) the third electron goes into the t_2 orbital, a tetragonal Jahn-Teller distortion results, lowering the symmetry to D_{2d}. The resulting orbital containing the unpaired electron is spread equally over the four atoms. In forming V^0 (Figure 3.3.(c)) the next electron goes into b_2, paired off, further enhancing the tetragonal distortion. In this state the defect is again diamagnetic and no EPR is observed. Figure 3.3.(d) shows the V^- charge state where the additional electron goes into the degenerate e orbital and an additional Jahn-Teller distortion occurs. The unpaired electron is now localised on only two of the four atoms, consistent with the observation in the V^- spectrum.

The re-orientation of the defect between its different equilibrium conditions is possible. This phenomenon has been observed experimentally by EPR studies[45] after irradiation at 4 and 20K and a difference in activation energy for the vacancy in n and p-type material has been found[46]. Electrons are sometimes trapped in pairs at a defect providing no paramagnetism and this was explained by Anderson[47] who suggested that there was an effective negative correlation energy for electrons trapped at the defects. It was suggested that the energy gain associated with electron pairing in the dangling bonds of a defect, coupled with a large lattice relaxation, might overcome the Coulombic repulsion of the two electrons, supplying a net effective attractive interaction between the electrons (negative U) at the site. This effect was then shown to occur in the vacancy and the boron interstitial[40].

Considering the vacancy the inverted level order implies that V^+ is a metastable state with a reaction which will lower the energy of the system

$$2V^+ \rightarrow V^0 + V^{++} \quad \textbf{(3.30)}$$

This is confirmed by the fact that V^+ is only seen by photoexcitation at cryogenic temperatures[48]. The kinetics of the V^+ decay after the light is turned off reveals an activation energy of around 0.057 eV which can be interpreted as

$$V^+ \rightarrow V^0 + h^+ \quad \textbf{(3.31)}$$

locating the donor state at $\approx E_V + 0.05$. The vacancy level at $E_V + 0.13$ (see Table 3.1) can be observed by DLTS[49,50] and this has been attributed to the second donor state of the vacancy[40] which implies a two stage emission in the DLTS experiment

$$V^{++} \rightarrow V^+ + h^+ \rightarrow V^0 + 2h^+ \quad \textbf{(3.32)}$$

Normally each hole emission would be detected separately in a DLTS study as the temperature is scanned because for a normal defect a hole is bound progressively more strongly as other holes are removed, requiring successively higher temperatures for each ionisation event. The inverted negative U order however means that the hole involved in the first ionisation is bound more strongly than the second, therefore at a temperature where the first hole is emitted the second hole should follow immediately. In the DLTS experiment therefore only a single peak is observed which reflects the level at $E_V + 0.13$ and its amplitude is a factor of two larger than normal[51].

3.4.2 The Divacancy

It is well known that divacancies are formed as secondary events via agglomeration of two single vacancies however there is also evidence to suggest that divacancies can created by a direct collision process during electron irradiation when two adjacent atoms are knocked out of the lattice[52,53]. The divacancy has been observed using EPR studies[3] to form upon the disappearance of the vacancy signal. It arises from the combination of the V^+ and the V^- charge states resulting in a single donor and two acceptor levels in the forbidden bandgap.

The structure and annealing kinetics of the divacancy in silicon have been extensively investigated by EPR studies[53,54,55]. The single positive charge state of the divacancy exhibits Jahn-Teller distortion as four of the silicon neighbours pull together by pairs to form weak reconstructed bonds, leaving the unpaired electron to divide between the dangling bonds on the two silicon atoms at the opposite extremes of the defect (Figure 3.4.)[53,55]. A very similar case is observed for the single negative charge state for which three electrons are accommodated between the two atoms.

There has been much discussion over the past thirty years on the position and behaviour of the different deep levels which the divacancy introduces into the bandgap. The donor level has been identified in the literature with two groups of experimental values centring around $E_V + 0.19$ eV[56,57,58] and $E_V + 0.25$ eV[39,49,55,59] respectively and these values have all been attributed to the divacancy. Londos[60] however noted an increase in activation energy with increasing temperature and postulated that the lower value was due to a silicon self-interstitial which is loosely bonded to the divacancy. As the temperature is increased this divacancy-interstitial complex was assumed to disassociate, liberating the self-interstitial. Recent evidence however[61,62] suggests that this difference could be attributed to the conversion of the divacancy at $E_V + 0.19$eV to another defect at $E_V + 0.24$ eV, possibly a divacancy-oxygen complex.

The negative charge state of the divacancy (VV^-) was also first identified using EPR[53,54,55] and DLTS studies have determined the energy level to be between $E_C - 0.46$

eV[63,64] and E_C – 0.41 eV[65,66]. The divacancy also has another level that has been observed by DLTS at around Ec-0.23eV[63,65,66] which has been attributed to the double negative ($VV^{=}$) charge state of the divacancy. The annealing characteristics of the divacancy vary according to sample preparation and electron irradiation energy[66]. The defects induced by higher irradiation energy usually anneal the fastest and the divacancy usually anneals at temperatures lower than 300^0C. The presence of oxygen can also enhance the annealing rate as it acts as a sink for the divacancy.

3.4.3 The Vacancy Oxygen Pair

The interstitial oxygen atom (O_I) is the dominant trap for the mobile vacancy producing the vacancy-oxygen pair (VO) or the A centre which can be detected by EPR[67], infra-red[68] and DLTS[38,65]. The A centre forms a single acceptor level at Ec - 0.17eV which has been compared to the divacancy[69] and these two defects have been implicated in lifetime control, largely from DLTS and other electrical measurements and are therefore possible recombination centres. The concentration of the A centre is reduced considerably after 5 hours at 317^0C, possibly annealing to form another defect. The irradiation energy has been observed to have little effect on the annealing rate[69] but material history, such as high initial oxygen concentration, significantly affects the annealing rate. However it is not only the oxygen concentration which affects the rate, the concentration of other impurities must also be considered.

3.5 Interstitial Defects

The interstitial is mobile at 4K and therefore does not remain in the locality of the vacancy[45,46] after irradiation. The interstitial has never been directly detected but other defects which form as a direct result of interaction with the interstitial have been observed. The work on interstitial defects was pioneered by Watkins and Corbett[70] and was reviewed by Kimerling[41] who summarised the interstitial defect reactions in a hierarchical structure and this is shown in Figure 3.5.. However this work is by no means definitive because interstitial reactions and interactions are still the subject of much discussion and speculation[71] such as the metastability of certain defects[72,73,74].

The sequence of interstitial defect reactions is initiated by the creation of the self-interstitial which may be trapped by a substitutional atom. This in turn is ejected from its lattice site as an interstitial itself. This process is known as the *Watkin's Replacement Mechanism*[41,43] which is generally valid for group three impurity reactions and is shown in Figure 3.6. The hierarchical reaction sequence described by Kimerling suggests that, depending upon the relative impurity concentrations, the carbon and boron interstitial are formed preferentially. Many other interstitial reactions were investigated using annealing studies and are also discussed by Kimerling[41].

3.5.1 Boron Related Interstitial Defects

The boron interstitial can exist in different charge states, $B_I^{(0/+)}$ and $B_I^{(-/0)}$, which exhibit themselves as levels within the bandgap at E_C–0.13eV and E_C–0.45eV respectively[40]. At low temperatures the boron interstitial is mobile and it undergoes diffusion limited reactions with other impurities and defects such as the interstitial carbon and oxygen. It is therefore expected that interstitial defects will be related to the boron concentration. The boron interstitial exhibits negative U properties[40] which may explain the association of B_I-B_I which results from the attraction of two oppositely charged B_I, $2B_I^0 \rightarrow B_I^+ + B_I^-$.

The boron interstitial-oxygen interstitial pair (B_IO_I) has been observed at Ec-0.26eV after 1MeV room temperature irradiation[39] and is commonly referred to as E1. A similar level was identified after 4.2K irradiation and annealing of the boron interstitial[40,74]. The B_IO_I is proportional to the boron concentration in the material[39,40]. It is doubly positive when empty and positive when occupied and this has been inferred from capture cross section measurements.

Further evidence for the structure of this defect as B_IO_I is provided by comparing the defect production rate as a function of both the oxygen and boron content of the material[75]. Defect production is proportional to the oxygen content and relies upon the amount of boron present with a linear relationship up to a boron concentration of $2*10^{16}$ cm^{-3}. However at higher concentrations the production rate is suppressed or saturated suggesting competition from another defect for the B_I.

A defect related to the B_I at Ec-0.29eV that anneals at 200^0C has been observed[39,40,75] and a proportional relationship with both oxygen and boron resulted in the suggestion of the defect structure as BOV[39,40]. However later work has shown the level to be independent of oxygen and therefore a preferential identification of the B_IC_S pair has been made[75].

Drevinsky[75] found the introduction rate of E1 to be sensitive to the carbon concentration and to saturate at high oxygen concentrations suggesting competition for oxygen by some other defect. B_IO_I is stable until 150-250^{0}C therefore the B_IO_I and C_IO_I defects are reaction controlling defects and may be labelled as secondary defects. As E1 anneals, a deep level commonly referred to as H4 has been observed to grow[75] and this has been described as the dissociation of B_IO_I to form B_IC_S. If the carbon concentration is greater than 6.5×10^{16} cm^{-3} then concentrations of B_IC_S are five times lower than in the material with a carbon concentration of 2.5×10^{15}. This suggests the presence of a stronger competitor for the carbon such as C_IO_I. A level has been identified as C_IO_I and dominates in high oxygen material suppressing reactions between the boron related defects.

B_IC_S is the dominant defect observed in floatzone material with boron concentrations below 1×10^{16} cm^{-3} whilst B_IB_S dominates in more highly doped material. It is competition from this defect for available boron in material with B>1×10^{16} cm^{-3} that causes a saturation in the formation of B_IO_I. B_IB_S persists, although at only 20% of the initial concentration, even after annealing at 400^{0}C in N_2. The formation of B_IC_S at 200^{0}C has been correlated with a degradation in charge carrier lifetime of silicon solar cells[76] as recovery is observed simultaneously when this defect anneals. Earlier work noted reverse annealing at 200^{0}C[77].

3.5.2 Carbon Related Interstitial Defects

Carbon atoms normally occupy substitutional lattice sites (C_S) and the activation energy for diffusion has been determined as 3.1eV[78]. The carbon interstitial C_I at Ev+0.28eV[39] is formed when a mobile silicon interstitial produced by irradiation collides with a carbon substitutional atom, ejecting the carbon atom from its lattice site. The activation energy for diffusion of this defect has been observed as 0.38eV[79] therefore at relatively low temperatures carbon interstitials begin to migrate by thermally activated diffusion to be captured by various traps. The C_I has been observed by EPR[80], DLTS[81] and IR absorption[82] experiments. Initially the C_I in room temperature irradiated silicon was found to be stable up to 250^{0}C using EPR[83] but it was also successfully annealed at room temperature[84]. More recently however in a comprehensive study of carbon in silicon, its stability has been observed to be 70-100^{0}C[58].

When the C_I anneals a new peak in the DLTS spectrum forms at around E_V+0.36eV. It has been suggested that the C_I may be trapped by the A centre which gives rise to the carbon oxygen vacancy (COV) complex[39,85]. A signal due to the COVV complex was observed using EPR[86] and another related level was observed as COV which is a donor level at Ev+0.33eV. Controlled thermal and radiation induced annealing experiments however demonstrated the preferential growth of the high and low temperature sides of the peak and confirmed that this peak was actually due to two defects[87]. These two mechanisms were labelled as a fast component and a slow component. Analysis of capture cross section results[88] showed two defects contributing to the Ev+0.36eV peak with $\sigma_1=5\times10^{-18}$ cm^{-2} and $\sigma_2=1.2\times10^{-16}$ cm^{-2} with σ_1 contributing to 90% of the peak and σ_2 contributing 10%.

This was further investigated by scanning DLTS and this confirmed the presence of two closely spaced defects at Ev + 0.344eV and Ev + 0.370eV. They were at first identified as COVV and $C_SSi_IC_S$[89] but this was later changed to C_IO_I and $C_SSi_IC_S$[90]. The C_IO_I has been identified by EPR[85], Photoluminescence[91] and IR absorption[92] and the $C_SSi_IC_S$ has also been observed using EPR[93], Photoluminescence[94] and IR absorption[95]. The proportion of each defect depends on the oxygen concentration present in the material therefore the C_IO_I centre will dominate in Czochralski material whereas the $C_SSi_IC_S$ will dominate in float-zone material[90,96].

3.6 Summary

The defects described in this chapter have all been collated into Table 3.1 which shows some of the more common defects which have been observed in irradiated silicon and includes some of the different results obtained for the divacancy. The capture cross-sections shown are for majority carriers and some of the diffusion activation energies (DAE) are also given. The behaviour of the defects formed by the irradiation damage, and their interaction with other defects[97] is slowly being understood[41], thus permitting the application of this knowledge to devices such as solar cells[98].

Recent evidence however has suggested that the irradiation induced defect identification is far from complete[61,62] even for well known centres such as the divacancy. There have also been problems linking device response to displacement damage[99]. The relation of the microscopic defect behaviour and the macroscopic parameters such as the reverse current, the generation, or the recombination lifetime is proving difficult to unravel with several different defects being implicated in lifetime control.

Table 3.1 Some of the more common Defects Observed in Boron Doped Silicon

Defect	Symbol	Energy Level	Ref	Notes
Vacancy	$V^{(+/++)}$	$E_v + 0.13$ eV	40,51	Anneals, 30 mins 215K[63]
Vacancy	$V^{(0/+)}$	$E_v + 0.05$ eV	40	
Vacancy	$V^{(=)}$	DAE=0.18eV	48	
Vacancy	$V^{(++)}$	DAE=0.32eV	100,2	
Vacancy	$V^{(0)}$	DAE=0.45eV	100	
Divacancy	$VV^{(-/0)}$	$E_C - 0.46$eV	63,64	
Divacancy	$VV^{(-/0)}$	$E_C - 0.41$eV	65,66	$CCS^{66} \approx 1.62\times10^{-16}$
Divacancy	$VV^{(=/-)}$	$E_C - 0.23$eV	63,65,66	$CCS^{66} \approx 0.60\times10^{-16}$ $DAE^{66} \approx 1.47$eV Binding AE ≈ 1.6eV
Divacancy	$VV^{(0/+)}$	$E_V + 0.19$eV	56,57,58	$CCS^{65} \approx 4\times10^{-16}$ $CCS^{38} \approx 2\times10^{-16}$
Divacancy ?	$VV^{(0/+)}$	$E_V + 0.25$eV	39,49,55	
Divacancy	$VV^{(0/+)}$	$E_V + 0.19$eV	61,62	$CCS^{62} \approx 3.6\times10^{-16}$
Divacancy-oxygen ?	$VVO^{(0/+)}$	$E_V + 0.24$eV	61,62	$CCS^{62} \approx 1\times10^{-14}$
Vacancy-oxygen	$VO^{(-/0)}$	$E_C - 0.17$eV	67,68,69	
Boron Interstitial	$B_I^{(0/+)}$	$E_C - 0.13$ eV	40	
Boron Interstitial	$B_I^{(-/0)}$	$E_C - 0.45$ eV	40	Anneals at 240K
Boron-oxygen	$B_IO_I^{(+/++)}$	$E_C - 0.26$eV	58,64,75	Anneals at 150-200^{0}C
Boron-carbon	B_IC_S	$E_V + 0.26$eV	58	Anneals at 400^{0}C
Boron-boron	B_IB_S	$E_V + 0.30$eV	58,75	Anneals above 400^{0}C
Carbon Interstitial	C_I	$E_V + 0.28$	39	$CCS \approx (\geq 1\times10^{-17})^{80}$ Anneals at 70-100^{0}C[58] $DAE^{79} = 0.38$eV
Carbon-oxygen	C_IO_I	$E_V + 0.344$eV	90	$CCS \approx (1.2\times10^{-16})^{88}$ Anneals at 350-450^{0}C[91]
Carbon-silicon-carbon	$C_SSi_IC_S$	$E_V + 0.37$eV	90	$CCS \approx (5 \times 10^{-18})^{88}$
Carbon-carbon	C_IC_S	$E_C - 0.16$eV	83,101	

3.7 References

---

[1] Bergh, A.A., and Dean, P.J., Proc. IEEE 60, p.156, (1972).

[2] Watkins, G.D., An EPR study of the lattice vacancy in silicon., J. Phys. Soc. Japan, 18, Supp.2, p.22, (1963).

[3] Watkins, G.D., and Corbett, J.W., Defects in Electron Irradiated Silicon: EPR of the divacancy, Physical Review B, 138, 2A, p.543, (1964).

[4] Watkins, G.D., and Corbett, J.W., Defects in irradiated silicon: Electron spin resonance of the silicon A centre, Physical Review, 121, p.4, (1961).

[5] Corbett et al: Defects in Semiconductors: Infrared absorption of the Si A centre, Physics Review B, 121, 4, p.1015, (1961).

[6] Lang, D.J., DLTS: A new method to characterise traps in semiconductors, Journal of Applied Physics, 45, p.3023, (1974).

[7] Tada, H.Y., et al, Solar Cell Radiation Handbook, JPL Publication 82-69, Jet Propulsion Laboratory, California Institute of Technology, (1982).

[8] Dienes, G.J., and Vineyard, G.H., Radiation effects in solids, Interscience Publishers Inc., New York, (1957).

[9] Seitz, F., and Koehler, Displacement of atoms during irradiation, Solid State Physics 2, p.305, Academic Press, (1956).

[10] Anspaugh, B., GaAs Solar Cell Radiation Handbook, JPL Publication 96-9, Jet Propulsion Laboratory, California Institute of Technology, (1996).

---

[11] Blood, P. and Orton, J.W.: The electrical characterisation of semiconductors: majority carriers and electron states, Techniques of Physics, Vols. 13 & 14, Academic Press, London, (1992).

[12] Blood, P. and Orton, J.W.: The electrical characterisation of semiconductors: minority carriers, Techniques of Physics, Vols. 13 & 14, Academic Press, London, (1992).

[13] Bourgoin, J., and Lannoo, M., Point defects in semiconductors II: Experimental aspects, Springer-Verlag, Berlin, (1983).

[14] Lannoo, M., and Bourgoin, J., Point defects in semiconductors I: Theoretical aspects, Springer-Verlag, Berlin, (1981).

[15] Miller, G.L., et al, Annual review of materials science, Palo Alto: Annual reviews Inc., Vol. 7, p.377, (1977).

[16] Grimmeiss, H.G., Annual review of materials science, Palo Alto: Annual reviews Inc., Vol. 7, p.341, (1977).

[17] Milnes, A.G., Deep impurities in semiconductors, John Wiley, New York, (1973).

[18] Jaros, M., Deep levels in semiconductors, Adam Hilger, Bristol, (1982).

[19] Bohr, N., The penetration of atomic particles through matter, Kgl. Danske Videnskab. Selskab, Mat.-fys. Medd., 18, 8, (1948).

[20] Loferski, J.J., and Rappaport, P., Radiation damage in Ge and Si detected by carrier lifetime changes – Damage thresholds, Physical Review, 111, 2, p.232, (1958).

---

[21] Flicker, H., et al, Radiation defect introduction rates in n- and p-type silicon in the vicinity of the radiation damage threshold, Physical Review, 128, 6, p.2557, (1962).

[22] Gersimenko, N.N., et al, Threshold energy for the formation of radiation defects in semiconductors, Soviet Physics – Semiconductors, 5, 8, p.1439, (1972).

[23] Kinchin, G.W., and Pease, R.S., The displacement of atoms in solids by radiation, Reports on progress in Physics, 18, 1, (1955).

[24] Berger, M.J., and Seltzer, S.M., Tables and energy losses and ranges of electrons and positrons, NASA SP-3012, (1964).

[25] Berger, M.J., and Seltzer, S.M., Additional stopping power and range tables for protons, Mesons and electrons, NASA SP-3036, (1966).

[26] Janni, J.F., Atomic data and nuclear data tables, Proton range-energy tables, 1keV-10GeV, Part 1 Compounds and Part 2 Elements, Academic Press, New York, (1992).

[27] Rosenzweig, W., et al, Solar cell degradation under 1-MeV electron bombardment, Bell. Syst. Tech. Jou., 42, p..399, (1963).

[28] Caughey, D.M., and Thomas, R.E., Carrier mobility's in silicon empirically related to doping and field, Proc. IEEE, 55, p.2192-2193, (1967).

[29] Abakumov, V.N., Perel, V.I., and Yassievich, I.N., Nonradiative recombination in semiconductors, Modern problems in condensed matter sciences, Volume 33, North-Holland, (1991).

[30] Luttinger, J.M., and Kohn, W., Phys. Rev., 97, p.869, (1955).

---

[31] Kohn, W., and Luttinger, J.M., Phys. Rev., 98, p.915, (1955).

[32] Kohn, W., Solid State Phys., 5, p.257, (1957).

[33] Pantelides, S.T., and Sah, C.T., Phys. Rev. B., 10, p.638, (1974).

[34] Thomson, J.J., Philos. Mag., 47, p.337, (1924).

[35] Lax, M., Phys. Rev., 119, p.1502, (1960).

[36] Abukamov, V.N., and Yassievich, I.N., Zh. Eksp. & Teor. Fiz., 71, p.657, (Sov.Phys.-JETP), (1976).

[37] Fahey, P.M., et al, Review of point defects in silicon, Rev. Mat. Phys., 61, 2, (1989).

[38] Kimerling, L.C., Defect states in electron bombarded silicon: capacitance transient analysis, Inst. Phys. Conf. Ser. No. 31, p.221, (1977).

[39] Mooney, P.M., Cheng, L.J., Suli, M., Gerson, J.D., and Corbett, J.W.: Defect energy levels in boron doped silicon irradiated with 1MeV electrons, Physics Review B, 15, 8, p.3836, (1977).

[40] Watkins, G.D., and Troxell, J.R., Negative-U properties for point defects in silicon, Phys. Rev. Lett., 44, 9, p.59, (1980).

[41] Kimerling, L.C., Asom, M.T. and Benton, J.L., Interstitial Defect Reactions in Silicon, Materials Science Forum, 38-41, p.141, (1989).

[42] Pantelides, S.T. (ed), Deep Centres in Semiconductors, (Chapter 3, The lattice vacancy in silicon, Watkins, G.D.), Gordon and Breach Science Publishers, (1986).

---

[43] Watkins, G.D., A review of EPR studies in irradiated silicon, Radiation Damage in Semiconductors, p.97, Dunod, Paris, (1964).

[44] Watkins, G.D., in Lattice Defects in Semiconductors, Inst. Phys. Conf. Series 23, p.1, London, (1975).

[45] Watkins, G.D., EPR of a trapped vacancy in boron doped silicon, Physical Review B, 13, 6, p.2511, (1976).

[46] Watkins, G.D., An EPR study of the lattice vacancy in silicon, Jnl. Phys. Soc. Jap., 18, II, 22, (1968).

[47] Anderson, P.W., Phys. Rev. Lett. 34, p.953, (1975).

[48] Watkins, G.D., et al, in Lattice Defects in Semiconductors, Huntley, F.A. (ed), The Institute of Physics Conf. Series 23, p.1, (1974).

[49] Kimerling, L.C., in Radiation Effects in Semiconductors, Urli, N.B. (ed), The Institute of Physics Conf. Series 31, p.221, (1976).

[50] Brabant, J.C., et al, in Radiation Effects in Semiconductors, Urli, N.B. (ed), The Institute of Physics Conf. Series 31, p.200, (1976).

[51] Baraff, G.A., Kane, E.O., and Schluter, M., Theory of the silicon vacancy: An Anderson negative U system, Physical Review B, Vol. 21, 12, (1980).

[52] Corbett, J.W., and Watkins, G.D., Phys.Rev. Lett. 7, p.341, (1961).

[53] Corbett, J.W., and Watkins, G.D., Phys.Rev. 138, p.555, (1965).

[54] Cheng, L.J., et al, 1.8-, 3.3-, and 3.9-u bands in irradiated silicon: correlations with the divacancy, Phys. Rev, 152, 2, p.761, (1966).

[55] Watkins, G.D., and Corbett, J.W., Phys.Rev. 138, A543, (1965).

[56] Londos, C.A., Divacancy production in low temperature electron irradiated silicon, Phys. Rev. B 35, 14, p.7511, (1987).

[57] Asghar, M., et al, Study of alpha-radiation induced deep levels in p-type silicon, J. Appl. Phys., 73, 9, p.4240, (1993).

[58] Drevinsky, P.J., and Caefer, C.E., Carbon-related defects in silicon, Conf. Proc. Defect Control in Semiconductors, 1, p.341, (1990).

[59] Lee , Y.H., et al, A transient capacitance study of radiation induced defects in aluminium doped silicon, Phys. Stat. Sol., 57, p.697, (1980).

[60] Londos, C.A., Phys. Stat. Sol. A, 132, p.43, (1992).

[61] Trauwaert, M.A., et al, Low temperature anneal of the divacancy in p-type silicon: A transformation from V_2 to V_xO_y complexes ?, Appl. Phys. Lett., 66, 22, p.3057, (1995).

[62] Trauwaert, M.A., et al, On the behaviour of the divacancy in silicon during anneals between 200 and 350^0C, Materials Science Forum, 196-201, p.1147, (1995).

[63] Londos, C.A., J. Phys. Chem. Sol., 47, p.1147, (1986).

[64] Londos, C.A., Room temperature irradiation of p-type silicon, Phys. Stat. Sol. A, 92, p.609, (1985).

---

[65] Brotherton, S.D., et al, Photoionization cross section of electron irradiation induced levels in silicon, J. Appl. Phys., 54, 9, p.5112, (1983).

[66] Evwaraye, A.O., and Sun, E., Electron irradiation induced divacancy in lightly doped silicon, J. Appl. Phys. 47, p.9, (1976).

[67] Watkins, G.D., and Corbett, J.W., Defects in irradiated silicon: Electron spin resonance of the silicon A centre, Physical Review, 121, p.4, (1961).

[68] Corbett et al: Defects in Semiconductors: Infrared absorption of the Si A centre, Physics Review B, 121, 4, p.1015, (1961).

[69] Brotherton, S.D. and Bradley, P., Defect production and lifetime control in electron and γ-irradiated silicon, J. Applied Physics, 53, p.5720, (1982).

[70] Watkins, G.D., Defects in irradiated silicon: EPR and electron nuclear double resonance of interstitial boron, Physical Review B, Vol.12, 12, p.5824, (1975).

[71] Nubile, et al, Defects in low temperature electron-irradiated silicon p-type silicon, J. Appl. Phys., 72, 7, p.2673, (1992).

[72] Song, L.W., et al, A molecular rebonding bistable defect in silicon: the interstitial carbon-substitutional carbon pair, Materials Research Society Symp. Proc. Volume 104: Defects in electronic materials, p.79, (1988).

[73] Chantre, A., Metastable defect reactions in silicon, Materials Research Society Symp. Proc. Volume 104: Defects in electronic materials, p.37, (1988).

[74] Bains, S.K., and Banbury, P.C., A bistable defect in electron irradiated boron doped silicon, J. Phys. C: Solid State Phys. 18, L109-116, (1985).

---

[75] Drevinsky, P.J., et al, Proc. 13th. Int. Conf. Def. Semiconductor., p.807, (1984).

[76] Drevinsky, P.J., et al, Influence of oxygen and boron on defect production in irradiated silicon, Materials Research Society Symp. Proc. Volume 104: Defects in electronic materials, p.167, (1988).

[77] Weinberg, I., and Schwartz, C.K., Origin of reverse annealing in radiation damaged silicon solar cells, Appl. Phys. Lett.., 36, p.693, (1980).

[78] Newman, R.C., (in Oxygen, Carbon, Hydrogen and Nitrogen in Crystalline Silicon, *ed.* Mikkelsen, J.C., *et al*, 1986), Proc. Mats. Res. Soc. Symp., **59**, p.403, (1985).

[79] Tipping, A.K., and Newman, R.C., *Semi. Sci. Tech.*, **2**, p.315, (1987).

[80] Lee, Y.H., *et al*, Carbon interstitial in electron irradiated silicon, *Sol. St. Comm.*, **21**, p.109, (1977).

[81] Kimerling, L.C., et al, Defect states in proton bombarded silicon at T < 300K, Inst. Phys. Conf. Ser., 46, p.273, (1979).

[82] Woolley, R., and Lightowlers, E.C., Electronic and vibrational absorption of interstitial carbon in silicon, *Materials Science Forum, 10-12, Defects in Semiconductors*, p.929-934, (1986).

[83] Brower, K.L., EPR of a Jahn-Teller distorted (111) carbon interstitiality in irradiated silicon, Physical Review B, Vol. 9, 6, (1974).

[84] Benton, J.L., et al, Identification of interstitial carbon related defects in silicon, Materials Research Society Symp. Proc. Volume 104: Defects in electronic materials, p.85, (1988).

---

[85] Lee, Y.H., et al, EPR of a Carbon-Oxygen-Divacancy complex in irradiated silicon, Phys. Stat. Sol. (a), 41, 637, (1977).

[86] Davies, G., et al, A model for radiation damage effects in carbon doped crystalline silicon, Semiconductor. Sci. Tech., 2, p.524, (1987).

[87] Fredrickson, A.R. et al, Radiation induced carbon related defects in p-type silicon, J. Appl. Phys. 65, p.8, (1989).

[88] Londos, C.A., Carbon related radiation damage centres and processes in p-type silicon, Semiconductor. Sci. Tech., 5, p.645, (1990).

[89] Ferenczi, G., *et al*, Identification of the carbon associated radiation damage levels in silicon, *Materials Science Forum*, **10-12**, p.947-952, (1986).

[90] Ferenczi, G., et al, Correlation of the concentration of the carbon-associated radiation damage levels with the total carbon concentration in silicon, J. Appl. Phys, 63 (1), p.183, (1987).

[91] Trombetta, J.M., and Watkins, G.D., Identification of an interstitial carbon-interstitial oxygen complex in silicon, *Appl. Phys. Lett.*, **51**, 14, p.1103, (1987).

[92] Davies, G., *et al*, *J. Phys. C: Sol. St. Phys.*, **19**, p.841, (1986).

[93] Brower, K.L., *Phys. Rev. Lett.*, **B9**, p.2607, (1974).

[94] O'Donnell, K.P., et al, Origin of the 0.97eV luminescence in silicon, Physica 166B, p.258, (1983).

[95] Davies, G., *et al*, *J. Phys. C: Sol. St. Phys.*, **16**, p.5503, (1983).

---

[96] Vanhellemont, J., *et al*, Generation and annealing behaviour of MeV proton and 252Cf irradiation induced deep levels in silicon diodes, *IEEE Trans. Nucl. Sci.*, **41**, 3, p.479, (1994).

[97] Sun, Q., et al, Effect of carbon on oxygen precipitation in silicon, J. Appl. Phys. 67, 9, p.4313, (1990).

[98] Akhter, P., et al, Effect of oxygen and carbon impurities on the performance of silicon single crystal solar cells, Semiconductor. Sci. Tech., 6, p.135, (1991).

[99] Yamaguchi, M., *et al*, *J. Appl. Phys.* **86,** p.217, (1999).

[100] Watkins, G.D., Troxell, J.R., and Chattergee, A.P., in Defects and Radiation Effects in Semiconductors, Inst. Phys. Conf. Series 46, p.16, London (1979).

[101] Markevich, V.P. and Murin, L.I., *Sov. Phys. Semiconductor.*, **22**, 5, p574, (1988).

FIGURE 3.1. COMPUTED DISPLACEMENT RATES FOR INCIDENT ELECTRONS IN SILICON

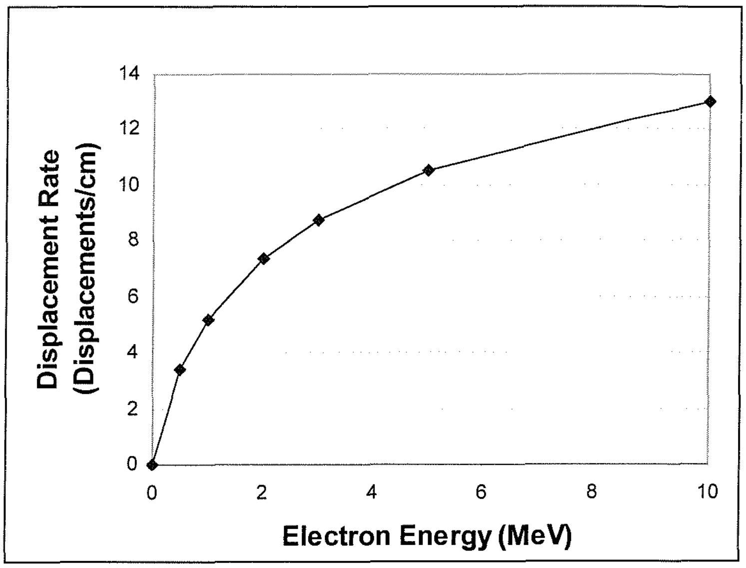

FIGURE 3.2. COMPUTED DISPLACEMENT RATES FOR INCIDENT PROTONS IN SILICON

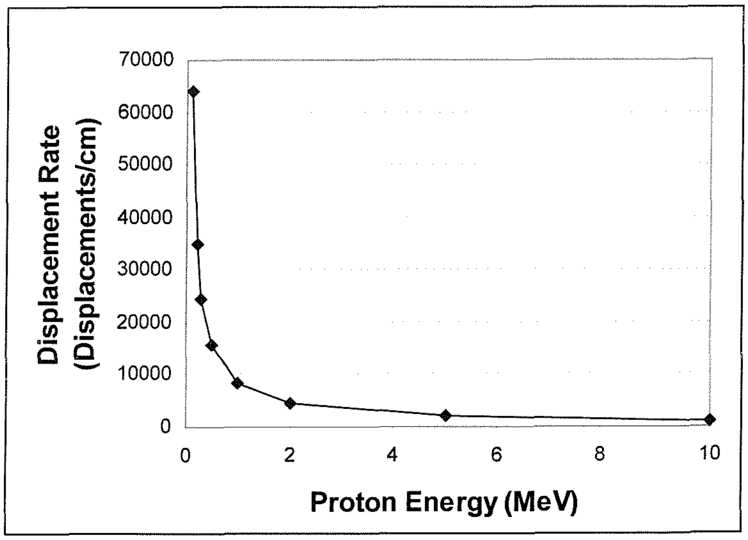

FIGURE 3.3. LCAO-MO MODEL FOR THE VARIOUS CHARGE STATES OF THE VACANCY IN SILICON DEDUCED FROM EPR STUDIES

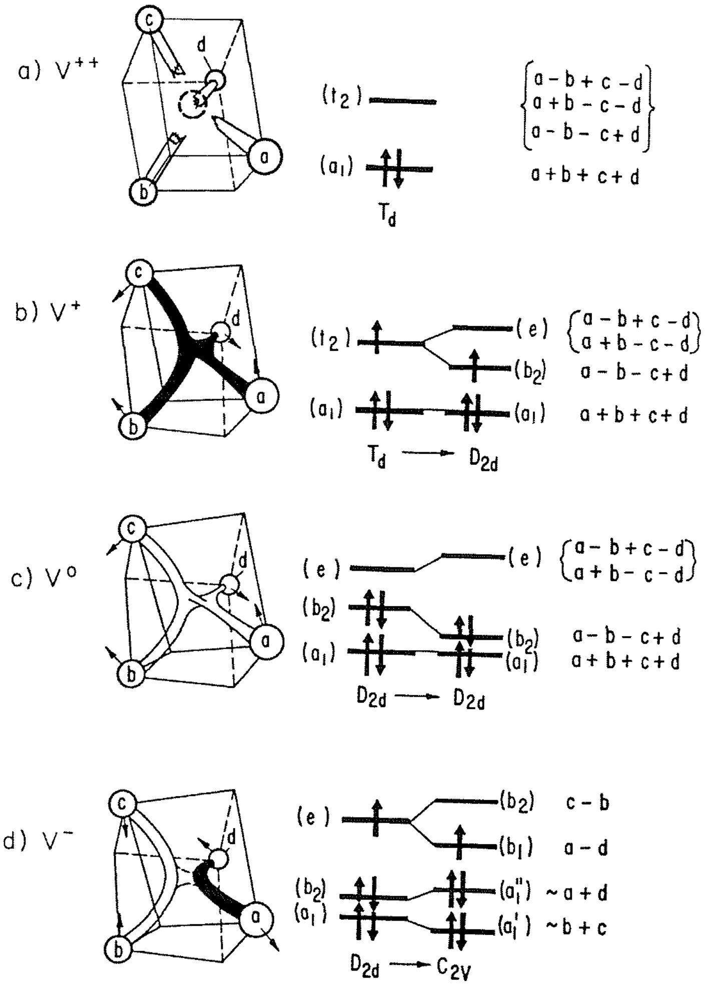

FIGURE 3.4. SIMPLE MODEL OF THE POSITIVE CHARGE STATE OF THE DIVACANCY VV^+ DEDUCED FROM EPR STUDIES

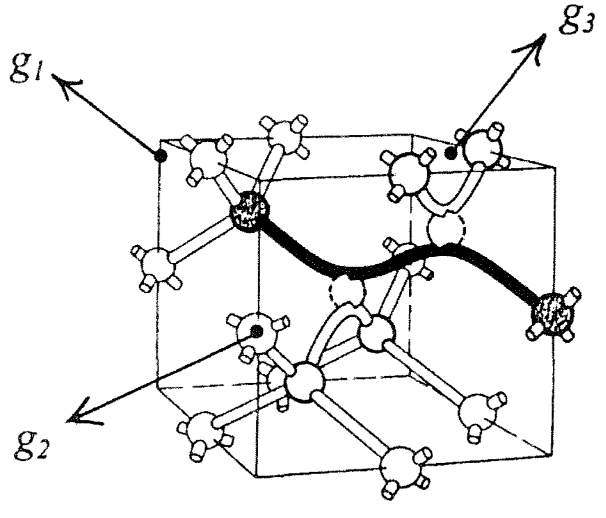

FIGURE 3.5. KIMERLINGS' INTERSTITIAL HIERARCHY

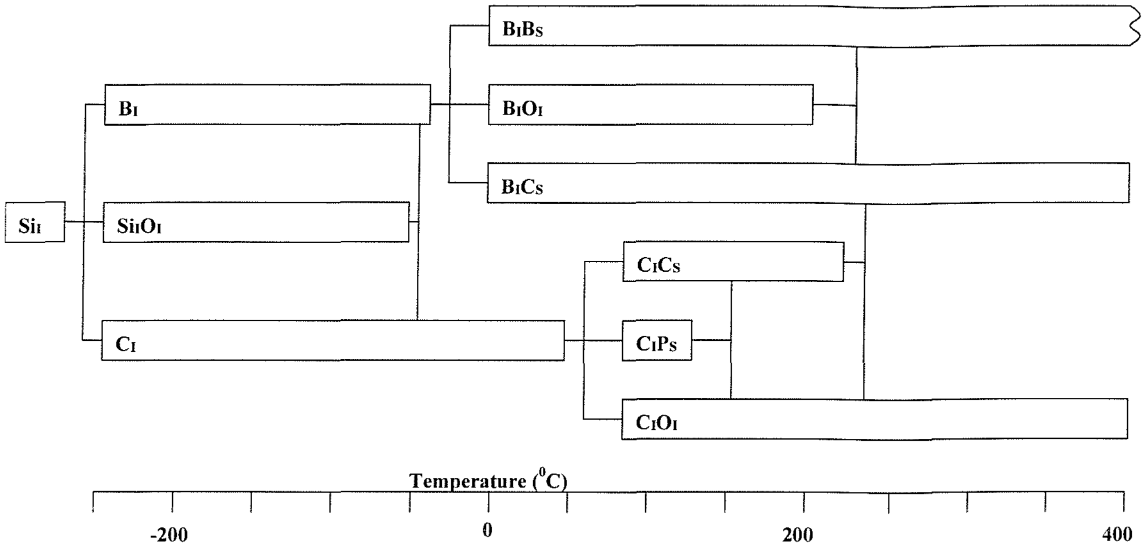

FIGURE 3.6. THE WATKINS REPLACEMENT MECHANISM FOR INTERSTITIAL DEFECT REACTIONS

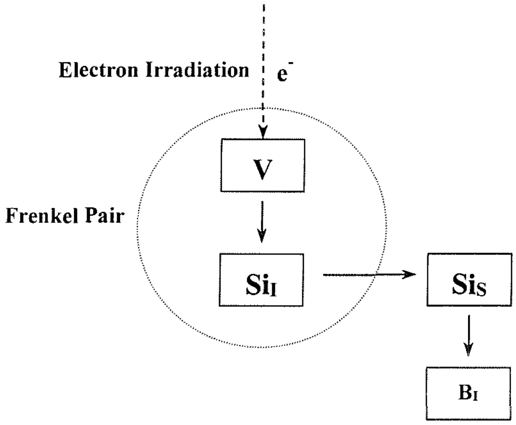

CHAPTER FOUR

DEEP LEVEL TRANSIENT SPECTRSCOPY

4.1 Introduction

The identification of defects is important in order to evaluate material quality and eliminate those defects with adverse effects. One of the first methods used to study deep level defects was the Thermally Stimulated Current (TSC)[1,2] method which observed thermally stimulated trap emptying by studying the current in excess of the normal dark current as a function of temperature. Thermally Stimulated Capacitance (TSCAP)[3] techniques evolved from Thermally Stimulated Current (TSC) methods in the early 1970's and were used to determine the approximate trap concentration and the thermal activation energy of trapped electrons and holes by monitoring capacitance changes in a semiconductor junction.

Deep Level Transient Spectroscopy (DLTS)[4] improved the sensitivity of these methods and has now become a widely used technique to characterise defects in semiconductors[5,6]. Since being introduced many varieties of this technique have evolved to cover a wide variety of applications[7,8,9,10,11,12,13,14]. Majority carriers are injected into the vicinity of the junction by a bias pulse that fills the deep level traps near the junction with majority carriers. The emission of these carriers is subsequently monitored as a function of temperature and the data is displayed in the form of a characteristic DLTS spectrum where a peak corresponds to a deep level trap[15].

A deep level is a localised state in the bulk of the semiconductor and therefore is removed from both the conduction and valence bands and is not normally ionised at room temperature. In Si and GaAs defect levels which are further than 0.05eV from the band edge are considered to be deep levels (see Section 3.3). If the position of the trap varies with respect to the Fermi level, such as within the depletion region, the occupation of the trap may be altered by the application of an external bias (see Figure 4.1. and Section 4.4).

When the outer edge of the depletion region is increased from x_0 to x_d the position of the deep level with respect to the Fermi level adjusts to a new equilibrium position. The carrier capture and emission processes that occur at these deep levels can be detected at very low concentrations as changes in the diode current or capacitance and frequently this change is exponential. The analysis of this transient and its time constant yields information such as deep level emission rate, capture cross-section and concentration and the analysis of the transient as a function of temperature can yield further information about the position of the deep level in the bandgap.

4.2 Carrier Capture and Emission

Charge carrier capture and emission processes at deep levels are controlled by the occupation and hence charge state of the level. Four processes define the occupation of a deep level: the capture (c_n) and emission of electrons (e_n) and the capture (c_p) and emission of holes (e_p). Figure 4.2. shows these capture and emission processes: 4.2.(a) and (b) represent a minority and majority carrier trap in n-type material and 4.2.(c) and (d) show a minority and majority carrier trap in p-type material[6].

The emission rate of a deep level is temperature dependent and is characterised by an exponential function; it is an intrinsic property of the deep state itself. The capture process is determined by the free carrier concentration, *n*, and by the capture cross section of the deep level, σ. In a material with *n* free electrons per unit volume moving with a thermal velocity v_n, a deep level will be exposed to a flux of nv_n electrons per unit time. If the material contains N_t deep levels with the number of deep levels occupied by electrons at any instant, n_t, then the number of electrons captured by the $(N_t - n_t)$ unoccupied states in a short time interval, Δt, is[6]

$$\Delta n_t = \sigma_n v_n n(N_t - n_t)\Delta t \qquad \textbf{(4.1)}$$

and the capture rate per unoccupied state is

$$c_n = \frac{[\Delta n_t / \Delta t]}{(N_t - n_t)} \qquad \textbf{(4.2)}$$

and therefore the capture rate

$$c_n = \sigma_n v_n n \qquad \textbf{(4.3)}$$

Similarly the capture rate for holes can be derived

$$c_p = \frac{\Delta(N_t - n_t)/\Delta t}{n_t} = \sigma_p v_p p \qquad \textbf{(4.4)}$$

Detailed balance arguments[16] show the emission rate for electrons (e_p) and holes (e_n) to be as follows

$$e_n(T) = \frac{\sigma_n v_n N_c}{g} \exp\left(-\frac{E_c - E_t}{kT}\right) \tag{4.5}$$

$$e_p(T) = \frac{\sigma_p v_p N_v}{g} \exp\left(-\frac{E_t - E_v}{kT}\right) \tag{4.6}$$

where $v_n(v_p)$ = Thermal velocity of holes (electrons)

$N_c(N_v)$ = Density of states of the conduction (valence) band

$E_c(E_v)$ = Energy level of the conduction (valence) band

E_t = Energy level of the defect in the bandgap

g = Degeneracy of the defect level

A majority carrier trap in n-type material is defined when e_n>>e_p and a minority-carrier trap is defined by e_p>>e_n.

4.3 Junction Capacitance

A p-n junction contains a neutral region, a depletion region and a transition region as shown in Figure 4.3.(a). In the neutral region there are equal concentrations of positive and negative charge therefore the space charge density is equal to zero (see section 2.4.1). In the depletion region however there are no mobile charge carriers but the ionised dopants contribute to the space charge density. The transition region is usually very small compared to the depletion region and in this section the effects of this region will therefore be neglected. This is shown in Figure 4.3.(b) and is known as the depletion approximation.

The depletion region width is changed by the application of bias and can be found at zero bias using equation 2.21. If a reverse bias V_r is applied to the p-n junction the electrostatic potential across the junction increases by V_r and therefore becomes V_{bi} - V_r hence the depletion width becomes

$$W = \sqrt{\frac{2\varepsilon_s}{q}\left(\frac{N_A + N_D}{N_A N_D}\right)(V_{bi} - V_r)} \tag{4.7}$$

For a p^+n junction $N_A >> N_D$ therefore

$$W = \sqrt{\frac{2\varepsilon_s (V_{bi} - V_r)}{qN_D}} \tag{4.8}$$

The width of the depletion region therefore increases with the application of a reverse bias voltage. The depletion capacitance in a p-n junction is linked to the depletion width by the dielectric constant ε_s

$$C = \frac{\varepsilon_s}{W} \tag{4.9}$$

Combining equations 4.8 and 4.9 gives the capacitance as a function of the reverse bias

$$\frac{1}{C^2} = \frac{2(V_{bi} + V_r)}{q\varepsilon_s N_D} \tag{4.10}$$

The application of a reverse bias will therefore increase the depletion width and hence decrease the capacitance. Equation 4.10 also shows that a plot of $1/C^2$ versus V_r will, in a uniformly doped material, be linear. The slope of the graph will give the impurity concentration and the built-in voltage can be found from the intercept.

4.4 Applied Bias and Trap Occupancy

In a p-n junction one side is usually doped to a much higher concentration than the other and therefore the depletion region will extend mainly into the lightly doped side of the junction (see Section 7.1 for example calculation). These one sided junctions can therefore be though of in the same way as a Schottky barrier. Now consider an n-type Schottky barrier containing a uniform distribution of a majority carrier trap of energy E_t. The trap acts as a donor and is positive when empty and neutral when full[6]. The occupation of the trap is largely determined by the position of the Fermi level (see Figure 4.1.(a)). At low or zero bias the depletion region width is x_0, with the half filled point at

x_2, where $E_t = E_f$, which is termed the zero crossing point. This point is assumed to be an abrupt transition therefore capture processes are equal to emission processes, $c_n = e_n$.

The region $0<x<x_0$ is known as the depletion region and the region $x_2<x<x_0$ is known as the transition region[17]. The application of an external reverse bias V_r will cause the depletion width to adjust to a new state of equilibrium (Figure 4.1.(b)). This bias will immediately alter the equilibrium conditions, causing an increase in the depletion width and a relative change in position, with respect to the Fermi level, for some deep levels within the depletion region. Deep levels that are above the Fermi level and full will emit any carriers to the nearest band edge and the transition region width λ will change from $x_0 - x_2$ to $x_d - x_1$. Hence by applying a reverse bias voltage and then removing it the traps can be emptied and then refilled in a controlled manner.

The variation of the capture rate with distance, $c_n(x)$, as a result of the variation in the number of filled traps, $n(x)$, is illustrated in Figure 4.4.. The dashed line at x_2 represents the abrupt junction with no applied bias, the distribution of filled traps, $n_t(x)$, is shown by the solid curve up to x_1 and the abrupt junction under a bias V_r is shown by the dotted line. When $x<x_2(x_1)$ emission processes dominate as $c_n<<e_n$. When $x_2(x_1)<x<x_0(x_d)$ then $c_n>>e_n$ and capture dominates.

The rate of variation in trap occupation in the depletion region is given by summing the capture and emission processes across the whole junction however in the depletion region carrier concentrations are small and capture processes may therefore be neglected

$$\frac{dn_t}{dt} = -e_n n_t + e_p(N_t - n_t) \tag{4.11}$$

For an electron trap $e_n>>e_p$ the above equation may be simplified

$$\frac{dn_t}{dt} = -e_n n_t \tag{4.12}$$

The occupation of a deep level and its participation in a transient measurement technique therefore depends upon the response time of the trapped electrons. Processes involving free electrons are fast (10^{-12} to 10^{-9} s) in comparison to the trapped electrons and are therefore considered to be instantaneous. Provided the bias fill pulse is long the trapping time τ_f will be given by

$$\tau_f = (c_n N_t)^{-1} \tag{4.13}$$

Device lifetime will therefore be controlled by the total trap concentration N_t and the capture cross section of the trap.

4.5 Capacitance Transients

The variation of trap occupation as a function of applied bias has frequently been exploited to provide detailed information about deep levels. When a diode held under reverse bias V_r is returned to its quiescent state V_q (Figure 4.5.) the free electrons now above the Fermi level (see Section 4.4) will be instantaneously emitted to the conduction band. Electrons however that are trapped by deep levels will be emitted at a characteristic rate e_n and this will form a capacitance transient that is frequently exponential (see Figure 4.5.).

The net space charge density ρ(t) during the emission process can be written

$$\rho(t) = q[N_D + N_T - n_t(t)] \tag{4.14}$$

For a large reverse bias ($\lambda<x_d$) the time dependant capacitance during the emission process at constant bias can be found by combining equations 4.10 and 4.14

$$C(t) = C(\infty)\left[1 - \frac{n_t(t)}{N_D + N_t}\right]^{\frac{1}{2}} \tag{4.15}$$

where the final capacitance ($n_t(\infty)=0$) is

$$C(\infty) = A\left[\frac{\varepsilon_s q(N_D + N_t)}{2}\right]^{\frac{1}{2}} V^{-\frac{1}{2}} \tag{4.16}$$

where $V=V_{bi}+V_r$. When N_t and $n_t<<N_d$ the change in capacitance $\Delta C(t)=C(t)-C(\infty)$ can be written as

$$\frac{\Delta C(t)}{C(\infty)} = -\frac{n_t(t)}{2N_D} \tag{4.17}$$

When a trap is fully occupied it decays as[6]

$$n_t(t) = \frac{c_n + e_p}{c_n + e_p + e_n + c_p} N_t + \frac{e_n + c_p}{c_n + e_p + e_n + c_p} N_t \exp\left(-(c_n + e_p + e_n + c_p)t\right) \quad \textbf{(4.18)}$$

The transient response is therefore

$$\frac{\Delta C(t)}{C(\infty)} = -\frac{N_t}{2N_D} \exp\left(-e_n t\right) \quad \textbf{(4.19)}$$

and the capacitance increases exponentially with time as carriers are emitted from the trap. This equation is very important and is often used as the basis of capacitance transient techniques such as DLTS. It shows that the thermal emission rate can be obtained from the time constant and the amplitude of the transient $\Delta C(0)/C(\infty)$ is equal to N_t/N_D giving the trap concentration.

The rate of change of occupation of a deep level is $-e_nN_t$ when majority carrier emission predominates. Integrating this equation between the limits $n_t(t) = N_t$ when $t = 0$ and at equilibrium when $t = \infty$ and $N_t(t) = 0$ yields

$$n_t(t) = N_t \exp\left(-e_n t\right) \quad \textbf{(4.20)}$$

The capacitance change is proportional to the variation in $N_t(t)$ therefore

$$\Delta C(t) = -\Delta C_0 \exp\left(-e_n t\right) \quad \textbf{(4.21)}$$

where

$$\frac{\Delta C_0}{C} = \frac{1}{2}\left[\frac{x_1{}^2 - x_2{}^2}{x_d{}^2}\right]\frac{N_t}{N_D} \quad \textbf{(4.22)}$$

To differentiate between a minority and majority carrier trap the capacitance transient must be analysed. When a forward bias pulse is released trapped carriers are emitted to the nearest band edge at a characteristic rate which gives rise to a minority-carrier transient as shown in Figure 4.6.. Figure 4.5. illustrates the transient obtained for majority carriers in n-type material therefore it can be seen that the sign of the capacitance change is positive for a majority carrier trap and negative for a minority-carrier trap.

4.6 DLTS measurements

The DLTS system observes the capacitance transient in a rate window and the most common method has been the double box-car method. The double box-car method samples the transient with two gates at t_1 and t_2. The output signal is related to the difference $t_1 - t_2$ which is effectively producing a continual integral of the transient. The time constant τ of a capacitance transient can be observed through this window.

During the reverse bias fill pulse the trapped (majority) carriers are emitted at a rate e_n producing an exponential transient (equation 4.21) that can be written more generally as

$$C(t) = C_\infty + \Delta C_0 \exp\left(-\frac{t}{\tau}\right) \quad \textbf{(4.23)}$$

where the time constant $\tau = e_n^{-1}$ and ΔC_0 is given by equation 4.22 for a majority carrier trap.

The DLTS peak is formed as the capacitance change varies with temperature and the transient is observed through the rate window $t_1 - t_2$ (Figure 4.7.). The DLTS measurement is repeated with different rate window values which shifts the position of the peak. The normalised DLTS signal S(T) is derived from the capacitance measurements at time t_1 and t_2 where ΔC_q is the capacitance change due to the pulse at t = 0, therefore $\Delta C_q = C_\infty - C_0$

$$S(T) = \frac{C(t_2) - C(t_1)}{\Delta C_q} \quad \textbf{(4.24)}$$

If the capacitance is assumed to be exponential with the time constant τ_f then

$$S(T) = \exp\left[-\frac{t_1}{\tau_f}\right] - \exp\left[-\frac{t_2}{\tau_f}\right] \quad \textbf{(4.25)}$$

The emission rate is calculated by differentiating with respect to τ_f and equating the result to zero since the emission rate corresponds to the peak maximum of the DLTS spectrum

$$\tau_f = \frac{1}{e_n} = \frac{t_1 - t_2}{\ln\left[\frac{t_1}{t_2}\right]} \quad \textbf{(4.26)}$$

The peak height is proportional to ΔC_0 and is often used to give the trap concentration N_t by combining equations 4.19 and 4.21

$$N_t = \frac{\Delta C_0 2N_D}{C(\infty)} \tag{4.27}$$

The detection sensitivity of the DLTS procedure is determined by the measuring capacitance system. It is possible to obtain sensitivities of $\Delta C_0/C = 10^{-4}$ with the use of fixed offset capacitors. This means therefore that the smallest detectable concentration of traps is approximately 10^{-4} times the free carrier concentration. If N_D is equal to 10^{13} for example it is possible to detect defect concentrations as low as 10^9 cm^{-3}.

The height of the DLTS peaks frequently vary for the different rate windows and this is usually ascribed to the non-exponential decay of transients or the field dependence of emission rates. It has also been explained[18] by the changing shape of the Debye tail, the distribution of charge carriers at the edge of the depletion region, with changing reverse bias and temperature. This affects the occupancy of levels in the transition region and raises the capacitance in the depletion region which is most noticeable at low reverse bias. At high bias all the peaks tend to be the same height. Another author[19] however disagrees with the Debye tail theory noting that large peak height variations have been observed for both large and small reverse biases and suggests that field enhanced emission processes are not involved and some alternative theory is required. They argue that the large peak variations are due to a large temperature dependence of the capture cross section.

4.6.1 Activation Energy Determination

The thermal activation energy for electron or hole emission can be deduced from the temperature shift in the DLTS peak for different rate windows using a form of equation 4.5. A plot of $\ln(e_n/T^2)$ versus 1/kT takes account of the temperature dependence of $<v_{th}>$ and N_d and is known as an Arrhenius plot (Figure 4.8.). This plot produces a straight line graph from which the activation energy can be deduced from the gradient and the capture cross-section can be deduced from the intercept.

The electron and hole capture cross-sections may be independent of temperature, but in general they are not. Cascade capture via excited states of a Coulomb attractive centre increases at low temperatures where thermal re-emission of carriers from the shallow

Coulomb states is small (see Section 3.3). Experimentally it is found that $\sigma \propto T^{-n}$ (or $\sigma \propto T^{+m}$ for repulsive centres). Carrier capture by multiphonon emission via lattice relaxation is an important mechanism for deep levels[20,21] and in that case the capture cross-section has the form

$$\sigma = \sigma_{\infty} \exp\left(\frac{-E_{\sigma}}{kT}\right) \tag{4.28}$$

where E_{σ} is the thermal activation energy of the capture cross-section, thus a more general expression for the thermal emission rate of electrons to the conduction band is

$$e_n = \frac{\sigma\varepsilon_{\infty} v_n N_c}{g} \exp\left(\frac{-(\Delta E + E\sigma)}{kT}\right) \tag{4.29}$$

Here the thermal activation energy for emission of an electron to the conduction band determined from an Arrhenius plot has two components, the energy difference between the trap level and the bottom of the conduction band and the thermal activation energy of the capture cross-section. The Gibbs free energy ΔE can be defined as

$$E_c - E_T = \Delta E \equiv \Delta H - T\Delta S \tag{4.30}$$

where ΔH and ΔS are the changes in enthalpy and entropy due to the change in charge state of the level. Combining equations 4.5 and 4.29 gives

$$e_n = \frac{\sigma v_n N_c}{g} \exp\left(\frac{\Delta S}{k}\right) \exp\left(\frac{\Delta H}{kT}\right) \tag{4.31}$$

Thus the slope of the Arrhenius plot yields the enthalpy of the deep level, not the free energy, which can only be determined from optical measurements[16]. However from equation 4.30 it is easy to see that the activation energy obtained from the slope of an Arrhenius plot is equal to the free energy obtained at T=0K. This is generally not the same as the free energy at the measurement temperature, due to the temperature dependence of the band gap energy. For temperatures greater than absolute zero therefore, the exact position of the trap can only be determined when the temperature dependence of the band gap energy is known[22].

4.6.2 Capture Cross Section Measurement

The capture cross section is the cross sectional area over which the trap removes free carriers from the current. This provides a measure of the ability of a particular level for trapping either minority or majority carriers. There are two methods for determining σ_n (or σ_p). The first is by extrapolation of the Arrhenius plot, and calculation of σ from the intercept using the relationship described in equation 4.5. The other method is usually more accurate and involves the repetition of the DLTS temperature scan at a fixed rate window but with the fill pulse changed for each scan. As the pulse width increases so does the peak height and will eventually reach a maximum where all the traps are filled within the pulse width. The final plot consists of DLTS peaks displaced vertically. The peak height is related to the fill pulse width by

$$\frac{N_{T(tp\max)} - N_{T(tp)}}{N_{T(tp\max)}} = \exp\left(-\sigma_n N_D v_{th} t_p\right) \tag{4.32}$$

This can also be expressed as the proportion of empty traps

$$(1-F) = \exp\left[\frac{-t_p}{\tau_f}\right] \tag{4.33}$$

where $N_{T(tpmax)}$ = Trap concentration for a saturating pulse width
$N_{T(tp)}$ = Trap concentration due to a particular pulse width
τ_f = Trap characteristic filling time
t_p = Fill pulse width
F = $N_{T(tp)}/N_{T(tpmax)}$
1-F = Proportion of empty traps

The results obtained from these two methods may vary by order of magnitude because of high electric fields or the temperature dependence of the capture cross-section.

4.6.3 Deep Level Profiling

The deep level profile can provide useful information about the type of defect and its uniformity and is often used to investigate ion implantation damage, to identify diffusion tails, and to remove any influence of the electric field from the capture cross section measurements. The profile is obtained by varying the position of the observation window. This can be achieved by varying the steady state bias whilst all the other parameters remain fixed or by varying the size of the fill pulse whilst the steady state bias remains fixed.

The number of full traps at any time can be found by combining equations 4.15 and 4.16

$$n_t(t) = \frac{C(t)^2}{A^2 \varepsilon_s q}\left(2(V_0 - V_r) - N_D\right) \qquad \textbf{(4.34)}$$

This equation provides the basis for the DLTS deep level profiling experiment and is based on the following assumptions

1) The built-in voltage of the diode does not vary,
2) $dx_l = dx_d$ because N_D is uniform throughout the junction. This is valid if the number of observed traps is small compared to the doping concentration,
3) The depletion region is much larger than the transition region.

The profile obtained by changing the fill pulse changes x_d and C which leaves a dependence of C_0 on the applied voltage. The method that changes the bias is therefore preferable because the variable is the filling depth so as the fill pulse in increased, the region of observation is decreased thus causing a decreasing number of traps to be filled. However at high values of the fill pulse, the region of observation will approaching the same width as the transition region and therefore the effect of the Debye tail may become significant.

An alternative method is the application of two bias pulses of different heights which is known as the Double DLTS (DDLTS)[23] and this method ensures that all of the deep levels are well above the Fermi level are all subject to the same electric field. The effect of a non abrupt junction has been investigated using profiling techniques[19] and it was concluded that the effect of the Debye tail on trap filling can be avoided by using large reverse biases and forward bias fill pulses.

The profiling measurement is based upon the integration of Poisson's equation which gives the relationship of the applied voltage, to the depth from the junction, where the trap level, E_t crosses the Fermi level, E_f. The measurement is made at slightly different positions from the junction so a series of vertically displaced DLTS curves are attained.

However all profiling techniques require information about the width of the transition region in order to determine where N_t is being measured and all of the methods make use of the depletion approximation. Interpretation of profiling data should therefore be undertaken with great care.

4.7 Forward Bias Deep Level Transient Spectroscopy

Forward Bias or Junction DLTS[4] uses a forward-biased p-n junction to inject free minority-carriers into the material of interest where they can be captured at deep states. This capture process is then suppressed by applying a reverse bias and the trapped minority-carriers are released by thermal emission producing a transient in the depletion capacitance that can be monitored using DLTS techniques.

The experiment is conducted with a repetitive sequence of forward bias injection pulses of duration t_f to fill the traps with minority-carriers, followed by a steady reverse bias to terminate the capture process and facilitate the observation of thermal carrier emission (see Figure 4.9.(a)). The concentration of trapped minority-carriers as a function of time during this sequence is shown in Figure 4.9.(b). Usually the double box-car method is the most suitable method of transient analysis because of the long filling time that may be required to achieve maximum concentration of trapped minority-carriers. The rate window system is triggered at the end of the filling pulse to sample the emission transient at times t_1 and t_2 shown in Figure 4.9..

A relatively large current is required under forward bias to prime the trap therefore the filling pulse cannot be applied through the capacitance meter as in a conventional DLTS experiment. One method to overcome this problem is to use a system of fast FET switches triggered by an external pulse generator, to switch the diode from the reverse bias applied through the capacitance meter to the desired forward bias provided by the DC voltage supply.

The forward bias conditions can be monitored with a current transformer or with a voltage probe as close to the sample as practicable and this information can be used to estimate the injected carrier density. With sufficiently long filling time, t_f, the concentration of filled traps reaches the steady state given by

$$p_t^i = \frac{c_p + e_n}{c_p + e_n + c_n + e_p} N_t \tag{4.35}$$

For the specific case of a minority-carrier trap in n-type material (e_p>>e_n) and when the amplitude of the injection pulse is such that the carrier densities are sufficiently high that the capture processes dominate over thermal emission, then the occupancy at the start of the emission period is

$$p_t(0) = p_t^i(\infty) = \frac{c_p}{c_p + c_n} N_t \tag{4.36}$$

When c_p >>c_n the trap is completely filled with minority-carriers and such a filling pulse is called a saturating injection pulse. In the specific case of capacitance DLTS the transient can be described by[6]

$$\frac{\Delta C_0}{C} = \frac{1}{2}\left[\frac{x_1}{x_d}\right]^2 \left(\frac{c_p}{c_p + c_n}\right) \frac{N_t}{N_D} \tag{4.37}$$

In this experiment the transient amplitude depends not only on N_t but also on the capture cross sections of the trap and the injection conditions through c_n, c_p and x_1. Because the injected minority-carrier density is usually less than majority carrier density it is necessary that σ_{min} >> σ_{max} for saturation of the trap with minority-carriers. Fortunately for most traps the capture rate for one type of charge carrier is greater than the other so by choosing the material type it can usually be arranged that this condition is met.

The sign of the transient is opposite to that for majority carrier emission. Since majority carriers also enter the depletion region under forward bias, majority carrier emission peaks also appear in the FBDLTS scan although they can be distinguished from minority-carrier peaks by their sign.

4.7.1 Trap Filling by Minority-carrier Injection

The most difficult part of the FBDLTS experiment is to determine an accurate value for the minority-carrier density (p_n in a p^+-n forward biased junction). The band diagram is shown in Figure 4.10. where E_{Fp} and E_{Fn} are the Fermi level positions in neutral material on the p and n type sides of the junction. The quasi-Fermi level positions for holes and electrons (E_{Fh} and E_{Fe}) are taken to be horizontal extensions of these. The applied forward bias corresponds to the quasi-Fermi level separation and the depletion region extends from $-x_p$ to x_n. The depletion depth on the n-side under an applied reverse bias is indicated as x_d. The free carrier densities in undepleted material are n_0 and p_0.

To calculate the concentration and spatial distribution of holes injected across the junction into the region beyond x_n the simplest case when there is no recombination within the region $-x_p < x < x_n$, must be examined first. This initial analysis therefore assumes that (i) the depletion approximation is valid; (ii) the carrier densities are non-degenerate and determined by Boltzmann factors; (iii) the injected minority-carrier density is small compared with the majority carrier density; (iv) no recombination occurs within the forward bias depletion region.

It can be argued that[17] within the forward bias depletion region in the absence of recombination the quasi-Fermi levels are effectively horizontal so

$$n(x) = N_c \exp\left(-\frac{E_c(x) - E_{Fe}}{kT}\right) \qquad \textbf{(4.38)}$$

and

$$p(x) = N_v \exp\left(-\frac{E_{Fh} - E_v(x)}{kT}\right) \qquad \textbf{(4.39)}$$

Therefore

$$n(x)p(x) = n_i^2 \exp\left(-\frac{qV_f}{kT}\right) \qquad \left(-x_p < x < x_n\right) \qquad \textbf{(4.40)}$$

where n_i is the intrinsic carrier density. The hole concentration decreases from p_0 on the p-side of the junction to a value of $p_n(x_n)$ at the edge of the depletion layer on the n-side. At this point the electron density is $n(x_n) = n_0$ therefore

$$p_n(x_n) = \frac{n_i^2}{n_0} \exp\left(\frac{qV_f}{kT}\right) = p_{n0} \exp\left(\frac{qV_f}{kT}\right) \qquad \textbf{(4.41)}$$

This equation offers one means of estimating $p_n(x_n)$ from V_f, but this method may not be reliable because the voltage measured externally includes a voltage across the series resistance of the contact and material itself. Accurate correction for this voltage drop is difficult and large uncertainties can arise due to the exponential dependence of p_n on V_f. An alternative method is to calculate p_n from the measured injection current.

In the absence of recombination within the depletion region the current components in the forward bias depletion region are constant from $-x_p$ to $+x_n$, and for holes injected into the n-side this is given by

$$J_p = -(+q)D_p \frac{\partial p_n(x)}{\partial x}\bigg|_{x_n} = \frac{qD_p}{L_p}\{p_n(x_n) - p_{n0}\} \qquad \textbf{(4.42)}$$

The gradient of $p_n(x)$ is controlled by diffusion into n-type material and a similar expression can be written down for electrons injected into the n-side[24] so, where J is equal to the current in the external circuit, $J = J_n + J_p$. The diffusion current can therefore be derived from equations 4.41 and 4.42 giving

$$J_{diff} = \left\{\frac{qD_n n_{p0}}{L_n} + \frac{qD_p p_{n0}}{L_p}\right\} \times \left\{\exp\left(\frac{qV_f}{kT}\right) - 1\right\} \qquad \textbf{(4.43)}$$

If we define an injection ratio γ such that $J_p = \gamma J_{diff}$ then from equation 4.43

$$\gamma = \frac{D_p p_{n0}}{L_p}\left\{\frac{D_p p_{n0}}{L_p} + \frac{D_n n_{p0}}{L_n}\right\}^{-1} \qquad \textbf{(4.44)}$$

and since qV>>kT combining equations 4.41 and 4.43 with $p_{n0}=n_i^2/n_0$ gives

$$p_n(x_n) = \frac{L_p}{qD_p}\gamma J_{diff} \qquad \textbf{(4. 45)}$$

and the question of determining $p_n(x_n)$ becomes the problem of estimating L_n and L_p for a particular sample. This can be simplified to some extent by noting that $D_{n,p}=\mu_{n,p}(kT/q)$ and that $p_{n0}=n_i^2/n_0$ and $n_{p0}=n_i^2/p_0$ therefore by equating $n_0=N_D$ and $p_0=N_A$,

$$\gamma = \frac{\mu_p}{N_D L_p}\left\{\frac{\mu_p}{N_D L_p} + \frac{\mu_n}{N_A L_n}\right\}^{-1} \qquad \textbf{(4.46)}$$

and since N_A>>N_D for a p^+-n junction this effectively becomes

$$\gamma = \frac{N_A}{N_A + N_D} \approx 1 \qquad \textbf{(4.47)}$$

This shows that the hole injection ration should be of the order of unity in these structures. Equation 4.43 suggests that for qV>kT the forward bias current-voltage characteristic of a junction is represented by

$$J = J_0 \exp\left(\frac{qV_f}{nkT}\right) \tag{4.48}$$

with n = 1, similar to a Schottky barrier. In practice however it is found that n lies in the range between 1 and 2. This behaviour is caused by a current due to recombination of electrons and holes via traps in the forward bias depletion region between $-x_p$ and x_n. It can be shown[17] by considering a recombination centre in a concentration N_r, with $\sigma_n = \sigma_p = \sigma$, that the maximum value of the recombination rate per unit volume is (qV/kT)

$$R \approx \frac{1}{2}\sigma \upsilon N_r n_i \exp\left(\frac{qV_f}{2kT}\right) \tag{4.49}$$

and then the recombination current is

$$J_{rec} \approx \int_{-x_p}^{x_n} qRdx \approx \frac{q(x_p + x_n)}{2}\sigma \upsilon N_r n_i \exp\left(\frac{qV_f}{2kT}\right) \tag{4.50}$$

The total current is given by the sum of the diffusion current outside the depletion region and the recombination current within it. Since the latter varies as the exponential of qV_f/kT then the J-V characteristic can be approximately represented by an equation of the form of equation 4.48 with n equal to between 1 and 2. Generally speaking the recombination current is dominant at low bias, with J_{diff} taking over as V_f is increased because of the stronger V_f dependence. At very high injection the bands in the regions outside the depletion region do not remain flat and a current component due to drift in an electric field must be added to the diffusion and recombination components. The J-V curve may also be distorted at high current by the voltage drop across the diode series resistance[25].

4.8 Minority-carrier Capture at a Minority-carrier trap

A method to measure the minority-carrier capture rate first suggested by Wang and Sah[26] monitors the capacitance transients after steady state injection of minority-carriers in a range of densities. In the p-side the electron occupation at the trap during the steady state electron injection is determined by competition between the electron and hole capture events since the thermal emission events can be neglected at low temperature measurements. Thus we have[26]

$$N_T = N_{TT}\frac{c_n N}{c_n N + c_p P} \tag{4.51}$$

If N and P are known then the size of the capacitance transients (ΔC) versus N gives c_n/c_p. If c_p is known then c_n is determined. The capacitance transients detected at various injection levels are given by

$$\Delta C(N) = \Delta C_1 \frac{c_n}{c_n N + c_p P} \tag{4.52}$$

where C_l is independent of N and is the ΔC one would observe if all the traps are filled by the minority-carriers or electrons. It must be emphasised that the size of the transient observed in experiments at saturation is

$$\Delta C(\infty) = \Delta C_1 \frac{c_n}{c_n + c_p} \tag{4.53}$$

and is less than ΔC_l unless $c_n >> c_p$. This means that a knowledge of both capture rates is necessary before one can relate the magnitude of the transient from a minority-carrier trap to its true concentration.

In this equation N is essentially the electron density at the boundary of the junction space-charge layer and the quasi-neutral p-type base for a diode with a long diffusion length. For diodes with a short diffusion length some spatial averaging would be necessary. If $c_n >> c_p$ filling of the trap by electrons is achieved at low injection under forward bias and P is simply the doping density corrected by deionization effect[27].

N is related to the measured injection current at low doping levels ($<10^{15}$) by taking the injection efficiency as unity at low injection[28]. For doping higher than about 10^{15} cm^{-3} it may be necessary to assess the injection efficiency by electrical measurement[28,29]. Assuming that the injection current used is dominated by the diffusion component[30] then N at the base boundary of the junction space-charge layer is given by

$$N = \left(\frac{JL}{qD_n}\right)\tanh\left(\frac{W}{L}\right) \tag{4.54}$$

where W is the base layer thickness, L is the electron diffusion length and J is the injection current density. Inverting equation 4.52 gives

$$\frac{1}{\Delta C(N)} = \frac{1}{\Delta C_1}\left(1 + \frac{c_p P}{c_n}\frac{1}{N}\right) \tag{4.55}$$

The 1/ΔC versus 1/N plot should therefore be a straight line if the measured injection current is dominated by the diffusion component. c_n can therefore be obtained from the ratio of the fitted slope to the fitted intercept at y axis.

4.9 Minority-carrier Capture at a Majority Carrier Trap

The measurement of the minority-carrier capture cross-section of a majority carrier trap requires both minority and majority carrier pulses. Figure 4.11. illustrates this process using injection at a p+-n junction as an example where the majority carriers are electrons and the trap is located in the upper half of the bandgap[31].

The traps are filled with majority carriers with a short circuit pulse A of duration greater than c_n^{-1} so that all the traps are occupied (Figure 4.11.). Within a time much shorter than e_n^{-1} (so that the trap remains full) a forward bias injection pulse B of duration t_f is applied to the diode to induce capture of minority-carriers. When the diode is returned to its reverse bias the traps which remain occupied with majority carriers empty by thermal emission. The amplitude of this thermal emission transient provides a measure of the number of traps not filled with minority-carriers at the end of the injection pulse, $n_t(t_f)$.

At the start of the injection pulse the traps have been filled by majority carrier capture and we assume this dominates over thermal emission so

$$n_t(0) = N_t \tag{4.56}$$

The capture process during the injection pulse can be described by the equation

$$n_t(t_f) - n_t(\infty) = \{N_t - n_t(\infty)\}\exp\lfloor -(c_n + c_p)t_f \rfloor \qquad \textbf{(4. 57)}$$

with

$$n_t(\infty) = \frac{c_n}{c_n + c_p} N_t \qquad \textbf{(4.58)}$$

It is necessary that $c_n < c_p$ for minority-carrier capture to be observed. In the subsequent majority carrier emission period $n_t = 0$ when $t_e = \infty$ and the DLTS emission signal is therefore proportional to $n_t(t_f)$

$$S_e(t_f) \propto n_t(t_f) \qquad \textbf{(4.59)}$$

The fraction of traps not filled with minority-carriers in the interval t_f can be given by the function

$$\begin{aligned} F'(t_f) &= \frac{n_t(t_f) - n_t(\infty)}{n_t(0) - n_t(\infty)} \\ F'(t_f) &= \frac{S_e(t_f) - S_e(\infty)}{S_e(0) - S_e(\infty)} \end{aligned} \qquad \textbf{(4.60)}$$

and from equations 4.56 and 4. 57 this represents

$$F'(t_f) = \exp\lfloor -(c_n + c_p)t_f \rfloor \qquad \textbf{(4.61)}$$

$S_e(0)$ is the signal measured in the absence of pulse B and if $c_n << c_p$ then $S_e(\infty)$ is close to zero by definition. The capture rate for electrons can be measured by the conventional pulse width variation technique and c_p can now be determined from a logarithmic plot of $F'(t_f)$.

If c_n can be measured by the conventional technique if $c_p \approx c_n$ then c_p can simply be measured from the amplitude of the signal without pulse B, $S_e(0)$, and with a long injection pulse, $S_e(\infty)$. This gives $n_t(0)$ and $n_t(\infty)$ respectively, then from equations 4.56 and 4.58

$$\frac{S_e(\infty)}{S_e(0)} = \frac{c_n}{c_n + c_p} \qquad \textbf{(4.62)}$$

This experiment is only satisfactory for c_p within about a decade larger or smaller than c_n, though since $p_n < n_0$ it is possible to measure values of σ_p significantly greater than σ_n.

4.10 Selective Detection of Recombination Centres using DD-DLTS

Another variation of the DLTS technique known as double-double DLTS (DD-DLTS) measurement mode allows recombination spectroscopy. The principle of the method is that two types of excitations are applied periodically in reverse time sequence before the measurement periods (Figure 4.12.(a)) and the capacitance transient is measured using a weight function (Figure 4.12.(b))[32].

These weight functions produce the difference of the two transients and this ensures selective detection of recombination centres by suppressing transients of non-recombination centres. The recombination centres interact with both types of carriers so when the pulse lengths are appropriately set the last filling pulse determines the charge state of the centres.

The shape of the resulting spectrum is step-like and arises from recombination centres only. If DD-DLTS is performed at the same rate as DLTS the steps can be associated with corresponding peaks because they appear at the same temperature and thus the relevant recombination centres can be identified (for example see Huppi[33]).

4.11 Minority-carrier Trap Spectroscopy

Minority-carrier Trap Spectroscopy (MCTS)[34] is a similar technique to DLTS but the charge carriers are injected by illumination rather than by an electrical bias fill pulse. The electron hole pairs can be introduced for example by an AlGaAs laser with a wavelength greater than the band gap of 870nm. Both minority and majority carriers are generated by the absorption of light while the sample is held under reverse bias so the carriers are separated by the field.

Light is provided in the form of a short pulse from the laser which illuminates the sample uniformly. The laser is controlled by the pulse generator unit of the DLTS system which synchronises the measurement pulse with the optical fill pulse. This pulse changes the occupation of the deep levels in the depletion region and therefore forms a capacitance transient (Figure 4.6.).

The photocurrent generated in the illuminated sample is derived from two sources. The incident light is mostly absorbed in the depletion region close to the surface, forming electron hole pairs which are then separated by the electric field. The second current component is from the minority-carriers generated by the absorption of light deeper in the material but still within a diffusion length of the depletion layer. The minority-carriers diffuse to and then drift through the junction but in contrast the majority carriers generated in the bulk of the material are repelled by the potential of the field. This diffusion current of minority-carriers is effectively injecting carriers into the depletion region. The change in the number of minority-carriers in the depletion region is therefore large in comparison with the number of majority carriers.

Deep levels initially occupied by majority carriers will capture minority-carriers at a characteristic rate depending on their capture cross section and the density of minority-carriers. The laser source allows the minority-carrier emission process to be monitored as a capacitance change in the normal manner and therefore the normal DLTS equations apply. Another technique known as Recombination DLTS has been developed at Southampton that combines DLTS and MCTS to enable the direct observation and characterisation of recombination centres which are efficient in the capture of both minority and majority carriers[7].

4.12 Limitations of DLTS

Although DLTS is a powerful technique great care must be taken when interpreting the results. DLTS is most powerful when combined with other techniques such as Electron Paramagnetic Resonance (EPR), Fourier Transform Infra Red (FTIR), Photoluminescence (PL), and annealing studies to positively identify a new level[35].

In order that DLTS measurements relate to derived equations accurately the following conditions must apply

- The transition region (λ) must be small compared to the depletion layer width (W). This is best achieved by using high reverse bias,

- The levels are uniformly distributed, with field independent emission rates, thus allowing an exponential transient to be assumed,
- Only a single emission process occurs at each deep level,
- The concentrations of traps is much smaller than the total concentration of ionised states in the depletion layer ($N_t << 0.1\ N_D$).

Care should also be taken when determining the capture cross section to allow for both temperature and field effects since they are emitted from the equations, so the results should be taken at a series of temperatures. Another potential source of error occurs due to traps that are at the edge of the depletion region which are not always completely filled as they are the subject to the effects of the electric field and this can distort the transient. This may be avoided by operating at high quiescent reverse bias.

4.13 References

[1] Bube, R.H., J. Appl. Phys. 31, 2, p.315, (1960).

[2] Williams, R., J. Appl. Phys. 37, 9, p.3411, (1966).

[3] Sah, C.T., et al, Thermally stimulated capacitance (TSCAP) in p-n junctions, Appl. Phys. Lett.., 20, 5, p.193, (1972).

[4] Lang, D.V., DLTS: A new method to characterise traps in semiconductors, J. Appl. Phys., 45, 7, p.3023-3032, (1974).

[5] Kimerling, L.C., New developments in Defect studies in Semiconductors, IEEE Trans. Nucl. Sci., NS-23, 6, p.1497, (1976).

[6] Blood, P. and Orton, J.W.: The electrical characterisation of semiconductors: majority carriers and electron states, Techniques of Physics, Vols. 13 & 14, Academic Press, London, (1992).

[7] Markvart, T., *et al*, *17th Int. Conf. Defects in Semiconductors, Gmunden, Austria*, p.1381, (1993).

[8] Chatre, A., Vincent, G., and Bois, D., Deep level optical spectroscopy in GaAs, Phys. Rev. B, B23, p.5335, (1981).

[9] Okushi, H., and Tokumaru, Y., Isothermal Capacitance Transient Spectroscopy for determination of deep level parameters, Jap. J. Appl. Phys. 19, 6, L335-L338, (1980).

[10] Okushi, H., et al, Determination of the density of state distribution of a-Si:H by Isothermal Capacitance Transient Spectroscopy, Jap. J. Appl. Phys. 20, 7, L549-L552, (1981).

[11] Brotherton, S.D., Photocurrent DLTS in silicon, J. Appl. Phys. 55, 10, p.3636, (1984).

[12] Auret, F.D., and Nel, M., Single scan defect identification by DLTS using a two-phase lock-in amplifier (IQDLTS), J. Appl. Phys. 63, 3, p.973, (1988).

[13] Morimoto, J., et al, Spectral analysis of deep level transient spectroscopy (SADLTS), Jap. J. Appl. Phys., 26, 10, p.1634, (1987).

[14] Li, G.P., and Wang, K.L., J. Appl. Phys. 57, 4, p.1016, (1985).

[15] Lang, D.V., Space charge spectroscopy in semiconductors, Thermally stimulated relaxation of solids, (Ed. Braunlich, P.), Springer-Verlag, p.93-113, (1979).

[16] Miller, G.L., et al, Capacitance transient spectroscopy, Ann. Rev. Mats. Sci. 7, p.377-448, (1977).

[17] Sze, S.M., Physics of Semiconductor Devices, Second Edition, John Wiley and Sons Inc., (1981).

[18] Rockett, P.I., and Peaker, A.R., Calculation of deep state profiles from transient capacitance data, Appl. Phys. Lett. 40, 11, p.957, (1982).

[19] Zhao, J.H., et al, The effect of the non abrupt depletion edge on deep trap profiles determined by DLTS, J. Appl. Phys., (1987).

[20] Henry, C.H. and Lang, D.V., Phys. Rev. B, 15, p.989-1016, (1975).

[21] Lang, D.V. and Henry, C.H., Phys. Rev. Lett. 35, p.1525-1528, (1975).

[22] Grimmeiss, H.G., Deep levels in semiconductors, Ann. Rev. Mats. Sci. 7, p.341-376, (1977).

[23] Lefevre, H., and Schulz, M., Double correlation technique (DDLTS) for the analysis of deep level profiles in semiconductors, Appl. Phys. Lett. 12, p.45-53, (1977).

[24] Orton, J.W., and Blood, P.: The electrical characterisation of semiconductors: minority carriers, Techniques of Physics, Vols. 13 & 14, Academic Press, London, (1992).

[25] Nussbaum, A., Semiconductors and Semimetals Vol. 15, Academic Press, (1981).

[26] Wang, A.C., and Sah, C.T., J. Appl. Phys. 57, p.4645, (1985).

[27] Woodley, T.J. and Sah, C.T., Solid State Electron. 20, p.385, (1977).

[28] Neugroschel, A., Lindholm, F.A., and Sah, C.T., IEEE Trans. Electron Devices ED-24, p.662, (1977).

[29] Neugroschel, IEEE Trans. Electron Devices ED-28, p.108, (1981).

[30] Sah, C.T., Noyce, R.N., and Schockley, W., Proc. IRE 45, p.1228, (1957).

[31] Blood, P., and Orton, J.W., The electrical characterization of semiconductors: majority carriers and electron states, Techniques of Physics, Volume 14, Academic Press, (1992).

[32] Dozsa, L., Selective detection of deep recombination centres, Sol. St. Elect. 29, 9, p.861, (1986).

[33] Huppi, M.W., Proton irradiation of silicon: complete electrical characterisation of the induced recombination centres, J. Appl. Phys. 68, 6, p.2702, (1990).

[34] Brunwin, R., et al, Detection of minority-carrier traps using transient spectroscopy, Electronics Letters, 15, 12, p.349, (1979).

[35] Peaker, A.R., and Hamilton, B., The characterisation of electrically active impurities using DLTS and related techniques, Electrochem. Lett. 15, p.348, (1979).

FIGURE 4.1.(a) A DEEP LEVEL IN A SCHOTTKY BARRIER AT ZERO APPLIED BIAS

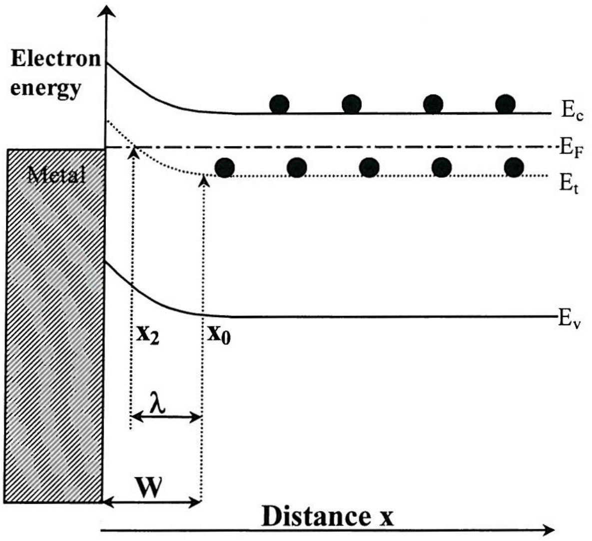

FIGURE 4.1.(b) A DEEP LEVEL IN A SCHOTTKY BARRIER UNDER REVERSE BIAS

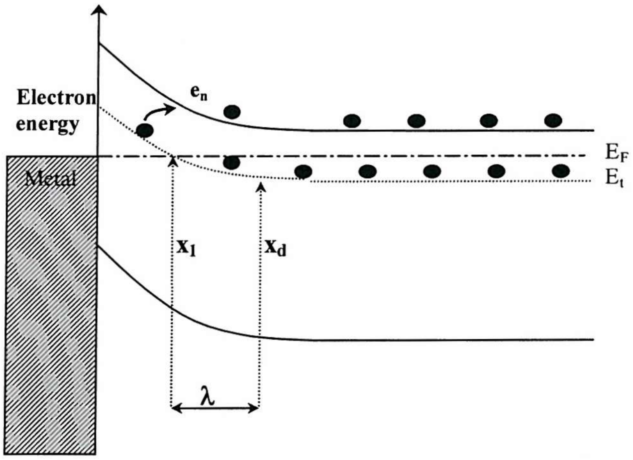

FIGURE 4.2.(a) MINORITY CARRIER CAPTURE AND EMISSION AT A DEEP LEVEL IN N-TYPE MATERIAL

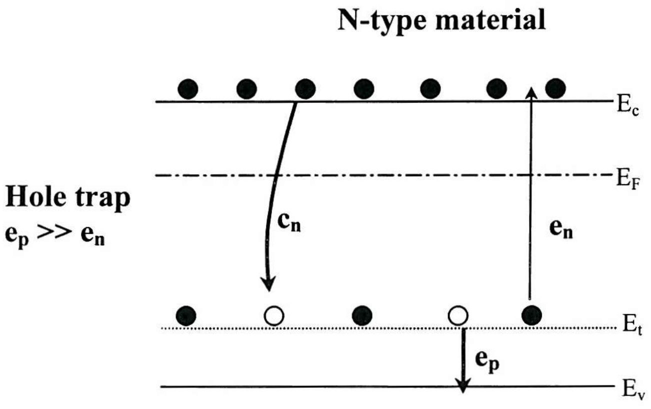

FIGURE 4.2.(b) MAJORITY CARRIER CAPTURE AND EMISSION AT A DEEP LEVEL IN N-TYPE MATERIAL

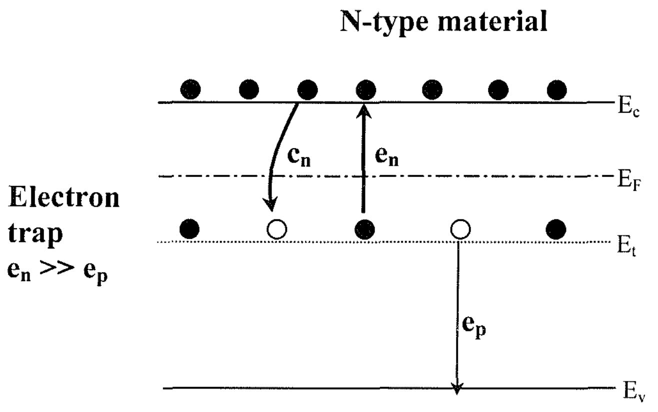

FIGURE 4.2.(c) MINORITY CARRIER CAPTURE AND EMISSION AT A DEEP LEVEL IN P-TYPE MATERIAL

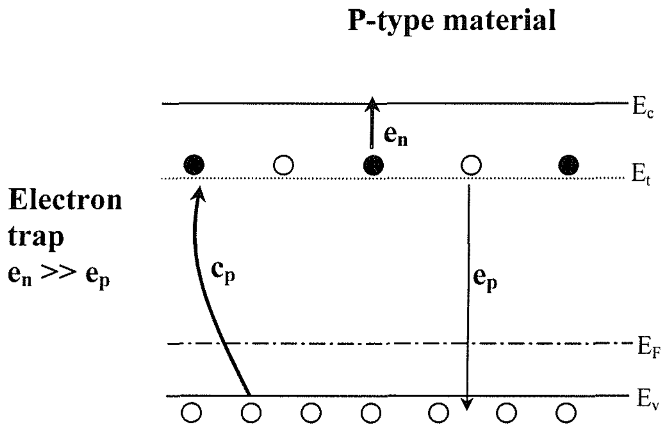

FIGURE 4.2.(d) MAJORITY CARRIER CAPTURE AND EMISSION AT A DEEP LEVEL IN P-TYPE MATERIAL

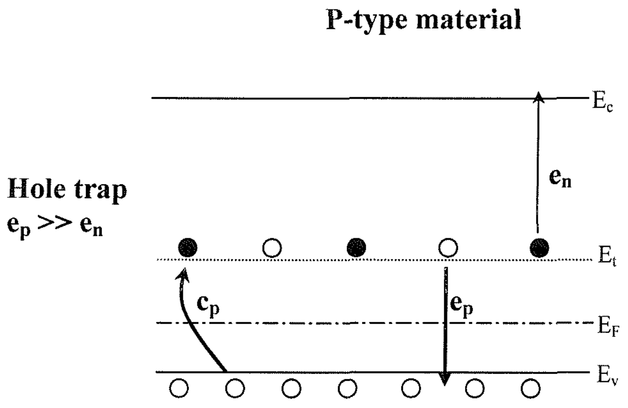

FIGURE 4.3.(a) CHARGE DENSITY ON EITHER SIDE OF A P-N JUNCTION
FIGURE 4.3.(b) CHARGE DENSITY ON EITHER SIDE OF A P-N JUNCTION USING THE DEPLETION APPROXIMATION

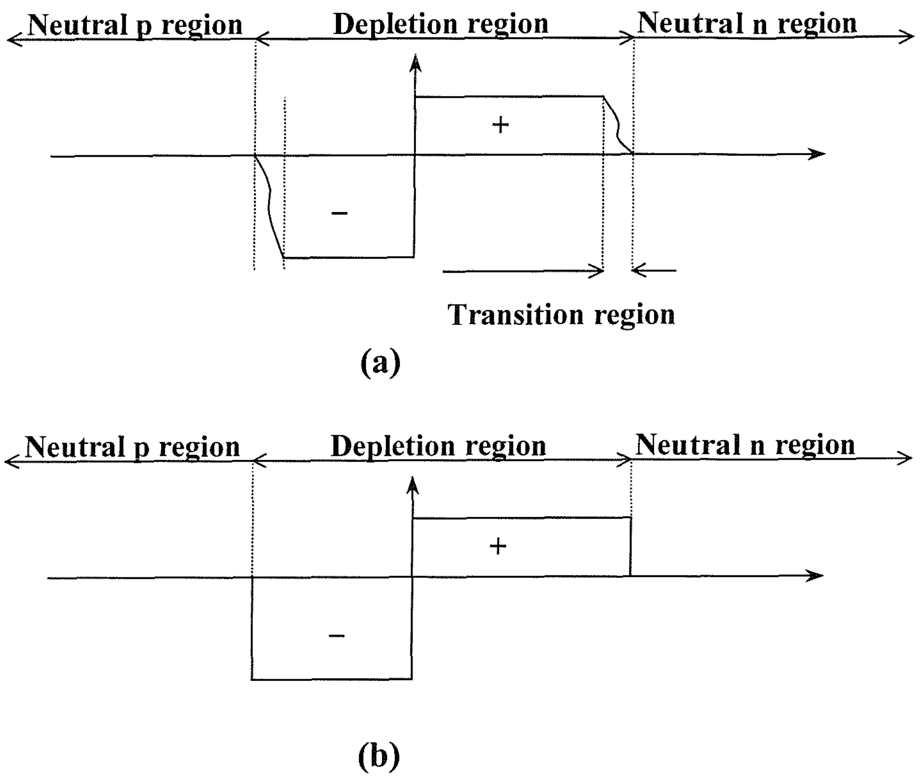

FIGURE 4.4. VARIATION OF THE CAPTURE RATE WITH DISTANCE ACROSS THE DEPLETION REGION

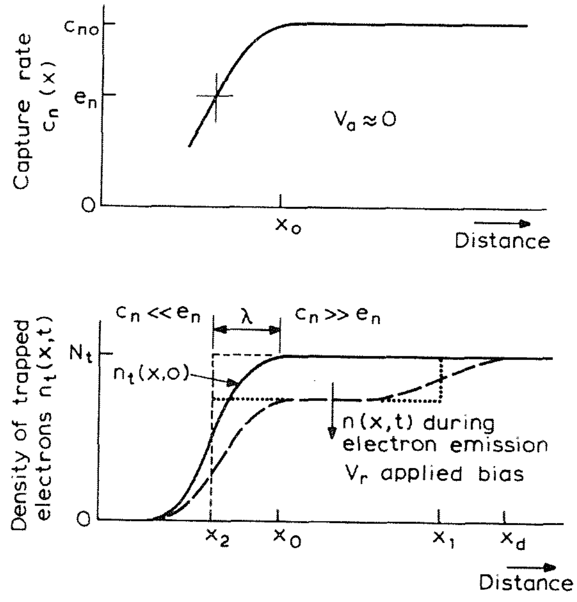

FIGURE 4.5. CAPACITANCE TRANSIENT FOR AN ELECTRON TRAP IN N-TYPE MATERIAL. THE TRAP EMPTIES WITH EMISSION RATE e_n FROM C_0 (t=0) TO C_∞ AFTER A REVERSE BIAS PULSE V_r

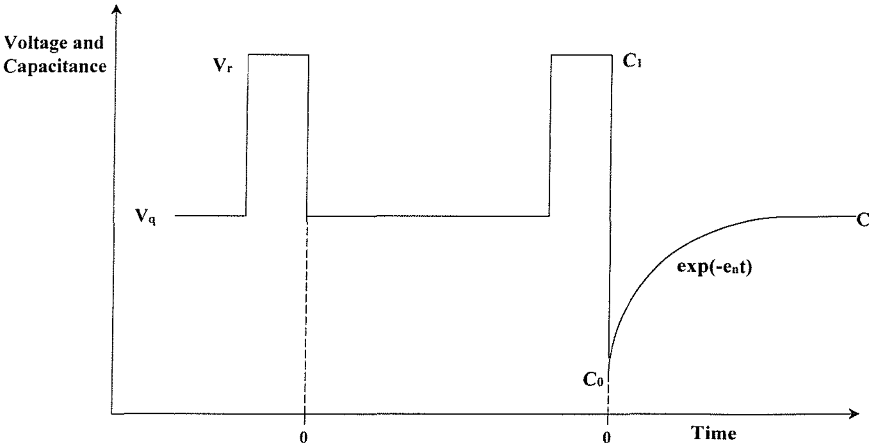

FIGURE 4.6. CAPACITANCE TRANSIENT FOR A HOLE TRAP IN N-TYPE MATERIAL. THE TRAP EMPTIES WITH EMISSION RATE e_n FROM C_0 (t=0) TO C_∞ AFTER A REVERSE BIAS PULSE V_r

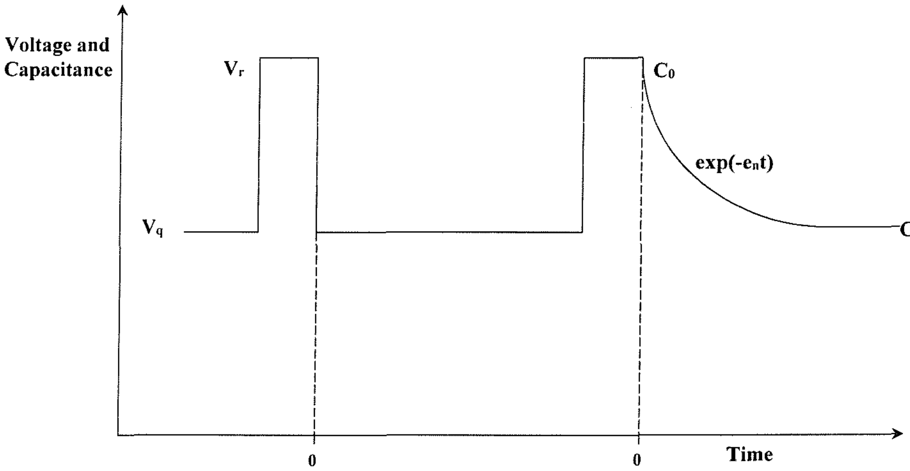

FIGURE 4.7. ANALYSIS OF A CAPACITANCE TRANSIENT THROUGH A RATE WINDOW ($t_1 - t_2$) AS THE TEMPERATURE IS SLOWLY COOLED

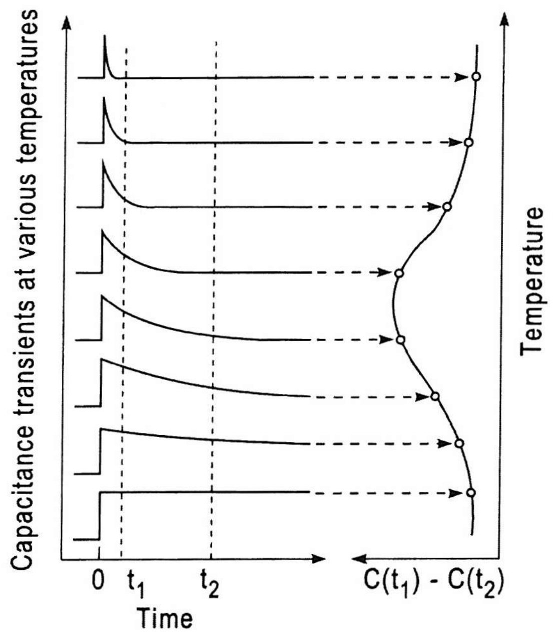

FIGURE 4.8. A TYPICAL ARRHENIUS PLOT FOR SIX DIFFERENT RATE WINDOWS

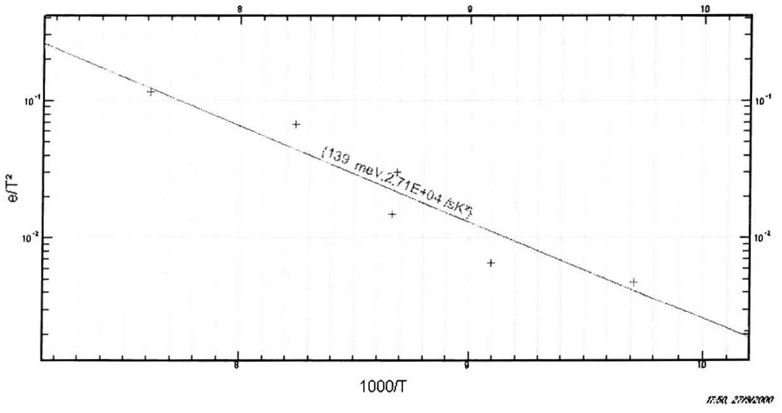

FIGURE 4.9. (A)VOLTAGE PULSE SEQUENCE (B)THE NET CONCENTRATION OF TRAPPED HOLES IN A FBDLTS EXPERIMENT IN WHICH MINORITY-CARRIER TRAPS ARE PRIMED BY INJECTION

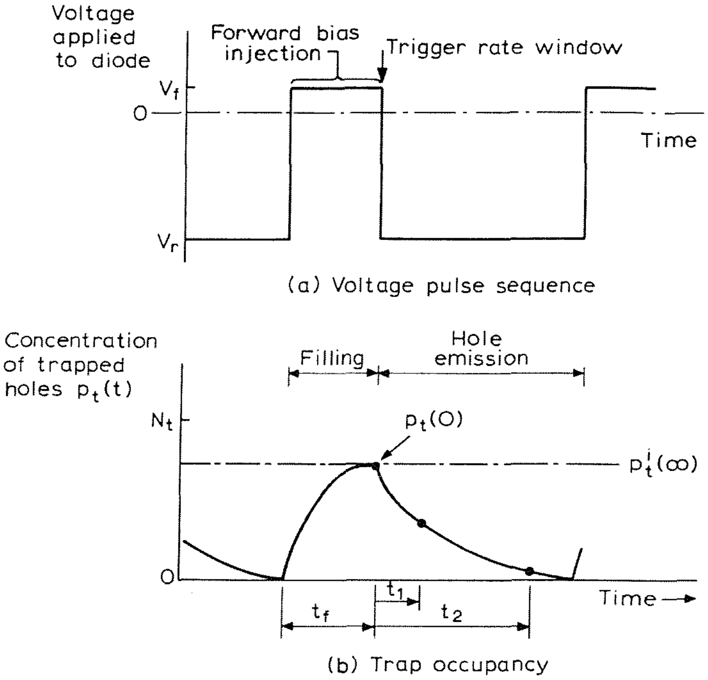

FIGURE 4.10. BAND DIAGRAM OF A P+N JUNCTION UNDER FORWARD BIAS V_F SHOWING INJECTION OF HOLES INTO N-TYPE MATERIAL OVER A DISTANCE OF ORDER OF A DIFFUSION LENGTH L_P. THE JUNCTION IS AT x=0 AND THE FORWARD BIAS DEPLETION REGION EXTENDS FROM $-x_P$ TO x_n AND THE DEPLETION DEPTH IS x_d

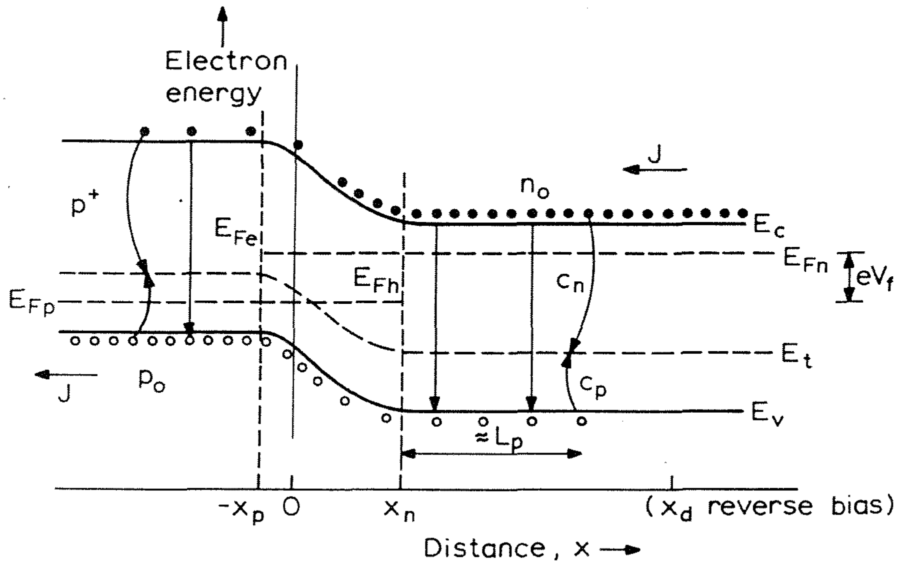

FIGURE 4.11. INJECTION AT A P+-N JUNCTION WHERE THE MAJORITY CARRIERS ARE ELECTRONS AND THE TRAP IS LOCATED IN THE UPPER HALF OF THE BANDGAP

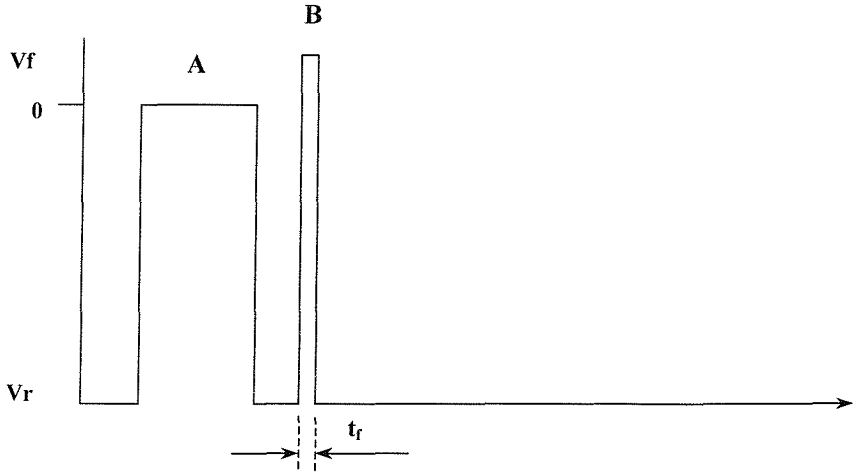

FIGURE 4.12. (A) DD-DLTS FILLING AND INJECTION PULSE SEQUENCE (B) WEIGHTED BOX-CAR GATE SETTING

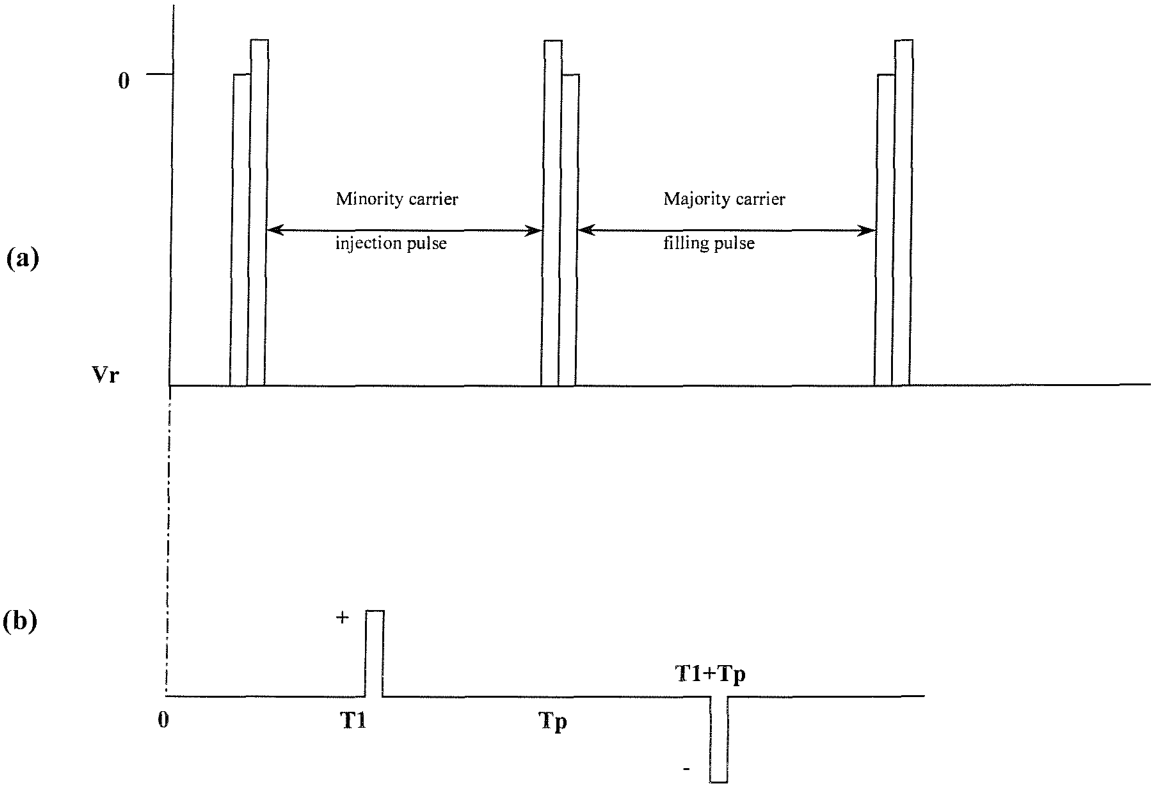

CHAPTER FIVE

EXPERIMENTAL

5.1 Introduction

This chapter contains the specifications of the solar cells used in this study and also describes the irradiation procedure used to introduce deep level defects into the forbidden bandgap. The sample preparation and the apparatus used in the DLTS, MCTS and FBDLTS experiments is then described. Finally the apparatus and procedure used to obtain the IV characteristics and spectral response of these cells is given.

The BSF/BSR Czochralski and float-zone silicon solar cells used in this report have been extensively studied in many previous projects[1,2,3,4,5,6]. These references therefore contain additional information about the manufacture and processing of these cells as well as a great deal of information about the defects which have been introduced by particle irradiation. The PERL and PERT cells were manufactured at the University of New South Wales, Sydney, Australia and additional data for these cells can be found in references 7 (PERL cells) and 8 (PERT cells).

5.2 Float Zone Silicon Solar Cells

These cells were manufactured by Telefunken System Technik (TST), Heilbronn, Germany from float-zone silicon wafers of varying boron content. These wafers had a range of different resistivities from 0.3 to 115Ω and these specifications are given in Table 5.1. In a previous study[5] the IV characteristics were determined before irradiation and these results are also shown in Table 5.1.

Table 5.1 - Float Zone Solar Cell Specifications

Batch No.	Wafer	Resistivity (Ω cm)	Boron Doping (cm^{-3})	Isc (mA/cm^{-2})	Voc (mV)	Pmax (mW/cm^{-2})	FF %
54,47	111	0.3	2.70E+16	35.55	606	21	66.9
50,55	100	0.94	7.80E+15	35.35	597	21	76.6
49	100	10	7.00E+14	37.70	539	20	74.8
48	100	115	9.70E+13	38.95	467	18	74.6

5.3 Czochralski Silicon Solar Cells

These cells were also manufactured by Telefunken using a standard process. The junction was formed by a shallow (0.1μm) phosphorus diffusion into a boron doped silicon substrate prior to contact formation. The specifications and IV characteristics prior to irradiation are shown in Table 5.2.

Table 5.2 - Czochralski Solar Cell Specifications

Batch No	Wafer	Resistivity (Ω cm)	Boron (cm^{-3})	Oxygen (cm^{-3})	Isc (mA/cm^{-2})	Voc (mV)	Pmax (mW/cm^{-2})
67	111	7 to 13	17E+14	3.3E+17	26.92	542	11.53
68	111	7 to 13	13E+14	6.9E+17	27.02	539	11.51
69	100	13 to 14	7.6E+14	1.28E+18	26.72	534	11.21

These cells other were manufactured from wafers with a homogenous distribution of dissolved oxygen which varied in concentration[2]. They also have a heavily doped region at the back of the cell known as a Back Surface Field (BSF) and a diffuse Back Surface Reflector (BSR) (see Figure 2.8) which reflects most of the light which passes through the cell back again improving collection efficiency. Some of these cells also have a thin Titanium Dioxide antireflection coating which significantly improves the cells efficiency.

5.4 High Efficiency Silicon Solar Cells

Most of the samples used in this study were high efficiency PERL (passivated emitter, rear locally diffused)[7] and PERT (passivated emitter, rear totally-diffused)[8] cells fabricated using a variety of different materials and dopants at the University of New South Wales (UNSW). PERL cells formed on high quality FZ substrates have demonstrated a record 24.7% efficiency[7] and the PERT cells were developed to improve the cell fill factors for higher substrate resistivities[8]. The PERL cells (Figure 5.1.) have high quality surface passivation by TCA grown oxide to most of the front and rear cell surfaces. The front and rear metal contact areas are passivated by heavily diffused boron and phosphorus regions. The inverted pyramids on the front surface and rear surface mirror create an excellent light trapping scheme in these cells. The narrow front metal fingers are formed by photolithography and thickened by electrically plated silver. A double-layer ZnS/MgF_2 antireflection coating (DLAR) has also been applied to some of these cells to further reduce surface reflection. The PERT cells have an additional light boron diffusion into the entire rear surface of the cell.

To maximise cell performance, as much light as possible of useful wavelengths should be coupled into and absorbed by the cell. Modern cell designs such as the Passivated Emitter, Rear Locally diffused (PERL) cell (Figure 5.1.) incorporate several features of a primarily optical nature to achieve this result[9].

The inverted pyramids along the top surface serve primarily to reduce reflection of the incident light in these cells. Most of the incident light will hit one of the side walls of the pyramids and therefore the reflected light will be reflected downwards and hence have another chance of entering the cell. The pyramids are covered with an oxide layer of appropriate thickness to act as an antireflection coating. In the more recent designs[10], this oxide layer is grown thin and a double-layer antireflection coating is applied to further improve the absorption efficiency.

Surface passivation also significantly improves cell efficiency by reducing the surface recombination velocity. The abrupt ending of the crystal at the surface leads to a high density of defects that act as traps in the forbidden bandgap. The SiO_2 layer (see Figure 5.1.) saturates or passivates these traps which therefore become ineffective. This layer is simply formed by high temperature treatment under oxygen and additional annealing under forming gas can further reduce the surface recombination rate to 10-100 cm/s. In addition weakly absorbed light reaching the rear of these cells is reflected by the very efficient reflector formed by the combination of the rear oxide layer covered by an aluminium layer.

All of these cells have a 100 crystal orientation. They are then etched to reveal the 111 surface and this creates an "inverted pyramid" structure that has around 75% more surface area. The n-type (phosphorus) samples have a junction depth of around 0.6μm and the p-type samples have a junction depth of around 0.3μm. All of these PERL/PERT cells are described in Table 5.3.

Table 5.3 – High Efficiency PERL/PERT Solar Cell Specifications

Cell Name	Material	Dopant	Resistivity (Ωcm)	Thickness (μm)	Oxygen (ppm)	Passiv.	Antirefl.
Wn08-2	CZ (N)	Phosphorus	5.5	400	16	PERT	Pyramid
Wn08-6	CZ (N)	Phosphorus	1.3	400	18	PERT	Pyramid
Wn04-5	FZ (N)	Phosphorus	0.9	400	< 0.1	PERL	DLAR
Ws12-7	CZ (P)	Gallium	5.3	220	19	PERT	DLAR
Ws10-7	FZ (P)	Boron	4.0	390	< 0.1	PERL	DLAR
Ws09-3	MCZ (P)	Boron	4.8	400	1.2 – 2.3	PERL	DLAR
Ws15-4	CZ (P)	Aluminium	0.73	280	17.7	PERT	Pyramid
Ws14-8	CZ (P)	Indium	14.5	275	16.4	PERT	Pyramid

5.5 Cell Irradiation

Some of the float-zone cells were irradiated in a previous study with 1MeV electrons to a fluence of 1×10^{16} ecm^{-2} at the Jet Propulsion Laboratory, Pasadena, and IV measurements were made immediately after each treatment was completed[5]. These cells that were stabilised by 48 hours of AM0 illumination after irradiation and used for the DLTS studies have been labelled as 48b, 49b and 50b respectively. The cells that were irradiated but not illuminated after this irradiation have been labelled 48f, 49f and 50f respectively.

The czochralski cells were also irradiated by 1MeV electrons but firstly at a fluence of 2.5×10^{11} ecm^{-2} using the Van de Graff accelerator at the Central Research Division, BICC, London. They were then successively irradiated to 3×10^{14}, 1×10^{15}, 3×10^{15} and 1×10^{16} electrons per cm^2 and stabilised by 48 hour AM0 illumination between each step[2]. The cells that were selected for DLTS measurement have been labelled as 67b, 68b and 70b respectively. Some of the Czochralski cells were proton irradiated by 10MeV protons to a fluence of 3×10^{11} protons/cm^2 and these have been labelled as 67c, 68c and 69c respectively. The FZ and CZ cells described above were tested and irradiated in the early 1990's and then stored in the dark at room temperature. The measurements carried out in this study were then closely compared to the earlier results and it was found that the storage of these cells had not affected the composition or concentration of the observed defects.

Electron irradiation (1MeV) at room temperature was used in this study to introduce deep level defects in all of the PERL/PERT cells using the Van de Graaff accelerator at the University of Delft in the Netherlands. Three fluence levels were chosen, 1E14, 1E15 and 3E15 electrons/cm^2, and the IV characteristics were measured before and after the irradiations.

5.6 IV Characteristics

The AM0 current-voltage (IV) characteristics of the silicon solar cells used in this study have been determined before and after electron irradiation. The measurements of the BSF/BSR Czochralski and float-zone cells were carrier out at the excellent facilities (Class A, IEC60904) at the Defence Evaluation and Research Agency (DERA) in Farnborough, England, using their LAPSS solar simulator. LAPSS stands for Large Area Pulsed Solar Simulator and these simulators have the capability of uniformly illuminating a large area (up to 5m diameter) at source-to-target distances of around 11m with the full AM0 intensity. These systems produce a pulse of light that lasts for around 2ms. The data is then accumulated during a time period of around 1ms in the central portion of the pulse. The measurement therefore requires the use of an electronic load which can sweep through the entire load voltage range during this time, together with a fast data collection system that allows the simultaneous reading of the cell voltage, current, and output during the load sweep. In addition to the advantage of a close match to the sun, these systems have the very desirable attribute of not heating up the test specimen during measurement. This solar simulator has been calibrated to match the AM0 intensity (136.8 mW/cm^2) by measuring the output from a primary standard cell. The normalised LAPSS spectrum is shown in Figure 5.2. together with the actual AM0 spectrum.

The AM0 IV characteristics of the PERL/PERT cells were also measured using the excellent facilities at DERA. The excellent light trapping scheme incorporated in these cells meant that the LAPSS simulator could not be used to measure these cells. These cells were therefore measured using constant illumination under a calibrated AM0 light intensity. The temperature was kept at a constant 25^{0}C using a temperature controlled sample stage and the cells were held in place by a vacuum arrangement.

5.7 Spectral Response

A purpose-built solar simulator was used to determine the spectral response of the silicon cells and Figure 5.3. shows the layout of this equipment. The test cell is illuminated with an AM1.5 bias lamp to approximate normal operating conditions. The Xenon lamp spectrum (Figure 5.4.) is then chopped at a frequency of around 100Hz and filtered using a narrowband (≈10nm) interference filter. Seventeen different filters are used to determine the spectral response at 50nm intervals between 300 and 1100nm and the transmission characteristics of the 350nm filter as an example are shown in Figure 5.5.

The current produced from the cell is then measured by the voltage drop across a 1Ω precision resistor which is fed into the lock-in amplifier to separate the different components of the signal. The lock-in amplifier (Stanford Research Systems SR810) uses a technique known as phase-sensitive detection to single out the component of the signal generated by the narrowband illumination of the test cell from the background noise. The response from the test cell is then compared to a reference cell of known response to determine the relative spectral response. This process is then repeated using all of the filters from 300 to 1100nm to obtain the relative spectral response of the cells over the entire wavelength range. This relative response can then be converted to absolute values because the short-circuit current is known and is equal to the area under the spectral response curve.

5.8 DLTS Studies

This section briefly outlines the sample preparation that was carried out in a previous study[5] on the Czochralski and float-zone cells, and also describes the procedure used to prepare the PERL/PERT cells for the DLTS measurements.

5.8.1 Small Area Definition

In order to perform DLTS measurements a small area of the cell needs to be isolated because the capacitance of the cell would otherwise exceed the limit of the DLTS capacitance meter. This was achieved for the BSF/BSR Czochralski and float-zone cells by spraying a solution of black wax through a mask to define the areas required prior to etching the cell to remove the contacts and the n-type layer from the surface of the cell. This procedure is defined in more detail in Table 5.4. The area of the cell was then defined by photography and enlargement and one of these mesas is shown in Figure 5.6..

Table 5.4 - Etching Sequence For Mesa Definition

Procedure	Method	Chemical	Symbol
Remove TiO antireflection coating	5 sec immersion	Hydrofluoric acid	HF
Spray black wax through mask to define 2mm^2 mesa areas	Dissolve black wax to obtain correct consistency	1,1,1-trichloroethane	CH_3CCl
Dry wax for 30 mins and remove mask			
Heat sample to 80 ^{0}C to melt wax and seal mesa area			
Examine mesas for pinholes and spray more wax if necessary			
Paint back of cell with two coats of black wax			
Remove Ag in contacts	10 min. immersion	Ammonium Hydroxide Hydrogen Peroxide	$1NH_4OH$ $1H_2O_2$ $4MeOH$
Remove Pd in contacts	3 min immersion	Nitric acid Hydrochloric acid	HNO_3 HCl
Remove Ti in contacts	Dip	Hydrofluoric acid	HF
Remove Al in contacts	Dip	Orthophosphoric acid	H_3PO_4
Clean sample	IPA, Deionized water		
Etch mesas	30 sec immersion in CP4a (5:3:3)	Nitric acid Hydrofluoric acid Acetic acid	HNO_3 HF CH_3COOH
Rinse to remove black wax		1,1,1-trichloroethane	CH_3CCl

The PERL/PERT cells were prepared for measurement using a simpler technique after it was discovered that cutting the cells into small pieces achieved the same result as the mesa definition technique. These cells were therefore simply cut into small rectangular pieces using a diamond saw and carefully measured using a digital vernier.

5.8.2 Sample Mounting

The samples used for the DLTS studies were mounted using silver DAG on to an alumina based contact pad. Gold-platinum ink was patterned on to the ceramic to create a back contact pad and several small bond pads to which the mesa's top contact was attached using a fine gold wire (see Figure 5.7.). The ceramic ensures electrical isolation from the DLTS sample stage whilst allowing good thermal conduction.

5.9 The DLTS System

The instrument used for these experiments was manufactured by Bio-Rad (Microscience Division) model no. DL4600 (Figure 5.8.). The DLTS system is computer controlled and has been upgraded to run using TrapView for Windows which enables the normal operating procedures and results analysis to be automatically calculated. There is also a wide range of options such as the trap libraries which allow the user to customise the measurements and manipulate the data produced.

The samples were first mounted in the cryostat using heat sink compound or silver paint and Figure 5.9. shows the cryostat chamber. The chamber was then evacuated to less than 10^{-2} torr. The liquid nitrogen pump was then submerged into a dewar of liquid nitrogen and the heating unit of the DLTS was switched on. The temperature of the sample is monitored by a platinum resistance thermocouple which is located on the sample stage in close contact with the sample. The temperature is then controlled by varying the output of the heater and pump to achieve the desired temperature gradient.

The first stage in the DLTS process is to obtain a plot of the capacitance change as a function of the applied voltage. This data is then plotted as $1/C^2$ against V to determine the doping density of the lightly doped side of the junction. The capacitance at the quiescent reverse bias voltage is then also noted and these values are passed on to the DLTS program.

The sample is held at the quiescent reverse bias V_R before the majority carriers are injected by the electrical fill pulse V_F (Figure 5.10.). The pulse width is large enough to fill all the available traps and the width between the pulses is determined by the selected rate window. The capacitance of the sample is measured by the Boonton capacitance meter and the bulk of the capacitance is offset. The capacitance transient produced is then processed and analysed by the central processing unit. The capacitance transient and pulse logic can also be monitored by oscilloscope and in this study a PicoScope ADC-200 virtual instrument has been used.

The DLTS set-up procedure must first be carried out to define the measurement parameters.

1. The pulse heights must first be set and typical values are –5.00V for the measurement phase and –0.30V is commonly used for the filling pulse,
2. The fill pulse width must also be set and a typical value used is 6ms,
3. The scale of the Boonton meter must be reduced to the smallest possible value to obtain the most accurate result (usually 30pF or less),
4. The bulk of the capacitance must then be offset to enable detection of the small fluctuations caused by the bias pulse,
5. The sensitivity of the signal processor is then set and it is often necessary to perform several quick scans to determine the most appropriate value,
6. The rate windows and the scan direction (increasing or decreasing temperature) are then defined,
7. The scan range and rate are then set and a rate of 0.1K/s is commonly used to minimise the error induced by temperature lag.

This procedure is then carried out using several different rate windows to enable an Arrhenius plot to be constructed. An Arrhenius plot is a plot of the emission rate ($\ln e/T^2$) against the temperature (1000/T) and the slope of this graph gives the approximate activation energy of the trap[11]. The intercept of the Arrhenius plot gives a value for the majority-carrier capture cross-section. A more accurate value for the capture cross-section however can be obtained by slowly reducing the width of the fill pulse and repeatedly scanning one of the peaks (see Section 4.6.2).

5.10 The FBDLTS System

A relatively large current is required under forward bias to prime the trap therefore the filling pulse cannot be applied through the capacitance meter as in a conventional DLTS experiment (see Section 4.7). The Boonton capacitance meter was therefore isolated during the fill pulse phase of the experiment using a Fast Pulse Interface (FPI). This system of fast FET switches isolates the Boonton during the fill pulse phase by switching from the reverse bias applied through the Boonton capacitance meter, to the forward bias applied directly to the sample. The FPI then switches back to allow the capacitance change to be measured in the usual manner during the reverse bias phase.

The forward bias conditions during the experiment were measured using a small resistor in series with the forward bias supply. This information was then used to estimate the injected carrier density as described in Section 4.7.1.. The dark IV characteristics were also measured at various temperatures by mounting the samples into the cryostat to assess the injection conditions. These results were then used to obtain a more accurate estimate of the electron concentration during the experiments (see Section 8.7.2).

5.11 The MCTS System

To investigate defects that trap minority carriers the p-n junction can either be forward biased or alternately the minority carriers can be injected by illumination with light of above band gap energy. This method provides more accurate results and greater control of the number of minority carriers that are injected for reasons that are fully explained by Blood and Orton[11]. The minority carriers are injected using an AlGaAs/GaAs semiconductor laser of variable power up to 100mW. This laser is aligned above the sample using the locating pins to obtain the greatest sensitivity and the laser output power as a function of the dial setting is shown in Figure 5.11.. The diode is held at the quiescent reverse bias and the minority carriers are then injected using laser injection to provide the optical fill pulse. The results can then be analysed in the same way as the conventional DLTS technique.

5.12 References

---

[1] Markvart, T., *et al,* Electron and photon degradation of boron doped FZ silicon solar cells, Proc. 3rd Europ. Symp. "Photovoltaic generators in space", ESA SP-173, p.109-114, (1982).

[2] Markvart, T., Willoughby, A.F., and Dollery, A.A., Silicon solar cells with improved radiation resistance, *Proceedings of the 19th Photovoltaics Specialists Conference, New Orleans, USA*, p.709-714, (1987).

[3] Peters, J.W., Markvart, T., et al, Defect interactions in silicon solar cells, Presented at the Second Workshop on Radiation-Induced and/or Process-Related Electrically Active Defects in Semiconductor-Insulator Systems, North Carolina, September 10-13, (1989).

[4] Peters, J., Markvart, T., and Willoughby, A.F.W., *Materials Science Forum* **83-87**, p.1539-1544, (1992).

[5] Peters, J.W., The role of defects in the radiation damage of solar cells, PhD Thesis, Engineering Materials, University of Southampton, (1993).

[6] Markvart, T., Parton, D.P., Peters, J.W. and Willoughby, A.F.W.: DLTS of Recombination Centres in Semiconductors, Presented at the 17th International Conference on Defects in Semiconductors, Gmunden, Austria, p.1381, (1993).

[7] J. Zhao, A. Wang and M.A. Green, Progress in Photovoltaics 7, p.471, (1999).

[8] J. Zhao, A. Wang and M.A. Green, 16th Photov. Solar Energy Conf., Glasgow, UK, B1/53, (2000).

[9] Green, M.A., Silicon Solar Cells, Centre of Photovoltaic devices and systems, University of New South Wales, (1995).

---

[10] Zhao, J., and Green, M.A., IEEE Trans. Electron Devices 38, p.1925, (1991).

[11] Blood, P. and Orton, J.W.: The electrical characterisation of semiconductors: majority carriers and electron states, Techniques of Physics, Vols. 13 & 14, Academic Press, London, (1992).

FIGURE 5.1. PASSIVATED-EMITTER REAR LOCALLY DIFFUSED (PERL) SOLAR CELL DESIGN

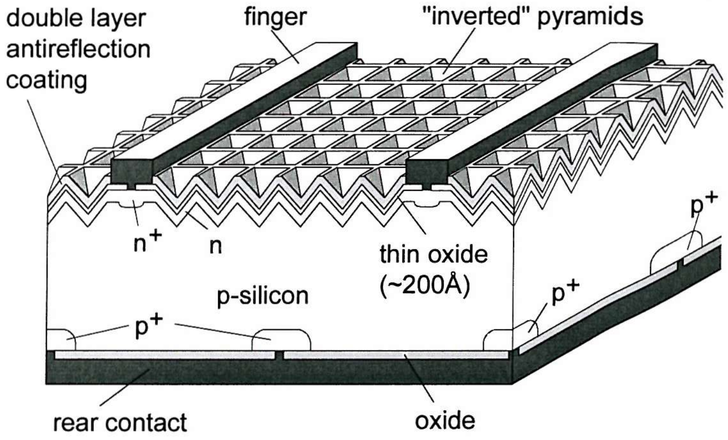

FIGURE 5.2. NORMALISED LAPSS SPECTRUM COMPARED TO THE AM0 SOLAR SPECTRUM

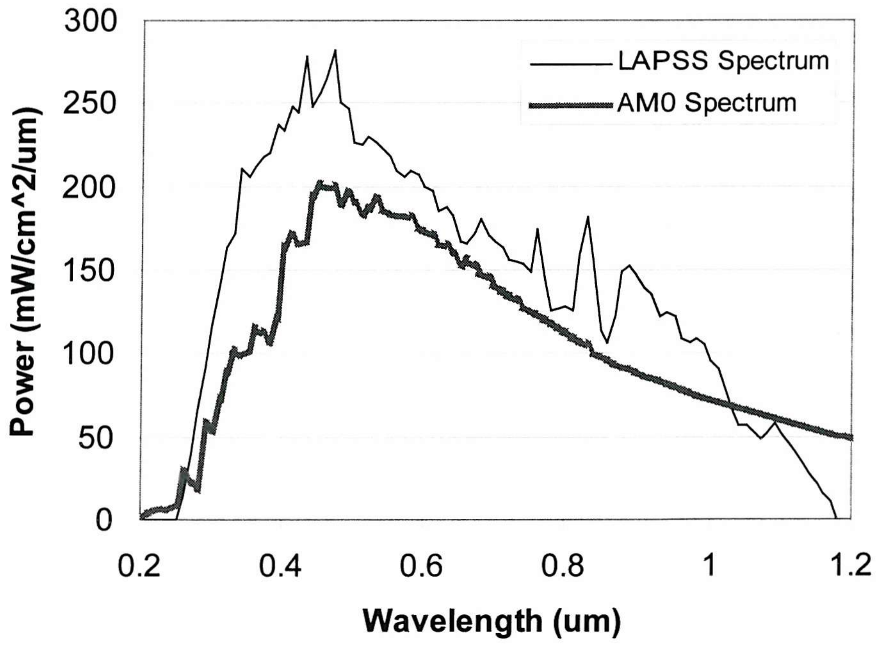

FIGURE 5.3. SCHEMATIC OF THE SOLAR SIMULATOR USED TO DETERMINE SPECTRAL RESPONSE

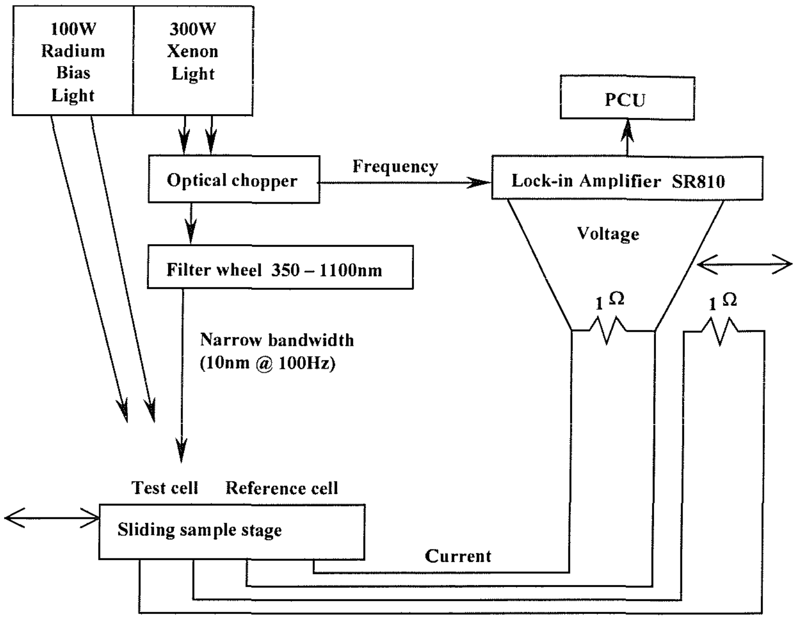

FIGURE 5.4. SPECTRUM OF THE 300W XENON LAMP

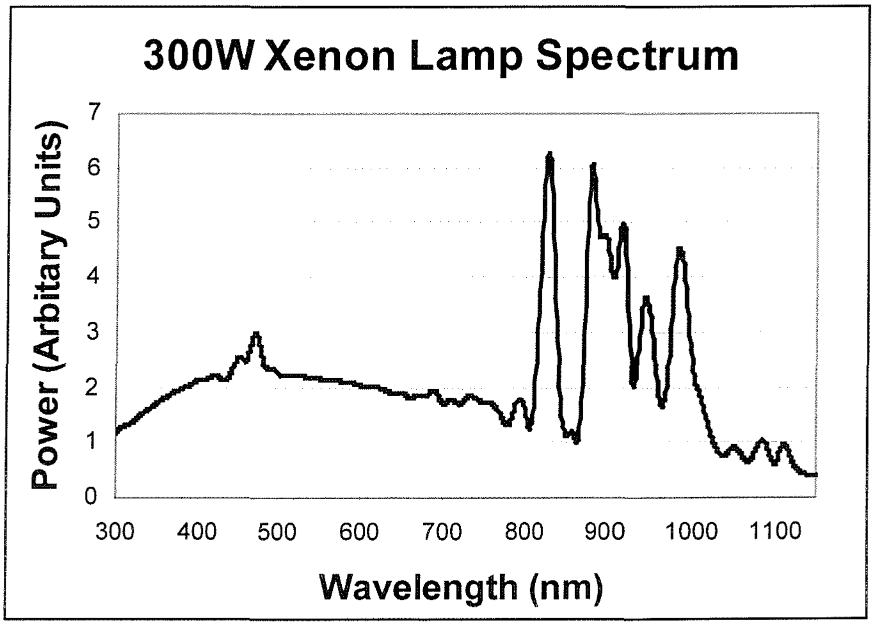

FIGURE 5.5. TRANSMISSION CHARACTERISTICS OF THE 350NM NARROW BANDPASS FILTER

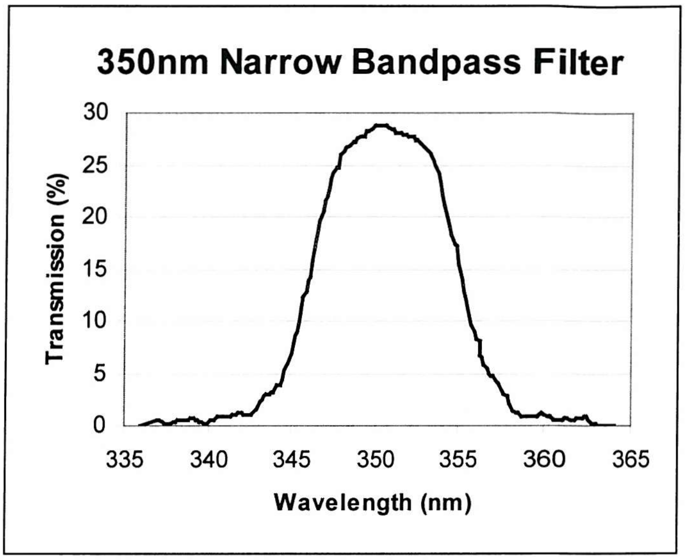

FIGURE 5.6. ENLARGED PHOTOGRAPH OF A TYPICAL MESA DIODE

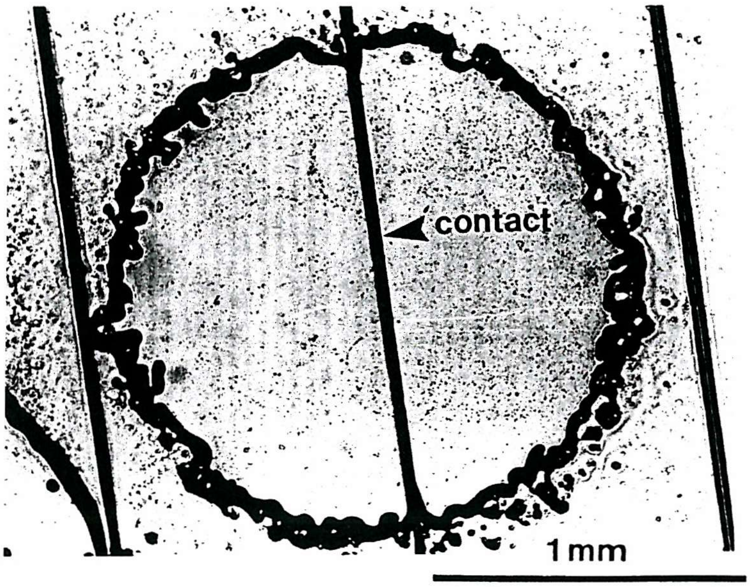

FIGURE 5.7. CONNECTION OF THE MESA DIODES TO THE ALUMINA BASED CERAMIC FOR DLTS MEASUREMENTS

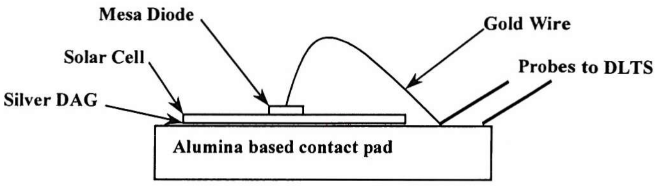

FIGURE 5.8. PHOTOGRAPH OF THE DLTS SYSTEM

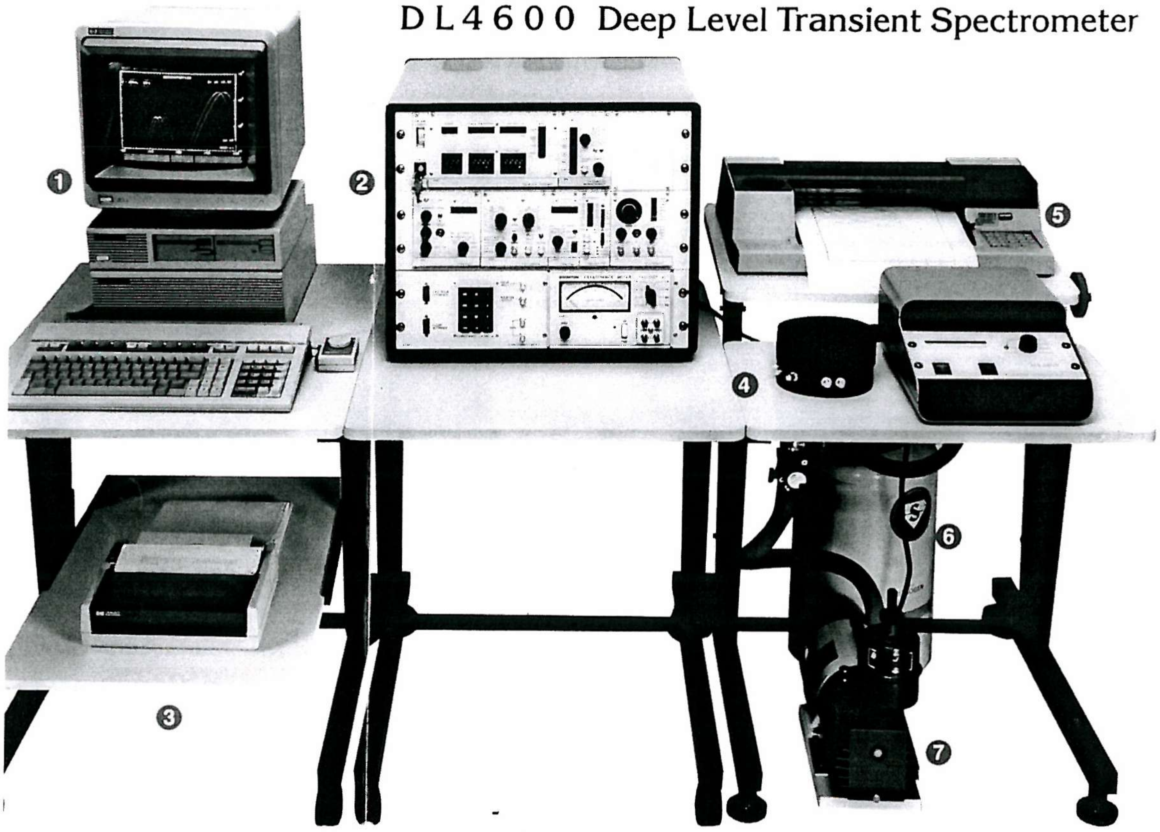

FIGURE 5.9. THE DLTS CRYOSTAT CHAMBER

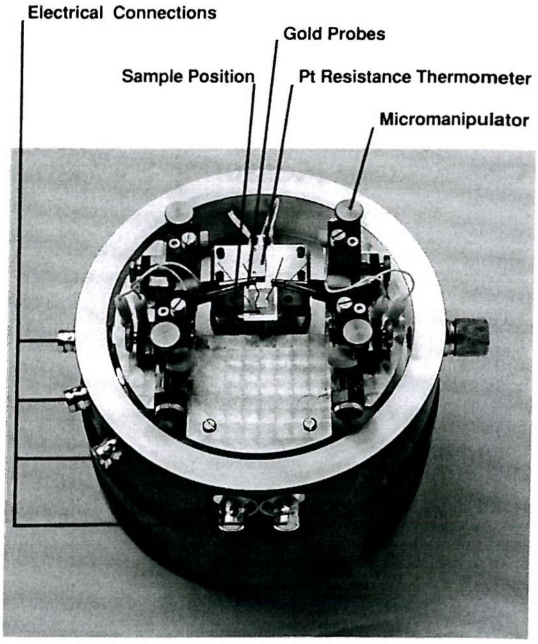

FIGURE 5.10. SIMPLIFIED BLOCK DIAGRAM OF THE DLTS SYSTEM

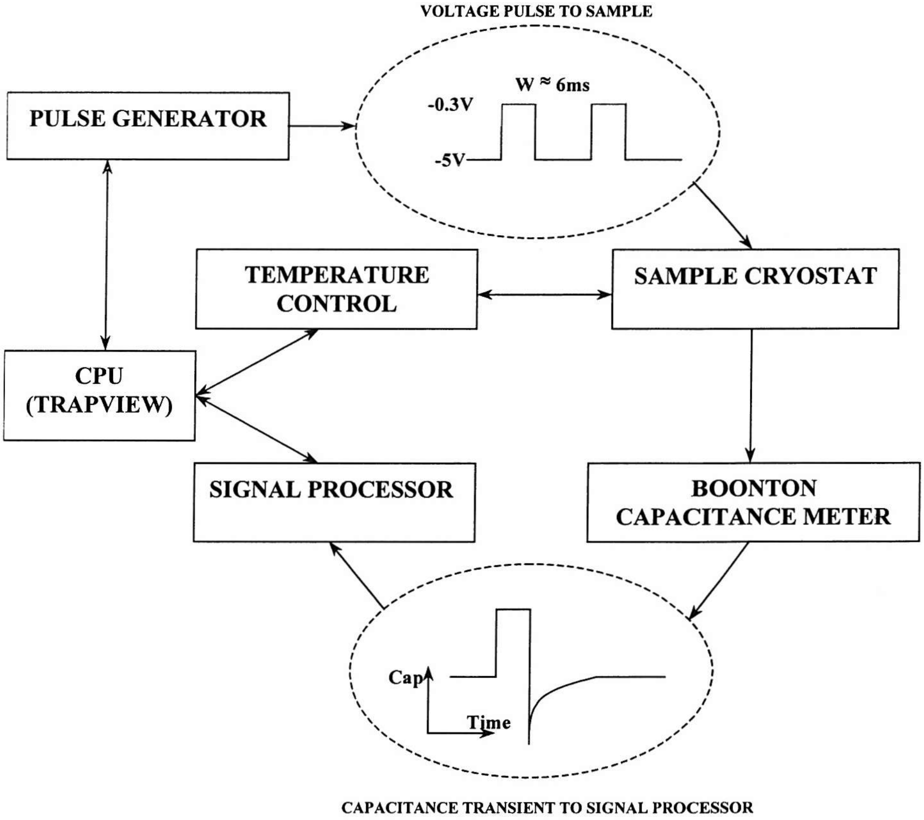

FIGURE 5.11. OUTPUT POWER OF THE AlGaAs LASER DURING CONTINUOUS OPERATION AS A FUNCTION OF LASER POWER DIAL SETTING

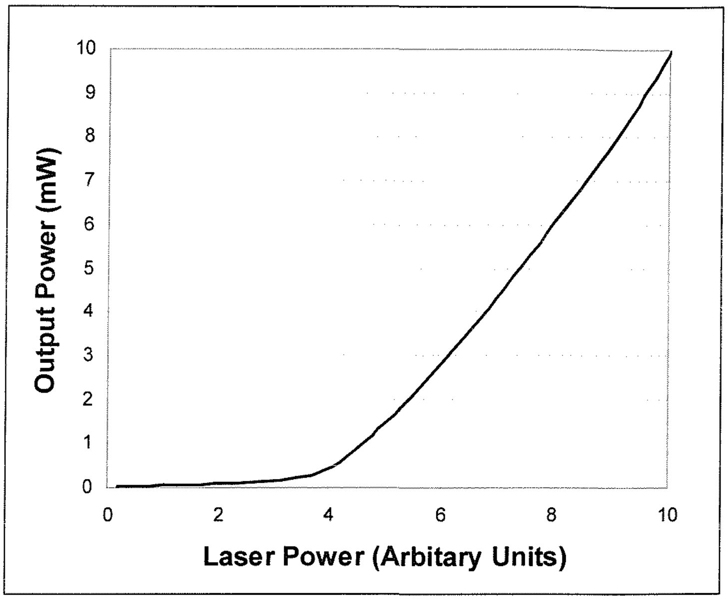

CHAPTER SIX

PRESENTATION OF RESULTS

6.1 DLTS Results of Gold Doped N-type Silicon

The DLTS plot (1000/s rate window) obtained from the gold doped n-type silicon sample can be seen in Figure 6.1.. The doping density was obtained from a standard CV plot and is around 1.1×10^{14} cm^{-3}. The results obtained from these experiments have been summarised in Table 6.1 which shows all the levels observed and their capture cross-sections determined from the intercept of the Arrhenius plots.

Table 6.1 – Defect Levels Observed in the Gold Doped N-type Silicon Standard

Peak Label	Concentration $\times 10^{13}$ (cm^{-3})	Energy Level (eV)	Capture Cross-Section (cm^2)
G1	0.46	$E_C - 0.159$	1.4×10^{-14}
G2	2.6	$E_C - 0.254$	1.1×10^{-15}
G3	1.4	$E_C - 0.277$	1.6×10^{-16}
G4	1.0	$E_C - 0.509$	3.4×10^{-15}

These levels have been observed in silicon by other workers. Morooka[1] observed similar levels at E_C-0.16, E_C-0.24, E_C-0.30, E_C-0.54, which were attributed to different forms of substitutional gold atoms. The level at E_C- 0.16 was only observed occasionally by Morooka and at very low concentrations. The levels observed in this study can therefore be attributed to different forms of the substitutional gold atoms. This sample was also used to investigate the hysterisis error in the DLTS system. There was a small (<0.5K) temperature lag observed in the system when the temperature was ramped at the rate of 0.2K/s. The temperature was therefore ramped at 0.1K/s in all of the experiments detailed below. This ensured that the hysterisis error was negligible in all of these experiments.

6.2 DLTS of BSF/BSR Float-zone Silicon Solar Cells (Photon Annealed)

The BSF/BSR Czochralski and float-zone silicon solar cells used in the first part of this report have been extensively studied in many previous projects[2,3,4,5,6,7]. These references therefore contain additional information about the manufacture and processing of these cells as well as a great deal of information about the defects introduced by particle irradiation. The specifications of the BSF/BSR float-zone cells are given in Section 5.2 and Table 5.1.

Float-zone silicon cell 49d was stabilised by 48 hours of AM0 illumination after being irradiated by 1×10^{16} electrons/cm^2 and three main defects were observed that can be seen in Figure 6.2.. These defects have been labelled F1, F2 and F3 and the results obtained from standard Arrhenius plots are shown in Table 6.2. Also shown are two smaller defects, F4 and F5 that were also observed in these cells.

Table 6.2 – Defect Levels Observed in Float-zone Silicon Solar Cell 49d

Cell No.	Peak Label	Concentration $\times10^{13}$ (cm^{-3})	Energy Level	Capture Cross-Section (cm^2)
49d M5	F1	1.3	Ev + 0.183	2.4×10^{-16}
	F2	1.7	Ev + 0.292	1.9×10^{-14}
	F3	1.4	Ev + 0.361	3.0×10^{-15}
	F4	1.0	Ev + 0.431	2.4×10^{-15}
	F5	0.5	Ev + 0.501	9.6×10^{-16}

6.3 DLTS of BSF/BSR Czochralski Silicon Solar Cells

These cells are described in Section 5.3 and Table 5.2. Two main defects were observed in the Czochralski silicon cells and these have been labelled C1 and C3 in Figure 6.3.. Table 6.3 details the energy levels and capture cross-sections determined from the slope and intercept of the Arrhenius plots for cell no. 67b.

Table 6.3 – Defect Energy Levels Observed in Czochralski Silicon Solar Cell 67b

Cell No.	Peak Label	Concentration $\times10^{13}$ (cm^{-3})	Energy Level	Capture Cross-Section (cm^2)
67b M3	C1	1.7	Ev + 0.192	5.0×10^{-16}
	C3	4.2	Ev + 0.361	2.7×10^{-15}

Minority carrier trap spectroscopy (MCTS) was also used on these cells to observe the minority carrier traps formed by the electron irradiation. One large trap was observed and the energy level of this defect was found to be at Ec-0.26eV from an Arrhenius plot.

6.4 DLTS of P-on-N type cells

These cells have a phosphorus doping density of 4.6×10^{14} cm^{-3} and were irradiated by 3×10^{15} electrons/cm^{2} at the University of Delft, Netherlands. Figure 6.4. shows a typical DLTS scan and the peaks have been labelled N1 to N4. Table 6.4 shows the results of the standard Arrhenius plots. The results for the energy level and capture cross-section of peak N1 however are difficult to obtain because this peak appears at the low temperature limit of the apparatus. The peak labelled N3 appears as a shoulder on the low temperature side of peak N4 and therefore cannot be resolved (see Figure 6.5.).

Forward bias DLTS was also used on these cells to reveal the traps capable of capturing minority carriers (holes) in these cells. Figure 6.6. shows one of these scans that reveals one large peak in the spectrum labelled MN1. To achieve saturation of the minority carrier traps several levels of forward bias were chosen to ensure complete trap occupation. Figure 6.7. shows two of these scans at 1Volt and 1.7V. It was found that the height of peak MN1 was constant at any forward bias over 1.7V and the trap was therefore completely filled with minority carriers.

Table 6.4 – Defect Energy Levels Observed in N-type Silicon Cell PNA

Cell No.	Peak Label	Concentration $\times10^{13}$ (cm^{-3})	Energy Level	Capture Cross-Section (cm^{2})
PNA	N1	17	***Ev + 0.277***	***6.8×10^{-9}***
	N2	0.45	Ev + 0.292	7.5×10^{-13}
	N4	0.57	Ev + 0.463	7.3×10^{-14}
FBDLTS	MN1		Ec - 0.335	2.7×10^{-15}

6.5 High Efficiency PERL/PERT Silicon Solar Cells

All of these cells described in Table 5.3 have a 100 crystal orientation. They are then etched to reveal the 111 surface and this creates an "inverted pyramid" structure that has around 75% more surface area. Some of these cells also have a double-layer antireflection coating (DLAR) that further improves the absorption of the incident light (see Table 5.3). The n-type (phosphorus) samples have a junction depth of around 0.6μm and the p-type samples have a junction depth of around 0.3μm. The doping densities have been determined using the standard technique of plotting the capacitance against the reverse bias voltage and these results are shown in Table 6.5.

Table 6.5 - Doping Densities of the PERL/PERT cells determined from Capacitance Voltage Plots

Cell No.	Type	Resistivity (Ωcm)	Doping Density ($\times 10^{14}$)
PNA	CZ (Ph)		4.9
Wn082c41	CZ (Ph)	5.5	11
Wn086c22	CZ (Ph)	1.3	46
Wn0453e1	FZ (Ph)	0.9	54
Ws154	CZ (Al)	0.73	110
Ws107i3	FZ (Bo)	4.0	40
Ws93k2	MCZ (Bo)	4.8	30
Ws127k1	CZ (Ga)	5.3	36
Ws158i2	CZ (In)	14.5	8.8

6.6 DLTS of the High Efficiency Phosphorus Doped Czochralski cells

The DLTS studies on these cells revealed four defects of varying concentrations (see Figure 6.8. and Table 6.6). CZ(5.5)1 appeared at the low temperature limit of the apparatus and it was therefore difficult to get accurate results for this defect. CZ(5.5)5 appeared at around 290K but was only present in small concentrations and therefore an Arrhenius plot could not be constructed for this level (see Figure 6.9.).

Table 6.6 – Defect Energy Levels Observed in Phosphorus Doped Czochralski cell Wn082c41

Cell No.	Peak Label	Concentration $\times 10^{13}$ (cm^{-3})	Energy Level	Capture Cross-Section (cm^{-2})
Wn082c41	CZ(5.5)1	50		
CZ(Ph) 5.5	CZ(5.5)2	0.95	Ev + 0.138	5.5×10^{-18}
	CZ(5.5)4	6.1	Ev + 0.272	2.2×10^{-17}
	CZ(5.5)5	0.82		
FB	FB(5.5)1		Ev + 0.441	1.1×10^{-10}

Forward bias DLTS studies on these cells revealed one large minority carrier trap that has been labelled FB(5.5)1 and is also described in Table 6.6 and Figure 6.10..

The phosphorus doped czochralski cells with a higher doping level (1.3 Ohm.cm) contained the same defects as the lower doped sample (5.5 Ohm.cm) in different concentrations (see Table 6.7 and Figure 6.11.). The defect CZ(1.3)3 could also be seen in these samples as a shoulder on the low temperature side of the peak CZ(1.3)4 and this defect was also present in the lower doped samples in a smaller concentration (see CZ(5.5)3 in Figure 6.9.).

Table 6.7 – Defect Energy Levels Observed in Phosphorus Doped Czochralski cell Wn086c2

Cell No.	Peak Label	Concentration $\times 10^{13}$ (cm^{-3})	Energy Level	Capture Cross-Section (cm^{-2})
Wn086c22	CZ(1.3)1	31	Ev + 0.208	1.6×10^{-11}
CZ(Ph) 1.3	CZ(1.3)2	1.6	Ev + 0.171	4.9×10^{-17}
	CZ(1.3)3			
	CZ(1.3)4	8.6	Ev + 0.399	9.5×10^{-15}

6.7 DLTS of the High Efficiency Phosphorus Doped Float-zone cells

Two large and one smaller majority carrier peaks were observed in these cells and these peaks are shown in Table 6.8. together with the one minority carrier trap FBP1 that was observed using FBDLTS.

Table 6.8 – Defect Energy Levels Observed in Phosphorus Doped Float-zone cell Wn0453e1

Cell No.	Peak Label	Concentration $\times 10^{13}$ (cm^{-3})	Energy Level	Capture Cross-Section (cm^{-2})
Wn0453e1	FZP1	21	Ev + 0.232	2.5×10^{-10}
FZ (Ph)	FZP2	0.55	Ev + 0.245	4.1×10^{-14}
	FZP3	6.5	Ev + 0.483	7.7×10^{-13}
FBDLTS	FBP1		Ec – 0.484	5.5×10^{-15}

6.8 DLTS of the High Efficiency Boron Doped Float-zone cells

These cells were also irradiated by 3×10^{15} electrons/cm^2 and two large majority carrier peaks were observed in the DLTS spectrum (see Figure 6.12.). These peaks have been labelled FZB1 and FZB3 and are described in Table 6.9.

Table 6.9 – Defect Energy Levels Observed in Boron Doped Float-zone cell Ws107i

Cell No.	**Peak Label**	**Concentration $\times10^{13}$ (cm^{-3})**	**Energy Level**	**Capture Cross-Section (cm^{-2})**
Ws107i3	FZB1	0.39	Ev + 0.211	6.4×10^{-15}
	FZB3	1.3	Ev + 0.375	1.2×10^{-14}

These cells degrade further after irradiation when illuminated by infra-red light. This is known as the photon effect[8] and was found have a complex dependence on base resistivity[2]. The DLTS results for one of these samples after 48 hours of AM0 illumination are shown in Figure 6.13. and Table 6.10. The defect labelled FZB2 has appeared and an Arrhenius plot has been constructed for this defect.

Table 6.10 – Defect Energy Levels Observed in Boron Doped Float-zone cell Ws107i after 48 hours AM0 illumination

Cell No.	**Peak Label**	**Concentration $\times10^{13}$ (cm^{-3})**	**Energy Level**	**Capture Cross-Section (cm^{-2})**
WS107i3	FZB1	0.4	Ev + 0.205	1.6×10^{-15}
FZ (Bo)	FZB2	0.33	Ev + 0.277	5.4×10^{-14}
	FZB3	1.3	Ev + 0.365	2.0×10^{-15}

6.9 DLTS of the High Efficiency Boron Doped Magnetically-Confined Czochralski cells

The DLTS results for these cells show two main peaks in the spectrum that have been labelled MCZ1 and MCZ3 in Figure 6.14.. The results from the Arrhenius plots are given in Table 6.11.

Table 6.11 – Defect Energy Levels Observed in Magnetically-confined Czochralski cell Ws93k2

Cell No.	Peak Label	Concentration $\times 10^{13}$ (cm^{-3})	Energy Level	Capture Cross-Section (cm^{-2})
Ws93k2	MCZ1	0.36	Ev + 0.181	1.2×10^{-16}
MCZ(Bo)	MCZ3	0.99	Ev + 0.334	1.9×10^{-15}

FBDLTS and MCTS was also carried out on these cells and showed that their were no minority carrier traps detectable in these samples. After 48 hours of AM0 illumination a new defect appeared between MCZ1 and MCZ3 and this new peak has been labelled MCZ2 in Figure 6.15.. The results from the standard Arrhenius evaluation are given in Table 6.12.

Table 6.12 – Defect Energy Levels Observed in Magnetically-confined Czochralski cell Ws93k2 after 48 hours of AM0 illumination

Cell No.	Peak Label	Concentration $\times 10^{13}$ (cm^{-3})	Energy Level	Capture Cross-Section (cm^{-2})
Ws93k2	MCZ1	0.46	Ev + 0.178	1.5×10^{-16}
MCZ(Bo)	MCZ2	0.29	Ev + 0.275	4.7×10^{-14}
48h Photon	MCZ3	1.1	Ev + 0.353	1.2×10^{-15}

6.10 DLTS of the High Efficiency Gallium Doped Czochralski cells

Two large majority carrier peaks were also observed in these cells (see Figure 6.16.) and these peaks have been labelled CZG1 and CZG3. The Arrhenius plot results are shown in Table 6.13.

Table 6.13 – Defect Energy Levels Observed in the Gallium doped Czochralski cell Ws127k3

Cell No.	Peak Label	Concentration $\times 10^{13}$ (cm^{-3})	Energy Level	Capture Cross-Section (cm^{-2})
Ws127k3	CZG1	0.46	Ev + 0.194	5.3×10^{-16}
CZ (Ga)	CZG3	2.0	Ev + 0.396	2×10^{-14}

6.11 DLTS of the High Efficiency Indium Doped Czochralski cells

These cells contained two hole traps after electron irradiation (see Figure 6.17.) and they have been labelled CZI1 and CZI3 (see also Table 6.14 for Arrhenius plot results).

Table 6.14 – Defect Energy Levels Observed in the Indium doped Czochralski cell Ws158i2

Cell No.	Peak Label	Concentration $\times 10^{13}$ (cm^{-3})	Energy Level	Capture Cross-Section (cm^{-2})
Ws158i2	CZI1	0.34	Ev + 0.219	1.7×10^{-16}
CZ(In)	CZI3	1.5	Ev + 0.377	2.6×10^{-14}

6.12 DLTS of the High Efficiency Aluminium Doped Czochralski cells

These cells contained four hole traps that have been labelled CZA1 to CZA4 in Figure 6.18. The concentration of these defects and the data from the Arrhenius plots is summarised in Table 6.15

Table 6.15 – Defect Energy Levels Observed in the Aluminium doped Czochralski cell Ws154j1

Cell No.	Peak Label	Concentration $\times 10^{13}$ (cm^{-3})	Energy Level	Capture Cross-Section (cm^{-2})
Ws154j1	CZA1	0.42	Ev + 0.195	4.1×10^{-16}
CZ(Al)	CZA2	1.4	Ev + 0.253	1.9×10^{-16}
	CZA3	2.1	Ev + 0.370	3.1×10^{-15}
	CZA4	1.0	Ev + 0.496	3.4×10^{-14}

6.13 FBDLTS of the Gallium doped cells

To try and find the minority-carrier capture cross-section of the H(0.19) defect FBDLTS on the CZG cells was carried out at a variety of forward bias voltages (see Figure 6.19.). As the forward bias voltage was increased the CZG1 peak reduced in height whereas the CZG3 peak remained relatively constant. This effect has been observed before[9] in aluminium doped cells and this suggests that peak CZG1 has a large electron capture cross-section. To ensure that there are no minority carrier traps interfering with the results MCTS was also carried out on these samples. Figure 6.20. shows the MCTS results and it can be seen that there are no significant minority carrier traps. This effect will now be examined in much greater detail in Chapter 8.

6.14 Dark IV Characteristics of the High Efficiency PERL/PERT Cells

The dark current-voltage (IV) characteristics of the PERL/PERT cells were measured at 298K using a HP Parameter Analyser located in the Electronics (ECS) department at Southampton University. The curves were measured for the irradiated cells (3E15 electrons/cm^2) and Figure 6.21. shows the results for the aluminium (CZA) and indium (CZI) doped cells. The results for the FZB and the MCZ cells are shown in Figure 6.22. and the IV curves measured for the phosphorus doped float-zone (FZP) and czochralski (CZP5.5 and CZP1.3) cells are given in Figure 6.23.. The results for the FZB cells are also compared to a standard boron doped czochralski cell (69/10/1) in Figure 6.24..

These characteristics were also measured for the CZG cells at different temperatures by measuring the voltage drop across a small resistor in series with the forward bias voltage supply. The cells were mounted in the DLTS cryostat chamber and the DLTS temperature control system was used to carefully control and monitor the cell temperature. These results are shown in Figure 6.25. for various temperatures.

6.15 IV Characteristics of the BSF/BSR Czochralski and Float-zone Silicon Solar Cells

The IV characteristics have been determined under AM0 (136.8mA/cm^2) conditions at the Defence Evaluation and Research Establishment, Farnborough and these results are compared to the results attained in previous studies. These results are labelled "Dera99" for this study, "RAE" for the data obtained from Reference 6, and "Telef" for the data that was supplied by Telefunken and measured before deposition of the anti-reflection coating. The short-circuit current (I_{SC}) and the open circuit voltage (V_{OC}) have been compiled in Table 6.16 and the complete IV characteristic for cell 68/8/2 is shown in Figure 6.26. This data will now be used in Chapter Seven to examine the reduction in diffusion length caused by particle irradiation.

Table 6.16 – IV Characteristics for the Czochralski Silicon Solar Cells

Cell No.	I_{SC} (A)	V_{OC} (V)	Irradiation	Comments	Data Source
67-13	0.0260	0.5377	None	No AR	RAE
67-13	0.0254	0.5292	1 E14 1 MeV E	No AR	RAE
67-13	0.0249	0.5270	3 E14 1 MeV E	No AR	RAE
67-13	0.0233	0.5048	1 E15 1 MeV E	No AR	RAE
67-14	0.0229	0.4857	3 E15 1 MeV E	AR LAYER	Dera 99
68-4	0.0365	0.5381	None	AR LAYER	Dera 99
68-4	0.0359	0.5460	None	AR LAYER	RAE
68-4	0.0270	0.5390	None	No AR	Telef
68-8	0.0361	0.5366	None	AR LAYER	Dera 99
68-8	0.0353	0.5449	None	AR LAYER	RAE
68-8	0.0271	0.5390	None	No AR	Telef
68-8-2	0.0256	0.5338	None	No AR	RAE
68-8-2	0.0251	0.5255	1 E14 1 MeV E	No AR	RAE
68-8-2	0.0248	0.5291	3 E14 1 MeV E	No AR	RAE
68-8-2	0.0235	0.5046	1 E15 1 MeV E	No AR	RAE
68-8-2	0.0210	0.4567	1 E16 1 MeV E	No AR	Dera 99
68-9	0.0362	0.5374	None	AR LAYER	Dera 99
68-9	0.0349	0.5455	None	AR LAYER	RAE
68-9	0.0271	0.5410	None	No AR	Telef
68-9-2	0.0215	0.4545	1 E16 1 MeV E	No AR	Dera 99
68-10	0.0362	0.5374	None	AR LAYER	Dera 99
68-10	0.0346	0.5445	None	AR LAYER	RAE
68-10	0.0264	0.5400	None	No AR	Telef
68-7-2	0.0222	0.4854	3 E11 10MeV P	No AR	Dera 99
68-13	0.0257	0.5319	None	No AR	RAE
68-13	0.0254	0.5239	1 E14 1 MeV E	No AR	RAE
68-13	0.0250	0.5278	3 E14 1 MeV E	No AR	RAE
68-13	0.0232	0.4996	1 E15 1 MeV E	No AR	RAE
69-10-1	0.0233	0.4795	3 E15 1 MeV E	AR LAYER	Dera 99
69-16	0.0233	0.4795	3 E15 1 MeV E	AR LAYER	Dera 99
69-3-2	0.0232	0.4778	3 E15 1 MeV E	AR LAYER	Dera 99

6.16 Spectral Response of the BSF/BSR Czochralski and Float-zone Silicon Solar Cells

The spectral response of the Czochralski cells has been determined using the solar simulator described in Chapter Five. These results have been calibrated by comparison with results obtained from DERA, Farnborough where these cells were also tested. These relative values for the spectral response were then converted to absolute values using the short-circuit current given in Table 6.16 . Figure 6.27. shows the absolute spectral response of cell no. 68 before and after deposition of the antireflection coating and before irradiation. Solar cell 68/8/2 was tested before deposition of the antireflection coating and three results from this batch for cells 68/4, 68/8 and 68/9 were obtained after deposition of the antireflection coating and this shows the accuracy of these measurements.

The irradiation of solar cells causes a reduction in the minority-carrier diffusion length and hence the spectral response of solar cells (see Chapters Two and Three) and this is shown in Figure 6.28.. Cell no. 68/13 which is unirradiated is shown and compared to cell no. 68/9/2 that was irradiated with a fluence of 1×10^{16} (1MeV)electrons/cm^2 and cell no. 68/7/2 which was irradiated with 10MeV protons to a fluence of 3×10^{11} protons/cm^2. Finally some of the results from a previous study[6] that are to be modelled in Chapter Seven are given here for completeness. Figure 6.29. shows the effect of electron irradiation on cell 67/13, Figure 6.30. shows effect on cell no. 68/8/2 and the effect on cell 68/13 is shown in Figure 6.31..

6.17 Electrical Characteristics of the High Efficiency PERL/PERT Cells

The AM0 IV characteristics were measured for the eight different types of PERL/PERT cells before and after irradiation at three levels of 1MeV electron irradiation, 1×10^{14}, 1×10^{15} and 3×10^{15} electrons/cm^2. All of these results are shown in Table 6.17. The spectral response was also measured for these cells and Figure 6.32. shows the results for the FZP5.5 cells. Figure 6.33. shows the results for the CZP1.3 cells and Figure 6.34 details the spectral response of the FZP cells. Figure 6.35 shows the CZG spectral response, Figure 6.36 gives the FZB result and Figure 6.37 shows the spectral response of the MCZ cells. The CZA spectral response is detailed in Figure 6.38 and the spectral response of the CZI cells is shown in Figure 6.39.

Table 6.17 – AM0 IV Characteristics of the High Efficiency PERL/PERT Cells before and after 3 levels of 1MeV Electron Irradiation

Cell Type	Batch No.	Wafer No.	Irradiation (cm^{-2})	J_{SC} (mA/cm^2)	V_{OC} (mV)	FF	Efficiency (%)
CZP 5.5	**WN08**	**2B**	0.E+00	40.50	657.4	0.690	13.43
PERT		**2B**	0.E+00	39.93	650.5	0.730	13.86
NO AR		**2E**	0.E+00	39.98	653.7	0.693	13.24
		2E	1.E+15	22.33	483.3	0.736	5.81
		2F	0.E+00	40.33	652.5	0.695	13.37
		2F	3.E+15	21.10	465.1	0.723	5.18
		2A1	0.E+00	38.00	646.1	0.718	12.89
		2A2	0.E+00	38.80	635.4	0.752	13.57
		2A3	0.E+00	39.60	644.6	0.712	13.27
		2A4	0.E+00	39.80	638.3	0.737	13.68
		2C1	0.E+00	39.00	654.4	0.700	13.09
		2C2	1.E+14	25.80	507.8	0.727	6.98
		2C3	0.E+00	40.80	658.1	0.707	13.87
		2C3	1.E+15	22.00	477.0	0.746	5.71
		2C4	3.E+15	21.00	461.2	0.712	5.04
		2D1	0.E+00	40.70	646.8	0.724	13.92
		2D1	3.E+15	20.50	463.0	0.736	5.10
		2D2	3.E+15	20.00	463.0	0.741	5.02
		2D3	3.E+15	21.10	460.6	0.706	5.00
		2D4	0.E+00	39.20	648.2	0.715	13.27
CZP 1.3	**WN08**	**6D**	0.E+00	40.18	678.3	0.579	11.53
PERT		**6D**	1.E+15	19.43	472.3	0.670	4.49
NO AR		**6E**	0.E+00	40.50	674.6	0.639	12.76
		6E	3.E+15	17.55	466.7	0.693	4.14
		6F	0.E+00	40.85	678.9	0.618	12.53
		6F	0.E+00	40.50	668.0	0.657	12.99
		6A1	0.E+00	40.20	652.7	0.734	14.08
		6A1	1.E+14	22.90	523.9	0.757	6.64
		6A2	0.E+00	39.00	654.3	0.745	13.91
		6A2	1.E+15	18.10	492.9	0.766	5.01
		6A3	3.E+15	17.00	472.5	0.760	4.48
		6A4	0.E+00	38.90	644.9	0.747	13.70
		6B1	0.E+00	38.00	653.5	0.726	13.17
		6B2	0.E+00	39.30	646.5	0.752	13.99
		6B3	0.E+00	38.10	645.6	0.739	13.30
		6B4	0.E+00	39.00	638.8	0.749	13.67
		6C1	0.E+00	39.10	611.9	0.780	13.63
		6C2	3.E+15	17.10	456.0	0.662	3.77
		6C3	0.E+00	40.00	675.8	0.675	13.37
		6C3	3.E+15	17.00	465.0	0.676	3.90
		6C4	3.E+15	17.00	469.8	0.717	4.21

FZP PERL AR	**WN04**	**5A**	0.E+00	38.73	684.5	0.605	11.71
		5A	0.E+00	36.85	683.9	0.698	12.86
		5B	0.E+00	41.93	695.8	0.544	11.60
		5C	0.E+00	39.73	700.5	0.608	12.37
		5D1	0.E+00	42.00	692.1	0.667	14.16
		5D2	0.E+00	31.90	691.7	0.798	12.89
		5D3	0.E+00	47.10	687.8	0.668	15.82
		5D4	0.E+00	38.60	691.3	0.750	14.60
		5E1	0.E+00	43.80	663.8	0.679	14.41
		5E2	3.E+15	20.10	472.2	0.685	4.76
		5E3	0.E+00	47.70	698.4	0.683	16.64
		5E3	3.E+15	20.00	434.7	0.543	3.45
		5E4	3.E+15	19.00	459.5	0.645	4.11
		5F1	0.E+00	46.60	695.8	0.670	15.88
		5F1	1.E+14	27.00	488.3	0.597	5.76
		5F2	0.E+00	47.90	685.4	0.625	14.99
		5F2	1.E+15	21.20	484.0	0.697	5.22
		5F3	0.E+00	45.90	632.8	0.690	14.66
		5F4	0.E+00	44.60	668.9	0.694	15.14
CZG PERT AR	**WS12**	**7B**	0.E+00	46.03	690.9	0.742	17.23
		7B	1.E+15	32.30	531.3	0.762	9.56
		7C	0.E+00	45.90	694.3	0.685	15.95
		7C	1.E+14	38.00	564.3	0.723	11.33
		7D	0.E+00	42.05	696.0	0.701	16.60
		7D	0.E+00	46.18	695.5	0.727	17.06
		7E	0.E+00	45.78	691.2	0.710	16.42
		7E	3.E+15	29.80	511.4	0.715	7.96
		7F	0.E+00	46.28	693.3	0.731	17.13
		7F	0.E+00	46.45	692.5	0.744	17.49
		7G	0.E+00	43.80	655.5	0.735	15.44
		7G	3.E+15	28.90	509.7	0.765	8.23
		7H	0.E+00	44.10	659.2	0.736	15.63
		7H	1.E+15	31.10	530.8	0.711	8.60
		7J	3.E+15	29.10	508.5	0.773	8.34
		7K	3.E+15	28.90	508.2	0.756	8.11
		7L	0.E+00	45.10	519.5	0.712	15.57
FZB PERL AR	**WS10**	**7A**	0.E+00	47.23	701.3	0.694	16.80
		7A	3.E+15	30.23	512.1	0.671	7.59
		7B	0.E+00	47.93	699.7	0.686	16.83
		7B	3.E+15	30.28	511.4	0.652	7.38
		7C	0.E+00	47.58	696.5	0.538	13.03
		7C	1.E+14	37.38	562.4	0.517	7.95
		7D	0.E+00	47.83	695.1	0.567	13.77
		7D	0.E+00	48.08	694.7	0.590	14.39
		7E	0.E+00	47.30	700.4	0.729	17.65
		7E	1.E+15	32.48	533.4	0.701	8.87
		7F	0.E+00	48.33	703.0	0.751	18.64
		7F	0.E+00	48.18	702.0	0.739	18.27
		7G	0.E+00	46.80	669.4	0.706	16.18
		7G	1.E+14	37.00	561.1	0.745	11.32
		7H	0.E+00	46.90	662.1	0.696	15.78

		7H	1.E+15	32.10	530.6	0.740	9.21
		7I	0.E+00	46.80	669.8	0.694	15.91
		7I	3.E+15	29.00	512.9	0.735	7.97
		7J	3.E+15	29.70	510.8	0.759	8.41
		7K	3.E+15	29.90	513.0	0.744	8.34
		7L	0.E+00	46.10	666.6	0.675	15.14
MCZB PERL AR	**WS09**	**3A**	0.E+00	48.38	704.1	0.781	19.43
		3A	0.E+00	47.50	702.6	0.780	19.04
		3B	0.E+00	48.53	704.0	0.775	19.36
		3B	0.E+00	48.38	703.2	0.789	19.62
		3C	0.E+00	47.55	702.2	0.769	18.76
		3C	1.E+14	38.55	560.2	0.746	11.77
		3D	0.E+00	48.40	702.7	0.773	19.22
		3D	1.E+15	33.08	529.2	0.745	9.53
		3E	0.E+00	47.05	700.5	0.759	18.29
		3E	3.E+15	30.60	510.4	0.742	8.47
		3F	0.E+00	48.15	702.5	0.780	19.29
		3F	3.E+15	30.63	510.6	0.743	8.49
		3G	0.E+00	44.70	659.8	0.742	16.00
		3G	1.E+14	38.20	560.9	0.749	11.74
		3H	0.E+00	46.70	660.2	0.721	16.25
		3H	1.E+15	32.10	527.5	0.759	9.40
		3I	0.E+00	45.00	640.8	0.715	15.08
		3I	3.E+15	29.10	510.1	0.769	8.33
		3J	3.E+15	29.90	509.8	0.775	8.65
		3K	3.E+15	30.00	509.1	0.744	8.28
		3L	0.E+00	46.00	658.7	0.709	15.70
CZA PERT NO AR	**WS15**	**4A**	0.E+00	32.28	574.0	0.791	10.72
		4A	1.E+14	27.55	559.5	0.791	8.91
		4B	0.E+00	32.50	579.8	0.789	10.87
		4B	1.E+15	25.65	545.2	0.778	7.95
		4C	0.E+00	32.85	577.5	0.778	10.79
		4C	3.E+15	24.50	524.6	0.756	7.10
		4E	0.E+00	32.83	578.2	0.789	10.95
		4E	0.E+00	32.98	577.9	0.779	10.85
		4F	0.E+00	33.10	578.9	0.785	10.99
		4F	0.E+00	33.25	578.8	0.773	10.87
		4G	0.E+00	32.90	579.9	0.754	10.49
		4G	1.E+14	28.20	563.0	0.773	8.97
		4H	0.E+00	33.00	574.8	0.731	10.12
		4H	1.E+15	24.10	539.8	0.789	9.51
		4I	0.E+00	32.90	576.9	0.726	10.06
		4I	3.E+15	23.00	514.9	0.478	4.13
		4J	3.E+15	23.00	520.8	0.746	6.51
		4K	3.E+15	23.20	523.2	0.767	6.82
		4L	0.E+00	31.90	575.2	0.732	9.81
CZI PERT NO AR	**WS15**	**8A**	0.E+00	41.58	676.0	0.763	15.67
		8A	0.E+00	41.68	675.4	0.768	15.82
		8B	0.E+00	42.73	676.6	0.765	16.18
		8B	0.E+00	41.98	675.6	0.755	15.64

8C	0.E+00	41.60	674.8	0.717	14.72
8C	1.E+14	34.63	541.2	0.680	9.32
8D	0.E+00	42.70	673.2	0.711	14.95
8D	1.E+15	29.98	504.8	0.686	7.59
8E	0.E+00	41.43	664.2	0.745	14.99
8E	3.E+15	28.03	488.8	0.730	7.31
8F	0.E+00	42.13	661.5	0.748	15.23
8F	3.E+15	28.08	488.8	0.724	7.27
8G	0.E+00	40.80	639.3	0.705	13.46
8G	1.E+14	35.10	542.7	0.713	9.93
8H	0.E+00	40.90	635.6	0.698	13.23
8H	1.E+15	28.90	504.0	0.769	8.18
8I	0.E+00	40.80	632.1	0.706	13.29
8I	3.E+15	27.00	486.2	0.751	7.19
8J	3.E+15	27.50	488.6	0.728	7.14
8K	3.E+15	27.00	485.9	0.751	7.21
8L	0.E+00	40.20	619.8	0.701	12.77

6.18 References

---

[1] Morooka, M., Tomokage, H., and Yoshida, M., Conf. Proc. Sci. and Tech. of Defect Control in Semiconductors, Yokohama, Japan, Sept 17-22, Ed. Sumino, K., Energy levels related to substitutional gold in silicon, p.291, (1989).

[2] Markvart, T., *et al*, Electron and photon degradation of boron doped FZ silicon solar cells, Proc. 3rd Europ. Symp. "Photovoltaic generators in space", ESA SP-173, p.109-114, (1982).

[3] Markvart, T., Willoughby, A.F., and Dollery, A.A., Silicon solar cells with improved radiation resistance, *Proceedings of the 19th Photovoltaics Specialists Conference, New Orleans, USA*, p.709-714, (1987).

[4] Peters, J.W., Markvart, T., et al, Defect interactions in silicon solar cells, Presented at the Second Workshop on Radiation-Induced and/or Process-Related Electrically Active Defects in Semiconductor-Insulator Systems, North Carolina, September 10-13, (1989).

[5] Peters, J., Markvart, T., and Willoughby, A.F.W., *Materials Science Forum* **83-87**, p.1539-1544, (1992).

[6] Peters, J.W., The role of defects in the radiation damage of solar cells, PhD Thesis, Engineering Materials, University of Southampton, (1993).

[7] Markvart, T., Parton, D.P., Peters, J.W. and Willoughby, A.F.W.: DLTS of Recombination Centres in Semiconductors, Presented at the 17th International Conference on Defects in Semiconductors, Gmunden, Austria, p.1381, (1993).

[8] Crabb, R.L., Photon induced degradation of electron and proton irradiated solar cells, Proc. 9th IEEE Photovoltaic Spec. Conf., p.328, (1972).

---

[9] Troxell, J.R., et al, Recombination-enhanced migration of interstitial aluminum in silicon, Phys. Rev. B, 19, 10, p.5336, (1979).

FIGURE 6.1. DLTS PLOT GOLD DOPED SILICON STANDARD

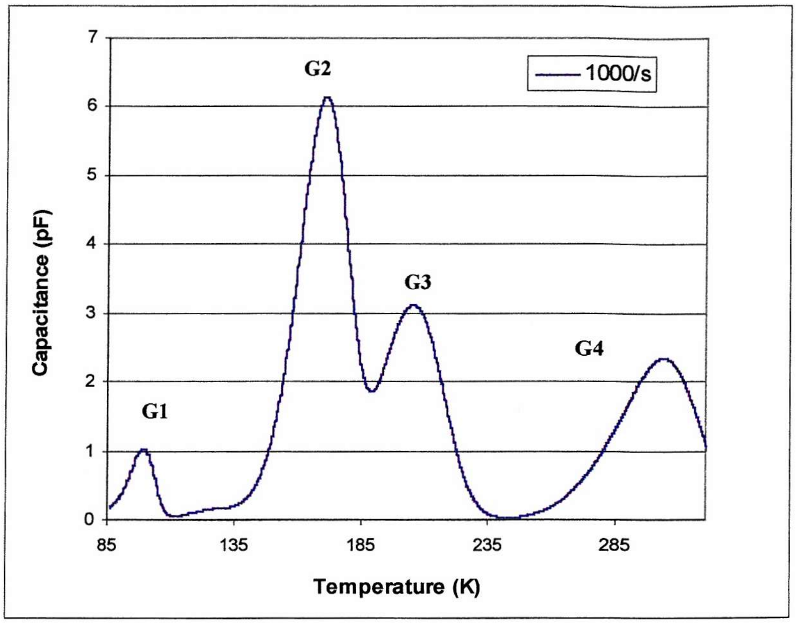

FIGURE 6.2. DLTS PLOT OF FLOAT ZONE SILICON CELL 49d (PHOTON SOAKED FOR 48 HOURS AFTER IRRADIATION)

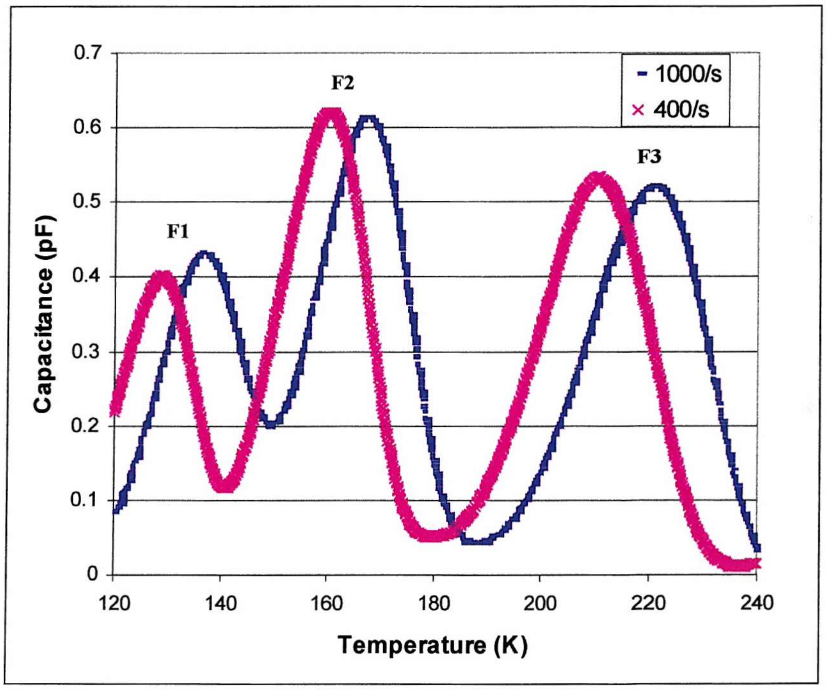

FIGURE 6.3. DLTS PLOT OF CZOCHRALSKI SILICON CELL 67b

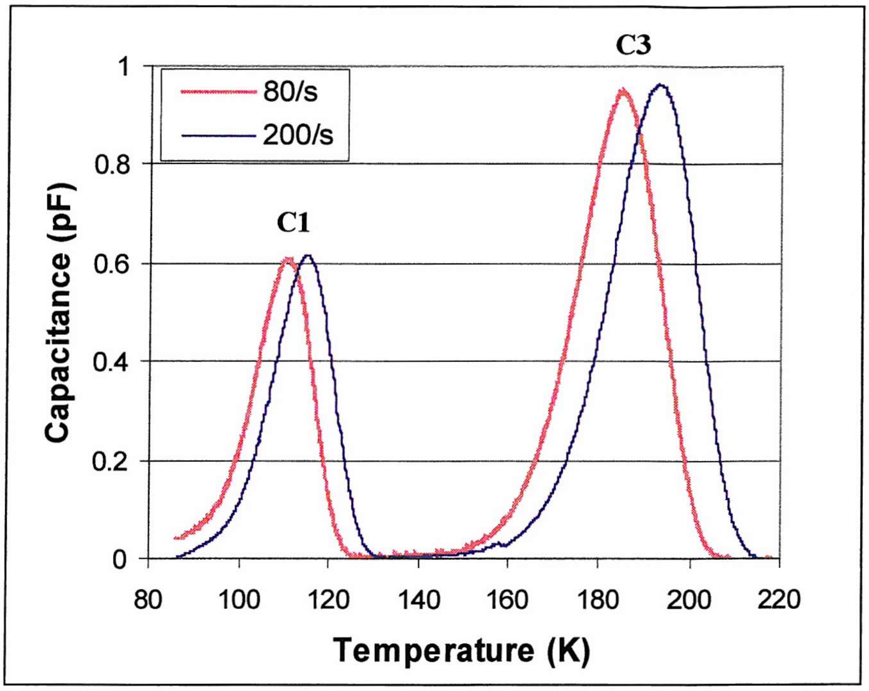

FIGURE 6.4. DLTS PLOT OF N-TYPE CELL PNA

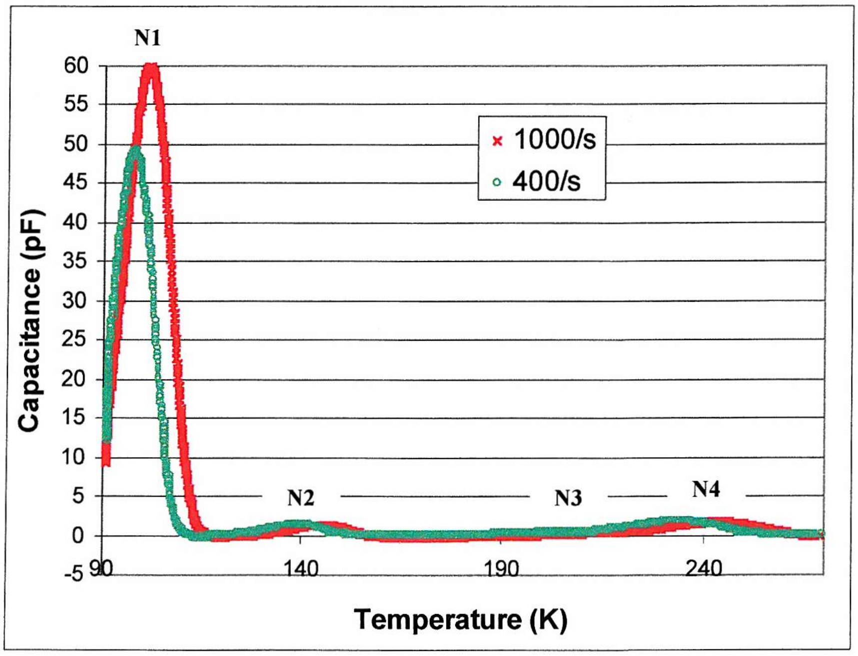

FIGURE 6.5. *DLTS PLOT OF N-TYPE CELL PNA 120 TO 270k*

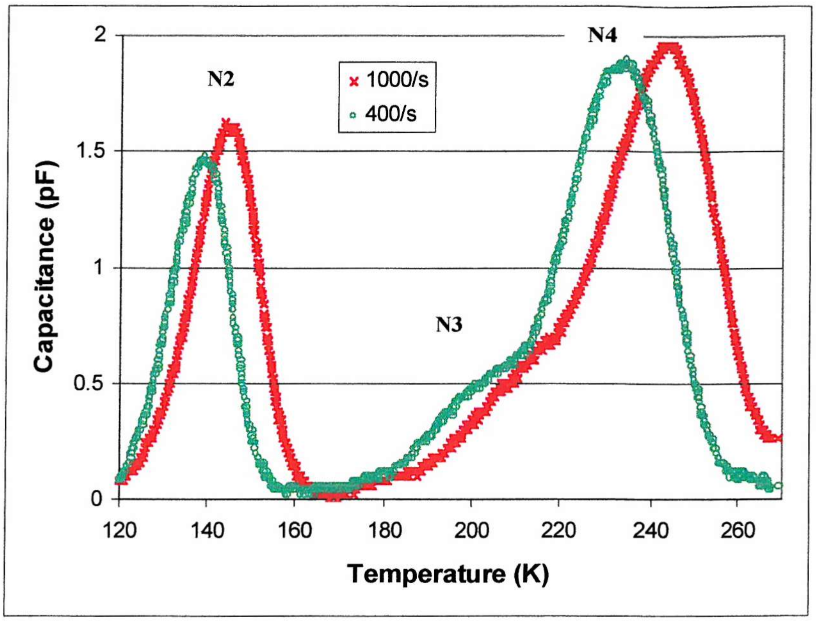

FIGURE 6.6. *FORWARD BIAS DLTS (FBDLTS) PLOT OF N-TYPE CELL PNA (3×10^{15} ELECTRONS/CM^2)*

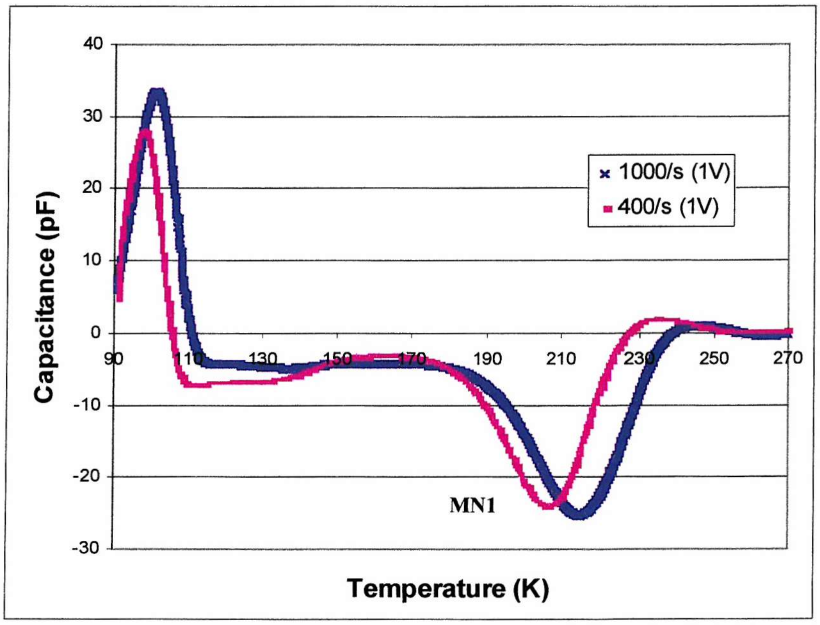

FIGURE 6.7. FBDLTS PLOT OF N-TYPE CELL PNA USING FORWARD BIAS OF +1V AND +1.7V

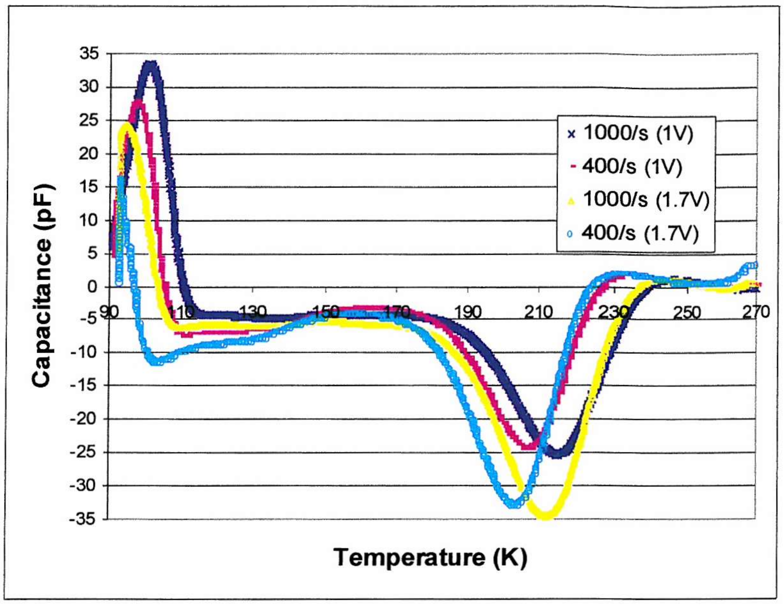

FIGURE 6.8. DLTS PLOT OF HIGH EFFICIENCY PHOSPHORUS DOPED CZOCHRALSKI SOLAR CELL Wn082c41 (3×10^{15} ELECTRONS/CM^2)

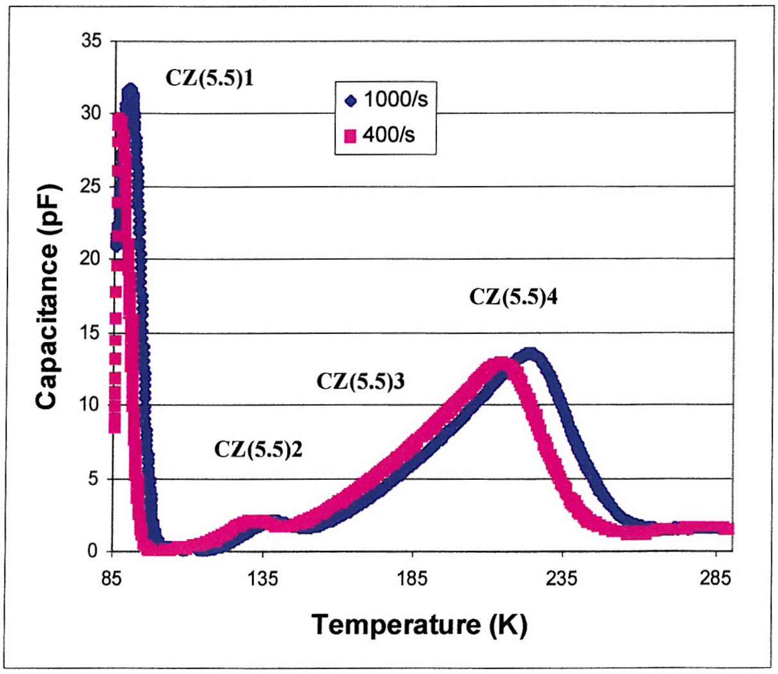

FIGURE 6.9. *DLTS PLOT OF HIGH EFFICIENCY PHOSPHORUS DOPED CZOCHRALSKI SOLAR CELL Wn082c41 (110 – 290K)*

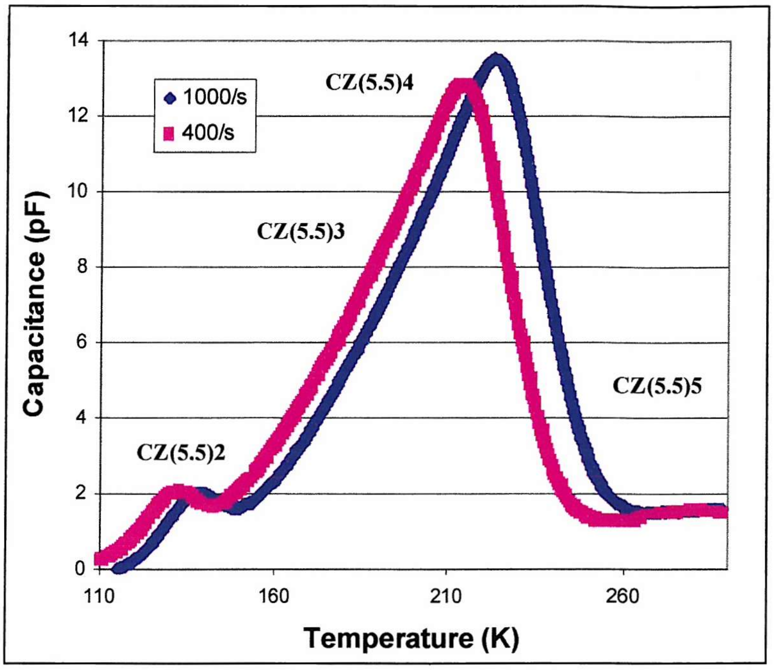

FIGURE 6.10. *FBDLTS PLOT OF HIGH EFFICIENCY PHOSPHORUS DOPED CZOCHRALSKI SOLAR CELL Wn082c41*

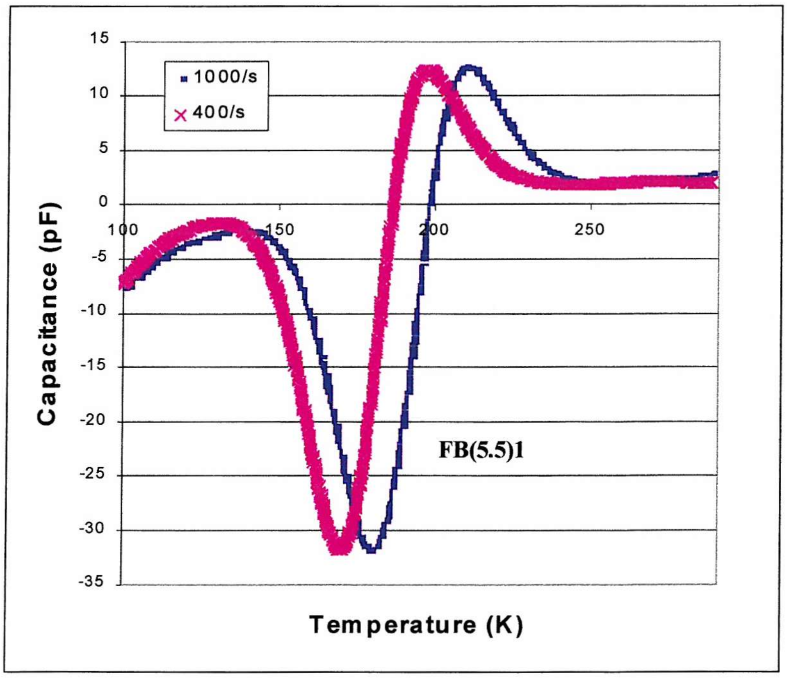

FIGURE 6.11. DLTS PLOT OF HIGH EFFICIENCY PHOSPHORUS DOPED CZOCHRALSKI SOLAR CELL Wn086c21

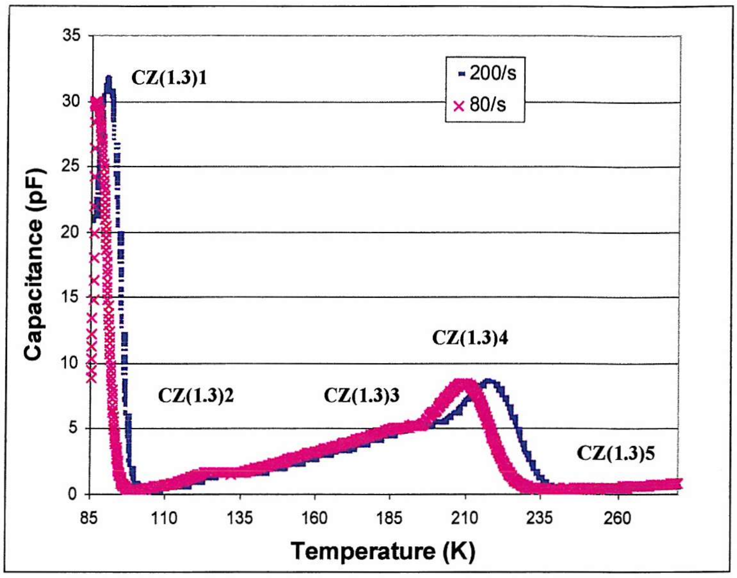

FIGURE 6.12. DLTS PLOT OF HIGH EFFICIENCY BORON DOPED FLOAT ZONE SOLAR CELL Ws107i (3×10^{15} ELECTRONS/CM^2)

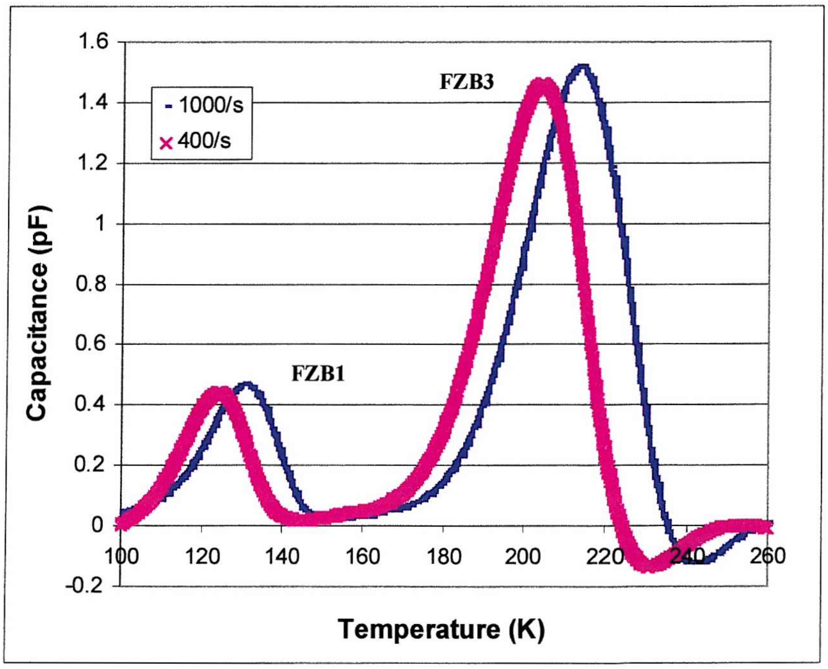

FIGURE 6.13. DLTS PLOT OF HIGH EFFICIENCY BORON DOPED FLOAT ZONE SOLAR CELL Ws107i AFTER 48 HOURS AM0 ILLUMINATION

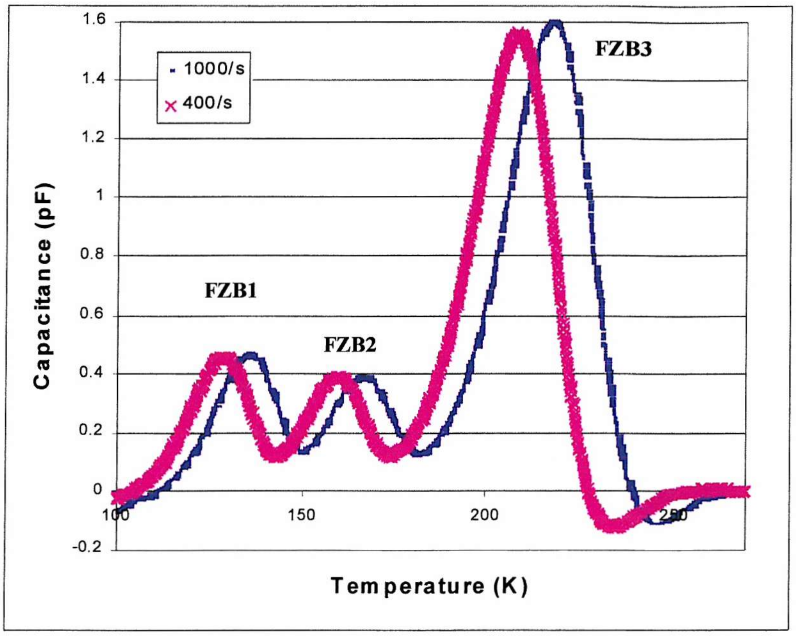

FIGURE 6.14. DLTS PLOT OF HIGH EFFICIENCY BORON DOPED MAGNETICALLY CONFINED CZOCHRALSKI SOLAR CELL Ws93k2

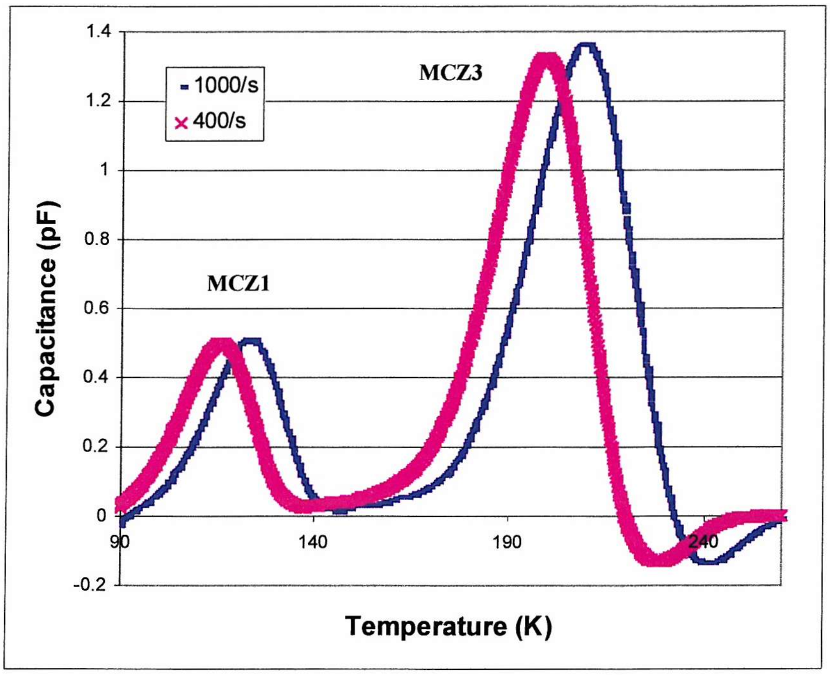

FIGURE 6.15. DLTS PLOT OF HIGH EFFICIENCY BORON DOPED MCZ SOLAR CELL Ws93k2 AFTER 48 HOURS OF AM0 ILLUMINATION

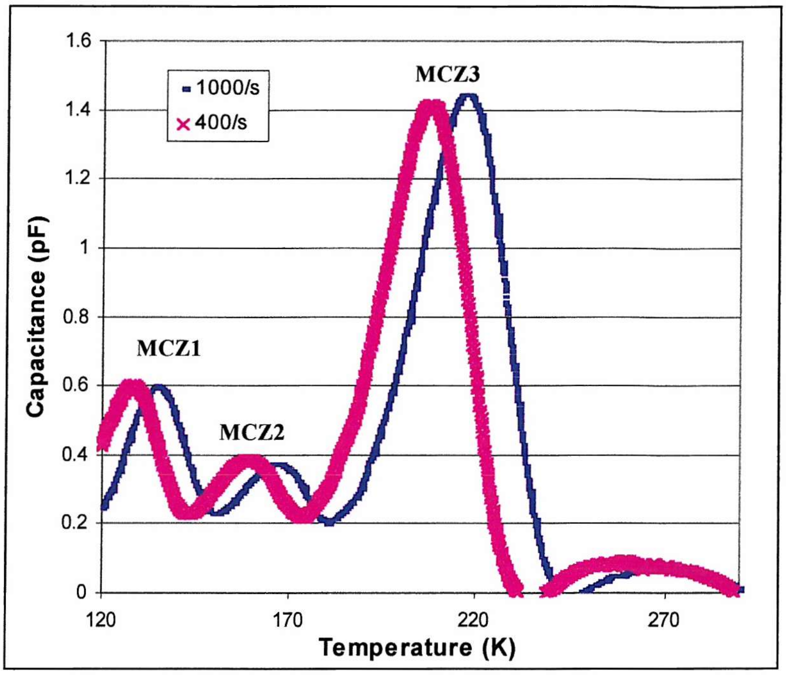

FIGURE 6.16. DLTS PLOT OF HIGH EFFICIENCY GALLIUM DOPED CZOCHRALSKI SOLAR CELL Ws127K1 (3×10^{15} ELECTRONS/CM^2)

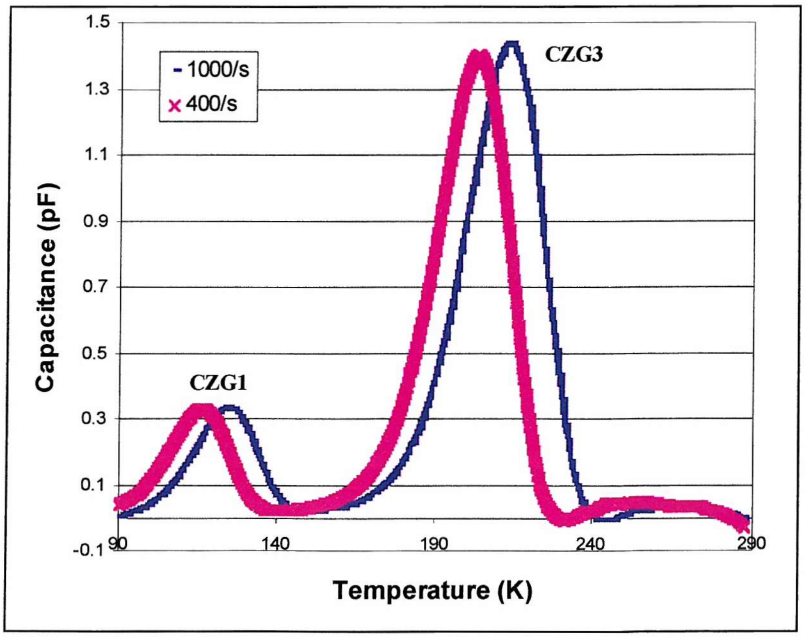

FIGURE 6.17. DLTS PLOT OF HIGH EFFICIENCY INDIUM DOPED CZOCHRALSKI SOLAR CELL Ws158i2

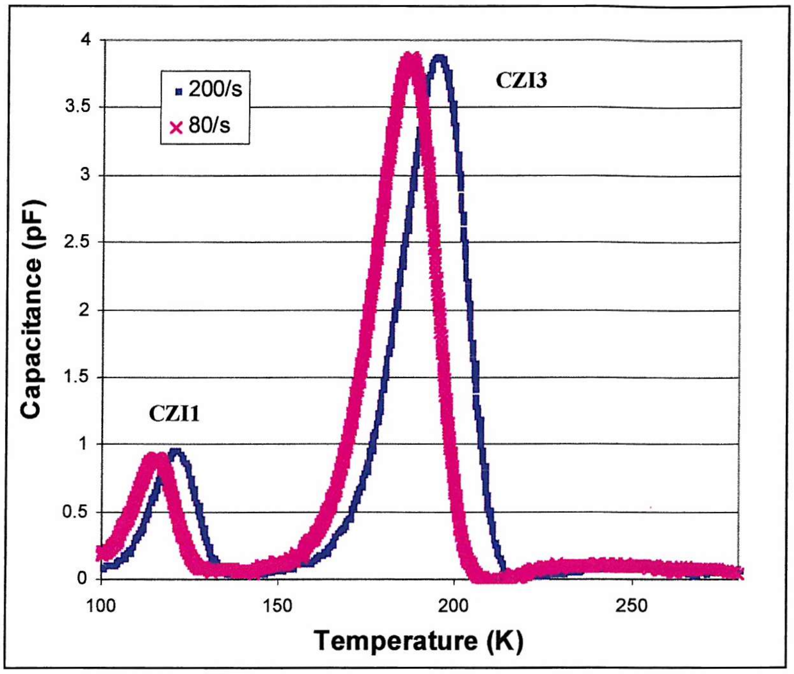

FIGURE 6.18. DLTS PLOT OF HIGH EFFICIENCY ALUMINIUM DOPED CZOCHRALSKI SOLAR CELL Ws154j1

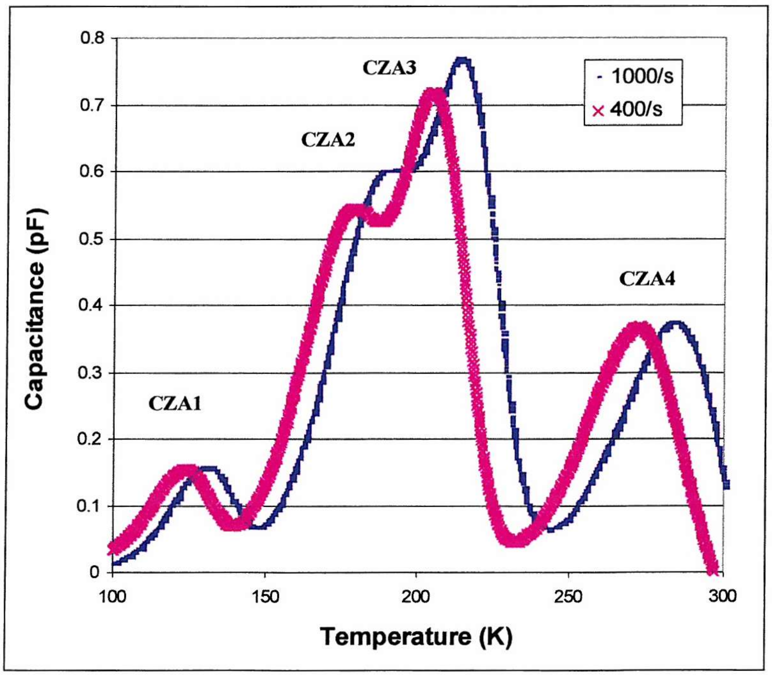

FIGURE 6.19. FBDLTS PLOT OF HIGH EFFICIENCY GALLIUM DOPED CZOCHRALSKI CELL (CZG)AT VARYING LEVELS OF FORWARD BIAS

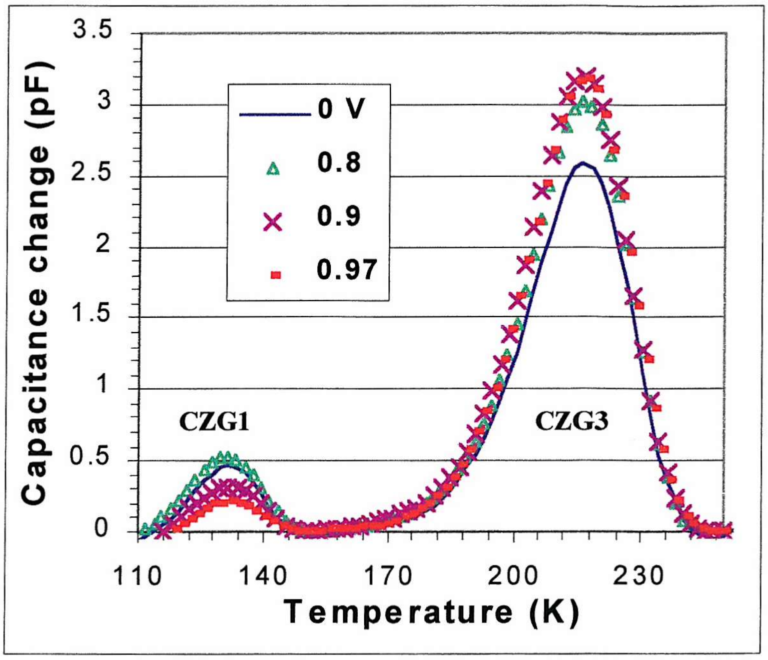

FIGURE 6.20. DLTS AND MCTS PLOTS (1000/S RATE WINDOW)OF HIGH EFFICIENCY GALLIUM DOPED CZOCHRALSKI CELL (CZG)

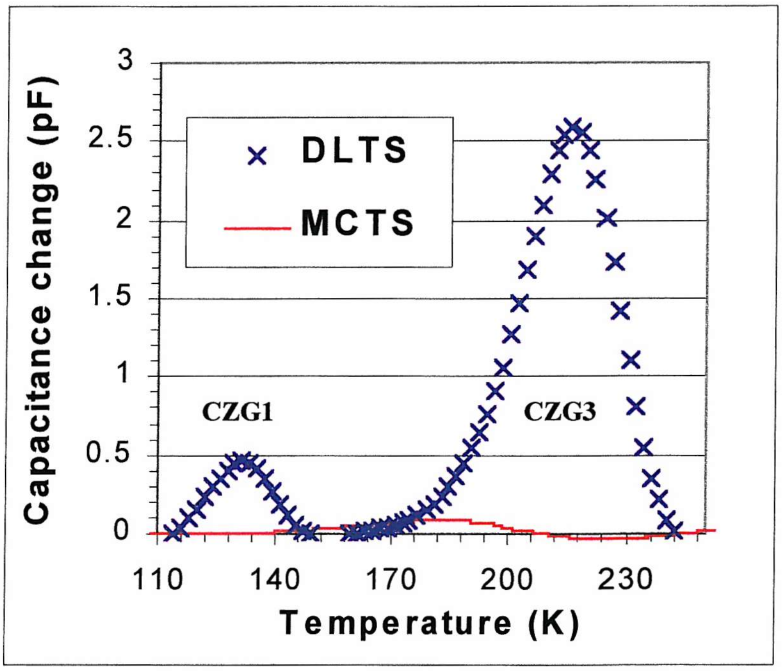

FIGURE 6.21. DARK IV CHARACTERISTICS OF IRRADIATED HIGH EFFICIENCY ALUMINIUM(CZA)AND INDIUM DOPED (CZI) CZOCHRALSKI CELLS AT 298K

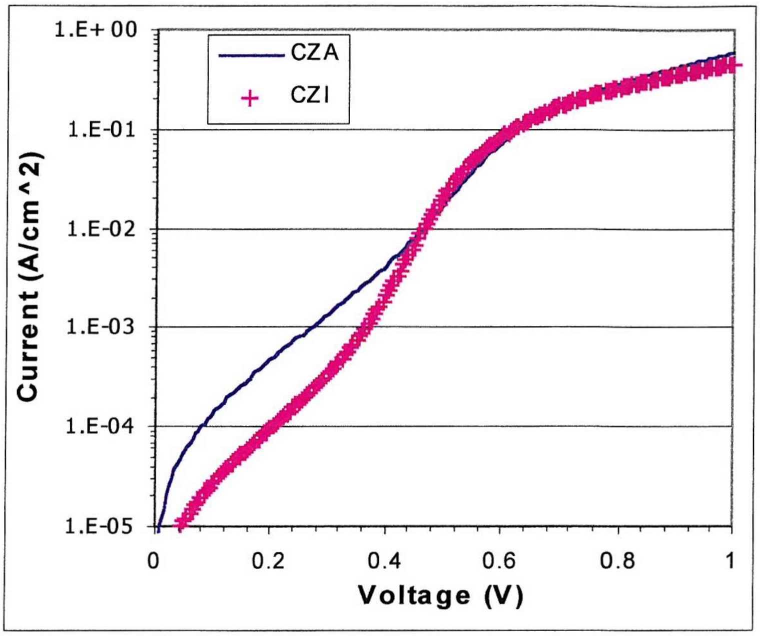

FIGURE 6.22. DARK IV CHARACTERISTICS OF IRRADIATED HIGH EFFICIENCY BORON DOPED FLOAT-ZONE (FZB)AND MAGNETICALLY-CONFINED CZOCHRALSKI (MCZ) CELLS AT 298K

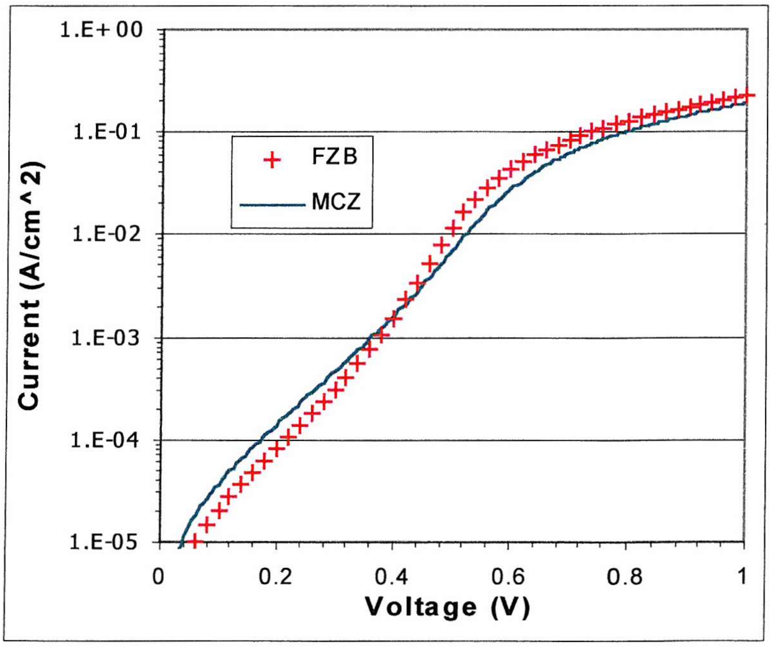

FIGURE 6.23. *DARK IV CHARACTERISTICS OF IRRADIATED HIGH EFFICIENCY PHOSPHORUS DOPED FLOAT-ZONE (FZP) CZOCHRALSKI (CZP5.5 AND CZP1.3) CELLS AT 298K*

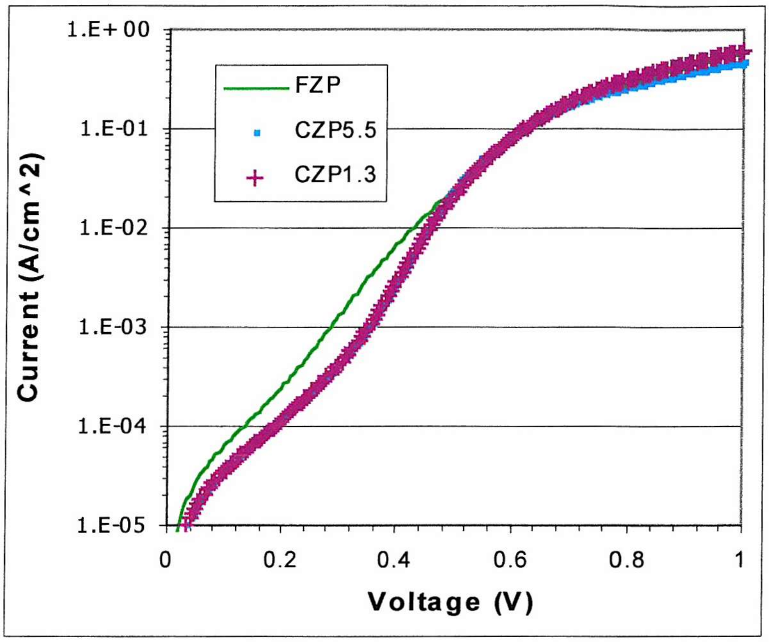

FIGURE 6.24. *DARK IV CHARACTERISTICS OF IRRADIATED HIGH EFFICIENCY BORON DOPED FLOAT-ZONE (FZB) CELLS COMPARED TO STANDARD BORON DOPED CZOCHRALSKI CELLS (STCZB) AT 298K*

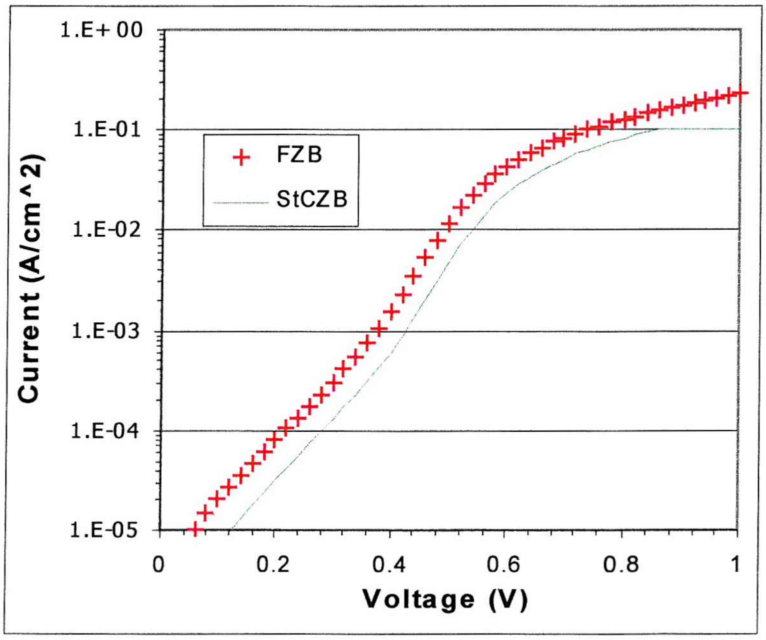

FIGURE 6.25. DARK IV CHARACTERISTICS OF IRRADIATED HIGH EFFICIENCY GALLIUM DOPED CZOCHRALSKI CELL (CZG) AT DIFFERENT TEMPERATURES

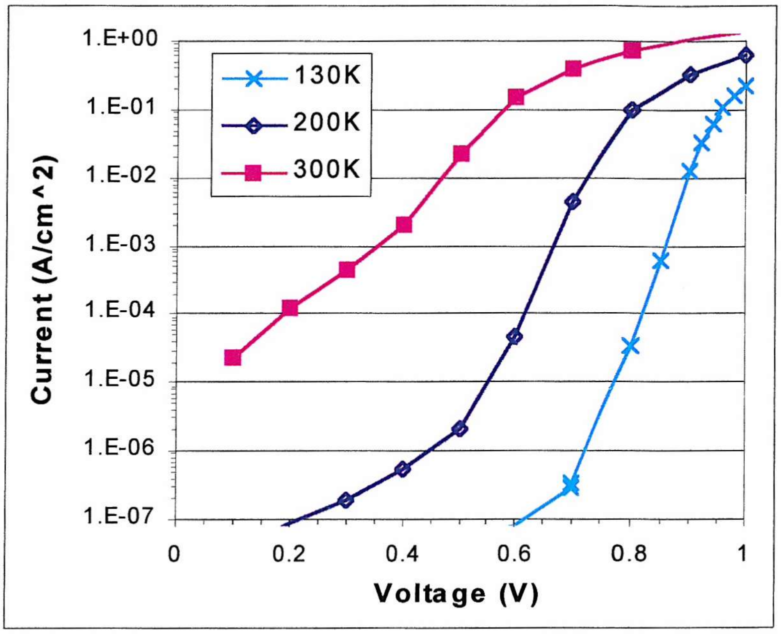

FIGURE 6.26. ILLUMINATED IV CHARACTERISTIC OF (2cm×2cm) UNIRRADIATED CZOCHRALSKI SILICON SOLAR CELL NO. 20168/8/2

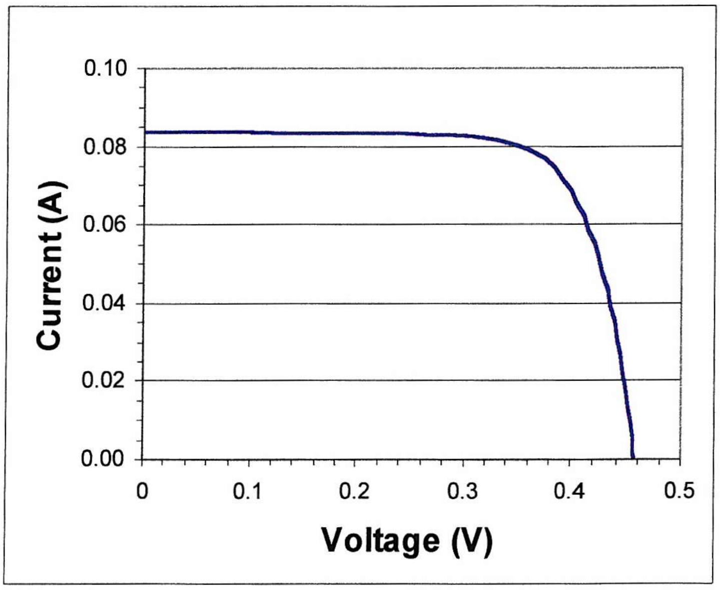

FIGURE 6.27. *ABSOLUTE SPECTRAL RESPONSE OF UNIRRADIATED CZOCHRALSKI SILICON SOLAR CELLS 20168/8/2 WITHOUT ANTIREFLECTION COATING AND 20168/4, 20168/8 AND 20168/9 WITH ANTIREFLECTION COATING*

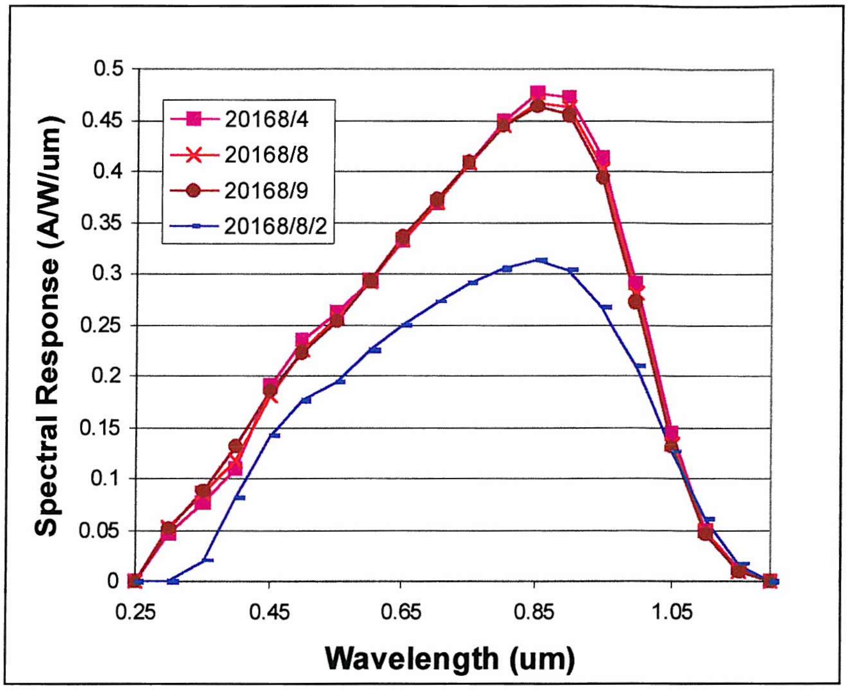

FIGURE 6.28. *ABSOLUTE SPECTRAL RESPONSE OF UNIRRADIATED CZOCHRALSKI SILICON SOLAR CELL 20168/13, 1MeV ELECTRON IRRADIATED (1×10^{16} cm^{-2}) CELL 20168/9/2 AND 10MeV PROTON IRRADIATED (3×10^{11} cm^{-2}) CELL 20168/7/2*

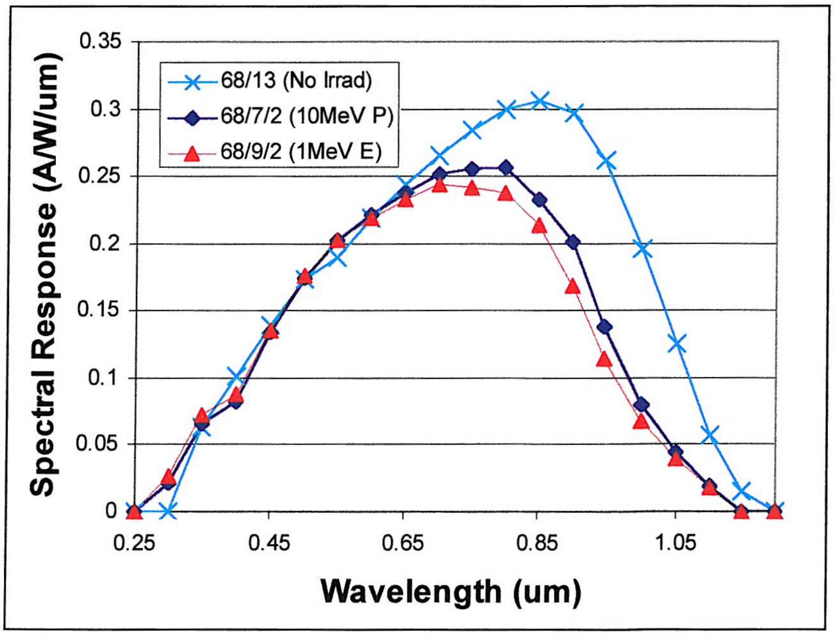

FIGURE 6.29. *ABSOLUTE SPECTRAL RESPONSE OF CZOCHRALSKI SILICON SOLAR CELL 20167/13 BEFORE AND AFTER VARYING FLUENCES OF 1MeV ELECTRON IRRADIATION*

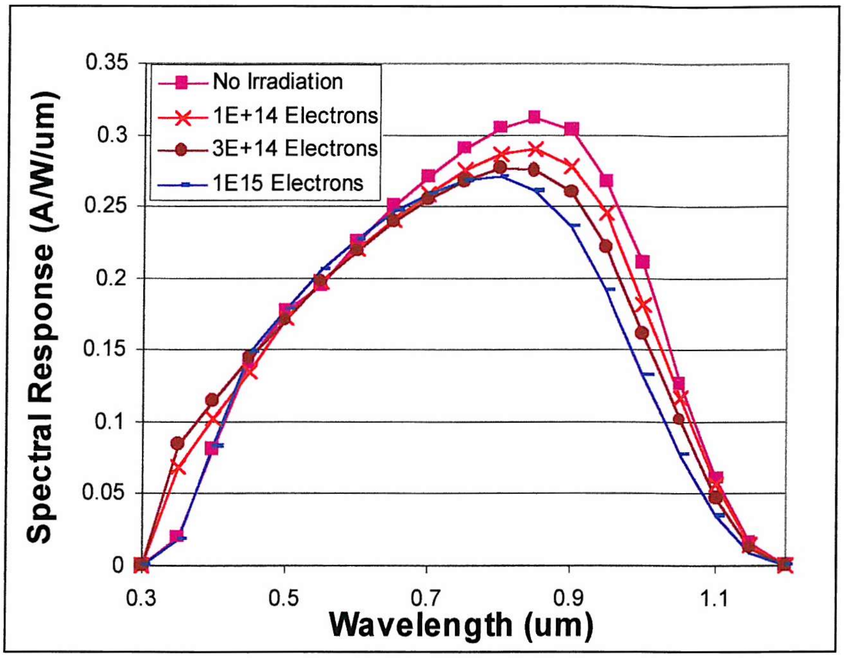

FIGURE 6.30. *ABSOLUTE SPECTRAL RESPONSE OF CZOCHRALSKI SILICON SOLAR CELL 20168/8/2 BEFORE AND AFTER VARYING FLUENCES OF 1MeV ELECTRON IRRADIATION*

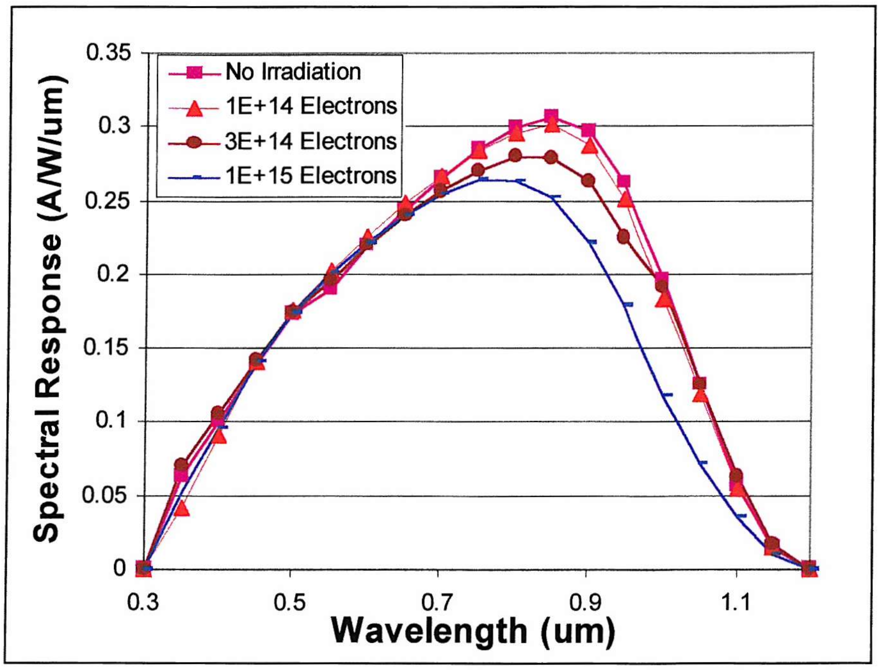

FIGURE 6.31. ABSOLUTE SPECTRAL RESPONSE OF CZOCHRALSKI SILICON SOLAR CELL 20168/13 BEFORE AND AFTER VARYING FLUENCES OF 1MeV ELECTRON IRRADIATION

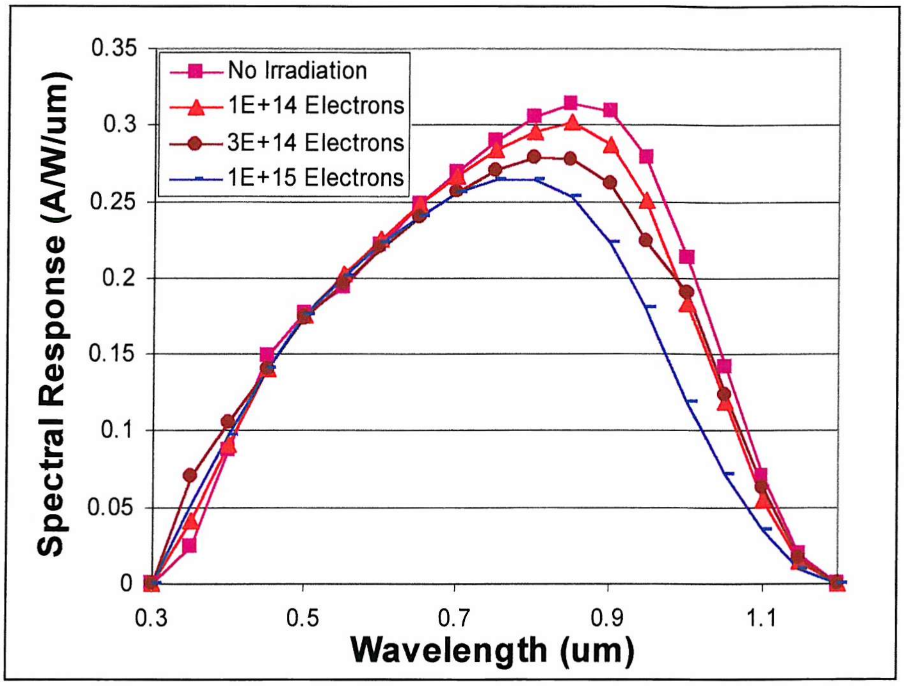

FIGURE 6.32. SPECTRAL RESPONSE OF THE HIGH EFFICIENCY PHOSPHORUS DOPED CZOCHRALSKI CELL (CZP5.5) AFTER 1E14, 1E15, AND 3E15 ELECTRONS/CM²

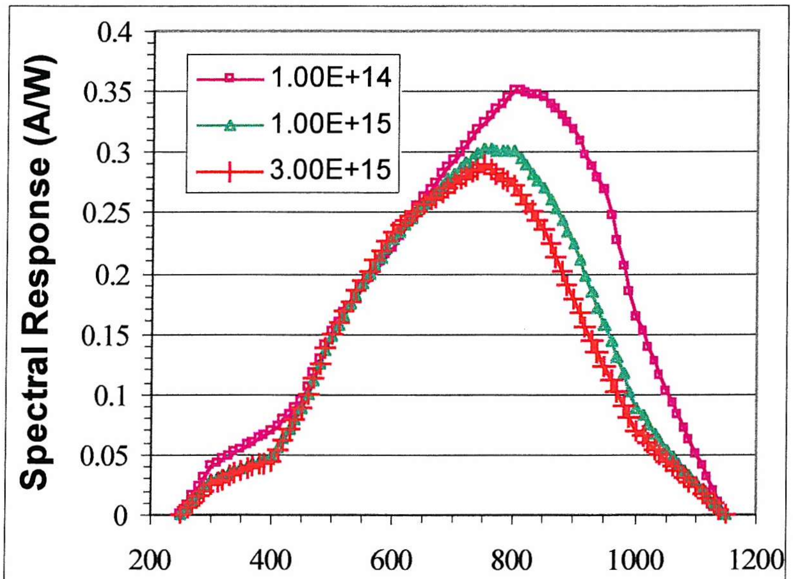

FIGURE 6.33. *SPECTRAL RESPONSE OF THE HIGH EFFICIENCY PHOSPHORUS DOPED CZOCHRALSKI CELL (CZP1.3) AFTER 1E14, 1E15, AND 3E15 ELECTRONS/CM^2*

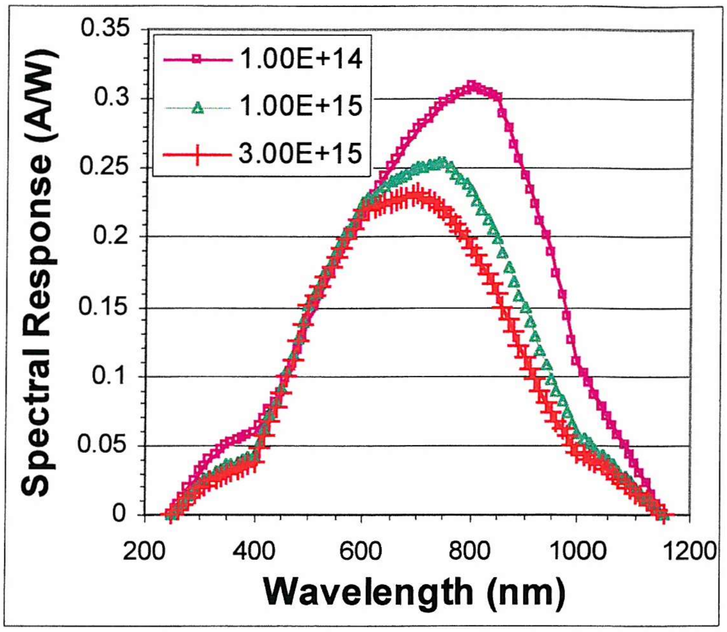

FIGURE 6.34. *SPECTRAL RESPONSE OF THE HIGH EFFICIENCY PHOSPHORUS DOPED FLOAT-ZONE CELL (FZP) AFTER 1E14, 1E15, AND 3E15 ELECTRONS/CM^2*

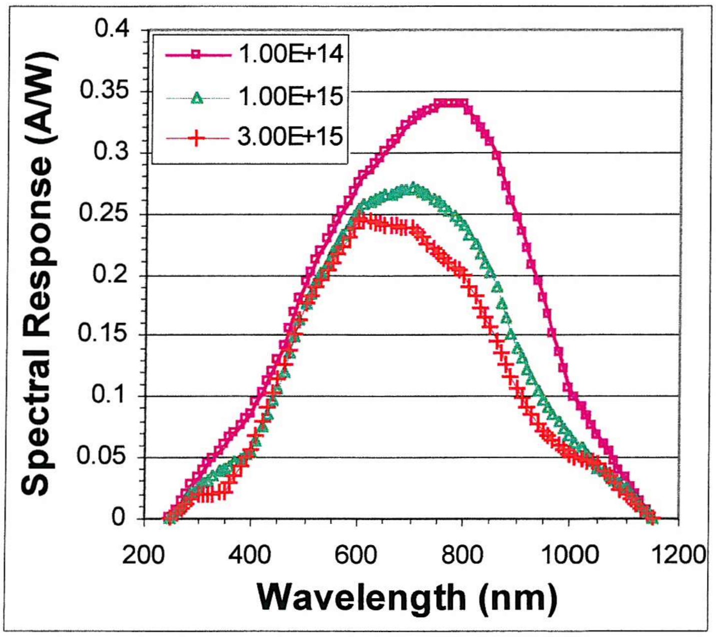

FIGURE 6.35. SPECTRAL RESPONSE OF THE HIGH EFFICIENCY GALLIUM DOPED CZOCHRALSKI CELL (CZG) AFTER 1E14, 1E15, AND 3E15 ELECTRONS/CM^2

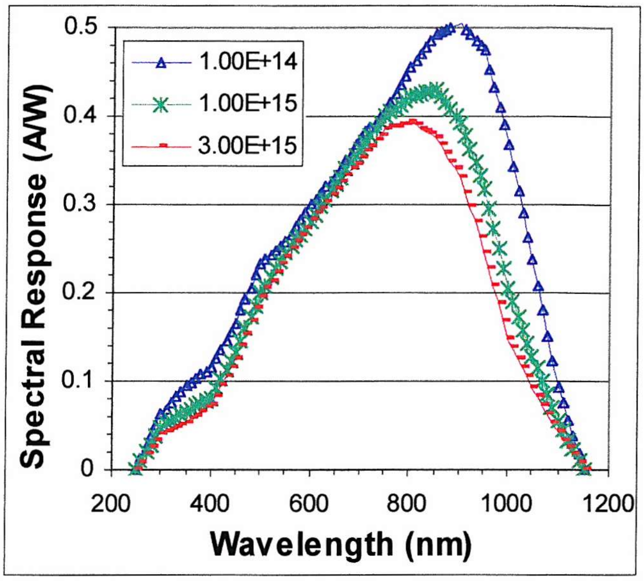

FIGURE 6.36. SPECTRAL RESPONSE OF THE HIGH EFFICIENCY BORON DOPED FLOAT-ZONE CELL (FZB) AFTER 1E14, 1E15, AND 3E15 ELECTRONS/CM^2

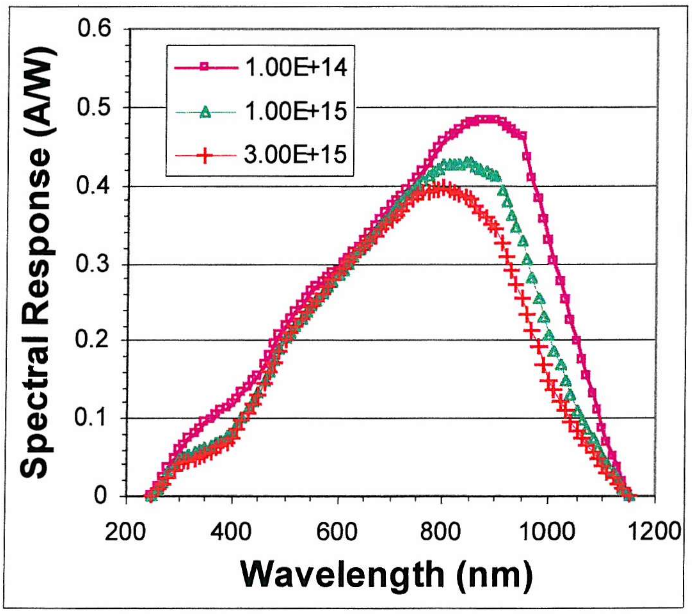

FIGURE 6.37. SPECTRAL RESPONSE OF THE HIGH EFFICIENCY BORON DOPED MAGNETICALLY-CONFINED CZOCHRALSKI CELL (MCZ) AFTER 1E14, 1E15, AND 3E15 ELECTRONS/CM^2

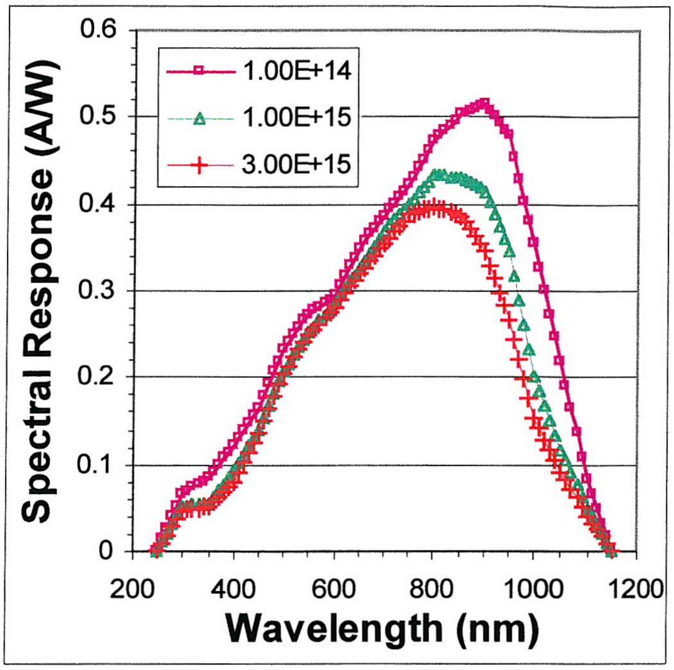

FIGURE 6.38. SPECTRAL RESPONSE OF THE HIGH EFFICIENCY ALUMINIUM DOPED CZOCHRALSKI CELL (CZA) AFTER 1E14, 1E15, AND 3E15 ELECTRONS/CM^2

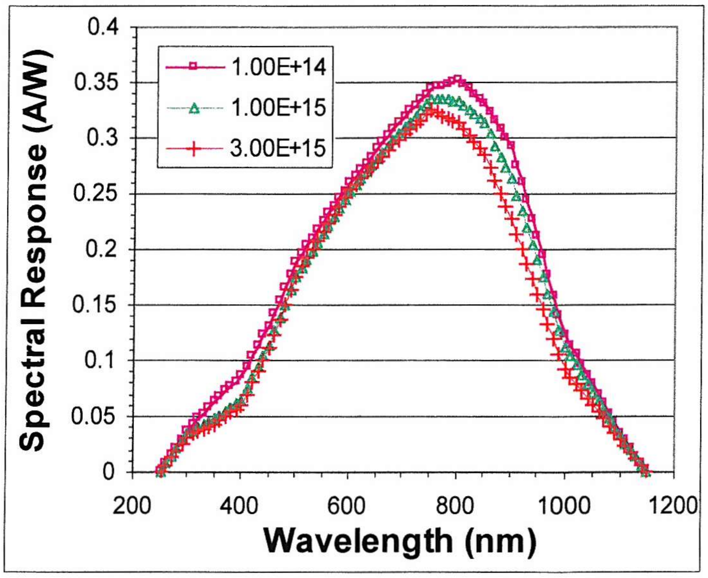

FIGURE 6.39. SPECTRAL RESPONSE OF THE HIGH EFFICIENCY INDIUM DOPED CZOCHRALSKI CELL (CZI) AFTER 1E14, 1E15, AND 3E15 ELECTRONS/CM²

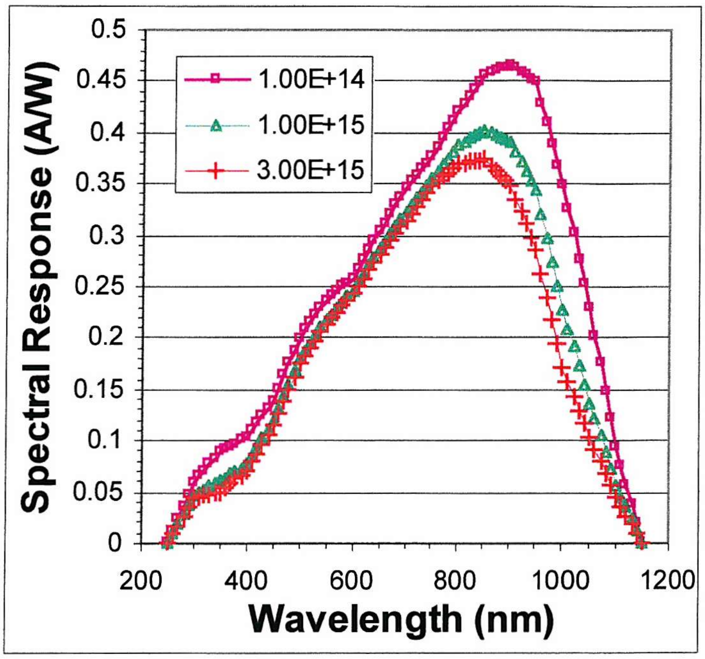

CHAPTER SEVEN

MODELLING OF SOLAR CELLS

7.1 Introduction

The electron radiation damage causes a steep reduction in the spectral response in the longer wavelength region of silicon solar cells (see Figures 6.30 to 6.40). The response at these wavelengths (0.8-1.0μm) can be directly related to a reduction in minority-carrier diffusion length in the base region of the solar cell[1]. The spectral response can therefore be used to determine this diffusion length using a least-squares fit to a model of the solar cell[2,3].

To attain the minority-carrier diffusion length a model must first be built to determine the theoretical spectral response of the silicon solar cells. The ideal characteristics are therefore considered first before extending this analysis to consider the BSF/BSR Czochralski silicon solar cells described in Chapter Five. PC1D Version 5.2 (see 4 and references therein) was then used to model the cells and these results are compared to the simpler model.

7.2 Modelling of an Ideal P-n Junction Diode

The equations given in chapter two can be used to compute the ideal characteristics of a silicon solar cell. This example calculation will then be extended and used to calculate the characteristics of the silicon solar cells described in chapter five. The calculations are lengthy and complex so a computer model has been built which includes all of the necessary calculations.

The first step is to enter the required silicon constants. Some of these constants vary depending on the reference used. Sze[5] for example gives values for the "Effective Density of States" and the "Intrinsic Carrier Concentration". Green[6] has improved on these values with a more accurate assessment of the intrinsic properties of silicon. These improved values have been used throughout the calculations and the symbols adopted are listed in the Glossary. Appendix One lists all the constants used and their values, some of which are temperature dependant.

The equations used for this analysis have been defined in chapter two and are shown in Figure 7.1.. This figure also shows how the data flows through the calculation to enable the determination of quantum efficiency and spectral response. Firstly the doping concentrations (N_A and N_D) must be given and this enables the calculation of the built-in voltage and the energy band diagram shown in Figure 7.2.. Using the calculated built-in voltage enables the depletion widths to also be determined. Table 7.1 shows the values used and the results obtained from this example calculation.

Table 7.1 – Calculated Built-in Voltage, Change in Fermi Level, and Depletion Width

Parameter	Symbol	Value	Units
Doping density in p-type material	N_A	1.25×10^{15}	cm^{-3}
Doping density in n-type material	N_D	5×10^{19}	cm^{-3}
Calculated			
Built-in voltage	V_{bi}	0.88	Volts
Change in Fermi level in n-type material	$E_f - E_{in}$	0.58	eV
Change in Fermi level in p-type material	$E_{ip} - E_f$	0.30	eV
Depletion Width	W	9.62×10^{-5}	eV
Depletion Width in n-type material	W_n	0.24×10^{-8}	eV
Depletion Width in p-type material	W_p	9.62×10^{-5}	eV

As expected the depletion layer extends mainly into the p-type region. The next step in the calculation is to enter the cells dimensions, and the minority carrier lifetimes. This enables the diffusion lengths to be calculated (See Figure 7.1.) and the depth of the depletion layer edges are also determined. Table 7.2 shows the values used and the results obtained.

All of these parameters are necessary for the next calculation which is for the photocurrent generated in each cell region when the cell is illuminated by the AM1.5 solar spectrum. The solar spectrum and the absorption coefficient are entered for each wavelength from 0.3 to 1.24μm in steps of 1/100μm. The photocurrent generated by each region of the solar cell can then be calculated for each wavelength using equations 2.49, 2.51 and 2.57 (See also Figure 7.1.).

Table 7.2 – Calculated Diffusion lengths and Depletion edge depths

Parameter	**Symbol**	**Value**	**Units**
Total cell thickness	H	0.24	mm
Junction depth	xj + W_n	0.001	mm
Carrier lifetime electrons in p-type	τ_n	1.5×10^{-5}	cm^{-3}
Carrier lifetime holes in n-type	τ_p	4×10^{-7}	cm^{-3}
Calculated			
Electron diffusion length in p-type	L_n	0.232	mm
Hole diffusion length in n-type	L_p	0.007	mm
Depth of the depletion edge in n-type layer	xj	0.001	mm
Depth of the depletion edge in p-type layer	H'	0.238	mm

The results of this calculation can be seen in Figure 7.3. and the total photocurrent calculated at each wavelength using equation 2.52 is also shown. The total photocurrent density obtained by the AM1.5 spectral distribution can now be calculated using

$$J_t = \int_{\lambda_{MIN}}^{\lambda_{MAX}} J_t(\lambda) d\lambda \qquad (7.1)$$

The total photocurrent generated by each region of the solar cell can now also be determined and this result is shown in Figure 7.4.. The cells quantum efficiency can now be calculated using equation 2.60 and this can also be shown for each cell region (Figure 7.5.). The spectral response can be calculated theoretically using equation 2.61 and the response from each cell region is shown in Figure 7.6..

7.3 Modelling of the BSF/BSR Silicon Solar Cells

The IV characteristics and spectral response of the solar cells described in chapter five can now be calculated by extending the model developed in the previous section to take into account the diffused n-type region, the antireflection layer, the BSF and the BSR.

7.3.1 IV Characteristics of Solar Cells

In a real solar cell the ideal equivalent circuit will be modified and may be though of as a current generator in parallel with loss mechanisms (Figure 7.7.). The first diode represents a bias-dependant dark current which is assumed to be due to diffusion of minority carriers into the junction from its neighbouring n and p-type layers. The second diode represents a model for losses due to carrier generation and recombination through defect centres located in the space-charge region. The ideal characteristics should also be modified to include the series resistance from ohmic loss in the front surface and the shunt resistance from leakage currents.

$$I = -I_L + I_1 + I_2 + I_{SH} \tag{7.2}$$

$$I = -I_L + I_{01}\left[\exp\left(\frac{V \pm IR_S}{kT}\right) - 1\right] + I_{02}\left[\exp\left(\frac{V \pm IR_S}{2kT}\right) - 1\right] + \frac{V \pm IR_S}{R_{SH}} \tag{7.3}$$

where I_L = Light generated Current

I_1 = Diffusion current

I_2 = Generation-recombination current

I_{SH} = Shunt resistance current

R_S = Series resistance

R_{SH} = Shunt resistance

k = Boltzmann constant expressed in units of eV/K

T = Absolute temperature

The current directions shown in Figure 7.7. represent the illuminated configuration and the + sign in the V±IR$_S$ term should be used. If the cell is placed in the dark the I_L term disappears, the power supply must supply current to the cell, and the current through R_S changes direction so the – sign is appropriate in the V±IR$_S$ term. In most solar cells the R_S term is small (R_S<0.1Ω) and the R_{SH} term is large[1] (R_{SH}>10000Ω) so in the first approximation the term on the right disappears as well as the term involving R_S.

The term J_{01} is known as the reverse-saturation current density and by modifying the expression of the ideal diode law (first derived by Shockley[7]) it is possible to calculate the diffusion current, I_1

$$J_{01} = \frac{I_{01}}{A} = qn_i^{\,2}\left[\frac{1}{N_D}\left(\frac{D_P}{\tau_P}\right)^{\frac{1}{2}} + \frac{1}{N_A}\left(\frac{D_n}{\tau_n}\right)^{\frac{1}{2}}\right] \tag{7.4}$$

$$J_1 = \frac{I_1}{A} = J_{01}\left[\exp\left(\frac{V}{kT}\right) - 1\right] \tag{7.5}$$

where N_A = Doping Concentration in p-type

N_D = Doping Concentration in n-type

D_p = Diffusion coefficient of holes

D_n = Diffusion coefficient of electrons

τ_p = Lifetime of holes

τ_n = Lifetime of electrons

q = Elementary particle charge

n_i = Intrinsic concentration

In a real solar cell the forward current can be dominated by the recombination current in the depletion region. The energy efficiency is generally reduced compared with that of an ideal diode. For single level centres near the intrinsic Fermi level the recombination current density under forward bias (J_{2f}) can be expressed as[8,9]

$$J_{2f} = \frac{I_2}{A} = \left(\frac{qn_iW}{\sqrt{\tau_p\tau_n}}\right) * \left(\frac{2\sinh\left(\frac{V}{2kT}\right)}{\frac{V_{bi} - V}{kT}}\right) * \left(\frac{\pi}{2}\right) \tag{7.6}$$

Under reverse bias the generation current is given by

$$J_{2r} = \frac{I_2}{A} = \frac{qn_iW}{2\sqrt{\tau_p\tau_n}}\left[\cosh\left(\frac{E_t - E_i}{kT} + \frac{1}{2}\ln\frac{\tau_p}{\tau_n}\right)\right]^{-1} \tag{7.7}$$

where W = Width of the depletion layer

V_{bi} = Built-in voltage

E_t = Trap level

E_i = Intrinsic Fermi level

This is assuming that the mobilities and doping levels on both sides of the junction are equal. However, this theory has been extended to include the case where the doping levels and lifetimes are different on either side of the junction[10] but it has been concluded that the difference is small enough to be neglected[9]. These equations should therefore be used to determine J_2 depending on whether the diode is under forward or reverse bias. It should be noted here that the lifetime in the depletion region has been estimated by averaging the lifetimes in the p and n-type regions which may introduce a small error. If the actual lifetime in the depletion region is known then this value should be used.

The depletion width is related to the doping density, the temperature and the bias voltage. For an abrupt junction the depletion width can be computed using the following expression commonly known as the C-V formula

$$\frac{1}{C}=\frac{W}{\varepsilon_S}=\left(\frac{2(V_{bi}\pm V-2kT)}{q\varepsilon_S N_B}\right)^{\frac{1}{2}} \tag{7.8}$$

In this expression V is the applied bias voltage (use the + sign for reverse bias and the – sign for forward bias, ε_S is the semiconductor permittivity and N_B is the doping density on the lightly doped side of the junction.

7.3.2 Antireflection Coating

Silicon has a high index of refraction which amounts to losses of 35-50% dependent on the wavelength of the incident light[11]. The reflection from the surface of bare silicon is calculated using the equation

$$R=\frac{(n-1)^2+k^2}{(n+1)^2+k^2} \tag{7.9}$$

The index of refraction (n)[12] and the extinction coefficient (k)[13] for intrinsic silicon at 300K are shown in Figure 7.8..

A reduction in reflection can be achieved using the "optical quarter wavelength" principle. The penetrating light beam is reflected at the barrier layer between the antireflection medium and the silicon (Figure 7.9.). Owing to continuity equations and conservation of energy, an electromagnetic wave undergoes a phase shift of $\pi/2$ upon entry into an optically denser medium. If the antireflection layer is chosen so that the optical path is equal to a quarter of the wavelength then light of this wavelength falling vertically is completely extinguished.

$$nd = \frac{\pi}{4} \tag{7.10}$$

According to Fresnel's formula the reflection factor is

$$R = \frac{r_1^2 + r_2^2 + 2r_1r_2\cos 2\vartheta}{1 + r_1^2r_2^2 + 2r_1r_2\cos 2\vartheta} \tag{7.11}$$

with

$$r_1 = \frac{n_0 - n_1}{n_0 + n_1} \tag{7.12}$$

$$r_2 = \frac{n_1 - n_2}{n_1 + n_2} \tag{7.13}$$

$$\vartheta = \frac{2\pi n_1 d_1}{\lambda} \tag{7.14}$$

where n_0 = Refractive index of the uppermost layer
n_1 = Refractive index of the antireflection layer
n_2 = Refractive index of silicon
d_1 = Depth of antireflection layer

Reflection is at its minimum where $n_1d_1=\lambda/4$

$$R_{\min} = \left(\frac{n_1^2 - n_0n_2}{n_1^2 + n_0n_2}\right)^2 \tag{7.15}$$

To calculate total reflection at thickness d_1 in relation to the wavelength of the incident light the refractive index of silicon is required (Figure 7.8.) as well as the refractive index of the coating material (Table 7.3.)[1].

Table 7.3 - Indices of Refraction of Antireflection Coating Materials at 300K

Material	n at λ = 589nm
MgF_2	1.38
Organic Film	1.40
SiO_2	1.46
Al_2O_3	1.76
SiO_x	1.8 – 1.9
Si_3N_4	2.05
Ta_2O_5	2.2
ZnS	2.36
TiO_2	2.62
CMG Coverglass	1.516
CMX Coverglass	1.527
CMZ Coverglass	1.49
Fused Silica	1.46 – 1.51

The reflection layer thickness is determined so that the minimum reflection occurs where maximum power is obtained from the incident light (0.60μm for terrestrial cells illuminated by the AM1.5 spectrum).

7.3.3 Back Surface Field

The back surface of a standard solar cell is completely metal coated to form the back contact of the cell. This increases the surface recombination velocity close to infinity and therefore many of the charge carriers are lost by recombination. This situation is dramatically improved by the creation of a highly doped p+ layer on the back surface of the solar cell base. This is known as a back surface field (BSF) and its effectiveness depends on several parameters

- The surface concentration of the p+ doping as well as its concentration profile and penetration depth,
- Recombination in the p-type layer itself,
- Charge carrier density at the junction (depends upon the relationship between diffusion length and crystal thickness).

This effect reduces the back surface recombination velocity quite dramatically[14] and results in a 5-10% improvement in the efficiency of cells fabricated on 10Ωcm p-type substrates[15]. A schematic band diagram is shown in Figure 7.10.[16]. The potential energy barrier $q\phi_p$ tends to confine minority carriers in the more lightly doped region. The BSF cell can be modelled as a normal cell of width $x_j + W + W_p$ with a very small recombination velocity at the back ($S_n < 100$ cm/s)[5]. This will enhance the spectral response at low photon energies and therefore the short-circuit current density will increase. The open-circuit voltage is also increased due to the increased short-circuit current, the decreased diode recombination current at the back contact, and the added potential energy between the p and p^+ regions.

7.3.4 Back Surface Reflector

To achieve maximum efficiency a silicon solar cell should ideally be made relatively thin (≈15μm)[17,18]. Silicon however has a relatively low absorption coefficient so much of the incident light will pass through a cell of this thickness. It is therefore important to provide some form of optical confinement or light trapping so that the light can be collected. Figure 7.11. shows the proportion of light that will be collected in relation to cell thickness for a standard silicon cell. The total power available to the cell is reduced by the contact shading and reflection from the front surface to give the internal power shown. The amount of light power which passes through the cell is also shown and related to the thickness of the cell. It can be seen that even with a thickness of 180 μm a significant amount of light (6%) is transmitted through the cell and this increases to over 20% for a thin-film (15μm) cell.

An effective method of light trapping is to fit the back surface of the solar cell with a random surface structure (Lambert's reflection). This diffuse reflector traps most of the light because the radiation can only exit via a narrow leakage cone due to the high refraction index of silicon[19]. Figure 7.12. shows this cone and fraction of light in the loss cone (L) can be calculated using

$$L = \sin^2 \Phi_C = \frac{1}{n^2} \qquad \textbf{(7.16)}$$

The refractive index of silicon varies in relation to wavelength therefore the fraction of light lost through this cone also varies and this relationship is shown in Figure 7.13.. It can be seen that only around 8% of the reflected radiation is lost by reemission.

Further improvements can be made by additional structuring of the front surface of the cell[20,21].

The total amount of absorbed light can be obtained by following an incident light beam over many reflections and summing up the absorption. The following definitions are used

P = Total light intensity arriving at cell
P_{in} = Intensity of light inside front surface (Total intensity minus losses by shading and reflection)
P_0 = Total intensity arriving at back surface reflector
P_1 = Total intensity arriving for second reflection
P_2 = Total intensity arriving for third reflection
R_b = Reflection coefficient of back surface reflector
R_f = Reflection coefficient of front surface
H = Total cell thickness
N = Refractive index of silicon

Assuming that the lateral directions are infinite then

$$P_0 = P_{in} e^{-\alpha H} \tag{7.17}$$

This gives the amount of light which passes through the cell and reaches the BSR. The amount of light which is reflected for absorption a second time is given by P_0R_b. This value in relation to wavelength can then be used to calculate the photocurrent generated by the second pass using the equations for photocurrent derived earlier. The proportion of light reaching the front of the cell is then given by

$$P_1 = (P_0 R_b) e^{-\alpha H} \tag{7.18}$$

Some of this light is lost (Figure 7.13.) but most is reflected again from the front surface and this is given by P_1R_f. This reflected light is again used to calculate the photocurrent generated by the third pass and the proportion of light reaching the BSR for a second time is now given by

$$P_2 = (P_1 R_f) e^{-\alpha H} \tag{7.19}$$

This process is repeated until all of the light has been accounted for, although in reality a standard cell of 200 μm thickness will absorb almost all of the light in the first two reflections.

7.3.5 Diffused N-type Layer

A "dead" layer is believed to exist adjacent to the surface of the device due to stress induced by the junction diffusion. The n-type top layer should therefore be divided into two layers with different lifetimes and mobility's. This top region with a narrow dead section near the surface and a wider section of higher lifetime near the junction edge is essentially equivalent to a uniform top region with a high recombination velocity at its surface[22]. The dead layer can therefore be modelled as a uniform top region with a short lifetime and a high surface recombination velocity of around 1×10^6 cm/sec.

7.4 Spectral Response and IV Characteristics of the BSF/BSR Czochralski Silicon Solar Cells

The model developed to calculate the ideal characteristics of a solar cell (see Figure 7.1.) can now be extended to consider the silicon solar cells described in chapter five. The equations have been modified to account for the diffused region, the reflection from the front surface, the BSR and the BSF. This now enables the characteristics of the Czochralski cell no. 68/9 (see chapters five and six) to be determined.

Firstly the shading of the cell by the front contacts must be accounted for and for this cell around 12% of the incident light is reflected from the contacts. This is shown in Table 7.4 which also shows the inputs and values used to calculate the cells spectral response and IV characteristics.

The reflection from the front surface has been reduced by the deposition of a thin (0.1μm) coating of Titanium Dioxide (TiO_2). Figure 7.14. shows the calculated reflection in relation to the wavelength of the incident light before (equation 7.9) and after (equation 7.11) deposition of the antireflection layer.

Table 7.4 – Input values for Silicon Solar Cell No. 68/9

Parameter	Value	Units	Notes
Cell No.	68/9		No irradiation
Temp	300	Kelvin	
Base Resistivity	20	Ohm.cm	
Top Contact Shading	12	%	
TiO_2 layer thickness	0.1	μm	
AM0 Power	0.1368	W/cm^2	
N_A	$1.3 * 10^{15}$	cm^{-3}	
N_D	$1.0 * 10^{19}$	cm^{-3}	
H	180	μm	
X_j	0.1	μm	
L_p	0.2	μm	Approximate estimate
L_n	80	μm	Determined by LSF method (section 7.4)
S_p	500000	cm/s	Approximates dead layer
S_n	1000	cm/s	Approximates BSF
R_b	90	%	Approximate estimate

The diffused n-type layer has been modelled as a shallow (0.1μm) region with uniform doping and a high surface recombination velocity (see Table 7.4) which approximates the effect of the "dead" layer (see section 7.2.5). Figure 7.15. shows how changing this surface recombination velocity affects the cells spectral response. The BSF has been modelled by using a low value for the surface recombination velocity and a short diffusion length (see Table 7.4). The BSR has been modelled using the equations given in section 7.2.4, and Figure 7.16. shows how this increases the spectral response in the longer wavelength region.

This model has now been developed sufficiently to determine the photocurrent generated by each region of the solar cell (no. 68/9) when illuminated by the AM0 spectrum. The quantum efficiency can now therefore be determined (see Figure 7.17.) and the spectral response of each region of the solar cell can be calculated (see Figure 7.18.).

The IV characteristics have also been calculated using the equations given in section 7.2.1 and Figure 7.19. shows the dark and illuminated IV characteristics of the cell chosen in this example. Table 7.5 summarises these results and also shows that from the IV curve the cells short-circuit current, open-circuit voltage, output power and efficiency can all be determined.

Table 7.5 – Calculated IV Characteristics of Silicon Solar Cell No. 68/9

Parameter	Value	Units	Notes
μ_p	57.01	cm^2/Vs	Calculated using equation 3.17
μ_n	1270.56	cm^2/Vs	Calculated using equation 3.16
D_p	1.47	cm^2/s	Calculated using equation 3.15
D_n	32.85	cm^2/s	Calculated using equation 3.14
τ_p	2.99×10^{-10}	s	Calculated using equation 3.13
τ_n	1.95×10^{-6}	s	Calculated using equation 3.13
V_{bi}	0.837	V	Calculated using equation 2.19
W	8.91×10^{-5}	cm	Calculated using equation 2.25
I_{sc}	36.34	mA	Calculated using equations 7.2, 7.4 and 7.6
I_{sc}	36.2	mA	Experimental from Table 6.16
V_{oc}	537.18	mV	Intercept of IV curve (see section 7.2.1)
V_{oc}	537.4	mV	Experimental from Table 6.16
I_m	32.9	mA	Determined from IV curve
V_m	433.0	mV	Determined from IV curve
P_m	14.25	mA	Determined from IV curve
FF	0.73		Calculated using equation 2.37
Efficiency	10.42	%	Calculated using equation 2.36

7.5 Determination of the Minority-Carrier Diffusion Length

The spectral response method of measuring diffusion length uses a fixed collector junction while varying the spatial distribution of carrier generation. Using optical injection this is readily achieved by varying the wavelength (and therefore the absorption coefficient) of the incident light[23]. There are several different ways of measuring this response that include the surface photovoltage method[24,25,26,27], the differential photocurrent method[28,29] and the least squares fitting method. The different methods for measuring the diffusion length have been reviewed and discussed in some detail by Woolam[30] and Tada[31].

When a shallow junction n+-p diode is illuminated by monochromatic radiation of low absorption coefficient, such as in the wavelength region 0.9-1.0μm for silicon, the experimentally measured current is essentially the photocurrent due to carriers collected from the neutral p-region[32] (see Figure 7.18.). The diffusion length in the p-type region of the solar cell (L_n) can therefore be extracted from a non-linear least squares fit of the experimental data (photocurrent density versus wavelength) to the theoretical data generated by applying equation 2.50. In this method L_n and S_n are taken as parameters and all the other terms such as α, R and D_n are assumed fixed and known. Thus J_n given in equation 2.50 has been expressed as $J_n = J_n(L_n,S_n,\lambda)$. In this expression L_n and S_n are varied in such a way that the deviation (the sum of the squares of the difference between experimental and theoretical J_n) is minimised.

This method can be improved by fitting the experimental data obtained in chapter six to the model which has been developed in section 7.3 for a more accurate assessment of the minority-carrier diffusion length. This has been carried out for cell 68/9 using the parameters given in Table 7.4 and a very good correlation between the experimental and theoretical data has been attained and this result is shown in Figure 7.20.. The diffusion length was altered while all the other parameters remained constant and using the least-squares fit method the diffusion length was determined to be around 80μm.

The theoretical IV characteristics for this cell have also been determined and are shown in Table 7.5. The correlation between the theoretical and experimentally determined I_{sc} and V_{oc} values is very good (see Table 7.5) despite the approximations and assumptions that were made in the development of this model.

The minority carrier diffusion length has also been determined using the same method for cells that were irradiated by electrons and protons for comparison. Figure 6.28 gives the experimental results for cell 68/13 prior to irradiation, and cells 68/9/2 and 68/7/2 after irradiation by 1×10^{16} (1MeV) electrons/cm^2 and 3×10^{11} (10MeV) protons/cm^2 respectively. The diffusion lengths have been determined by comparison between the experimental and theoretical data and the resulting diffusion lengths are around 72μm prior to irradiation, 17μm after 1×10^{16} (1MeV) electrons/cm^2 and around 24μm after 3×10^{11} (10MeV) protons/cm^2 respectively. Care should be exercised when interpreting the results for the minority-carrier diffusion length in the proton irradiated samples however because they may have a non-uniform minority-carrier lifetime in the active base region[31].

Finally the minority-carrier diffusion length has been determined for different fluence levels of electron irradiation for some of these cells. The experimental results shown in Figures 6.29 (67/13) and 6.30 (68/8/2) have been analysed and the results are shown in Table 7.6. The spectral response of the PERL/PERT cells (Figures 6.33 to 6.40) has also been analysed and the resulting diffusion lengths are shown in Table 7.6.

Table 7.6 – Diffusion Length and IV Characteristics of Cell 67/13 and diffusion length of cell 68/8/2

Cell No	Parameter	Value	Units	Irradiation / Notes
67/13	L_n	78	µm	None
	I_{sc}	26.60	mA	Calculated using equations 7.2, 7.4 and 7.6
	V_{oc}	544.89	mV	Intercept of IV curve (see section 7.2.1)
	I_m	24.13	mA	Determined from IV curve
	V_m	440.00	mV	Determined from IV curve
	P_m	10.62	mA	Determined from IV curve
	FF	0.73		Calculated using equation 2.37
	Eff	7.76	%	Calculated using equation 2.36
67/13	L_n	63	µm	(1×10^{14} 1MeV E/cm^2)
	I_{sc}	25.82	mA	Calculated using equations 7.2, 7.4 and 7.6
	V_{oc}	534.37	mV	Intercept of IV curve (see section 7.2.1)
	I_m	23.36	mA	Determined from IV curve
	V_m	430.00	mV	Determined from IV curve
	P_m	10.05	mA	Determined from IV curve
	FF	0.73		Calculated using equation 2.37
	Eff	7.34	%	Calculated using equation 2.36
67/13	L_n	55	µm	(3×10^{14} 1MeV E/cm^2)
	I_{sc}	26.13	mA	Calculated using equations 7.2, 7.4 and 7.6
	V_{oc}	529.01	mV	Intercept of IV curve (see section 7.2.1)
	I_m	23.62	mA	Determined from IV curve
	V_m	425.00	mV	Determined from IV curve
	P_m	10.04	mA	Determined from IV curve
	FF	0.73		Calculated using equation 2.37
	Eff	7.34	%	Calculated using equation 2.36
67/13	L_n	34	µm	(1×10^{15} 1MeV E/cm^2)
	I_{sc}	24.26	mA	Calculated using equations 7.2, 7.4 and 7.6
	V_{oc}	504.69	mV	Intercept of IV curve (see section 7.2.1)
	I_m	21.81	mA	Determined from IV curve
	V_m	402.00	mV	Determined from IV curve
	P_m	8.77	mA	Determined from IV curve
	FF	0.72		Calculated using equation 2.37
	Eff	6.41	%	Calculated using equation 2.36
68/8/2	L_n	72	µm	None
68/8/2	L_n	58	µm	(1×10^{14} 1MeV E/cm^2)
68/8/2	L_n	49	µm	(3×10^{14} 1MeV E/cm^2)
68/8/2	L_n	38	µm	(1×10^{15} 1MeV E/cm^2)
CZG	L_n	84	µm	(1×10^{14} 1MeV E/cm^2)

CZG	L_n	38	µm	(1×10^{15} 1MeV E/cm^2)
CZG	L_n	24	µm	(3×10^{15} 1MeV E/cm^2)
CZI	L_n	90	µm	(1×10^{14} 1MeV E/cm^2)
CZI	L_n	43	µm	(1×10^{15} 1MeV E/cm^2)
CZI	L_n	29	µm	(3×10^{15} 1MeV E/cm^2)
CZA	L_n	22	µm	(1×10^{14} 1MeV E/cm^2)
CZA	L_n	18	µm	(1×10^{15} 1MeV E/cm^2)
CZA	L_n	13	µm	(3×10^{15} 1MeV E/cm^2)
FZB	L_n	84	µm	(1×10^{14} 1MeV E/cm^2)
FZB	L_n	40	µm	(1×10^{15} 1MeV E/cm^2)
FZB	L_n	24	µm	(3×10^{15} 1MeV E/cm^2)
MCZ	L_n	86	µm	(1×10^{14} 1MeV E/cm^2)
MCZ	L_n	41	µm	(1×10^{15} 1MeV E/cm^2)
MCZ	L_n	25	µm	(3×10^{15} 1MeV E/cm^2)
FZP	L_n	16	µm	(1×10^{14} 1MeV E/cm^2)
FZP	L_n	7	µm	(1×10^{15} 1MeV E/cm^2)
FZP	L_n	4	µm	(3×10^{15} 1MeV E/cm^2)
CZP1.3	L_n	17	µm	(1×10^{14} 1MeV E/cm^2)
CZP1.3	L_n	7	µm	(1×10^{15} 1MeV E/cm^2)
CZP1.3	L_n	4	µm	(3×10^{15} 1MeV E/cm^2)
CZP5.5	L_n	28	µm	(1×10^{14} 1MeV E/cm^2)
CZP5.5	L_n	13	µm	(1×10^{15} 1MeV E/cm^2)
CZP5.5	L_n	9	µm	(3×10^{15} 1MeV E/cm^2)

7.6 Modelling of Solar Cells using PC1D

PC1D Version 5.2 has also been used to model the cells described above. PC1D is a quasi-one-dimensional finite element program for modelling semiconductor devices on personal computers[33,34] and is available from The Photovoltaics Special Research Centre at the University of New South Wales, Australia. The numerical method[35] employed in PC1D has proven to be remarkably efficient for solving the highly non-linear equations of electrons and holes in semiconductor devices. PC1D version 5 incorporates improved models for heavy doping effects such as free-carrier absorption and trap-assisted tunnelling.

PC1D solves the complete semiconductor device equations for arbitrary doping profiles whereas the model developed in section 7.3 only considers uniform doping profiles and includes several assumptions. The PC1D model should therefore provide more accurate results for the cells considered in this report. The quantum efficiency of the solar cells studied in this report have been compared with the first principles (FP) model to show the differences between these two models.

Several of the cells were used to compare these two models and here solar cell 68/9 has been chosen as an example. Inputting identical parameters into both models for this cell (see Table 7.4) with a uniformly doped n-type region gives the results for the internal and external quantum efficiency shown in Figure 7.21.. It can be easily seen that the PC1D results are nearly identical to the FP model results. The agreement between these models is therefore very good in the region used to calculate the minority-carrier diffusion length so the results given in section 7.4 have been validated and confirmed using PC1D.

PC1D can consider, in addition to the uniform doping profile examined so far, doping profiles such as exponential, gaussian and erfc profiles. Figure 7.22. shows the results obtained for cell 68/9 when using an exponential doping profile. PC1D can also be used to calculate the IV characteristics of solar cells and cell 68/9 has again been chosen as an example. Figure 7.23. shows the comparison between the results from the two models and as expected the first principles analysis produces a slightly higher result due to the assumptions inherent in these calculations.

In addition to the quantum efficiency PC1D also considers many different parameters and some of the important results for cell 68/9 with a uniform doping profile have been calculated. The current density as a function of position is shown in Figure 7. 24. and PC1D can also calculate the cumulative photogeneration and recombination as a function of position (Figure 7.25.). Finally the edges of the conduction and valence bands can also be plotted as a function of position together with the quasi-Fermi energies (Figure 7.26.).

7.7 References

[1] Anspaugh, B.E., GaAs Solar cell radiation handbook, NASA Publication, Jet Propulsion Laboratory (JPL96-9), (1996).

[2] J.J. Loferski and J.J. Wysocki, Spectral Response of Photovoltaic Cells, RCA Review, p.38, (1961).

[3] N.D. Arora et al, Appl. Phys. Lett. 37, p.325, (1980).

[4] Clugston, D.A., and Basore, P.A., PC1D Version 5: 32-bit solar cell modeling on personal computers, Presented at the 26th IEEE Photovoltaics Specialists Conference, (1997).

[5] Sze, S.M., Physics of Semiconductor Devices, Second Edition, John Wiley and Sons Inc., (1981).

[6] Green, M.A., Intrinsic Concentration, Effective Densities of States, and Effective Mass in Silicon, J. Appl. Phys., 67, p.6, (1990).

[7] Shockley, W, The theory of p-n junctions in semiconductors and p-n junction transistors, Bell Syst. Tech. J. 28, p.435, (1949).

[8] Sah, C.T., Noyce, R.N., and Shockley, W., Carrier generation and recombination in p-n junctions and p-n junction characteristics, Proc. IRE 45, p.1228, (1957).

[9] Hovel, H.J., Proc. 10th IEEE Photovoltaics Specialist Conf., p.34, (1973).

[10] Choo, S.C., Carrier generation-recombination in the space charge region of an asymmetrical p-n junction, Sol. St. Elect. 11, p.1069, (1968).

---

[11] Chelikowsky, J.R., and Cohen. M.L., Phys. Rev. B14, 2, p.556-582, (1976).

[12] Phillip, H.R., and Taft, E.A., Optical constants of silicon in the region 1 to 10 eV, Phys. Rev. 120, 1, p.37-38, (1960).

[13] Green, M.A., and Keevers, M., Optical Properties of Intrinsic Silicon at 300K, Prog. in Photovoltaics Vol. 3, (1995).

[14] Godlewski, M.P., et al, Low-high injection theory applied to solar cells, 10th IEEE Photovoltaic Specialists Conf., p.40-49, (1973).

[15] Gereth, R., et al, Contribution to the solar cell technology, Energy Conversion, Vol. 12, p.103-107, (1972).

[16] Mandelkorn, J., and Lamneck, J.H., Simplified fabrication of back surface electric field solar cells and novel characteristic of such cells, 9th IEEE Photovoltaic Specialists Conf., New York, p.66, (1973).

[17] Loferski, J.J., et al, 14th IEEE Photovoltaic Specialists Conference, p.375, (1980).

[18] Wolf, M., 14th IEEE Photovoltaic Specialists Conference, p.674, (1980).

[19] Goetzberger, A., Optical confinement in thin si-solar cells by diffuse back reflectors, 15th IEEE Photovoltaic Specialists Conference, p.867, (1981).

[20] Uematsu, T., et al, A new cell structure for very thin high efficiency silicon solar cells, IEEE TED 37, p.344, (1990).

[21] Green, M.A., et al, Characterisation of 23% efficient silicon solar cells, IEEE TED 37, p.331, (1990).

---

[22] Hovel, H.J., Solar cells in Willardson and Beer (Eds.), Semiconductors and Semimetals, Vol.11, Academic New York, (1975).

[23] Blood, P. and Orton, J.W.: The electrical characterization of semiconductors: measurement of minority carriers, Techniques of Physics, Vols. 13 & 14, Academic Press, London, (1992).

[24] Wang, E.y., et al, Surface photovoltage method extended to silicon solar cell junction, J. Electrochem. Soc., 121, 7, p.973, (1974).

[25] Chu, T.L., and Stokes, E.D., Minority carrier diffusion lengths in silicon slices and shallow junction devices, J. Electronic Mats., 7, 1, p.173, (1978).

[26] Saritas, M., and McKell, H.D., Diffusion length studies in silicon by the surface photovoltage method, Solid State Electronics, 31, 5, p.835, (1985).

[27] Chu, T.L., and Stokes, E.D., A comparison of carrier lifetime measurements by photoconductive decay and surface photovoltage methods, J. Appl. Phys., 45, 5, p.2996, (1978).

[28] Sukegawa, T., et al, Differential photocurrent method for measurement of the optical absorption coefficient and the minority carrier diffusion length in a semiconductor, IEEE Trans. on Electron Devices, ED-27, 7, p.1251, (1980).

[29] Stokes, E.D., and Chu, T.L., Diffusion lengths in solar cells from short circuit current measurements, Appl. Phys. Lett. 30, 8, p.425, (1977).

[30] Woolam, J.A., et al, Diffusion length measurements in solar cells – An analysis and comparison of techniques, Space Photovoltaic Research and Tech. Conf., NASA Conf. Pub., 2256, p.45, NASA Lewis, (1982).

[31] Tada, H.Y., et al, Solar cell radiation handbook, JPL Publication 82-69, Jet Propulsion Laboratory, California Institute of Technology, Pasedena, Calif., (1982).

[32] Arora, N.D., et al, Diffusion length determination in p-n junction diodes and solar cells, Appl. Phys. Lett. 37, 3, p.325, (1980).

[33] Clugston, D.A., and Basore, P.A., PC1D Version 5: 32-bit solar cell modeling on personal computers, Presented at the 26th IEEE Photovoltaics Specialists Conference, (1997).

[34] Basore, P.A., and Clugston, D.A., PC1D Version 4 for windows: from analysis to design, Presented at the 25th IEEE Photovoltaics Specialists Conference, (1996).

[35] Thorson. G.M. and Basore, P.A., Semiconductor device modelling on personal computers: PC1D Version 2, Electrosoft 2, 1, p.6-12, (1991).

FIGURE 7.1 FLOW CHART FOR THE THEORETICAL SOLAR CELL CALCULATIONS

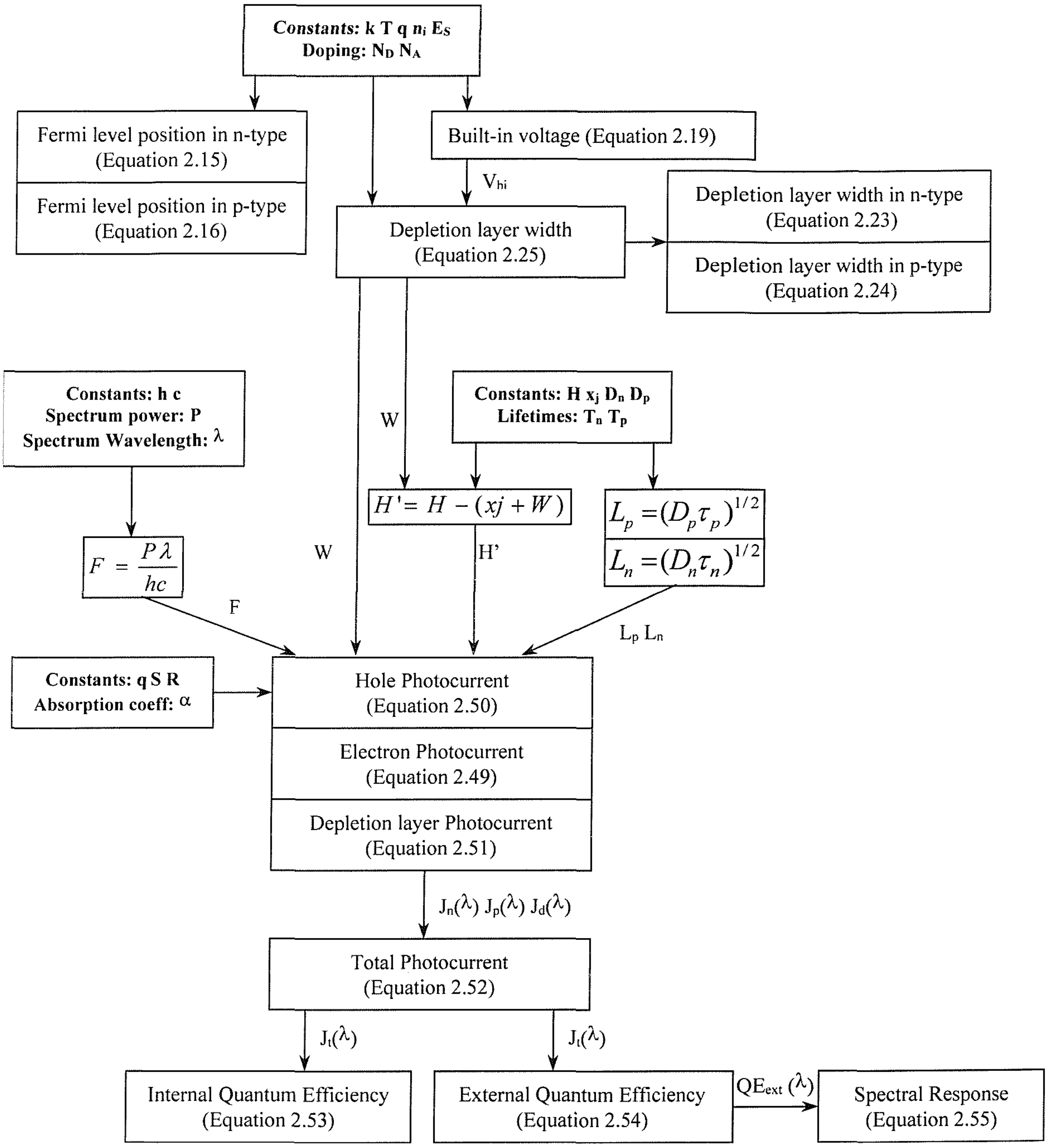

FIGURE 7.2. ENERGY BAND DIAGRAM

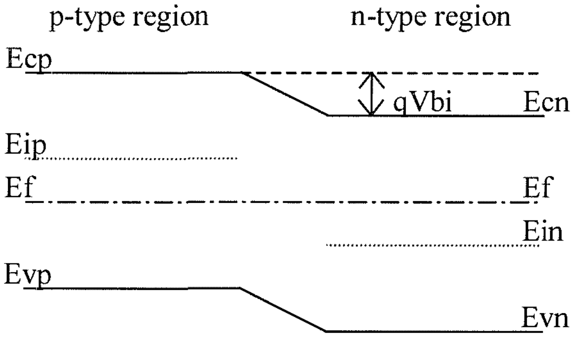

FIGURE 7.3. PHOTOCURRENTS GENERATED WHEN AN IDEAL P-N JUNCTION SOLAR CELL IS ILLUMINATED BY THE AM1.5 SPECTRUM

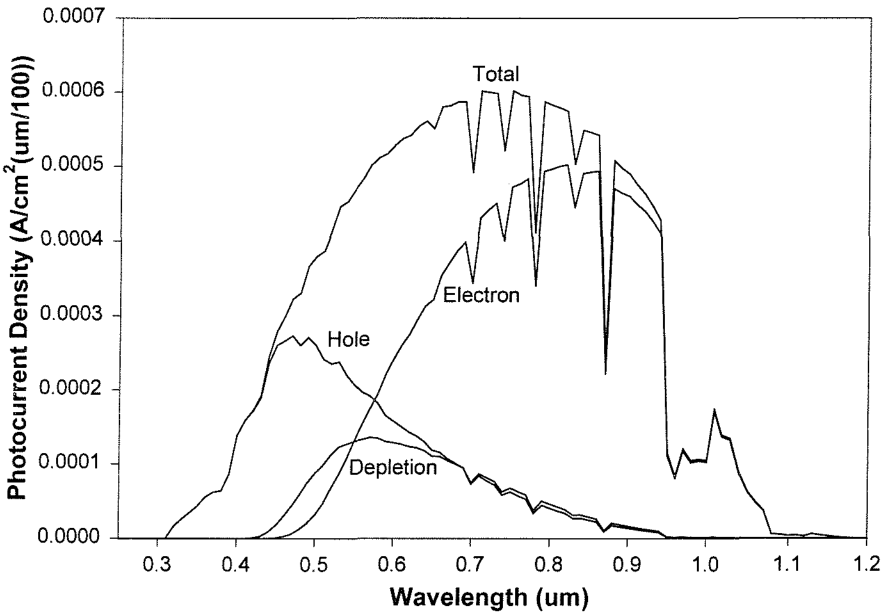

FIGURE 7.4. TOTAL PHOTOCURRENTS WHEN AN IDEAL P-N JUNCTION SOLAR CELL IS ILLUMINATED BY THE AM1.5 SPECTRUM

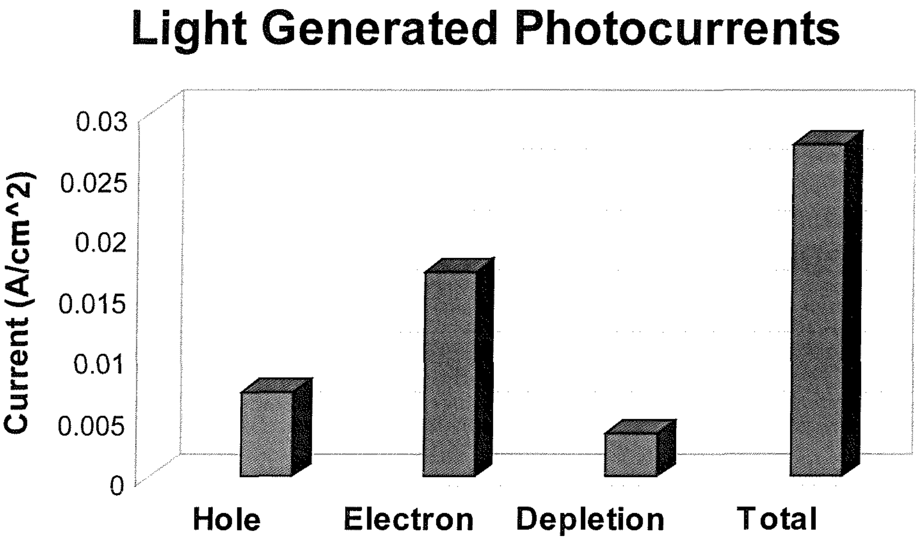

FIGURE 7.5. IDEAL QUANTUM EFFICIENCY OF A P-N JUNCTION SOLAR CELL

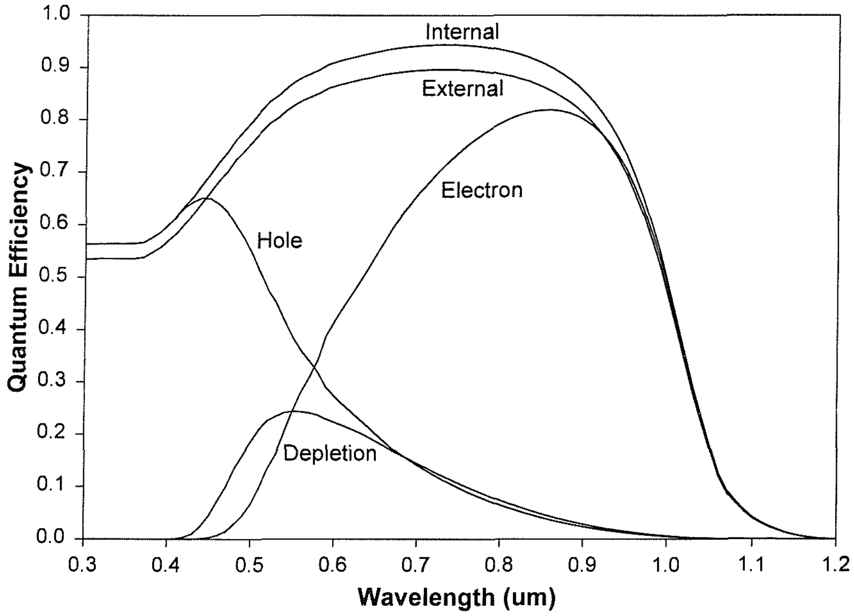

FIGURE 7.6. IDEAL SPECTRAL RESPONSE OF A P-N JUNCTION SOLAR CELL

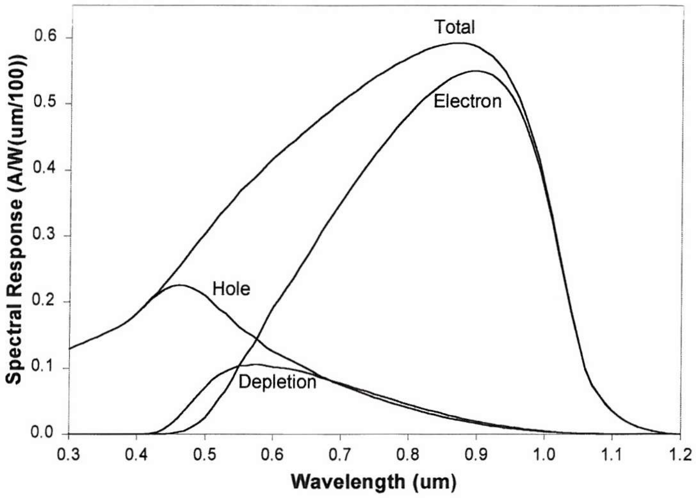

FIGURE 7.7. EQUIVALENT CIRCUIT OF AN ILLUMINATED SOLAR CELL

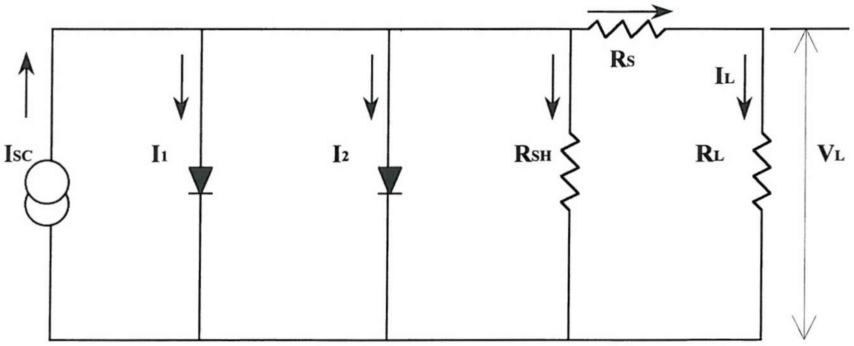

FIGURE 7.8. THE INDEX OF REFRACTION AND EXTINCTION COEFFICIENT OF PURE SILICON

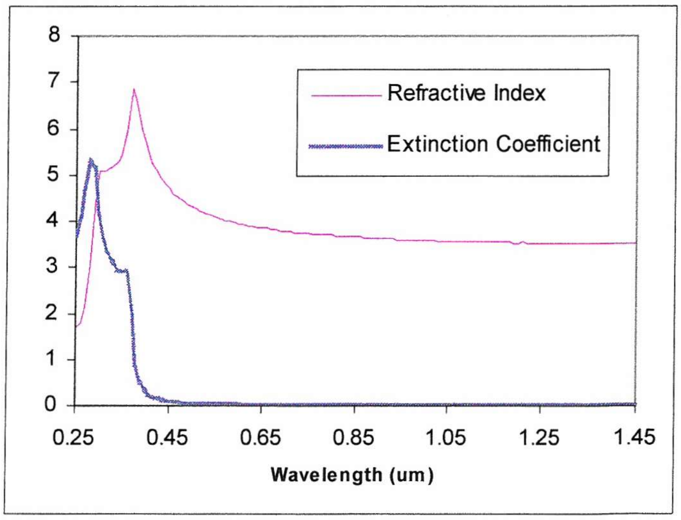

FIGURE 7.9. ANTIREFLECTION BEHAVIOR OF A THIN FILM

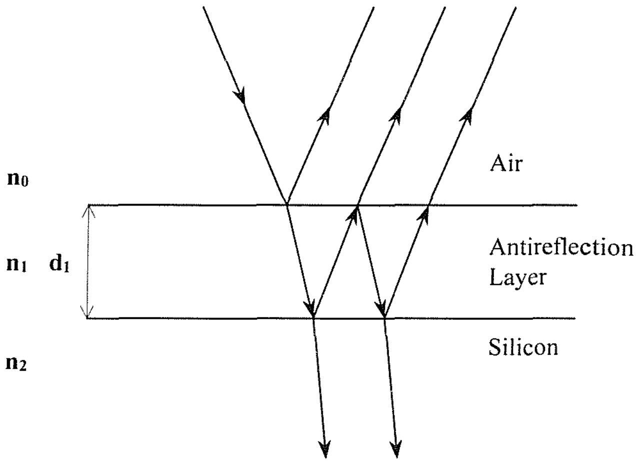

FIGURE 7.10. ENERGY BAND DIAGRAM FOR A N^+PP^+ BACK SURFACE FIELD SOLAR CELL

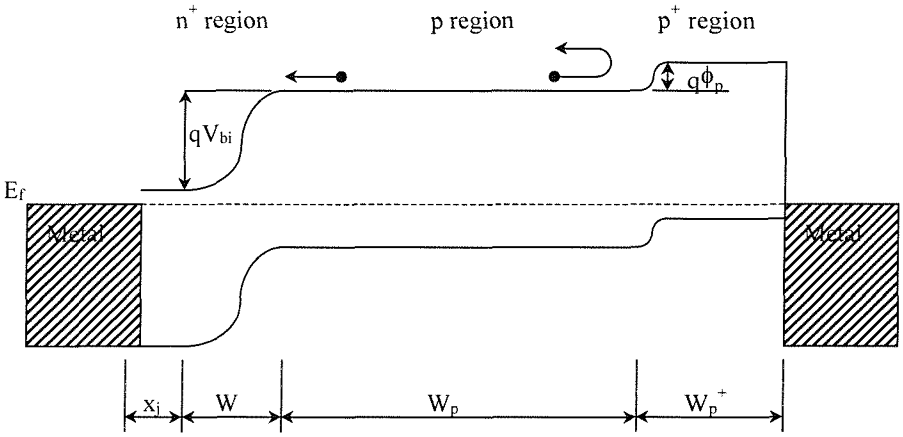

FIGURE 7.11. POWER LOST BY TRANSMISSION THROUGH A P-N JUNCTION SOLAR CELL IN RELATION TO CELL THICKNESS

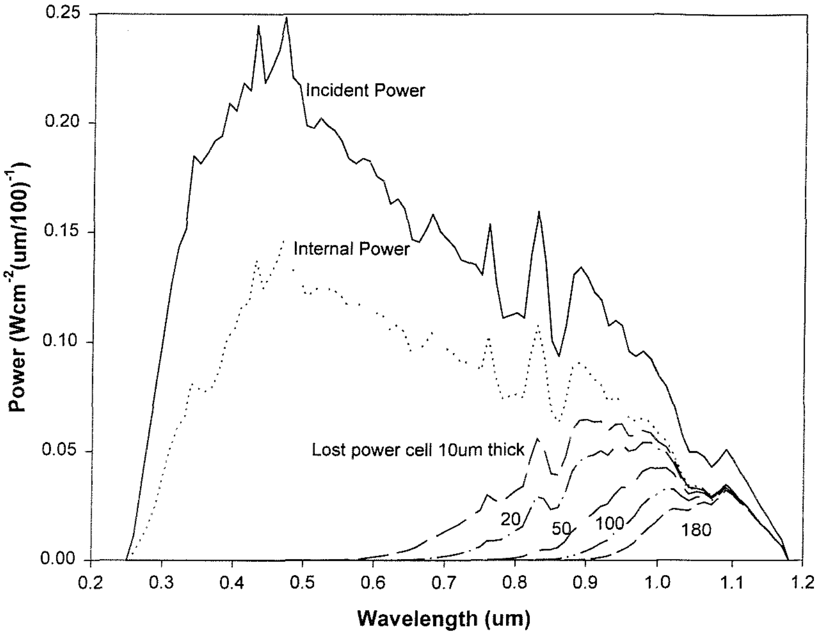

FIGURE 7.12. REFLECTION BEHAVIOR WITH RANDOM LAMBERT'S SURFACE STRUCTURE

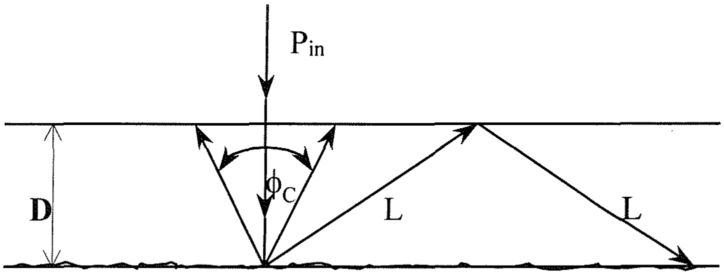

FIGURE 7.13. CALCULATED PERCENTAGE OF REFLECTED RADIATION LOST BY REEMISSION

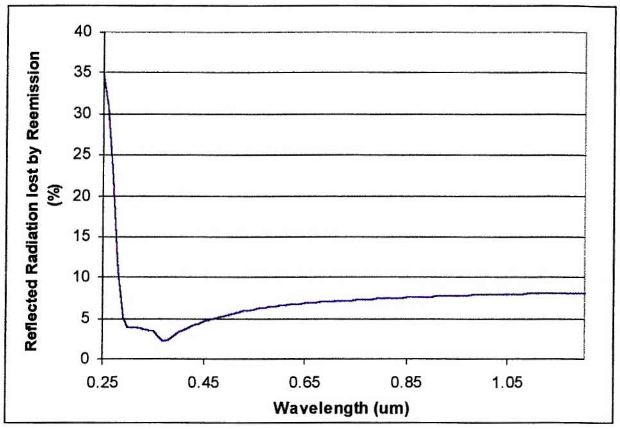

FIGURE 7.14. REFLECTION FROM THE SURFACE OF SOLAR CELL 20168/9 BEFORE AND AFTER DEPOSITION OF A 0.1μm TiO_2 ANTIREFLECTION LAYER

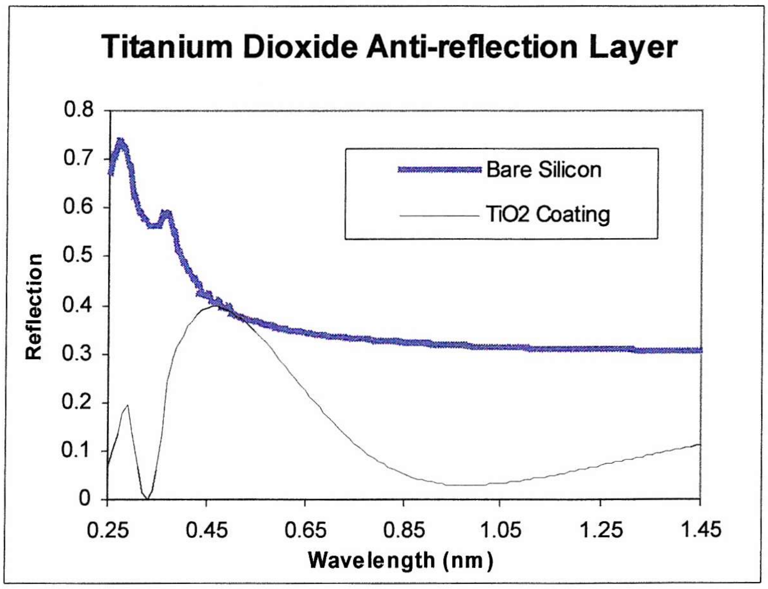

FIGURE 7.15. EFFECT OF CHANGING THE HOLE SURFACE RECOMBINATION VELOCITY ON THE SPECTRAL RESPONSE OF CELL 20168/9

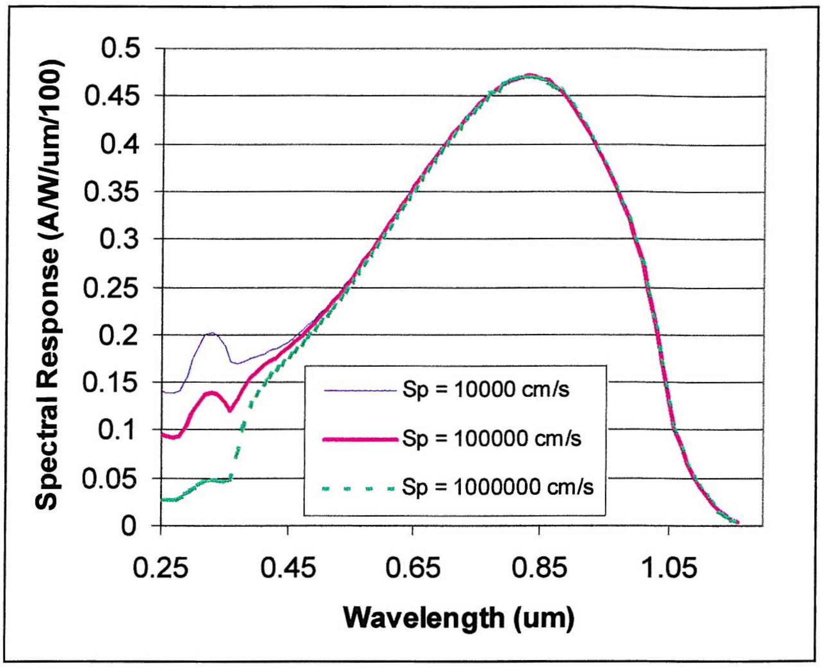

FIGURE 7.16. EFFECT OF THE BACK SURFACE REFLECTOR ON THE SPECTRAL RESPONSE OF CELL 20168/9

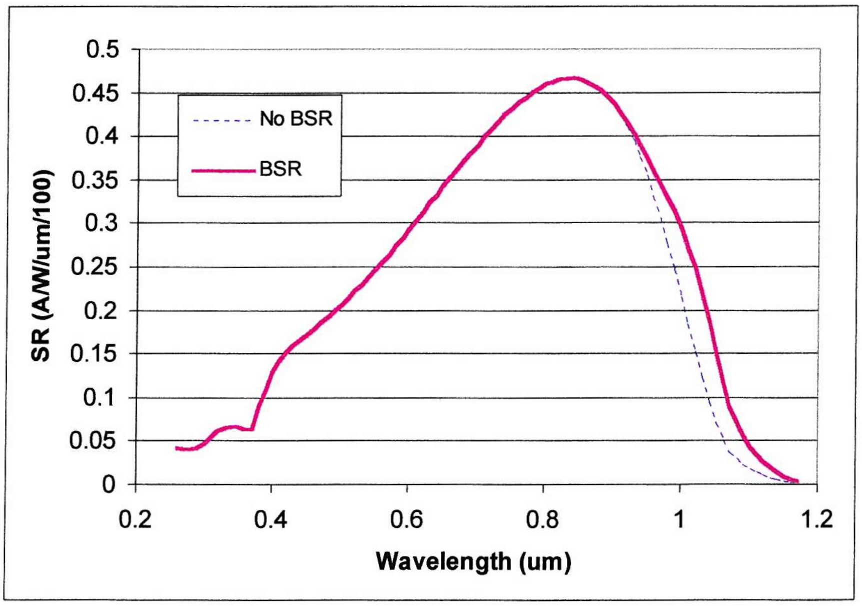

FIGURE 7.17. THE EXTERNAL AND INTERNAL QUANTUM EFFICIENCY OF CELL 20168/9

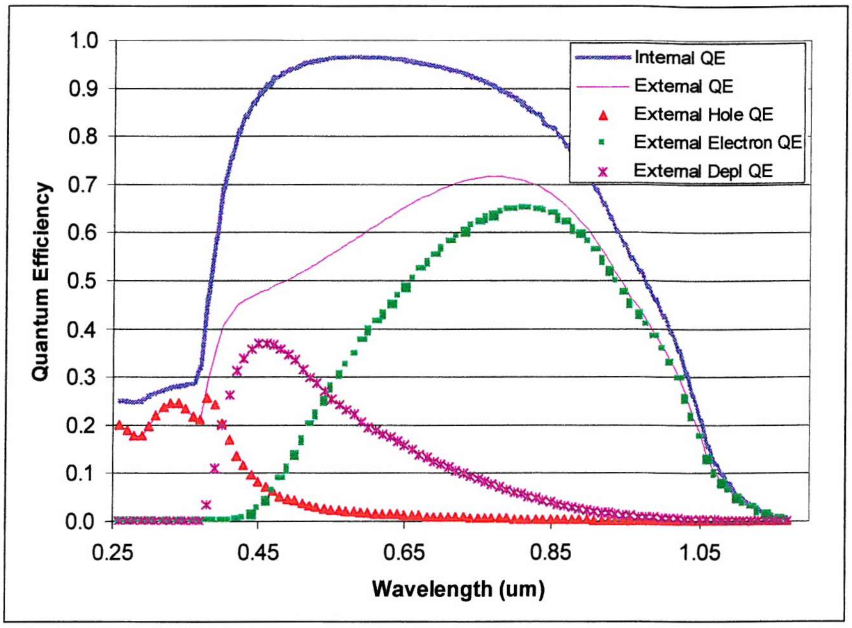

FIGURE 7.18. THE SPECTRAL RESPONSE OF CELL 20168/9

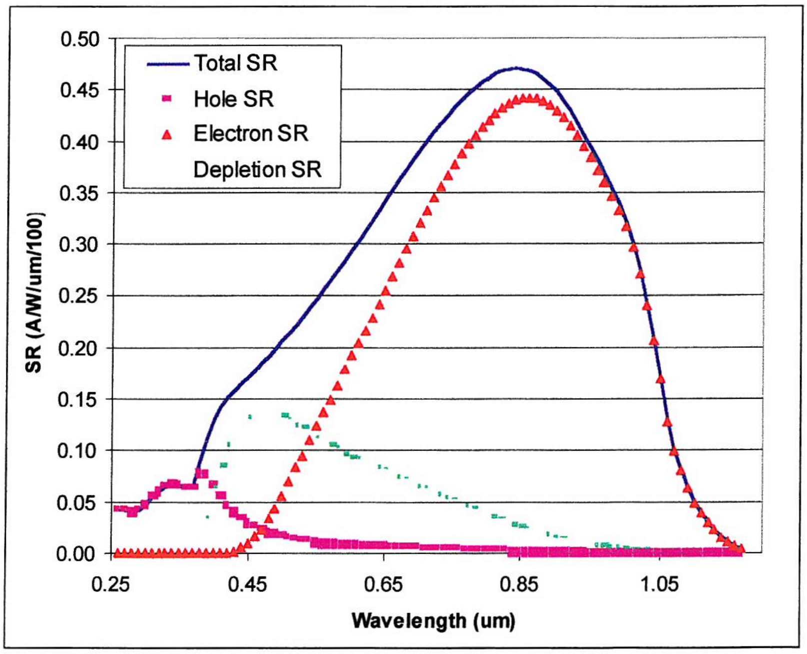

FIGURE 7.19. THE FORWARD BIASED DARK AND ILLUMINATED I-V CHARACTERISTICS OF CELL 20168/9

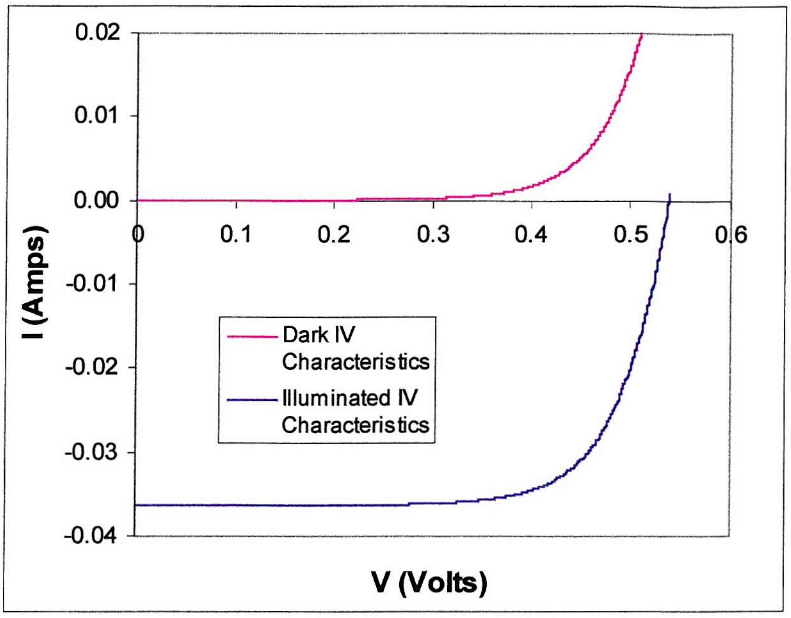

FIGURE 7.20. DIFFUSION LENGTH DETERMINATION CELL 20168/9

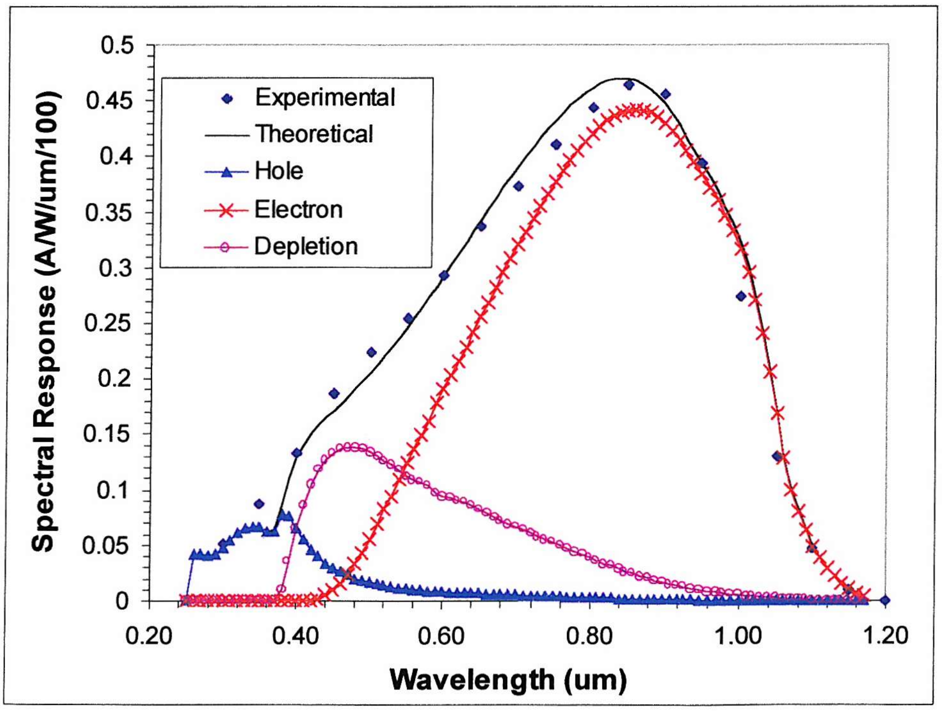

FIGURE 7.21. ***COMPARISON OF THE FIRST PRINCIPLES (FP) AND PC1D MODELS USED TO CALCULATE THE INTERNAL AND EXTERNAL QUANTUM EFFICIENCY OF SOLAR CELL 68/9 WITH A UNIFORM DOPING PROFILE IN THE N-TYPE REGION***

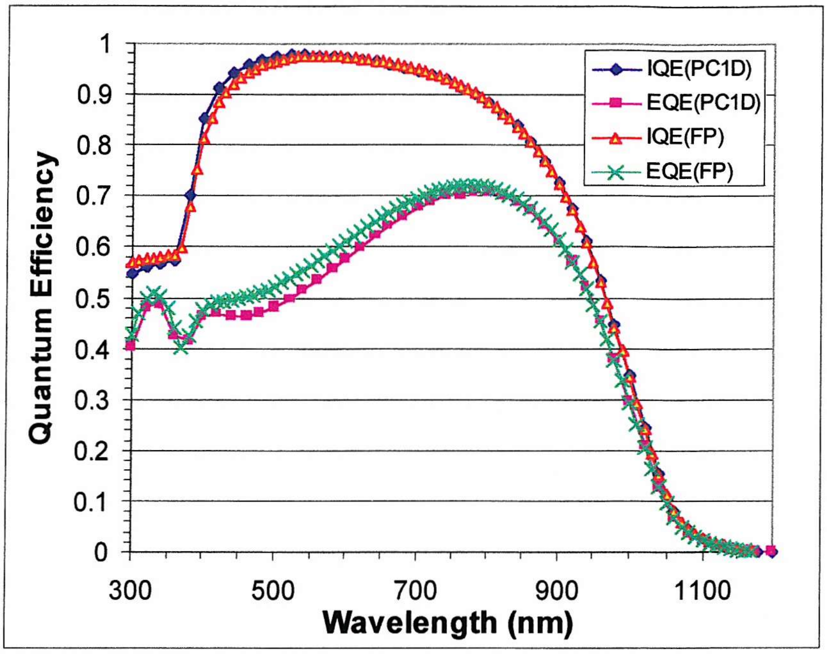

FIGURE 7.22. ***COMPARISON OF THE FIRST PRINCIPLES AND PC1D MODELS USED TO CALCULATE THE INTERNAL AND EXTERNAL QUANTUM EFFICIENCY OF SOLAR CELL 68/9 WITH AN EXPONENTIAL DOPING PROFILE IN THE N-TYPE REGION***

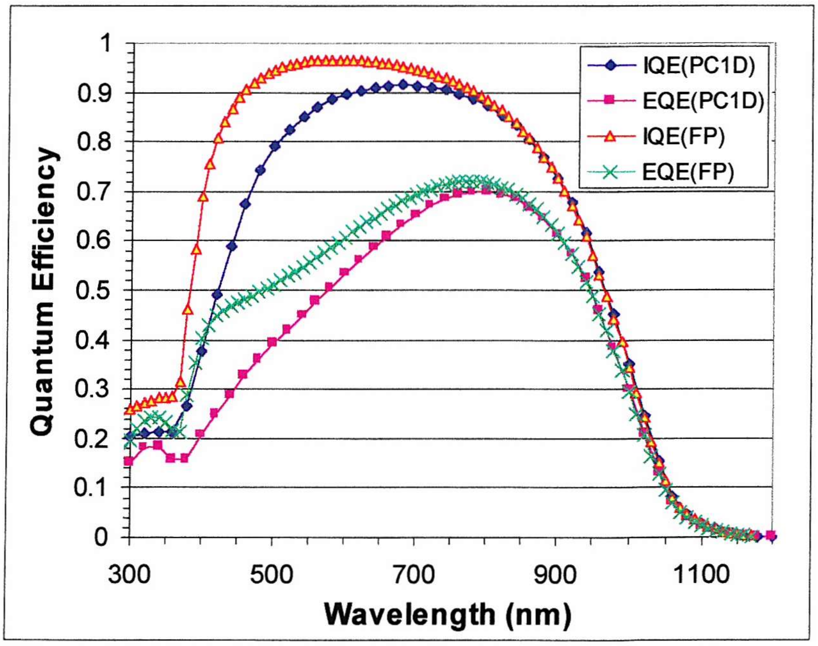

FIGURE 7.23. *COMPARISON OF THE FIRST PRINCIPLES AND PC1D MODELS USED TO CALCULATE THE CURRENT-VOLTAGE CHARACTERISTICS OF SOLAR CELL 68/9 WITH A UNIFORM DOPING PROFILE IN THE N-TYPE REGION*

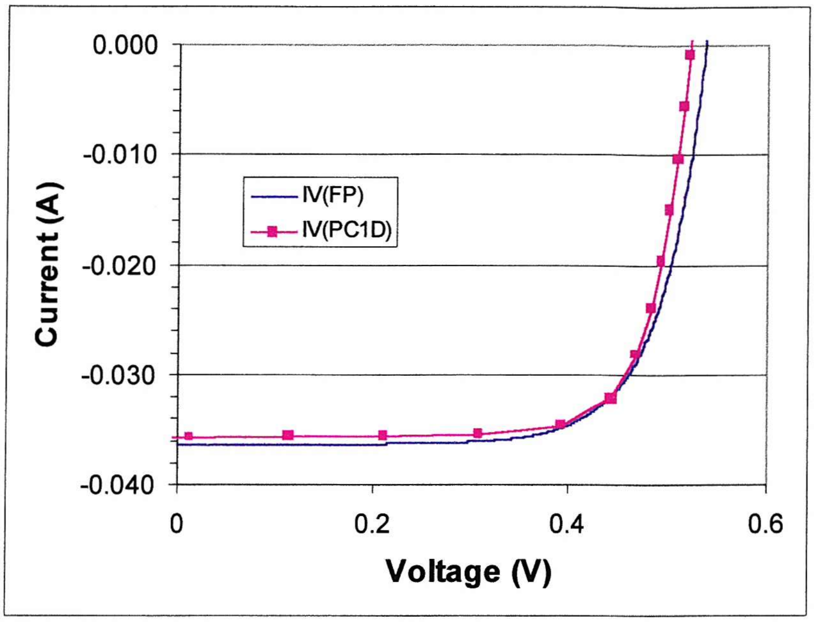

FIGURE 7.24. *CURRENT DENSITY FOR SOLAR CELL 68/9 (UNIFORM DOPING PROFILE) CALCULATED USING PC1D*

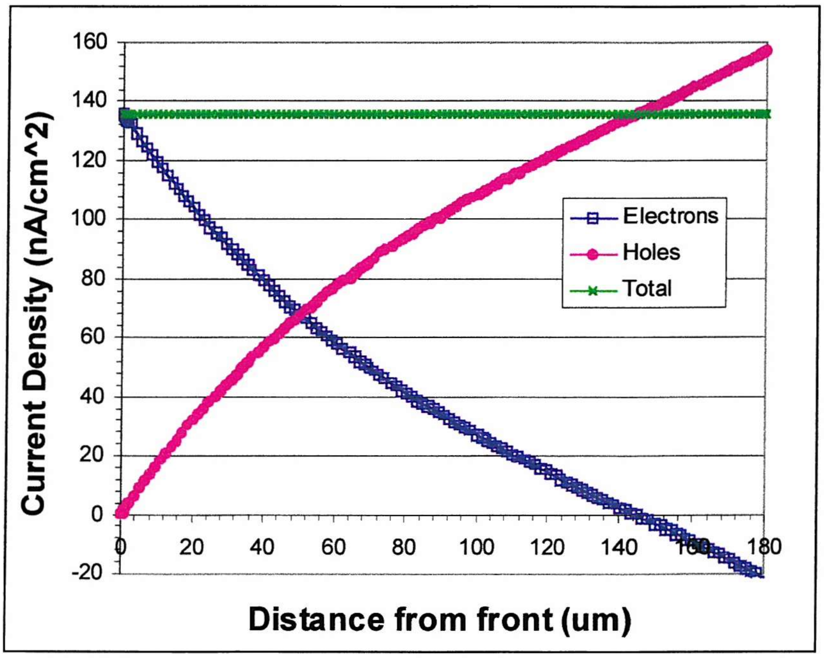

FIGURE 7.25. ***CUMULATIVE GENERATION AND RECOMBINATION FOR SOLAR CELL 68/9 (UNIFORM DOPING PROFILE) CALCULATED USING PC1D***

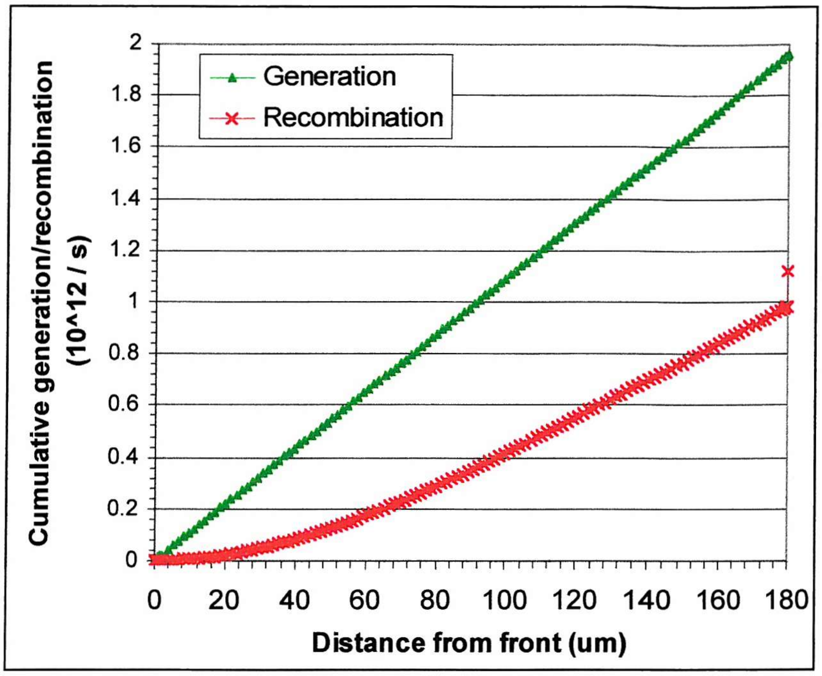

FIGURE 7.26. ***CONDUCTION AND VALENCE BAND EDGES AND QUASI-FERMI ENERGIES (QFE) FOR SOLAR CELL 68/9 (UNIFORM DOPING PROFILE) CALCULATED USING PC1D***

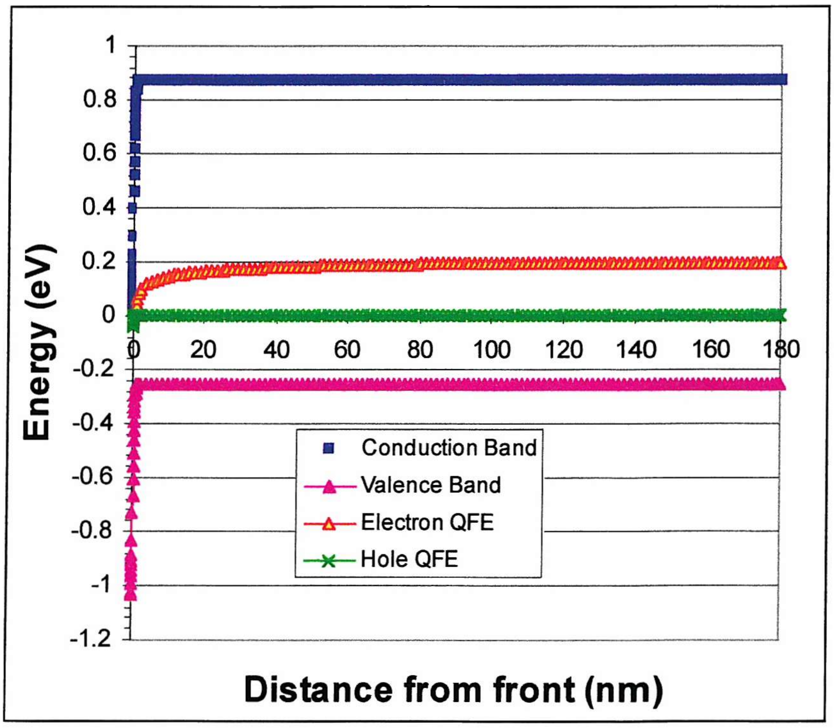

CHAPTER EIGHT

DISCUSSION OF RESULTS

8.1 Introduction

This chapter firstly examines the IV characteristics of the irradiated PERL/PERT cells and compares them to standard shallow junction and thin-film silicon space cells. The DLTS results are then used to identify the defects present in all of the silicon solar cells by comparison with the literature. The identification of the defect responsible for the observed reduction in the minority-carrier diffusion length is then discussed.

The behaviour of the divacancy ($VV^{+/0}$) level is then examined in relation to the charge carrier concentrations and a new technique is proposed to determine the minority-carrier capture cross-section. This data is then used to model the effect of the observed defects on the SRH lifetime and hence diffusion length. The relationship between the doping density and the radiation tolerance of solar cells is then discussed and it is shown that the $VV^{+/0}$ level may be solely responsible for this effect.

8.2 IV Characteristics of the PERL/PERT Cells before and after three Fluence Levels of 1MeV Electron Irradiation

The AM0 short-circuit currents (I_{SC}) and open-circuit voltages (V_{OC}) shown in Table 6.17 are summarised in Table 8.1 by selecting the average result for each type of PERL/PERT cell.

Table 8.1 – AM0 Short-circuit Currents and Open-circuit Voltages before and after three Fluence Levels of 1MeV Electron Irradiation

Substrate	Text	AM0 I_{SC} (mA/cm^2)				AM0 V_{OC} (mV/cm^2)			
(Dopant)	label	0	1E14	1E15	3E15	0	1E14	1E15	3E15
CZ (Ph5.5)	CZP1.5	40.8	25.8	22.3	21.1	658.1	507.8	483.3	465.1
CZ (Ph1.3)	CZP1.3	39.0	22.9	18.1	17.0	654.3	523.9	492.9	469.8
FZ (Ph)	FZP	46.6	27.0	21.2	19.0	695.8	495.0	475.0	459.5
FZ (Bo)	FZB	47.9	37.0	32.1	29.9	699.7	561.1	530.6	513.0
MCZ(Bo)	MCZ	47.5	38.6	33.1	30.6	702.6	560.2	529.2	510.6
CZ (Ga)	CZG	45.8	38.0	32.3	29.8	691.2	564.3	531.3	511.4
CZ (In)	CZI	41.4	34.6	30.0	28.0	664.2	541.2	504.8	488.8
CZ (Al)	CZA	32.9	27.6	25.7	24.5	577.5	559.5	545.2	524.6
CZ (Bo)	CZB	25.6	24.8	23.5	21.0	533.8	529.1	504.6	456.7
StCZ(B)	StCZ(B)	39.8	36.2	31.0	28.5	600	544	501	477
ThCZ(B)	ThCZ(B)	39	38.5	35.5	32.3	598	566	516	490

Also shown for comparison are the results from Tada et al[1] for standard silicon 10 Ohm.cm shallow junction space cells with a back surface field (BSF) and back surface reflector (BSR). The cells labelled StCZ(B) are 200μm thick and the cells labelled ThCZ(B) are thin-film cells 50μm thick.

The deposition of the DLAR coating improves[2] the I_{SC} by 13% and the V_{OC} by around 5mV (≈0.725%) so now all the PERL/PERT cells can be directly compared. PC1D was used to confirm that this assumption was valid for all levels of irradiation, and it was found that the difference between the predicted and experimental values was negligible. Table 8.2 shows the adjusted I_{SC} and V_{OC} and these results are shown graphically in Figures 8.1. (I_{SC}) and 8.2. (V_{OC}).

Table 8.2 – AM0 Short-circuit Currents and Open-circuit Voltages before and after three Fluence Levels of 1MeV Electron Irradiation after DLAR correction

Substrate	AM0 I_{SC} (mA/cm^2)				AM0 V_{OC} (mV/cm^2)			
(Dopant)	**0**	**1E14**	**1E15**	**3E15**	**0**	**1E14**	**1E15**	**3E15**
CZ (Ph5.5)	46.1	29.15	25.2	23.8	663.1	512.8	488.3	470.1
CZ (Ph1.3)	44.1	25.9	20.5	19.2	659.3	528.9	497.9	474.8
FZ (Ph)	46.6	27.0	21.2	19.0	695.8	495.0	475.0	459.5
FZ (Bo)	47.9	37.0	32.1	29.9	699.7	561.1	530.6	513.0
MCZ(Bo)	47.5	38.6	33.1	30.6	702.6	560.2	529.2	510.6
CZ (Ga)	45.8	38.0	32.3	29.8	691.2	564.3	531.3	511.4
CZ (In)	48.1	39.3	33.9	31.7	669.2	546.2	509.8	493.8
CZ (Al)	37.1	31.3	29.0	27.7	582.5	564.5	550.2	529.6
CZ (Bo)	25.6	24.8	23.5	*21.0*	533.8	529.1	504.6	*456.7*
StCZ(B)	39.8	36.2	31.0	28.5	600	544	501	477
ThCZ(B)	39	38.5	35.5	32.3	598	566	516	490

The AM0 efficiencies of the PERL/PERT cells are shown in Figure 8.3. which also allows for the deposition of the DLAR. The results for the FZB cells closely match the results of an earlier study[3] and the highest V_{OC} was obtained from the CZA cells. This was offset by a smaller I_{SC} so all the p-type cells were remarkably similar in efficiency after 3×10^{15} electrons/cm^2 (see Figure 8.3.). The lower doped CZ n-type cells (CZP5.5) are better than both the higher doped cells (CZP1.3) and the FZP cells as expected.

The results shown in Figure 8.3. for the n-type cells show that these cells are less resistant to radiation damage than the p-type cells, and their efficiency after irradiation is reduced by a higher doping level. This agrees well with results observed in other studies[1] although the damage coefficient in these cells is much higher because of the very high starting efficiencies.

The p-type cells are very similar in efficiency after irradiation even though four different dopants and three different substrates were used. The CZA cells were slightly lower in efficiency than the others although they had the highest open-circuit voltages after irradiation. They also had the highest doping density so a lower efficiency is to be expected because the damage coefficient of p-type solar cells has been shown to depend on the doping density[1]. The CZI cells have the lowest doping density and also have the highest short-circuit current after irradiation.

The CZG, FZB and MCZ cells had very similar doping densities and therefore their irradiated short-circuit currents were also very similar. The FZB and the MCZ cells were similar to the other p-type cells in efficiency directly after irradiation but further degradation was observed when these cells were subsequently illuminated (see Sections 6.10 and 6.11). Despite the varying materials and dopants used the commonly observed relationship between doping density and radiation tolerance can be seen in both the n- and p-type cells. The most suitable cells for development for space use are probably the CZG cells as they have been shown to be more tolerant to radiation damage at higher fluence levels[4,5] and they also do not degrade when initially illuminated unlike the standard CZB cells[6,7,8]. The CZI and CZA cells are also worth considering as an alternative to the CZB cells although further research is required to examine their resistance to radiation damage at higher fluence levels.

The fill factors and hence efficiencies were quite low (≈ 0.5 to 0.7) due to processing problems during manufacture[2] because fill factors of 0.8 and above are now commonly achieved for these cells. Figure 8.4. therefore uses a fill factor of 0.8 to show the efficiencies that can be easily achieved using these PERT/PERL cells and compares these efficiencies to standard shallow junction space cells. It is obvious that the high quality surface passivation and the high minority-carrier lifetimes in the PERT/PERL cells are vulnerable to space radiation damage. The junction depth in the p-type PERT/PERL cells of 0.3μm also reduces their resistance to radiation damage. The so called front dead-layer effect causes a reduction in the blue response for deeper emitter cells. Even so these cells still have a higher efficiency than the standard 200μm space cells, at all the radiation levels tested.

To improve the blue response these cells should be fabricated with a reduced surface doping concentration and smaller junction depth (≈0.1 μm). The combination of higher lifetime near the surface and narrower junction will greatly improve the response at high photon energies[9]. If the emitter junction depth therefore was optimised to a shallow 0.1μm these PERT/PERL cells would have a significantly improved radiation resistance[3].

Further improvements could be made by reducing the thickness of the cells. A thickness of less than 200μm can significantly improve the radiation resistance. The thin-film space cells shown in Figure 8.4. for example are around 1.5% more efficient after irradiation than similar 200μm cells (StCZ(B)). The UNSW has produced very high efficiency cells thinner than 50μm[10] so there is plenty of scope for improvement.

For many space missions[1] the maximum radiation level is equivalent to less than 1×10^{15} 1MeV electrons/cm^2. The p-type PERL/PERT cells are around 10% efficient at this level and significant improvements are possible using thinner cells with shallow junctions. PERL space cells 100μm thick for example should only have around a 1% efficiency reduction after 10 years in a 300km Low-Earth-Orbit (LEO)[11]. These PERL cells should therefore be suitable for these missions with minor modifications.

8.3 Identification of the Defects Detected in the Czochralski Cells

Standard boron doped czochralski BSF/BSR cells were studied using DLTS and MCTS and the resulting DLTS spectra are summarised in Figure 8.5. together with their approximate energy level. The peak seen in the DLTS spectrum of the Czochralski solar cells labelled H(0.19) is a hole trap with a position in the band gap of around $E_v + 0.19$eV. The introduction rate of this defect (≈0.0023 cm^{-1}) shows no dependence on the oxygen or boron content of the material[12] and has a majority carrier (holes in p-type material) capture cross-section (HCCS) of around 5×10^{-16} cm^2 (see Table 6.3). This defect has been observed many times in radiation damaged p-type silicon and has been attributed to the divacancy. The charge state of this defect has also been deduced as neutral before hole capture and is therefore labelled as $VV^{+/0}$ (see Section 3.4.2). The value for the HCCS is slightly smaller than quoted by other authors (see Table 3.1) although it is in agreement with the previous studies carried out on these cells[13,14].

The peak labelled H(0.36) is a hole trap with an energy level of around $E_V + 0.36$ and an introduction rate of around 0.003 cm^{-1} in cell 67. This defect is the most prominent in the Czochralski silicon samples and has been the subject of much speculation over the years (see Section 3.5.2). There are several possible candidates for this centre discussed in the literature such as the interstitial-substitutional carbon complex (C_IC_S)[15], the carbon-oxygen complex (C_IO_I)[16], and the carbon-oxygen-vacancy (COV)[17] complex.

Controlled thermal and radiation induced annealing experiments demonstrated the preferential growth of the high and low temperature sides of the peak and suggested that this peak was actually due to two defects [18]. This was also investigated by scanning DLTS and this confirmed the presence of two closely spaced defects at Ev + 0.344eV and Ev + 0.370eV that were identified as C_IO_I and $C_SSi_IC_S$[19,20]. Analysis of capture cross section results[21] showed two defects contributing to this peak with $\sigma_1=5\times10^{-18}$ cm^{-2} and $\sigma_2=1.2\times10^{-16}$ cm^{-2} with σ_1 contributing to 90% of the peak and σ_2 contributing 10%. It is therefore likely that this peak consists mainly of the C_IO_I defect with a smaller contribution from another carbon related centre.

It is therefore believed to consist of two closely spaced defects, C_IO_I and $C_SSi_IC_S$ that could explain the asymmetry and the broad nature of this peak. The proportion of these two defects is believed to depend upon the oxygen concentration of the material so in Czochralski silicon C_IO_I should dominate and in float-zone material $C_SSi_IC_S$ should be the dominant contributor. This could explain the slightly higher introduction rate observed in cell 68 (0.0035 cm^{-1}) because of the higher oxygen content of this sample (see Table 5.2). The HCCS determined for this defect (Table 6.3) is slightly larger than quoted in the literature (Table 3.1) although it is within the same order of magnitude .

MCTS studies detected another defect level (Section 6.3) that has a position of around E(0.26) and this defect has been detected before in the previous studies of electron irradiated boron doped czochralski silicon[22]. After much deliberation (see Section 3.5.1) this defect has been tentatively identified as the B_IO_I that forms when the boron interstitial anneals at around 240K (see Table 3.1) and is unique to the boron-doped CZ cells.

8.4 Identification of the Defects Detected in the Float-zone Cells

These cells also contain the divacancy ($VV^{+/0}$) and the carbon complex labelled F1 and F3 respectively in Table 6.3. They also contain an additional defect labelled F2 that was observed at around H(0.29). This peak is often associated with the so call "photon effect"[23] and is possibly the B_IC_S defect.

The peak labelled F4 is a hole trap at around H(0.42) that was also observed in a previous study[12] and the introduction rate of this defect was found to behave erratically after annealing. This defect was only detected in the boron-doped FZ cells and the observed concentrations varied between samples however overall it was found that this defect is independent of the boron concentration. This defect was also thought to be partly responsible for photon degradation[12] which occurs in the float-zone samples. It is possible that it may be same defect that has been observed by other workers[20] and it has also been suggested that it may be a vacancy-impurity related defect[24].

The peak labelled F5 in Section 6.2 has a position in the band gap of around H(0.50) and shows a weak dependence upon the boron content of the material. This is in agreement with a previous study[12] and could be the same as a level observed in a similar position by Mottet and Roizes[25] who suggested that it may be a level of the divacancy. The position of this level and level F4 near the mid-gap would suggest that they are both likely recombination centres.

8.5 Identification of the Defects Observed in the High Efficiency PERL/PERT Cells

The defects observed in the n- and p-type PERL/PERT cells are summarised in Table 8.3.

Table 8.3 – Defect Energy Levels and Concentrations observed using DLTS and FBDLTS

Growth (Dopant)	Defect Concentration cm^{-3} ×10^{12}			
	E(0.16)	**E(0.23)**	**E(0.42)**	**H(0.36)**
CZ (Ph5.5)	50	0.95	6.1	25
CZ (Ph1.3)	31	1.60	8.6	27
FZ (Ph)	21	0.55	6.5	
	H(0.19)	**H(0.27)**	**H(0.36)**	**E(0.26)**
FZ (B)	3.9		13	$<10^{12}$
FZ (B)+48h	4.0	3.3	13	$<10^{12}$
MCZ(B)	3.6		9.9	$<10^{12}$
MCZ(B)+48h	4.6	2.9	11	$<10^{12}$
CZ (Ga)	4.6		20	$<10^{12}$
CZ (In)	3.4		15	$<10^{12}$
CZ (B) (1E16cm^{-2})	17		42	$>10^{12}$
	H(0.19)	**H(0.25)**	**H(0.36)**	**H(0.48)**
CZ (Al)	4.2	14	21	10

8.5.1 DLTS of n-type PERT/PERL Silicon Solar Cells

The DLTS and FBDLTS results for the CZP5.5 cells are summarised in Figure 8.6. The position of the observed defects in the bandgap were estimated from the slope of the Arrhenius plots in the usual manner[26] and each peak has been labelled with the result. The electron trap labelled (E(0.16)) is commonly observed in n-type material and is usually identified as the "A centre" or oxygen-vacancy complex (see[27,28,29,63]). Its characteristic annealing behaviour and its energy level at E_C-0.16eV gave rise to this association[30]. The electron trap E(0.23) has an identical emission rate signature and activation energy to the results reported in the literature[31,47] for the doubly negatively charged acceptor state of the divacancy ($VV^{-/=}$).

The large electron trap E(0.42) is commonly observed in irradiation studies on silicon and has two components[31]; the negative charge state of the divacancy, $VV^{-/0}$ and the E centre or phosphorus-vacancy complex[63]. These two deep level defects are known to have similar activation energies and emission rate signatures, however their annealing behaviour is widely different. While the phosphorus-vacancy complex anneals out at around 150-200 ^{0}C[63,47], the $VV^{-/0}$defect tends to be stable up to 300^{0}C and sometimes higher[31]. Another level can be seen as a shoulder on the low temperature side of the

E(0.42) peak and cannot be characterised accurately due to the strong overlap. A similar level at E_C-0.36eV was observed by Walker and Sah[32], in studies on electron irradiation of silicon, and was found to anneal out at temperatures between 200 and 300^0C depending on the phosphorus concentration.

To identify the minority-carrier traps in the CZP5.5 cells FBDLTS was used with a fill pulse height of around 1.5V to ensure complete saturation of the defect levels. One large hole trap was observed using this technique and this peak has been labelled H(0.36) in Figure 8.6.. This defect is easily identified from its emission rate signature and activation energy as the commonly observed carbon related defect complex. The DLTS results for the CZ1.3 and FZP cells were very similar to the CZ5.5 cells with all the same defects being observed (see Figure 8.6.). The concentrations of each defect observed in all the silicon cells studied are summarised in Table 8.3.

8.5.2 DLTS of p-type Silicon Solar Cells

Figure 8.7. shows the two defects that were observed in the CZ (Ga) cells immediately after irradiation. These two defects were also observed in the FZ (Bo), MCZ (Bo), and CZ (In) cells. Comparison of the Arrhenius plots with published data shows that these two levels can be attributed to the transition from the positive to the neutral charge state of the divacancy[17,33] H(0.19) and the carbon related centre[34] or centres[20] respectively H(0.36).

After irradiation some of these cells were exposed to 48 hours of AM0 illumination and a further reduction in cell performance was observed for the FZ(B) and the MCZ(B) cells. This is known as the photon effect[23] and can be related to the substrate resistivity[35]. DLTS studies revealed the appearance of a new defect between the divacancy and the carbon related peak. Figure 8.8. shows the DLTS plot obtained for the MCZ (Bo) cells after 48 hours of AM0 illumination. This new defect had an energy level of around H(0.27) and the concentration of this defect is shown in Table 8.3.

The DLTS studies on the aluminium doped high efficiency cells (CZA) revealed four defects that are shown in Figure 8.9.. The identification of these defects can be obtained by cross-referencing the Arrhenius plot data with the results given in the literature. H(0.19) has been observed in all the p-type cells and can be identified as the positive charge state of the divacancy. H(0.36) is the carbon related peak observed in all the p-type cells, that is likely to consists mainly of the C_IO_I defect. Two of the levels observed, H(0.25) and H(0.48) are unique to the aluminium doped material. The H(0.48) level is usually attributed to the aluminium-vacancy pair and the H(0.25) level has been identified in the literature as the aluminium interstitial[47].

8.6 Forward Bias Injection of Minority-carriers in the CZG Cells

Recombination DLTS[36,37] (RDLTS) is thought to provide a convenient tool to characterise recombination centres in semiconductor solar cells. This technique relies on the simultaneous injection of electrons and holes in a controlled manner. Majority carriers are injected into the depletion region using an electrical fill pulse and minority-carriers are injected by illumination. This technique was examined in great detail however even with the laser on full power the electron concentration was calculated to be too small to deplete the divacancy ($VV^{+/0}$) concentration in the CZG cells and this was confirmed by experiment. Another method is therefore required to find the electron capture cross-section of this divacancy level in these cells.

A new experiment was devised and it was soon discovered that the electron concentration can be increased sufficiently to deplete the divacancy concentration using forward bias (see Section 6.13). As the forward bias voltage was increased the divacancy peak could be seen to reduce in height whereas the carbon peak remained relatively constant (Figure 6.19). MCTS was carried out on these cells and no minority-carrier defects were observed that could explain this behaviour (Figure 6.20). This effect has been observed before in aluminium doped samples and implies that the level is being saturated with minority-carriers, implying a large electron capture cross-section[38]. As the electron concentration increases the divacancy that has already trapped a hole begins to trap electrons that are then annihilated by recombination with the hole. This returns the divacancy to the neutral charge state and the divacancy will therefore no longer contribute to the observed DLTS signal.

8.6.1 Concentration of Divacancies Occupied by Holes

To examine the observed reduction in height of the divacancy peak with increasing forward bias it is necessary to first determine the reduction in concentration of occupied divacancy defects. The height of the DLTS peaks can be directly related to the concentration of these majority carrier traps using equation 4.22[39]

$$\frac{\Delta C_0}{C} = \frac{1}{2}\left\{\frac{x_1{}^2 - x_2{}^2}{x_d{}^2}\right\}\frac{N_t}{N_A} \qquad \textbf{(8.1)}$$

Here N_t is the trap concentration, N_A is the doping density, C is the capacitance at the quiescent reverse bias and ΔC_0 is the capacitance change at the maximum height of the peak. The depletion depths x_0 (at V_F) and x_d (at V_R) must be calculated at the temperature of each peak using

$$\frac{x}{\varepsilon_S} = \left(\frac{2(V_{bi} + V - 2kT)}{q\varepsilon_S N_A}\right)^{\frac{1}{2}} \qquad \textbf{(8.2)}$$

Here V_{bi} is the built-in voltage and ε_S is the semiconductor permittivity. Next the trap energy level is assumed to be equal to the activation energy determined by DLTS therefore $E_{na} = E_t - E_v$. $E_F - E_v$ can now also be determined using

$$p = N_v \exp\left(-\frac{E_F - E_v}{kT}\right) \qquad \textbf{(8.3)}$$

where N_v is the effective density of states in the valence band. The transition distance for band bending of $E_F - E_t$, (λ) can now be determined using

$$\lambda = \left(\frac{2\varepsilon_S\varepsilon_0}{q^2 N_A}(E_F - E_t\right)^{\frac{1}{2}} \qquad \textbf{(8.4)}$$

Table 8.4 details the results of equations 8.2, 8.3 and 8.4 calculated for the divacancy and carbon complex in the CZ(G) cells. Now x_1 (x_d - λ) and x_2 (x_0 - λ) can be determined equation 8.1 can be used to determine the trap concentration for each level of forward bias.

Table 8.4 – Calculation of the defects observed in the Gallium doped high efficiency cells under forward bias injection.

Defect	Divacancy	Carbon Complex	Units
$E_t - E_v$	0.19	0.36	eV
Peak Temperature	125	215	K
N_A	3.6×10^{15}	3.6×10^{15}	cm^{-3}
N_v	5.91×10^{18}	1.66×10^{19}	cm^{-3}
ε	11.9	11.9	F/m
ε_0	8.85418×10^{-12}	8.85418×10^{-12}	F/m
k	8.617×10^{-5}	8.617×10^{-5}	eV/K
q	1.60218×10^{-19}	1.60218×10^{-19}	C
$E_f - E_v$	0.080	0.156	eV
$E_f - E_t$	0.110	0.204	eV
λ	0.201	0.273	μm

Both the divacancy and carbon complex DLTS peaks initially increase in height. This is because the depletion width ($W = x_0 - x_d$) initially increases with increasing forward bias voltage. The DLTS signal is formed by the emission of holes from the depletion region therefore an increase in the width of this region increases the number of traps observed. This effect is accounted for in the calculation of the concentration of traps using equation 8.1. To confirm this the relative peak height of the carbon complex has been plotted next to the corresponding relative concentration (see Figure 8.10.). It is easy to see that the concentration of the carbon complex does not change with varying forward bias voltages. The divacancy peak on the other hand initially increases in height as the voltage increases due to the increasing depletion width. When a certain voltage is reached the divacancy peak then sharply reduces in height.

Figure 8.11. shows the concentration of divacancy traps occupied by holes (F_p) in relation to the forward bias voltage calculated using the above equations for the CZG cell. The divacancy is initially full of holes but as the voltage (and therefore the electron concentration) increases to around 0.85V, these electrons begin to recombine with the holes and return the divacancy to its neutral charge state.

Now if we define C_{MAX} as the maximum concentration of the divacancy (at $V_F = 0$) and C_{REL} as the concentration of the divacancy level occupied by holes at various injection levels then the fraction of divacancies occupied by holes F_p can be given as

$$F_p = \frac{C_{REL}}{C_{MAX}} \tag{8. 5}$$

Similarly the fraction of traps occupied by electrons F_n can be defined as

$$F_n = 1 - \frac{C_{REL}}{C_{MAX}} \tag{8.6}$$

The fraction of traps occupied by holes can also be related to the capture coefficient and concentrations of electrons and holes using the equation

$$F_p = \frac{c_p P}{c_n N + c_p P} \tag{8.7}$$

Combining equations 8.6 and 8.7 and rearranging therefore gives

$$\frac{C_{MAX}}{C_{REL}} = \frac{c_n}{c_p P} N + 1 \tag{8.8}$$

A plot of C_{MAX}/C_{REL} versus the electron concentration at various injection levels should therefore be a straight line, and if the hole capture rate is known, the electron capture rate can be determined from the fitted slope of the graph. This new technique is a combination of the FBDLTS technique and the RDLTS technique therefore can be called forward bias recombination DLTS (FBRDLTS).

8.6.2 Electron Concentration at the edge of the Depletion Region under Forward Bias

The electron concentration in the depletion region is required to determine the electron capture cross-section (see Equation 8.8) and is difficult to determine accurately. In order to understand what is happening in the depletion region under forward bias it is necessary to first examine the dark current-voltage (IV) characteristics. The ideal diode law states that

$$I = I_0\left(e^{\frac{qV}{kT}} - 1\right) \tag{8. 9}$$

Here I_0 is the saturation current density derived as

$$I_0 = A\left(\frac{qD_n n_i^2}{L_n N_A} + \frac{qD_p n_i^2}{L_p N_D}\right) \tag{8. 10}$$

In these equations the recombination in the depletion region was neglected on the basis that the depletion layer width is very small. However, the enhanced value of recombination in this region can make it quite important in some situations (see also Section 7.2). Including the depletion region recombination adds an additional term to the dark current-voltage characteristics, which then become

$$I = I_0\left(e^{\frac{qV}{kT}} - 1\right) + I_W\left(e^{\frac{qV}{2kT}} - 1\right) \tag{8. 11}$$

Here I_W has the value[40]

$$I_W = \frac{qAn_i\pi}{2\sqrt{\tau_{n0}\tau_{p0}}} \times \frac{kT}{q\xi_{\max}} \tag{8. 12}$$

where $\xi_{\max}$ is the maximum electric field strength in the junction. This can be determined for junctions uniformly doped on each side using the equation

$$\xi_{\max} = -\left[\frac{\frac{2q}{\varepsilon}(\varphi_0 - V)}{\left(\frac{1}{N_A} + \frac{1}{N_D}\right)}\right]^{\frac{1}{2}} \tag{8. 13}$$

The potential difference between the two sides of the diode, ψ_0, is given by

$$\varphi_0 = \frac{kT}{q}\ln\left(\frac{N_A N_D}{n_i^2}\right) \tag{8. 14}$$

These above equations should give identical results to the equations given in Section 7.2 and by using both sets of equations to calculate the IV curve means that the results can be double checked to ensure an accurate result.

Both sets of equations have been used to determine the dark current-voltage curve for the gallium doped high efficiency cells (CZG) at 125K. Figure 8.12. shows the resulting relationship and it can be seen that the recombination current dominates at low voltages (<0.6V) and the diffusion current alone determines the curve at greater voltages. This curve changes significantly with varying temperature and Figure 8.13. shows the current-voltage relationship at different temperatures.

This theoretical calculation can now be compared to the actual IV characteristics of the irradiated CZG cells measured in Section 6.14. Figure 8.14. shows this comparison at 300K and it can be clearly seen that the recombination current is actually much larger in reality than predicted by the theoretical equations. However, at higher voltages (around 0.5V at 300K) the current becomes composed mainly of the diffusion component before quickly tailing off due to the series resistance effect. This effect is not included in the theoretical equations but seriously limits the current at higher forward bias voltages[41].

The divacancy peak is observed at 125K (1000/s rate window) and at this temperature the theoretical and experimentally determined IV curves can now be compared (Figure 8.15.). It can be seen that in the region of interest (around 0.85 to 1V) the current is composed mainly of the diffusion current and quickly tails off due to the series resistance effect.

In the first instance the concentration of minority-carriers at the edge of the depletion region can be calculated from the forward bias voltage (see Section 4.7.1). The concentration increases exponentially with applied voltage and is classically described by the equation

$$n = n_{p0} e^{\frac{qV_F}{kT}} \tag{8. 15}$$

Here n_{p0} is the electron concentration at equilibrium ≈ n_i^2/N_A. This equation is derived from the ideal diode law and therefore neglects the recombination current.

A more accurate estimate of the electron concentration can be derived from the measured current density, assuming that the injection efficiency is unity (Section 4.7.1) and rearranging equation 4.37 gives

$$n_p = \frac{L_n}{qD_n} J_{diff} \tag{8.16}$$

However these equations are only valid if the current is dominated by the diffusion component. The divacancy is depleted of holes at a forward bias of between 0.85 and 1 V and in this region the series resistance effect must also be considered. Fortunately PC1D can be used to model the cell and includes the effect of the series resistance. Using this model a close correlation can be obtained between the theoretical and experimental IV characteristic in the 0.85 to 1V region (125K) by including the effect of a series resistance of 0.2 Ohms. To fit the model in the lower voltage region (<0.85V) the recombination current must also be considered. PC1D also models the recombination current, and by using a minority-carrier diffusion length (L) of 10μm, the model fits the experimental data perfectly. Figure 8.16. therefore compares the experimental results to the PC1D results for the CZG cell at 125K.

The same arguments apply to the CZG cell at 300K so to check these results the PC1D model was compared to the experimental IV characteristic at 300K. To fit the characteristics in the recombination current region a slightly longer diffusion length of 13μm has to be used, together with the series resistance of 0.2 Ohms. These results are shown in Figure 8.17. and validate the accuracy of the PC1D model.

Now the IV characteristics are closely matched in the region of interest PC1D can be used to determine the electron concentration at the edge of the depletion region for the CZG cells under forward bias. The results shown in Figure 8.11. are for two different rate windows and the temperature at which these peaks occur are different. The 400/s rate window peak occurs at 117K and the 1000/s rate window at 125K therefore Figure 8.18. shows the resulting electron concentration at 117 and 125K.

8.7 Determination of the Minority-carrier Capture Cross-section of the Divacancy

Equation 8.8 can now be used to estimate the electron capture cross-section of the divacancy. The hole concentration (P) can be assumed to be equal to the doping density and the hole capture cross-section[69,70] (c_p) at 125K is around 4.2×10^{-16} cm^2. C_{MAX}/C_{REL} is equal to $1/F_P$ and is shown in Figure 8.11.. Figure 8.19. shows the electron concentration determined using PC1D plotted against $1/F_P$ and it can be seen that it is a reasonable straight line. The theoretical line on this plot was determined using an electron capture cross-section of 3×10^{-13} cm^2 and a reasonable fit between the experimental and theoretical data was obtained.

To examine the limits of this analysis the electron concentration has been plotted against F_P in Figure 8.20.. The theoretical curves were plotted for an electron capture cross-section of 1×10^{-13} and 5×10^{-13} cm^2. These two curves therefore represent the minimum and maximum limits of the divacancies ($VV^{+/0}$) electron capture cross-section. The electron capture cross-section of the divacancy is therefore much larger than the hole capture cross-section.

This new FBRDLTS technique provides a simple method of determining the minority capture cross-section of a majority carrier trap and is conceptually similar to the method described by Wang and Sah[42]. The difference being Wang and Sah use forward bias injection to fill a trap with electrons, the FBRDLTS technique on the other hand uses electrons to deplete the hole concentration of a majority carrier trap. Great care however must be taken to ensure an accurate determination of the electron concentration during the experiment. It should also be noted that it may be possible to use the DDDLTS technique described in Section 4.9 to determine the minority-carrier capture cross-section of the $VV^{+/0}$ trap although an extremely accurate pulse generator would be required.

The capture cross-section of the defects observed in p-type silicon can also be estimated from theoretical calculations (see Section 3.3). A donor such as the divacancy for example, is in the neutral charge state before capture of a hole (see Section 3.4.2). The interaction radius (r) for the neutral vacancy can be estimated using the Thomas-Fermi method (Section 3.3.1) to be around 2.07Å. Assuming that the divacancy has similar properties the hole capture cross-section (using $\sigma = \pi r^2$) can be estimated to be 1.4×10^{-15} cm^{-2}. This value is larger than the experimental values by an order of magnitude and this is probably because the CCS depends on temperature and can also depend on the chemical nature of the impurity.

After hole capture the positively charged donor will then act as an attractive Coulomb centre to electrons[43] (see Section 3.3.2). Equation 3.24 can therefore now be used to estimate the electron capture-cross section to be around 10^{-14} cm^2 at 120K. Another simpler method can also be used to estimate the CCS. Assuming that the interaction radius for carrier capture is equal to the "re-normalised" Bohr radius (see Section 3.3.1), the CCS can be estimated to be around 1.7×10^{-13}cm^2 using equation 3.22.

These theoretical arguments show that the electron capture cross-section for an attractive centre is quite large. The estimate from equation 3.24 is probably the more accurate although it should be noted that the capture cross-section is also dependant on the defects' position in the bandgap and the chemical nature of the impurity. The positively charged divacancy level ($VV^{+/0}$) acts as an attractive Coulomb centre and therefore has a large electron capture cross-section. FBDLTS experiments show this to be at least 1×10^{-13} cm^2 and this value can also be estimated by theoretical arguments.

8.8 SRH Modelling of the Defects observed in the Irradiated CZ(G) Cells

In order to determine the lifetime controlling deep levels in the solar cells examined in this study the Shockley-Read-Hall (SRH) lifetime model[44,45,46] was used. The efficiency of a recombination centre with respect to the control of minority-carrier lifetimes strongly depends at high injection on the magnitude of the capture coefficients and on its concentration. At low injection it also depends on its energy level position within the bandgap. The defects E(0.16) and E(0.42) observed in n-type material are thought to control the SRH carrier lifetime in low doped silicon[69]. These defects are also present in p-type silicon although they are difficult to observe using DLTS because their hole capture coefficients are much larger than their electron capture coefficients[70].

The SRH lifetime at high-level injection is given by

$$\tau_{HL} = \tau_{n0} + \tau_{p0} \qquad \textbf{(8.17)}$$

where τ_{n0} and τ_{p0} are the minority-carrier lifetimes in heavily-doped n- and p-type silicon respectively. In the case of a single recombination centre,

$$\tau_{n0} = \frac{1}{c_n \times N_T} \qquad \textbf{(8.18)}$$

$$\tau_{p0} = \frac{1}{c_p \times N_T} \qquad \textbf{(8. 19)}$$

The capture coefficients are symbolised by c_n and c_p and are given by $c_n=\sigma_n v_n$ and $c_p=\sigma_p v_p$ respectively. Here σ is the capture cross-section, v is the thermal velocity and N_T is the trap concentration. It can be seen therefore that at high level injection a larger capture coefficient or a high concentration causes a greater reduction in the minority-carrier lifetime.

The lifetime at low-level injection τ_{LL} can be given by

$$\tau_{LL} = \tau_{n0}\left\{\exp\left(\frac{2E_i - E_T - E_F}{kT}\right)\right\} + \tau_{p0}\left\{1+\exp\left(\frac{E_T - E_F}{kT}\right)\right\} \qquad \textbf{(8.20)}$$

where E_i, E_F and E_T are the intrinsic Fermi level, Fermi level and the defect energy level respectively. The closer the energy level position to the mid-gap therefore, the more effective the deep centre functions as a recombination centre under low injection conditions in a device.

The SRH model can be used to determine the lifetime in terms of the injection level that is valid for v independent deep levels can be given by

$$\tau = \sum_{i=1}^{v} \tau_{n0,i}\left(1+\frac{p_i}{(p_0+\Delta n)}\right) + \tau_{p0,i}\left(\frac{n_i+\Delta n}{p_0+\Delta n}\right) \qquad \textbf{(8.21)}$$

where

$$\tau_{n0,i} = \frac{1}{c_{n,i}\times N_{T,i}} \qquad \textbf{(8.22)}$$

$$\tau_{p0,i} = \frac{1}{c_{p,i}\times N_{T,i}} \qquad \textbf{(8. 23)}$$

$$n_i = N_c \times \exp\left(\frac{E_c - E_{t,i}}{kT}\right) \qquad \textbf{(8.24)}$$

$$p_i = N_v \times \exp\left(\frac{E_{t,i} - E_v}{kT}\right) \qquad \textbf{(8.25)}$$

$\tau_{n0,i}$ and $\tau_{p0,i}$ are the electron and hole minority-carrier lifetimes for a specific trap respectively; $c_{n,i}$ and $c_{p,i}$ are the defect capture coefficients for electrons and holes; N_c and N_v are the effective densities of states in the conduction and valence bands; n_0 and p_0 are the thermal equilibrium concentrations of electrons and holes and Δn is the excess electron concentration.

Kimerling *et al* have demonstrated that the defects created by proton irradiation are similar to those created by electron irradiation[30,47] therefore the capture coefficients and entropy factors proposed by Hallen *et al*[69] and others[70] have been used to model these cells. The capture coefficients and their temperature dependence used in these studies are given in Table 8.5 and the SRH lifetime for each of the defects observed can now be determined in relation to the injection level. The electron capture cross-section of the positive charge state of the divacancy ($VV^{+/0}$) was determined to be at least 1×10^{-13} cm^2 at 125K. Assuming that the temperature dependence of the electron capture cross-section is similar to the temperature dependence of the hole capture cross-section gives the values shown in Table 8.5.

Table 8.5 – Defect Energy Levels, Capture Cross-sections[69,70] and Concentrations for the Defects Observed using DLTS

Defect	**H_T-H_V**	**Temp (K)**	**c_n (cm^3/s)**	**c_p (cm^3/s)**	**$N_T\times10^{13}$ (cm^{-3})**	**I (cm^{-1})**
CO	0.339	160 to 238	$5.1\times10^{-23}\times T^{5.2}$ 1.91×10^{-17} (300K)	$1.2\times10^{-10}\times T^{0.61}$ 1.91×10^{-16} (300K)	2.0	0.0067
$VV^{+/0}$	0.194	250 to 420	$2.1\times10^{-7}\times T^{0.20}$ 1×10^{-13} (125K) 7.7×10^{-14} (300K)	$2.1\times10^{-9}\times T^{0.20}$ 4.15×10^{-16} (125K) 3.23×10^{-16} (300K)	0.46	0.0015
Defect	**H_C-H_T**	**x_n**	**c_n (cm^3/s)**	**c_p (cm^3/s)**	**$N_T\times10^{13}$ (cm^{-3})**	
$VV^{0/-}$	0.421	182 to 266	$5.4\times10^{-9}\times T^{0.40}$ 2.60×10^{-15} (300K)	$2\times10^{-6}\times T^{-0.3}$ 1.78×10^{-14} (300K)	0.46	0.0015
OV	0.164	80 to 108	$1.4\times10^{-8}\times T^{0.50}$ 1.19×10^{-14} (300K)	$8\times10^{-8}\times T^{0.7}$ 2.13×10^{-13} (300K)	1.00	0.0033

The temperature intervals shown in Table 8.5 refer to the measurement temperatures for the capture coefficient data[69,70]. Some extrapolation of this data is therefore necessary to determine the capture coefficients at 300K and this may introduce a small error. This is because the capture process may be built up of several different processes[48], each dominating in different temperature intervals and thereby changing the temperature dependence.

The theoretical SRH lifetimes at 300K for the two divacancy charge states and the carbon complex in the CZG cells can now be determined and these are shown in Figure 8. 21.. The defect concentrations used are shown in Table 8.5 and the experimental lifetime (τ_n) shown was calculated from the diffusion length, L_n, (determined from the spectral response data to be 24µm in Table 7.6) using

$$\tau_n = \frac{L_n^{\ 2}}{D_n} \tag{8.26}$$

where D_n is the electron diffusion coefficient. This experimental lifetime was determined using an AM1.5 bias light (100 mW/cm^2) and PC1D can be used to estimate the electron concentration at the edge of the depletion region. Under short-circuit conditions PC1D gives this electron concentration to be 2.8×10^{11} and using open-circuit conditions gives the electron concentration to be 9.0×10^{12} cm^{-3}. When illuminated by the AM0 (136.8 mW/cm^2) spectrum the concentration in the p-type region was also calculated to be between 3.4×10^{11} and 1.1×10^{13} cm^{-3}. These cells therefore always operate under low injection conditions, whether illuminated by the AM1.5 or AM0 spectrum.

Figure 8.21. therefore shows that the positive charge state of the divacancy (VV$^{+/0}$) alone is enough to account for the observed degradation. The carbon complex and the other charge state of the divacancy (VV$^{-/0}$) can be completely ignored as their effect in these cells under low injection levels is negligible.

To gain a better understanding it is instructive to plot the injection level against the diffusion length and this is shown in Figure 8.22.. The SRH diffusion length increases from 21µm to 112µm at the higher injection levels when considering only the divacancy and carbon complex. This is not usually observed in experiments[69,70] because several important defects cannot be detected in p-type material by DLTS measurements. This is because some defects have a much larger hole capture coefficient than electron capture coefficient, and therefore a comparison with the defects observed in the n-type material must be made.

The defects observed in the CZP1.3 cells are shown in Table 8.3 and Figure 8.6.. The E(0.23) peak is most likely formed when the double negative divacancy charge state ($VV^{-/=}$) emits an electron. This repulsive defect centre (see Section 8.6) has a small electron capture cross-section and is therefore not involved in determining the CZG cells minority-carrier lifetime. The E(0.42) peak is probably the single negative charge state of the divacancy ($VV^{0/-}$) and may also consist of the PV centre. The $VV^{0/-}$ level is already included in the SRH model and the PV level will not exist in the CZG cells which do not contain phosphorus.

The E(0.16) peak is the A centre and has a large electron capture cross section[69]. The concentration of this defect in p-type material is unknown but an estimate can be obtained by comparison with the n-type cells. The divacancy is present in both types of material and both the divacancy and the A centre are unrelated to the doping density and dopant species. In the CZP1.3 cells the concentration of the A centre is 3.6 times the concentration of the divacancy (31/8.6) therefore the first estimate of the A centre's concentration is 1.6×10^{13} in the CZG cells ($3.6\times0.46\times10^{12}$).

The estimate of the A centre concentration in the p-type material can be confirmed using the ratio of the carbon complex and the A centre in similar n-type material. This should also give a reasonably accurate estimate because both the concentration of the divacancy and carbon complex do not depend on the doping level. Table 8.3 shows that the carbon complex and the divacancy are present in all the cells studied and the ratio (OV/CO) in the CZP1.3 cells was 1.15. This gives the A centre concentration to be 2.3×10^{13} ($1.15\times20\times10^{12}$). The A centre's concentration can therefore be estimated in the CZG cell to be around 2×10^{13} and this estimate is comparable with values used in similar studies[69,70].

If we now add the A centre to the SRH lifetime model see (Figure 8.23.) it can be seen that the A centre controls the lifetime under high injection conditions, and the divacancy ($VV^{+/0}$) acts in parallel with the A centre to give an AM0 diffusion length of 17μm. This is slightly lower than the experimentally determined value so the estimate of the A centre's concentration may be too high. Figure 8.24. therefore shows the effect of varying the A centre's concentration on the SRH lifetime model at 300K. The capture cross-sections[69,70] of the A centre shown in Table 8.3 are also slightly higher than given by some of the other studies[49,50] so the best possible estimate that can be attained for the A centre's concentration is 1×10^{13} cm^{-3} and this is used to calculate the SRH lifetime in Figure 8.25.

The SRH carrier lifetime in the gallium doped cells is therefore dominated by the divacancy level $VV^{+/0}$ under low injection conditions. The experimental results show a diffusion length in these cells of 24 μm (see Table 7.6). This compares very well with the SRH theoretical result at a similar injection level using an A centre concentration of 1×10^{13} cm^{-3}.

The A centre seems likely to control the high level carrier lifetime in these cells as observed in other studies[69,70] however the concentration of the A centre in p-type silicon needs to be directly measured to conclude with certainty the exact relationship. Measurement of the high injection lifetimes by an experimental method (such as measurement of the light induced photoconductance[51]) would help to complete this picture.

8.9 Doping Density and Radiation Tolerance

It is known that the resistance to radiation damage is related to the doping concentration, lower doped cells degrade less when exposed to proton or electron irradiation[1]. This effect can now be examined using the SRH model to help understand which defect is responsible for this effect. The SRH model constructed above to calculate the lifetimes of the divacancy charge states and the A centre can now be simply modified to consider various doping levels. The doping density will not significantly effect the concentration of the divacancy or the A centre because neither defect are dopant-related.

The results on the SRH model of changing the doping density from 1×10^{11} to 1×10^{16} cm^{-3} are shown in Figures 8.26. to 8.31., calculated using an A centre concentration of 1×10^{13} cm^{-3}. This clearly shows that the model predicts a reduction in the lifetime with increasing doping density and this is principally caused by the increasing effectiveness of the divacancy level $VV^{+/0}$ as the doping density increases. At levels higher than about 10^{17} cm^{-3} Auger recombination also becomes important[50].

At low doping levels the model shows the A centre to be responsible for the lifetime under low injection conditions and this result agrees with other studies[69,70]. As the doping level is slowly increased, the positive charge state of the divacancy defect level ($VV^{+/0}$) becomes a more effective recombination centre because it depends on the position of the Fermi level. At doping levels above 1×10^{14} the positive charge state of the divacancy becomes the dominant recombination centre and will reduce the minority-carrier lifetime accordingly.

The Fermi level in the p-type layer in relation to the doping density is given by the equation

$$E_F - E_V = kT\ln\left(\frac{N_V}{N_A}\right) \tag{8.27}$$

This equation has been used to calculate the effect of the doping density on the position of the Fermi level in p-type material in relation to the temperature and the result is shown in Figure 8.32.. Table 8.6 shows the position of the Fermi level in relation to doping density at 300K and also shows the SRH diffusion length associated with the $VV^{+/0}$ level in relation to the doping density and the injection level.

Table 8.6 – Fermi level Position Versus the Doping Density and Diffusion Length of the $VV^{+/0}$ defect level in relation to the Injection Level and Doping Density

Doping Density (cm^{-3})	1×10^{11}	1×10^{12}	1×10^{13}	1×10^{14}	1×10^{15}	1×10^{16}
E_F-E_V (eV)	0.416	0.357	0.297	0.238	0.178	0.118
Electron Conc. (cm^{-3})	**$VV^{+/0}$**	**Diffusion**	**Length**	**(L)**	**(μm)**	
1×10^{10}	99.86	38.40	23.25	21.12	20.90	20.87
1×10^{11}	228.77	99.36	38.25	23.22	21.12	20.90
1×10^{12}	***307.73***	***228.65***	***99.31***	***38.24***	***23.22***	***21.12***
1×10^{13}	***321.07***	***307.72***	***228.64***	***99.30***	***38.24***	***23.22***
1×10^{14}	322.50	321.07	307.71	228.64	99.30	38.24
1×10^{15}	322.65	322.50	321.07	307.71	228.64	99.30
1×10^{16}	322.66	322.65	322.50	321.07	307.71	228.64

The SRH lifetime of the $VV^{+/0}$ level under normal solar cell operating conditions (electron concentration around 3×10^{11} to 1×10^{13} cm^{-3}) therefore decreases rapidly as the doping density is increased (Table 8.6). This is because the recombination efficiency of a defect depends on the trap position in the bandgap as well as the concentration (see Equation 8.21). As the Fermi level approaches the trap energy level the recombination efficiency of the divacancy ($VV^{+/0}$) becomes higher, until the divacancy becomes a very efficient recombination centre at the higher doping levels. The effect of the changing Fermi level on the recombination efficiency of the divacancy ($VV^{+/0}$ charge state) may therefore explain the relationship between the doping density and the radiation tolerance of solar cells.

8.10 The Damage Coefficient and Doping Density

To examine the observed relationship between doping density and radiation tolerance in more detail it is instructive to calculate the damage coefficients. The reduction in the minority-carrier diffusion length caused by electron irradiation has been determined by modelling of the experimental results in Section 7.5 (see also Table 7.6). The behaviour of the damage coefficient in terms of the diffusion length can be described by equation 3.18 which is repeated here for completeness

$$\frac{1}{L_\phi^2}-\frac{1}{L_0^2}=K_L\phi=\sum\frac{I_{ri}\sigma_i v\phi}{D} \qquad \textbf{(8.28)}$$

Where L_ϕ = Final minority-carrier diffusion length
L_0 = Initial minority-carrier diffusion length
K_L = Diffusion length damage coefficient ($K_L=K_\tau/D$)
I_{ri} = Introduction rate of the ith recombination centre by irradiation
σ_i = Minority-carrier capture cross-section of ith recombination centre
V = Thermal velocity of minority-carriers
D = Diffusion coefficient

The diffusion length damage coefficients can now be determined from the data given in Table 7.6 using the first part of equation 8.28. The initial diffusion length in the

CZG cells was around 110μm before irradiation. This value was determined from the cells spectral response although the accuracy of this measurement was uncertain because of experimental problems. Figure 8.33. shows the diffusion length in relation to the electron fluence for the CZG cells and it can be seen that using a value of 5.5×10^{-11} for K_L gives a good fit to the experimental data. Fortunately changing the initial diffusion length only introduces a small error in this calculation because of the $1/L^2$ dependence. For example using $L_0 = 90\mu m$ gives L_ϕ to be 23.7μm and $L_0 = 150\mu m$ gives L_ϕ to be 24.3μm for a fixed value of the damage coefficient (3×10^{15} electrons/cm^2). The experimental error therefore in the determination of the initial diffusion length will only introduce a very small error in the calculated damage coefficient.

The damage coefficient has also been determined in a similar manner for all of the other PERL/PERT cells and one of the BSF/BSR czochralski cells (CZB 67/13 shown in Table 7.6) and these results are summarised in Table 8.7.

Table 8.7 – Calculated Damage Coefficients from the Spectral Response Data in Relation to the Doping Density

Cell Type	Doping Density (cm^{-3})	Damage Coefficient (K_L)
CZB	1.7E+15	5.5E-11
CZI	8.8E+14	3.7E-11
CZG	3.6E+15	6.6E-11
CZA	1.1E+16	2.0E-10
FZB	4.0E+15	5.5E-11
MCZ	3.0E+15	5.1E-11
Ref. 1	**Tada82**	
21Ωcm	6.4E+14	5.0E-11
10.6Ωcm	1.3E+15	8.0E-11
3.3Ωcm	4.3E+15	1.5E-10
1.3Ωcm	1.1E+16	2.3E-10
Ref. 54	**Minahan84**	
10Ωcm	1.4E+15	2.8E-11
1Ωcm	1.5E+16	1.2E-10
0.1Ωcm	2.4E+17	3.1E-10
FZP	5.4E+15	2.1E-09
CZP1.3	4.6E+15	2.1E-09
CZP5.5	1.1E+15	4.1E-10

This variation of solar cell response with base resistivity has been studied and reported[1,52,53,54] *in the literature and some of these values are included for comparison in* Table 8.7. This data is also plotted in Figure 8.34. for the p-type cells. Markvart[55] reviewed this relationship and showed that $K_L \approx 1\times10^{-9}/\rho$ where ρ is the resistivity in Ωcm although a $\rho^{-2/3}$ relationship has also been suggested[56,57]. The n-type cells showed a lower tolerance to electron radiation damage (see Table 8.7) and hence had higher damage coefficients. These coefficients for the n-type cells are plotted in relation to the dopant density in Figure 8.35. and are close to the literature data given by Yamaguchi[58].

Examination of Figure 8.34. clearly shows that the dopant density should be minimised to form radiation tolerant silicon solar cells. The relationship between dopant density and the damage coefficient can also be clearly seen in the PERL/PERT despite the fact that these cells were doped with different species and formed on a variety of substrates. The results shown for the FZB and the MCZ cells were before the AM0 illumination that induced further degradation. The cells that had the best radiation tolerance were therefore the CZG cells that were slightly more resistant to damage than the CZI, CZA and CZB cells.

Comparison of Table 8.6 with Figure 8.34. shows that the behaviour of the divacancy $VV^{+/0}$ may be responsible for this observed reduction in diffusion length with increasing dopant density. This is because the diffusion length after irradiation reduces rapidly with increasing doping density, and this effect can be explained by the divacancy ($VV^{+/0}$) level alone from the results shown in Table 8.6.

The occupation of this defect depends on the position of the Fermi level because this trap must contain a hole before it can capture an electron. The probability of occupation of a defect level by holes (F_P) can be given as[39]

$$F_P = \frac{n_t}{N_t} = \frac{1}{1 + g\exp\left(\dfrac{E_F - E_t}{kT}\right)} \qquad \textbf{(8.29)}$$

Here n_t is the number of occupied traps, N_t is the total number of traps and g is the ground-state degeneracy factor. For acceptor levels in silicon this value is 4 because each acceptor impurity level can accept one hole of either spin and the impurity level is doubly degenerate as a result of two degenerate valence bands at k=0[59]. Figure 8.36. shows the result of this above equation when applied to the $VV^{+/0}$ defect at 300K. The rapidly increasing occupation of the divacancy by holes with increasing doping density improves the ability of this level to act as a recombination centre and could therefore explain the relationship commonly observed between doping density and radiation tolerance.

The second part of equation 8.28 shows how the damage coefficient can be estimated from the introduction rate and capture cross-section of the defects involved in lifetime degradation. However this equation does not include the effect of the defects position in relation to the Fermi level, and can now therefore be improved with the information shown above.

The capture cross-section was estimated to be around 7.7×10^{-14} cm^2 at 300K for the divacancy and the introduction rate is also shown in Table 8.5. Using the second part of equation 8.28 gives the damage coefficient to be 7.2×10^{-11}. This value agrees with the best fit to the experimental results shown in Figure 8.34. at a dopant density of around 2×10^{15} cm^{-3}. Now if the change in damage coefficient with doping density is related to the occupation of the divacancy with holes then the change in the damage coefficient should be directly related to F_P given in equation 8.29.

Defining F_{2E15} as the fraction of divacancies occupied by holes at a doping density of $2\times10_{15}$ cm^{-3} the damage coefficient should therefore change with changing doping density by a factor of F_P/F_{2E15}. Combining this with equation 8.28 and rearranging gives

$$K_L = \frac{F_P}{F_{2E15}} \frac{I\sigma v}{D} \qquad \textbf{(8.30)}$$

Hence if the change in damage coefficient is directly related to the changing occupation levels of the divacancy defect then this equation can be used to determine the damage coefficient at any doping level for p-type silicon solar cells. It should be noted that the mobility of electrons in p-type material and hence the diffusion coefficient changes with doping density and these values are shown in Table 8.8, together with the theoretical damage coefficient (Ktheo) calculated using equation 8.30

Table 8.8 – Theoretically calculated Damage Coefficient using the Occupation level of the Divacancy Defect ($VV^{+/0}$) for a range of Doping Densities in p-type Silicon Solar Cells

Doping Density (cm^{-3})	Electron Mobility (cm^2/Vs)	Diffusion Coefficient (cm^2/s)	Hole Occupation (F_P)	Damage Coefficient (Ktheo)
1.00E+14	1447	37.41	0.044	5.91E-12
4.00E+14	1416	36.61	0.157	2.13E-11
1.00E+15	1377	35.60	0.317	4.44E-11
2.00E+15	1287	33.27	0.481	7.21E-11
3.00E+15	1294	33.45	0.582	8.67E-11
7.00E+15	1194	30.87	0.765	1.23E-10
1.00E+16	1140	29.47	0.823	1.39E-10
2.00E+16	1018	26.32	0.903	1.71E-10

The data shown in Table 8.8 can now be plotted together with the experimentally determined values and the values obtained from the literature (shown in Figure 8.34.) and this comparison is shown in Figure 8.37.. The experimental data shows a relationship between doping density and damage coefficient despite the fact that four different dopants were used. This diagram also clearly shows that the damage coefficient can indeed be determined at any doping density by only considering the occupation level of the divacancy defect ($VV^{+/0}$).

The theoretical curve (Ktheo) shown in Figure 8.37. depends critically on the electron capture cross-section of the divacancy and is well within the range of values obtained from the literature and also agrees well with the experimental data. The theoretical curve however should be treated with caution because it was assumed that the temperature dependence of the capture cross-section is the same for electrons and holes and this may not be strictly true. However, the fact that the variation in damage coefficient with doping density is directly proportional to the occupation of the divacancy ($VV^{+/0}$) level shows that this defect is probably responsible for this effect. The damage coefficient can now therefore be determined for any doping density with equations 8.29, and 8.30 using the introduction rate and capture cross-section of the divacancy ($VV^{+/0}$) shown in Table 8.5.

8.11 Summary

The identity of the recombination centre responsible for the lifetime control in irradiated silicon is still unclear in the literature. It has been suggested that in FZ silicon the divacancy level ($VV^{+/0}$) may be responsible[60,61] although it has also been suggested[62] that the A centre (VO) is the dominant centre. In another study both the A centre and the divacancy were assumed to act in parallel controlling the lifetime[63].

Zazoui and others[64,65,66] have conducted DLTS experiments in the temperature range of 300-600K and concluded that the defect responsible for the minority-carrier lifetime in p-type Czochralski silicon introduced by electron irradiation is a silicon dangling bond originating from a vacancy cluster[66]. It is unclear however if this defect is present at 300K or if it is formed by the unavoidable annealing of the experiment itself. Recent DLTS studies[5] carried out at the National Space Development Agency of Japan (NASDA) have indicated that the majority-carrier trap centre at Ev–0.36eV (carbon complex) also acts as a recombination centre that decreases the minority-carrier diffusion length.

In a study of phosphorus doped FZ silicon[67] a defect level at Ec-0.37eV was found to be an efficient recombination centre responsible for lifetime control. Temperature dependant lifetime measurements on proton irradiated float-zone materials[68] have also been used to indicate the dominant recombination centre under high injection conditions. These results gave an activation energy of 0.23±0.03eV for p-type FZ and 0.17±0.02eV for n-type FZ. This indicates that the dominant recombination centre in n-type FZ material is the A centre (VO complex), and in p-type material the B_IO_I or the divacancy ($VV^{+/0}$) are likely candidates.

Another study of proton irradiated low-doped n-type material[69] concluded that under low injection conditions the divacancy level at Ec-0.42 ($VV^{-/0}$) has the largest influence on lifetime and at a high injection level the A centre is mostly responsible. A recent study of low doped n and p-type electron irradiated FZ[70] silicon concluded that the levels which determine the lifetime in n-type silicon are the same as the levels that determine the lifetime in p-type silicon. That is, the low injection lifetime is controlled by the divacancy level Ec-0.42eV ($VV^{-/0}$) and the high injection level lifetime is mainly controlled by the A centre.

In this study the electron capture cross-section of the divacancy ($VV^{+/0}$) has been determined for the first time using a modified version of the FBDLTS technique. This has enabled a complete SRH model to be built to show that this defect is responsible for the reduction in minority-carrier diffusion length observed when the CZG cells are exposed to space radiation. The same arguments apply to the CZI cells as they contain the same defects in similar concentrations (see Table 8.3) so the $VV^{+/0}$ defect is also likely to control the irradiated SRH lifetime in these cells.

The irradiated CZA cells also contain the $VV^{+/0}$ level in a similar concentration and the observed reduction in diffusion length is also similar to the CZG cells. The CZA cells contain two other aluminium-related defect levels that cannot be ruled out but the $VV^{+/0}$ level alone is enough to account for the observed degradation in lifetime under low injection conditions. The boron-doped BSF/BSR czochralski cells also contain the divacancy ($VV^{+/0}$) in a similar concentration as well as the E(0.26) defect (probably the B_IO_I). The divacancy alone however is again enough to explain the observed degradation in these cells.

The FZB cells and the MCZ cells degrade further when exposed to illumination after irradiation (the "photon effect") therefore this defect must be included in the SRH model to determine the lifetime after exposure to AM0 illumination. The divacancy ($VV^{+/0}$) and the H(0.27) level therefore control the irradiated low level lifetime in these cells. Further evidence is provided by these cells that the divacancy ($VV^{+/0}$) is the dominant recombination centre under low injection conditions because these cells have a much lower concentration of oxygen and will hence have a much lower concentration of the A centre defect. Despite the low A centre concentration in these cells they still degrade upon irradiation in a similar manner to the CZG and CZI cells (see Figure 8.3.).

The electron capture cross-section of the divacancy ($VV^{+/0}$) has been determined for the first time and this provides compelling evidence that the divacancy ($VV^{+/0}$) is responsible for the observed SRH lifetime reduction in irradiated silicon solar cells. The divacancy has also been implicated in other studies[60,61,68,37] and these results confirm this identification.

It has also been shown that the ability of the divacancy ($VV^{+/0}$) level to act as a recombination centre increases, with increasing doping levels, and this is sufficient to explain the commonly observed relationship between base resistivity and radiation tolerance. The increase in damage coefficient with increasing doping density can therefore be described simply in terms of the introduction rate, capture cross-section and the probability of occupation of the divacancy defect level ($VV^{+/0}$).

8.12 References

---

[1] Tada, H.Y., Carter, J.R., Anspaugh, B.E. and Downing, R.G., Solar Cell Radiation Handbook, 3rd edition, JPL Publication 82-69, Jet Propulsion Laboratory, Pasedena, California, (1982).

[2] Private Communication with Dr Jianhua Zhao, Centre for Photovoltaic Engineering, UNSW, Sydney, Australia.

[3] Zhao, J., Wang A., and Green, M.A., 49th Int. Astron. Congress, Melbourne, R1.07, (1998).

[4] Khan, A., et al, 16th Photov. Solar Energy Conf., Glasgow, UK, (2000).

[5] Yamaguchi,M. *et al*, J. Appl. Phys. 86, p.217, (1999).

[6] Fischer, H., and Pschunder, W., Proc. 10th IEEE Photovoltaic Spec. Conf., Palo Alto, California, USA, p.404, (1973).

[7] Schmidt, J., et al, Proc. 26th IEEE Photovoltaic Spec. Conf., Anaheim, California, USA, p.13, (1997).

[8] Rein, S., et al, 16th European Photov. Spec. Conf., Glasgow, UK, 1-5 May (2000).

[9] Lindmayer, J., and Allison, J.F., The Violet Cell: An improved silicon solar cell, 9th IEEE Photovoltaic Spec. Conf., IEEE, New York, p.83, (1972).

[10] Wang, A., et al, Progress in Photov. 4, p.55, (1996).

---

[11] P.A.Iles, Prog. in Photov. 2, p.95, (1994).

[12] Peters, J.W., The role of defects in the radiation damage of solar cells, PhD Thesis, Engineering Materials, University of Southampton, England, (1993).

[13] Peters, J.W., Markvart, T., et al, Defect interactions in silicon solar cells, Presented at the Second Workshop on Radiation-Induced and/or Process-Related Electrically Active Defects in Semiconductor-Insulator Systems, North Carolina, September 10-13, (1989).

[14] Peters, J., Markvart, T., and Willoughby, A.F.W., *Materials Science Forum* **83-87**, p.1539-1544, (1992).

[15] Brower, K.L., Phys. Rev. B 9, p.2607, (1974).

[16] Davies, G., et al, J. Phys C 17, L499, (1984).

[17] Mooney, P.M., Cheng, L.J., Suli, M., Gerson, J.D. and Corbett, J.W., Phys. Rev. B 15, p.3836, (1977).

[18] Fredrickson, A.R. et al, Radiation induced carbon related defects in p-type silicon, J. Appl. Phys. 65, p.8, (1989).

[19] Ferenczi, G., *et al*, Identification of the carbon associated radiation damage levels in silicon, *Materials Science Forum*, **10-12**, p.947-952, (1986).

[20] Ferenczi, G., et al, Correlation of the concentration of the carbon-associated radiation damage levels with the total carbon concentration in silicon, J. Appl. Phys, 63 (1), p.183, (1987).

[21] Londos, C.A., Carbon related radiation damage centres and processes in p-type silicon, Semiconductor. Sci. Tech., 5, p.645, (1990).

[22] Drevinsky, P.J. et al, Mat. Res. Soc. Symp. Proc. 104, p.167 (1988).

[23] Crabb, R.L., Proc. 9th IEEE Photov. Spec. Conf., p.328, (1972).

[24] Irmscher, K., PhD Thesis, Humboldt Universitat, Berlin, Germany, (1985).

[25] Mottet, S. and Roizes, A., Defect formation kinetics in irradiated silicon at 300K, Inst. Phys. Conf. Ser. 46, p.281, (1977).

[26] Lang, D.V., J. Appl. Phys. 45, p.3023, (1974).

[27] Watkins, G.D. and Corbett, J.W., Phys. Rev. 121, p.1001, (1961).

[28] Huppi, M.W., J. Appl. Phys. 68, p.2702, (1990).

[29] Asghar, M., J.Appl. Phys. 73, p.3698, (1993).

[30] Kimerling, L.C. et al, Defect states in electron bombarded silicon: capacitance transient analysis, Inst. Phys. Conf. Ser. No. 31, p.221, (1977).

[31] Evwaraye, A.O., and Sun, E, J. Appl. Phys. 47, p.3776, (1976).

[32] Walker J.W. and Sah, C.T., Phys. Rev. B 7, p.4587, (1973).

[33] Watkins, G.D. and Corbett, J.W., Phys. Rev. 138, p.543, (1965) .

[34] Trombetta, J.M. and Watkins, G.D., Appl. Phys. Lett. 51, p.1103, (1987).

[35] T. Markvart et al, Proc. 3rd Europ. Symp. on Photov. Generators in Space, p.109, (1982).

[36] Markvart, T., Parton, D.P., Peters, J.W. and Willoughby, A.F.W.: DLTS of Recombination Centres in Semiconductors, Presented at the 17th International Conference on Defects in Semiconductors, Gmunden, Austria, p.1381, July (1993).

[37] Parton, D.P. and Markvart, T., Recombination Centres in Solar Cells: DLTS study, Proc. 12th European Photovoltaic Solar Energy Conf., Amsterdam, p.520, (1994).

[38] Troxell, J.R., et al, Recombination-enhanced migration of interstitial aluminum in silicon, Phys. Rev. B, 19, 10, p.5336, (1979).

[39] Blood, P. and Orton, J.W.: The electrical characterisation of semiconductors: majority carriers and electron states, Techniques of Physics, Vols. 13 & 14, Academic Press, London, (1992).

[40] Sah, C.T. et al, Proc. IRE 45, p.1228, (1957).

[41] Nussbaum, A., Semiconductors and Semimetals Vol. 15, Academic Press, (1981).

[42] Wang, A.C., and Sah, C.T., J. Appl. Phys. 57, p.4645, (1985).

[43] Abakumov, V.N., Perel, V.I., and Yassievich, I.N., Nonradiative recombination in semiconductors, Modern problems in condensed matter sciences, Volume 33, North-Holland, (1991).

---

[44] Shockley, W. and Read, W.T.: Phys. Rev., 87, p.335, (1952).

[45] Hall, R.N.: Phys. Rev., 87, p.387, (1952).

[46] Sah, C.T., Noyce, R.N. and Shockley, W.: Proc. IRE, 45, p.1228, (1957).

[47] Kimerling, L.C. et al, Inst. Phys. Conf. Ser. 46, p.273, (1979).

[48] Miller, G.L., Lang, D.V. and Kimerling, L.C., Ann. Rev. Mats. Sci. 7, p.377, (1977).

[49] Gubskaya, V.I., et al, Phys. Stat. Sol (a) 85, p585, (1984).

[50] Kuchinskii, P.V., and Lomako, V.M., Sol. St. Elect. 29, p.1041, (1986).

[51] Nagel, H., et al, 16th European Photov. Spec. Conf., Glasgow, UK, 1-5 May (2000).

[52] Downing, R.G., et al, The energy dependence of electron damage in silicon, Proc. 4th Photov. Spec. Conf., Vol. 1, A-5-1, (1964).

[53] Luft, W., and Rauschenbach, H.S., Effects of base resistivity on the characteristics of n-on-p silicon solar cells, Proc. 6th Photov. Spec. Conf., Vol. III, p.75, (1967).

[54] Minahan, J.A., and Trumble, T., 17th IEEE Photovoltaic Specialists Conference, p.144, (1984).

[55] Markvart, T., Review: Radiation damage in solar cells, J. Mats. Sci.: Mats. in Electr. 1, p.1, (1990).

[56] Srour, J.R. et al, Electron and proton damage coefficients in low resistivity bulk silicon and silicon solar cells, NASA Publication TM-X-3326, p.51, (1975).

[57] Weinberg, I., et al, 19th IEEE Photovoltaic Specialists Conference, p.548, (1987).

[58] Yamaguchi, M. and Ando, K., J. Appl. Phys. 63, p.5555, (1988).

[59] Sze, S.M., Physics of Semiconductor Devices, Second Edition, John Wiley and Sons Inc., (1981).

[60] Evyware, A.O., and Baliga, B.J., J. Electrochem. Soc. 124, p.193, (1977).

[61] Baliga, B.J. and Evwaraye, A.O., Correlation of lifetime with recombination centres in electron irradiated p-type silicon, J. Electrochem. Soc. 130, 9, p.1916, (1983).

[62] Corbett, J.W., and Watkins, G.D., Phys.Rev. 138, p.555, (1965).

[63] Brotherton, S.D. and Bradley, P., Defect production and lifetime control in electron and γ-irradiated silicon, J. Applied Physics, 53, p.5720, (1982).

[64] Zazoui, M., et al, Detection of defects responsible for lifetime in p-type silicon, Materials Science Forum, 143-147, p.189-194, (1994).

[65] Zazoui, M., et al, Recombination centres in Czochralski grown p-si, J. Appl. Phys., 74, 6, p.3944, (1993).

[66] Zazoui, M., et al, Recombination centres in electron-irradiated Czochralski silicon solar cells, J. Appl. Phys., 76, 2, p.815, (1994).

---

[67] Wang, F.P., et al, Novel electrical and annealing properties of defects in electron irradiated silicon p+n junctions, J. Appl. Phys., 68, 4, p.1535, (1990).

[68] Simoen, E., et al, The response of si p-n junction diodes to proton irradiation, Semi. Sci. Tech. 11, p.1434-1442, (1996).

[69] Hallen, A. et al, Lifetime in proton irradiated silicon, J. Appl. Phys. 79, 8, p.3906, (1996).

[70] Keskitalo, N., et al, J. Appl. Phys. 83, 8, p.4206, (1998).

FIGURE 8.1. AM0 SHORT-CIRCUIT CURRENTS, ADJUSTED TO ALLOW FOR THE DLAR, BEFORE AND AFTER 1 MEV ELECTRON IRRADIATION

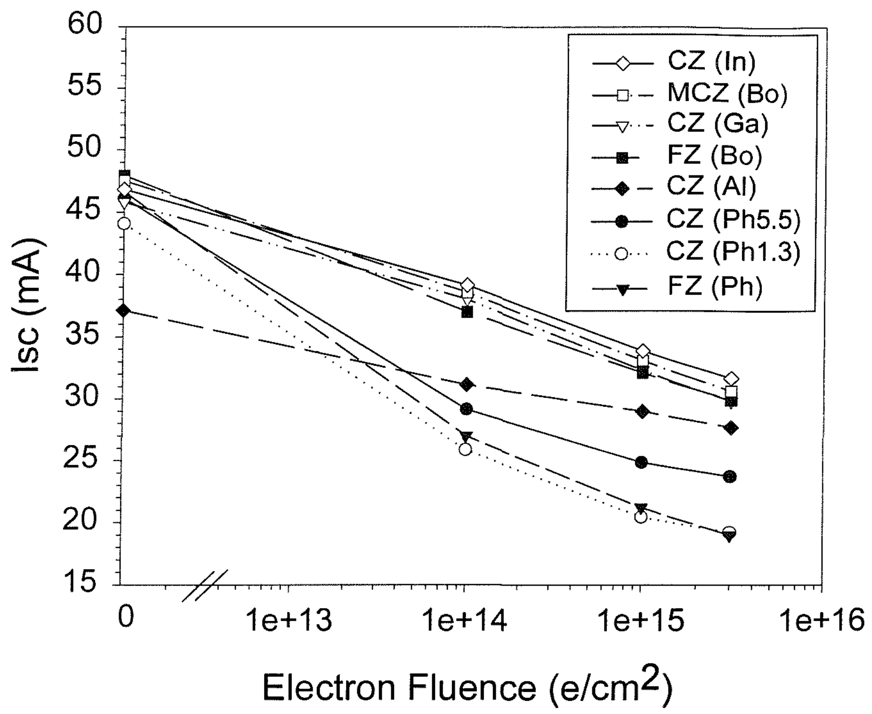

FIGURE 8.2. AM0 OPEN-CIRCUIT VOLTAGES, ADJUSTED TO ALLOW FOR THE DLAR, BEFORE AND AFTER 1 MEV ELECTRON IRRADIATION

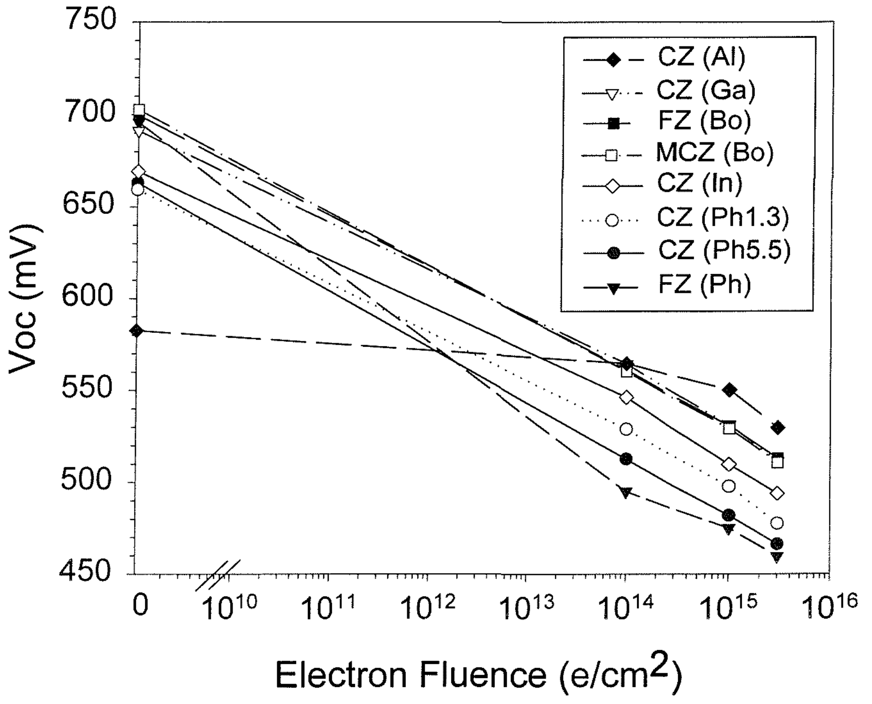

FIGURE 8.3. *AM0 EFFICIENCIES, ADJUSTED TO ALLOW FOR THE DLAR, BEFORE AND AFTER 1 MEV ELECTRON IRRADIATION*

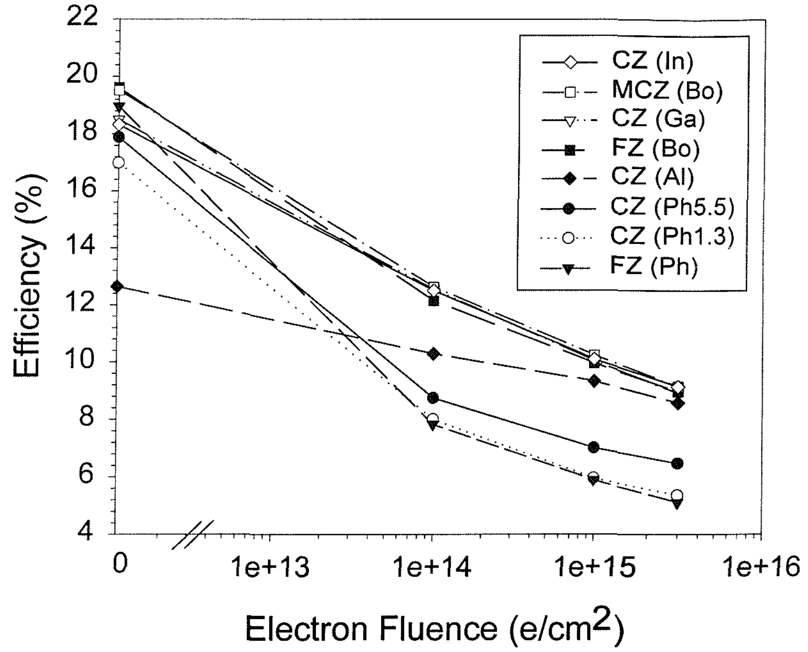

FIGURE 8.4. *AM0 EFFICIENCIES USING A FILL FACTOR OF 0.80 ADJUSTED TO ALLOW FOR THE DLAR, BEFORE AND AFTER 1 MEV ELECTRON IRRADIATION*

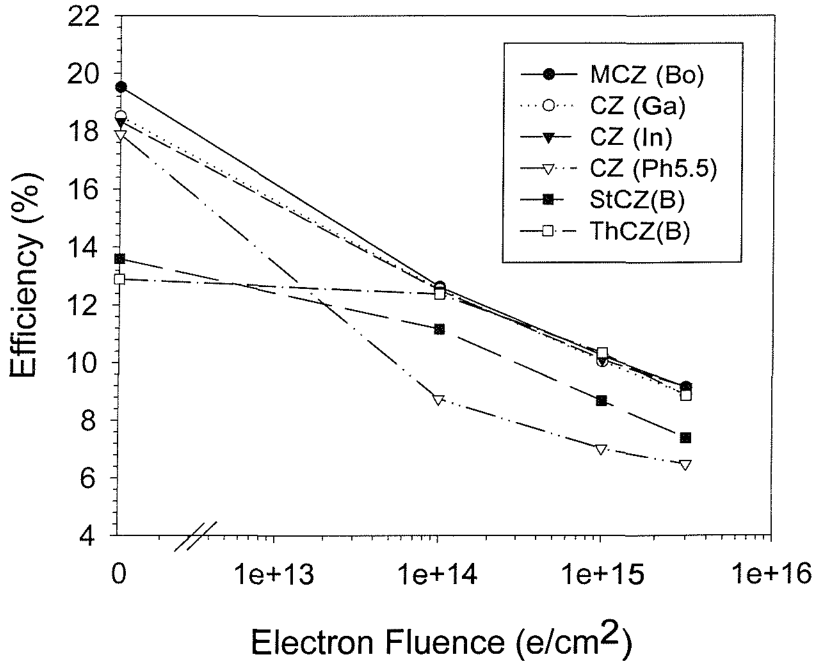

FIGURE 8.5. *DLTS AND MCTS PLOTS (RATE WINDOW 400/S) OF A BSF/BSR CZOCHRALSKI CELL (CZB) AFTER 1×10^{16} ELECTRONS/CM^2*

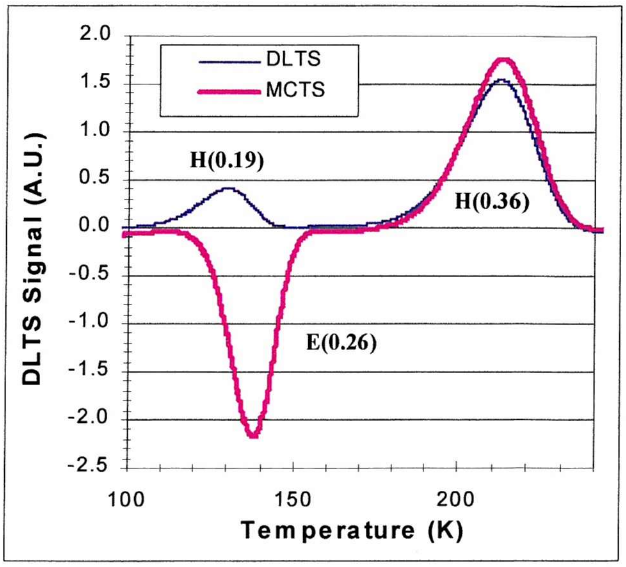

FIGURE 8.6. *DLTS AND FBDLTS PLOTS (RATE WINDOW 1000/S) OF A HIGH EFFICIENCY PHOSPHORUS DOPED CZOCHRALSKI CELL (CZ(5.5)) AFTER 3×10^{15} ELECTRONS/CM^2*

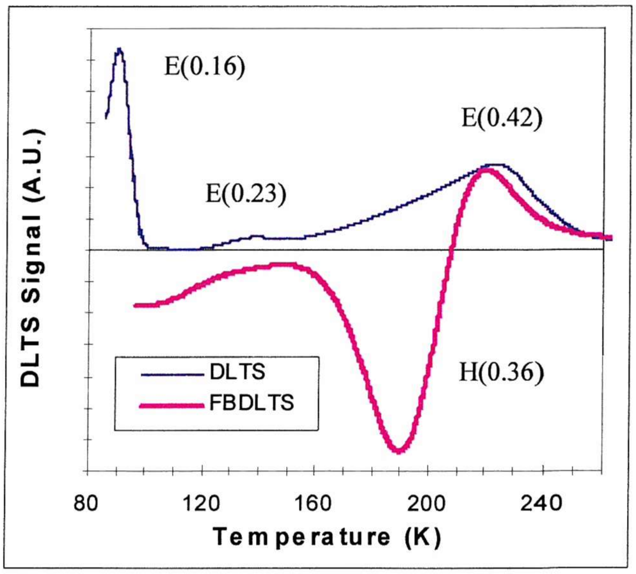

FIGURE 8.7. *DLTS PLOT (RATE WINDOW 1000/S) OF A HIGH EFFICIENCY GALLIUM DOPED CZOCHRALSKI CELL (CZG) AFTER 3×10^{15} ELECTRONS/CM^2*

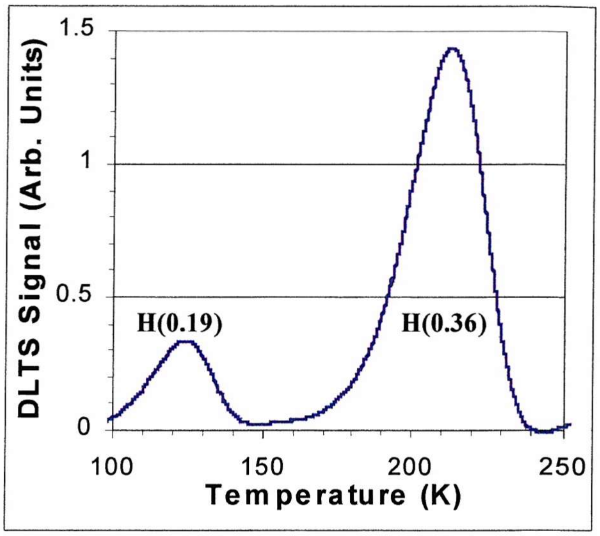

FIGURE 8.8. *DLTS PLOT (RATE WINDOW 1000/S) OF A HIGH EFFICIENCY BORON DOPED FLOAT-ZONE CELL (FZB) AFTER 3×10^{15} ELECTRONS/CM^2 AND 48 HOURS OF AM0 ILLUMINATION*

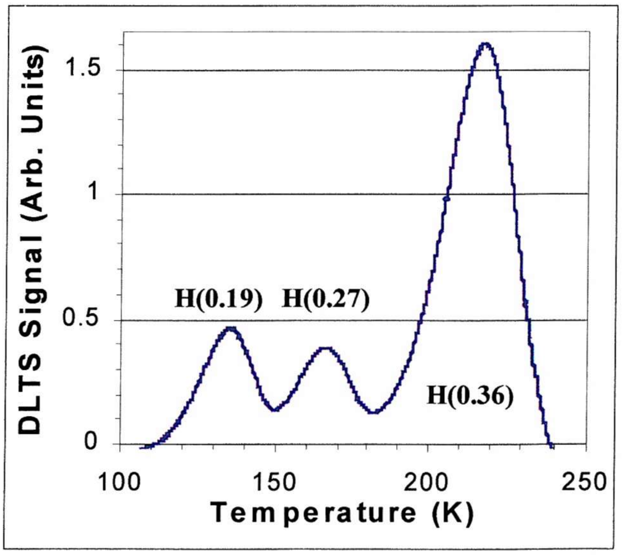

FIGURE 8.9. DLTS PLOT (RATE WINDOW 1000/S) OF A HIGH EFFICIENCY ALUMINIUM DOPED CZOCHRALSKI CELL (CZA) AFTER 3×10^{15} ELECTRONS/CM^{2}

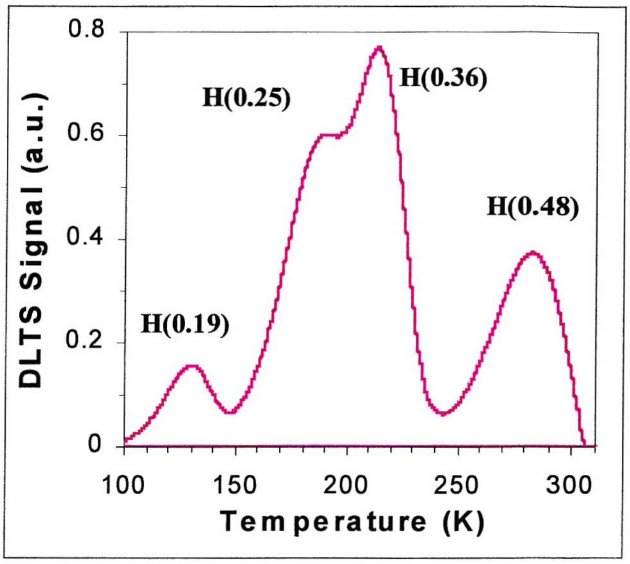

FIGURE 8.10. RELATIVE INCREASE IN THE CARBON COMPLEX PEAK HEIGHT IN RELATION TO THE RELATIVE INCREASE IN CONCENTRATION FOR THE CZG CELL

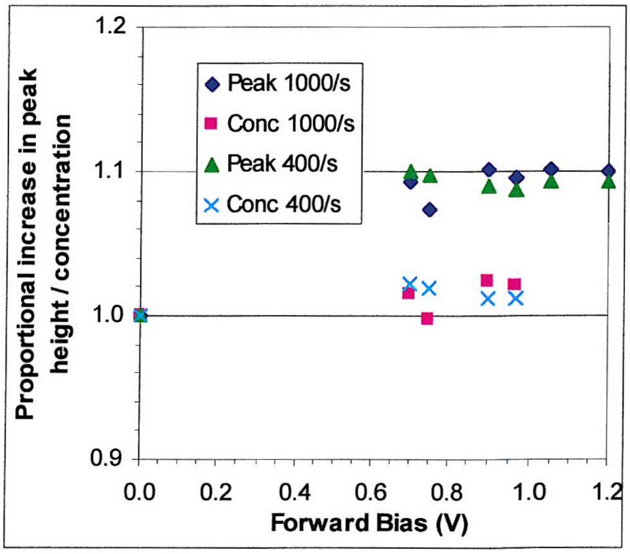

FIGURE 8.11. CONCENTRATION OF DIVACANCY TRAPS OCCUPIED BY HOLES (F_P) IN RELATION TO THE FORWARD BIAS VOLTAGE

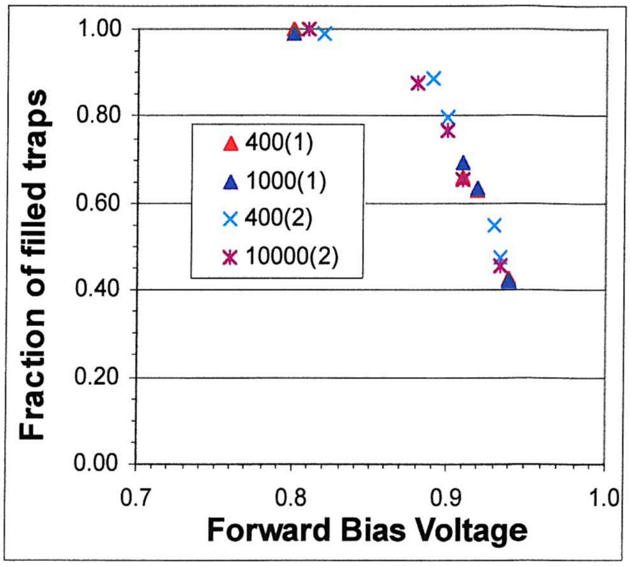

FIGURE 8.12. THEORETICAL DARK IV CHARACTERISTIC FOR THE CZG CELLS AT 125K SHOWING THE DIFFUSION AND RECOMBINATION COMPONENTS

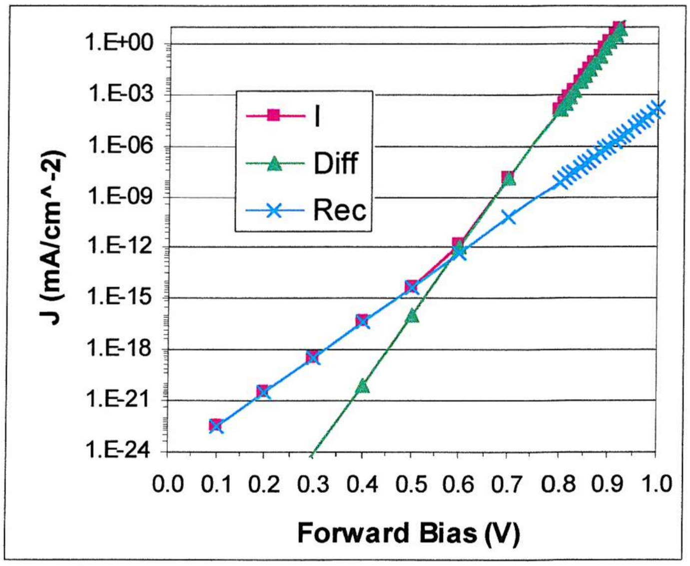

FIGURE 8.13. *THEORETICAL DARK IV CHARACTERISTIC FOR THE CZG CELLS AT VARYING TEMPERATURES*

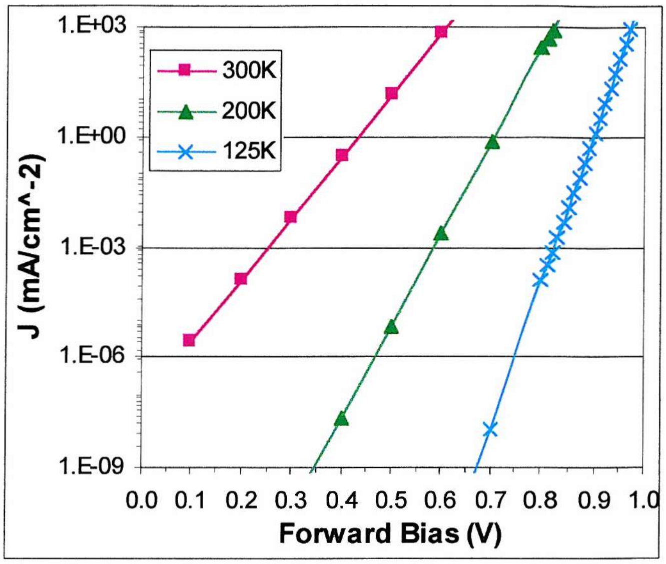

FIGURE 8.14. *THEORETICAL DARK IV CHARACTERISTIC COMPARED TO THE EXPERIMENTAL RESULTS FOR THE CZG CELLS AT 300K*

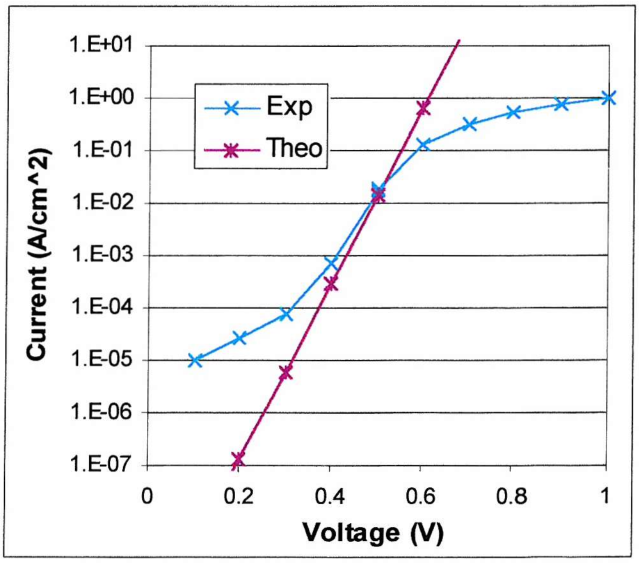

FIGURE 8.15. THEORETICAL DARK IV CHARACTERISTIC COMPARED TO THE EXPERIMENTAL RESULTS FOR THE CZG CELLS AT 125K

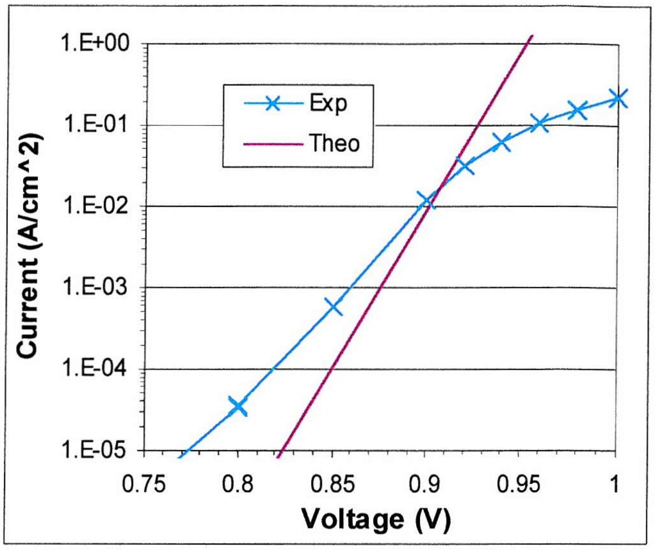

FIGURE 8.16. THEORETICAL DARK IV CHARACTERISTIC COMPARED TO THE EXPERIMENTAL AND PC1D RESULTS FOR THE CZG CELLS AT 125K

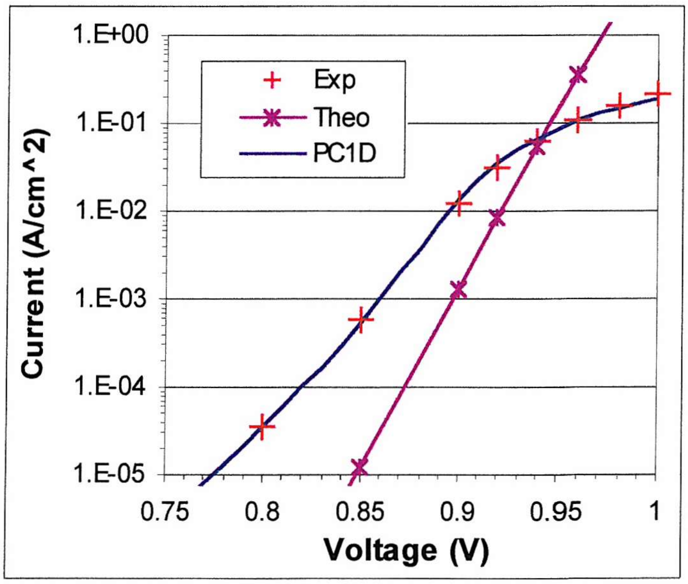

FIGURE 8.17. PC1D DARK IV CHARACTERISTIC COMPARED TO THE EXPERIMENTAL RESULTS FOR THE CZG CELLS AT 300K

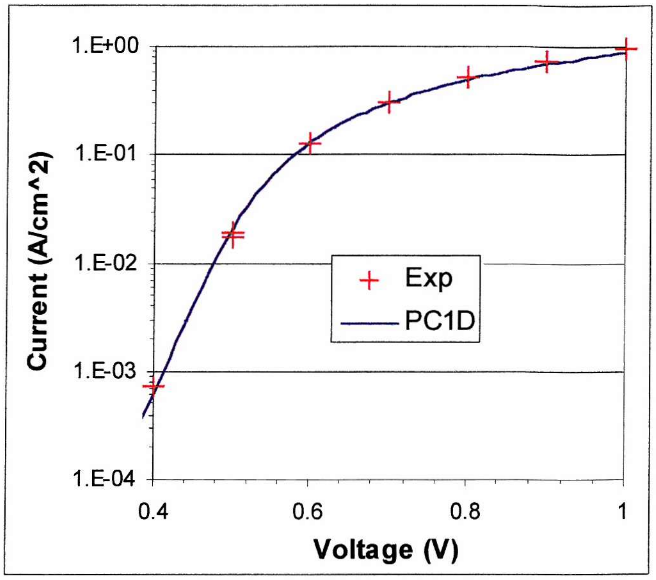

FIGURE 8.18. ELECTRON CONCENTRATION DETERMINED USING PC1D FOR THE CZG CELLS AT 117 AND 125K

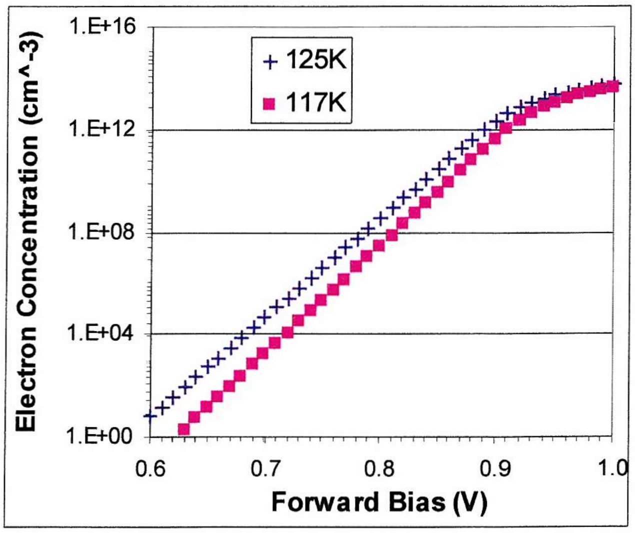

FIGURE 8.19. *1/FRACTION OF HOLE FILLED TRAPS (Fp) VERSUS ELECTRON CONCENTRATION FOR THE CZG CELLS DETERMINED FOR TWO DIFFERENT RATE WINDOWS AND COMPARED TO THE THEORETICAL RESULT FOR ELECTRON CAPTURE CROSS-SECTION = 3 × 10^{-13} CM^2*

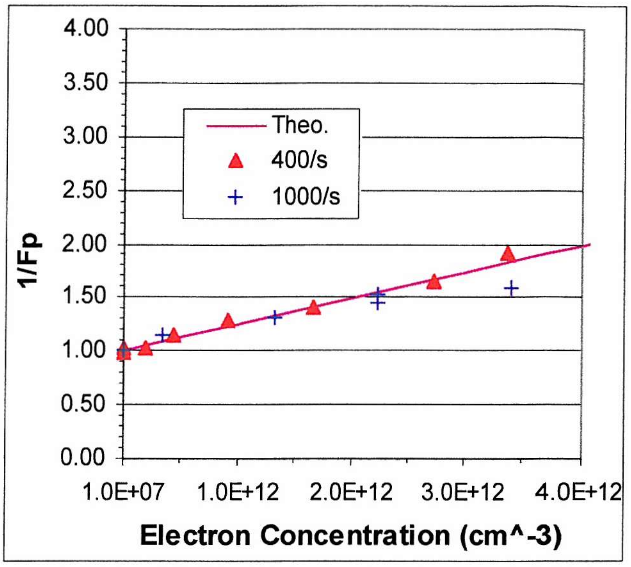

FIGURE 8.20. *FRACTION OF HOLE FILLED TRAPS (Fp) VERSUS ELECTRON CONCENTRATION FOR THE CZG CELLS DETERMINED FOR TWO DIFFERENT RATE WINDOWS AND COMPARED TO THE THEORETICAL LIMITS FOR ELECTRON CAPTURE CROSS-SECTION*

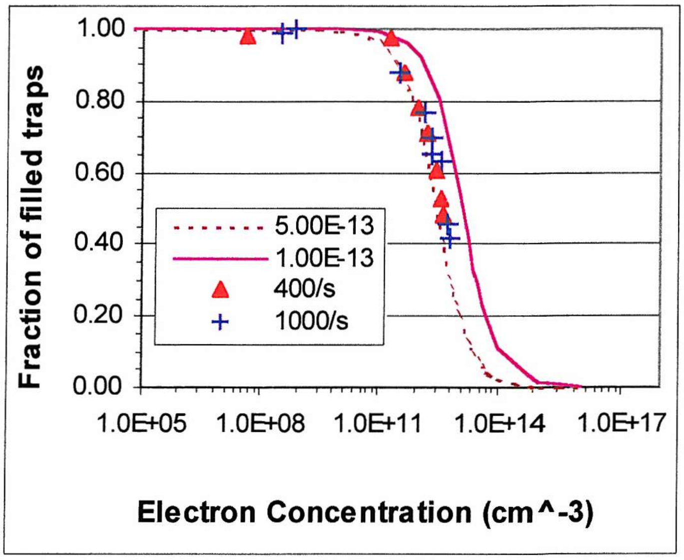

FIGURE 8.21. SRH MODEL OF THE DIVACANCY AND THE CARBON COMPLEX OBSERVED IN THE CZG CELLS COMPARED TO THE EXPERIMENTALLY DETERMINED MINORITY-CARRIER LIFETIME (CZGExp)

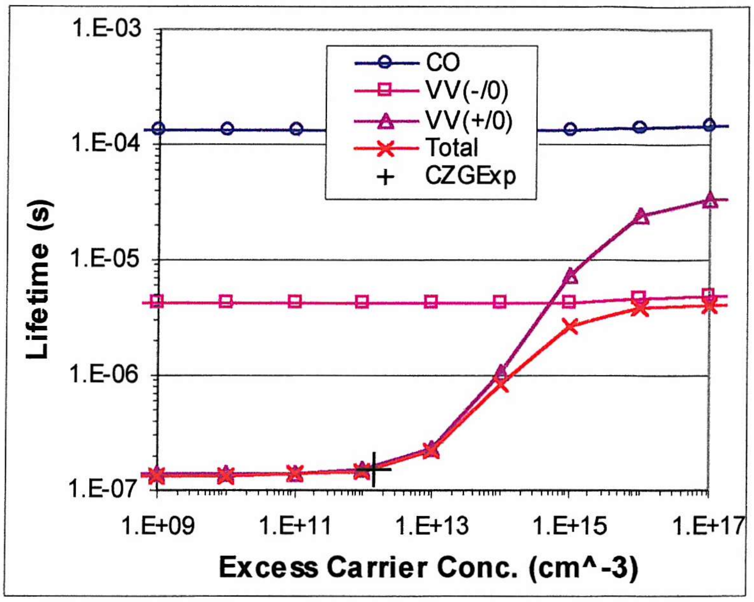

FIGURE 8.22. SRH MODEL OF THE DIVACANCY AND THE CARBON COMPLEX DIFFUSION LENGTHS OBSERVED IN THE CZG CELLS COMPARED TO THE EXPERIMENTALLY DETERMINED MINORITY-CARRIER DIFFUSION LENGTH (CZGExp)

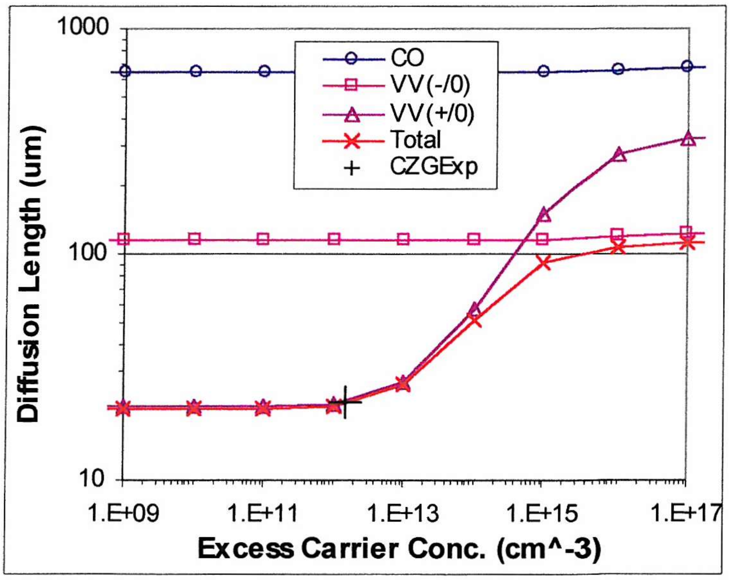

FIGURE 8.23. SRH MODEL OF THE A CENTRE (CONCENTRATION = 2E13 CM^{-3}), DIVACANCY, AND CARBON COMPLEX DIFFUSION LENGTHS CALCULATED FOR THE CZG CELLS COMPARED TO THE EXPERIMENTALLY DETERMINED MINORITY-CARRIER DIFFUSION LENGTH

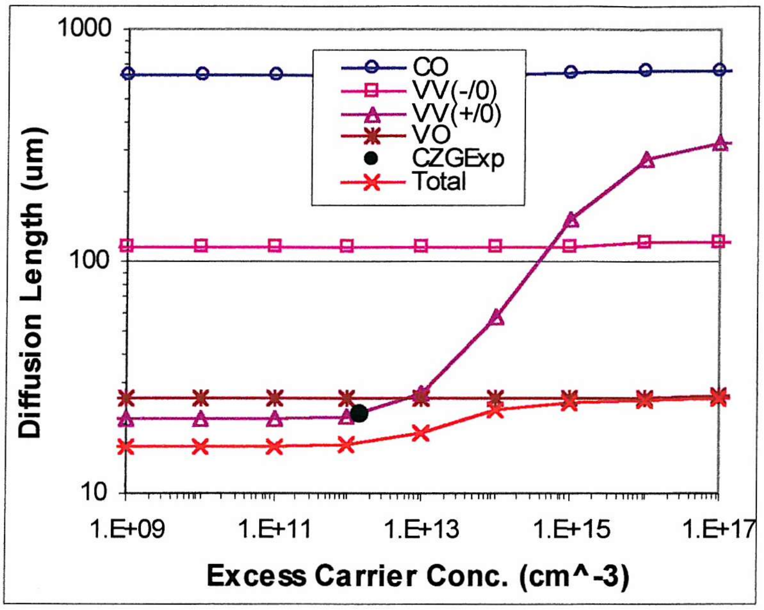

FIGURE 8.24. SRH MODEL OF THE A CENTRE AND DIVACANCY CALCULATED FOR THE CZG CELLS TO COMPARE THE EFFECT OF THE A CENTRE CONCENTRATION AT 1E12, 1E13 AND 3E13

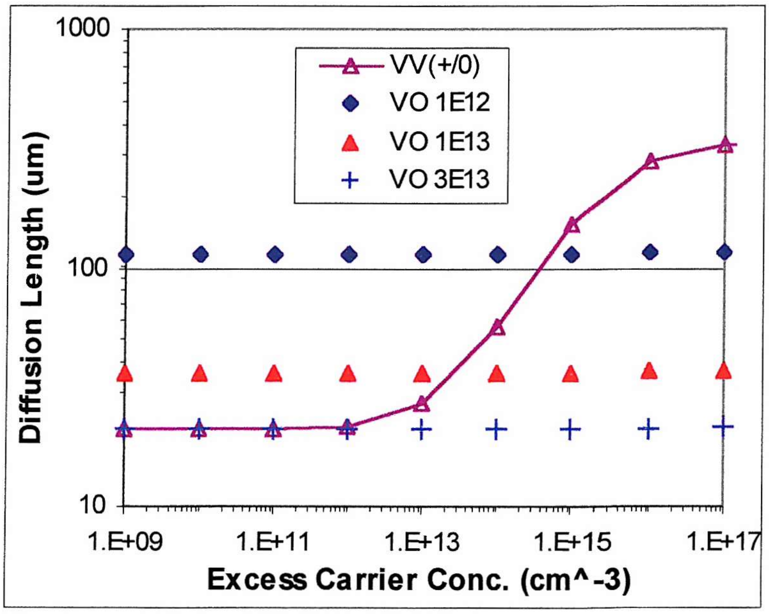

FIGURE 8.25. SRH MODEL OF THE A CENTRE (CONCENTRATION = 1E13 CM^{-3}), DIVACANCY, AND CARBON COMPLEX DIFFUSION LENGTHS CALCULATED FOR THE CZG CELLS COMPARED TO THE EXPERIMENTALLY DETERMINED MINORITY-CARRIER DIFFUSION LENGTH

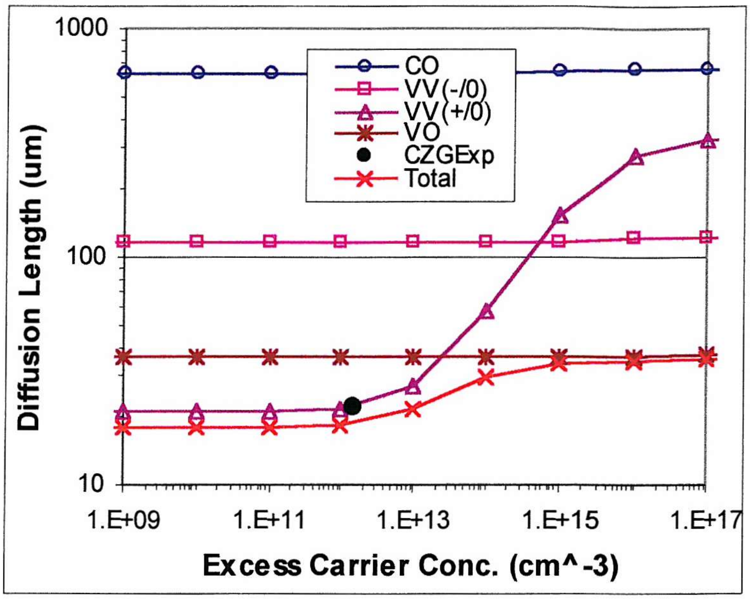

FIGURE 8.26. SRH MODEL OF THE A CENTRE AND DIVACANCY CALCULATED FOR A DOPING DENSITY OF 1E11 CM^{-3}

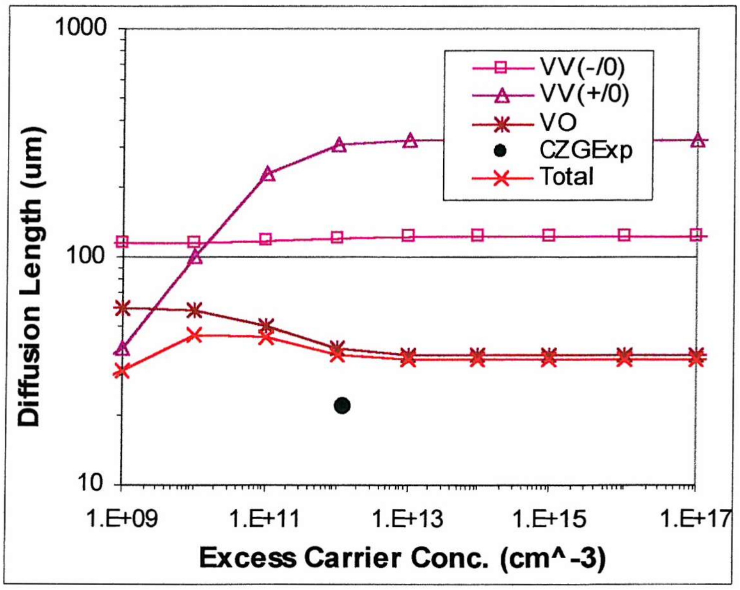

FIGURE 8.27. SRH MODEL OF THE A CENTRE AND DIVACANCY CALCULATED FOR A DOPING DENSITY OF 1E12 CM^{-3}

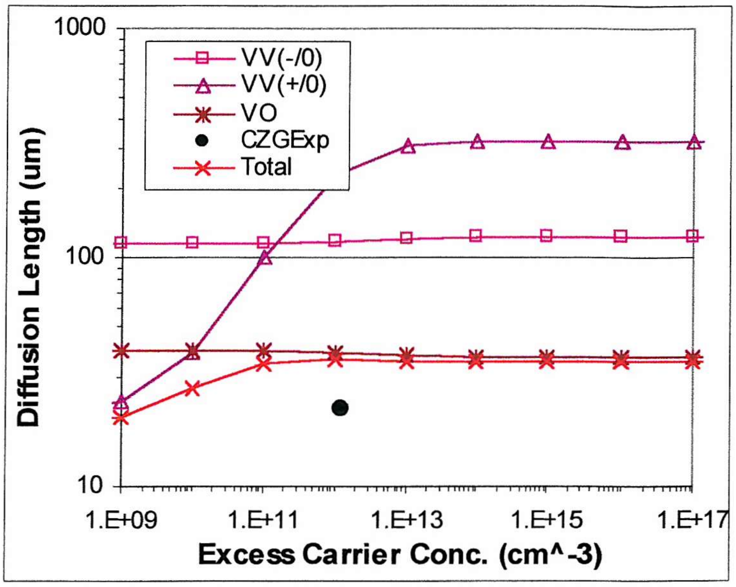

FIGURE 8.28. SRH MODEL OF THE A CENTRE AND DIVACANCY CALCULATED FOR A DOPING DENSITY OF 1E13 CM^{-3}

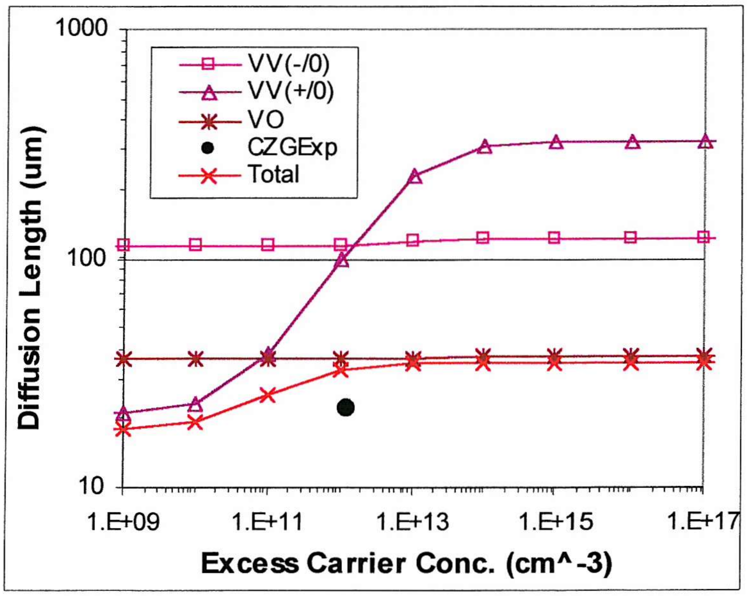

FIGURE 8.29. *SRH MODEL OF THE A CENTRE AND DIVACANCY CALCULATED FOR A DOPING DENSITY OF 1E14 CM^{-3}*

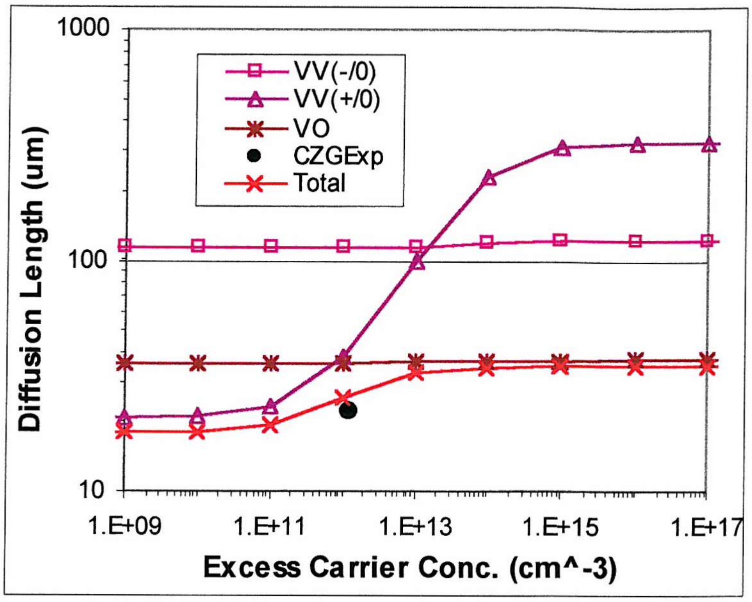

FIGURE 8.30. *SRH MODEL OF THE A CENTRE AND DIVACANCY CALCULATED FOR A DOPING DENSITY OF 1E15 CM^{-3}*

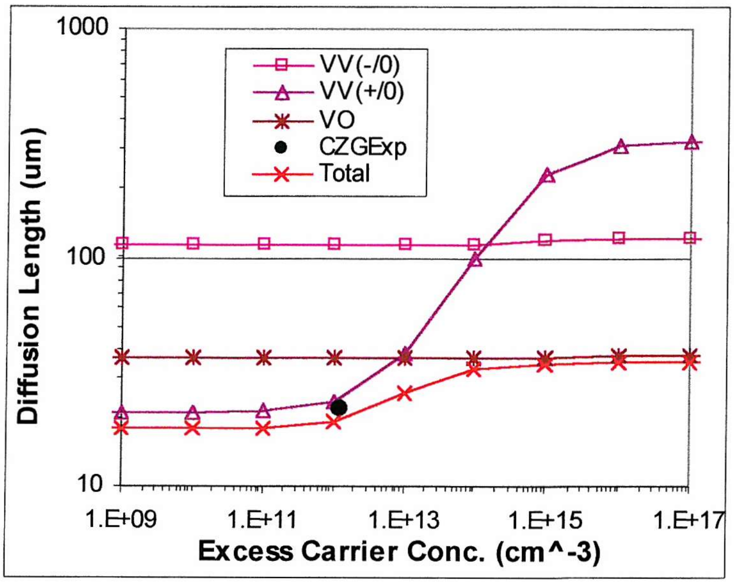

FIGURE 8.31. SRH MODEL OF THE A CENTRE AND DIVACANCY CALCULATED FOR A DOPING DENSITY OF 1E16 CM^{-3}

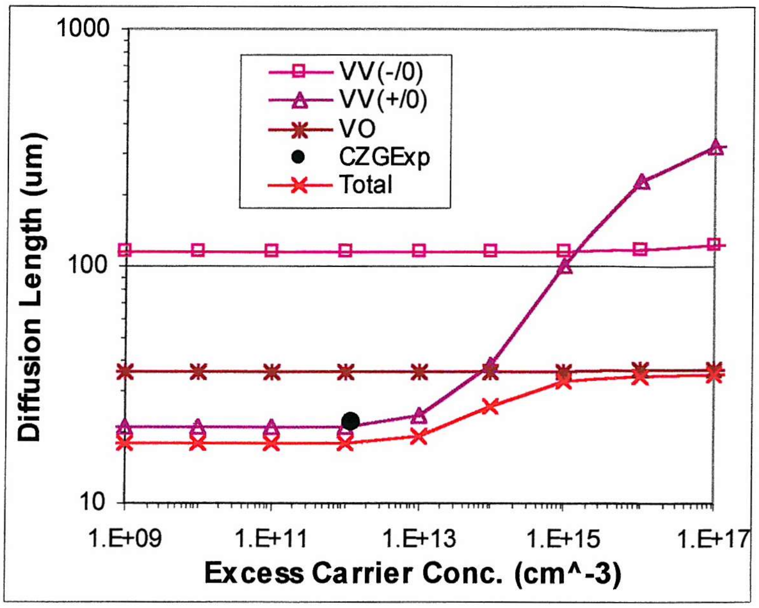

FIGURE 8.32. FERMI LEVEL POSITION VERSUS TEMPERATURE IN RELATION TO THE DOPING DENSITY

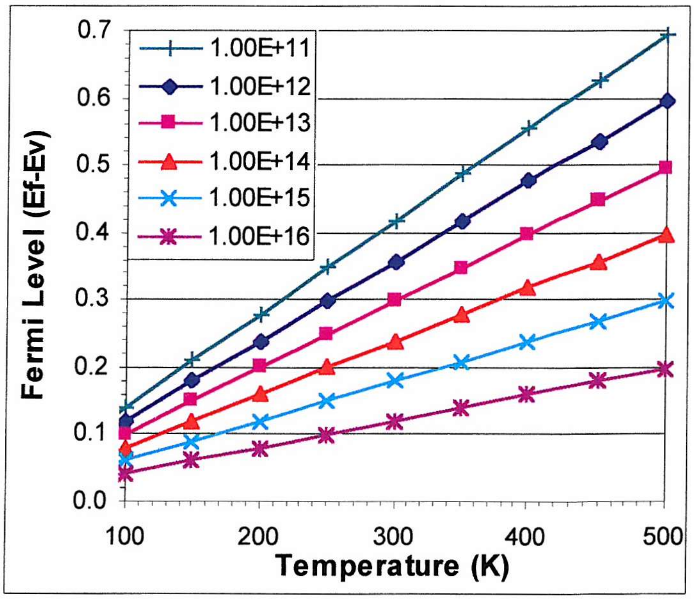

FIGURE 8.33. DIFFUSION LENGTH DAMAGE COEFFICIENT DETERMINATION FOR THE CZG CELL

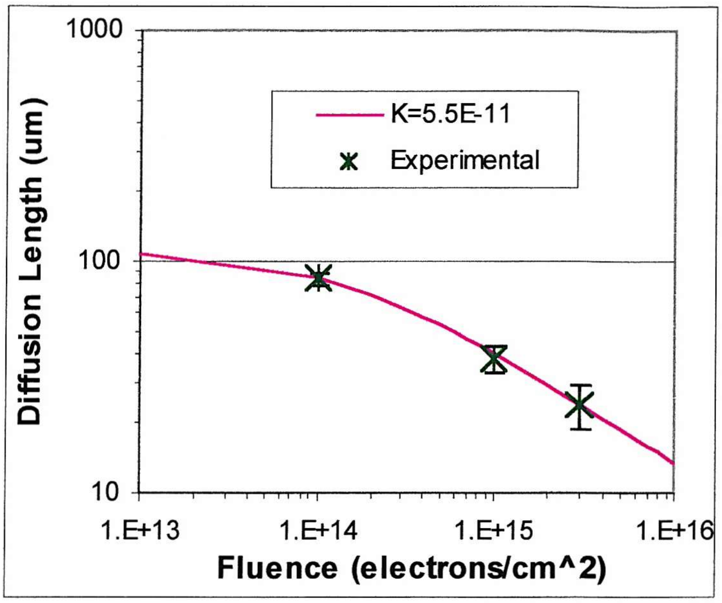

FIGURE 8.34. DIFFUSION LENGTH DAMAGE COEFFICIENT COMPARED TO THE DOPING DENSITY FOR P-TYPE SILICON SOLAR CELLS

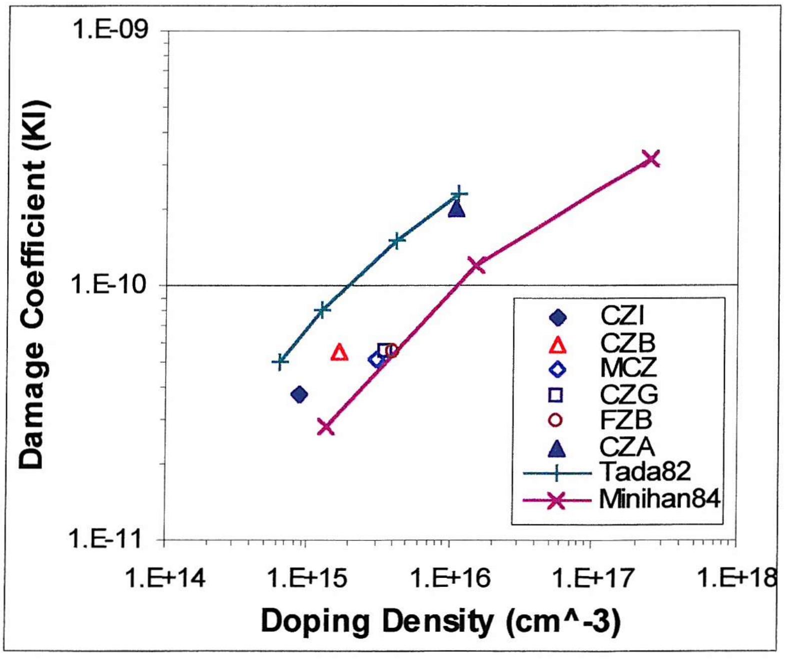

FIGURE 8.35. *DIFFUSION LENGTH DAMAGE COEFFICIENT COMPARED TO THE DOPING DENSITY FOR N-TYPE SILICON SOLAR CELLS*

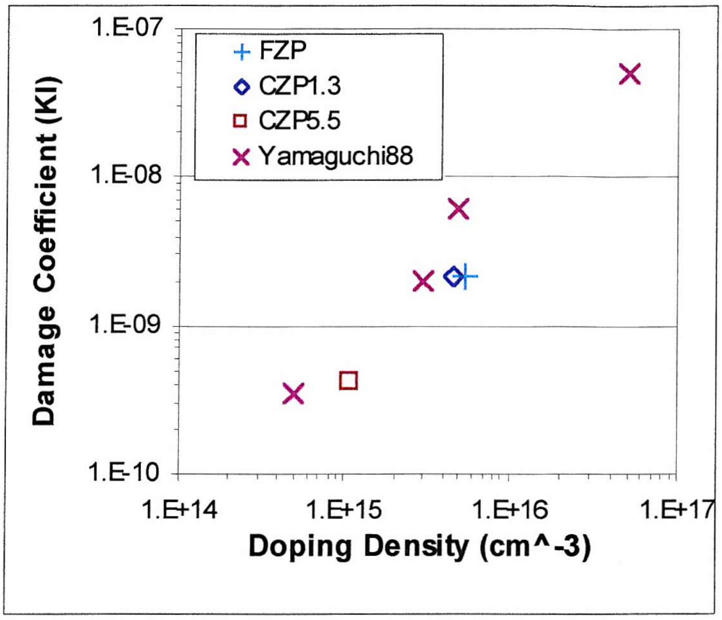

FIGURE 8.36. *PROBABILITY OF OCCUPATION BY HOLES AT 300K FOR THE DIVACANCY ($VV^{+/0}$) IN RELATION TO THE DOPANT DENSITY*

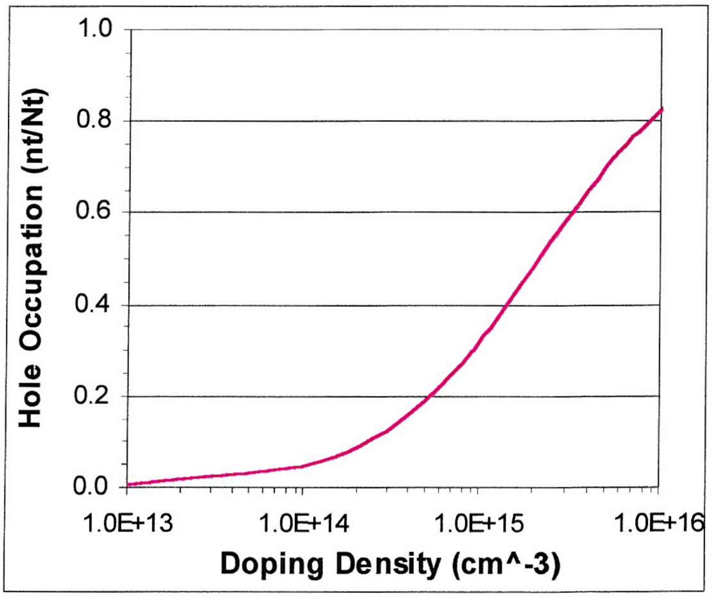

FIGURE 8.37. *DAMAGE COEFFICIENT THEORETICALLY DETERMINED (Ktheo) FROM THE OCCUPATION LEVEL AND CAPTURE CROSS-SECTION OF THE DIVACANCY (VV$^{+/0}$) COMPARED TO THE EXPERIMENTALLY DETERMINED VALUES AND THE LITERATURE DATA*

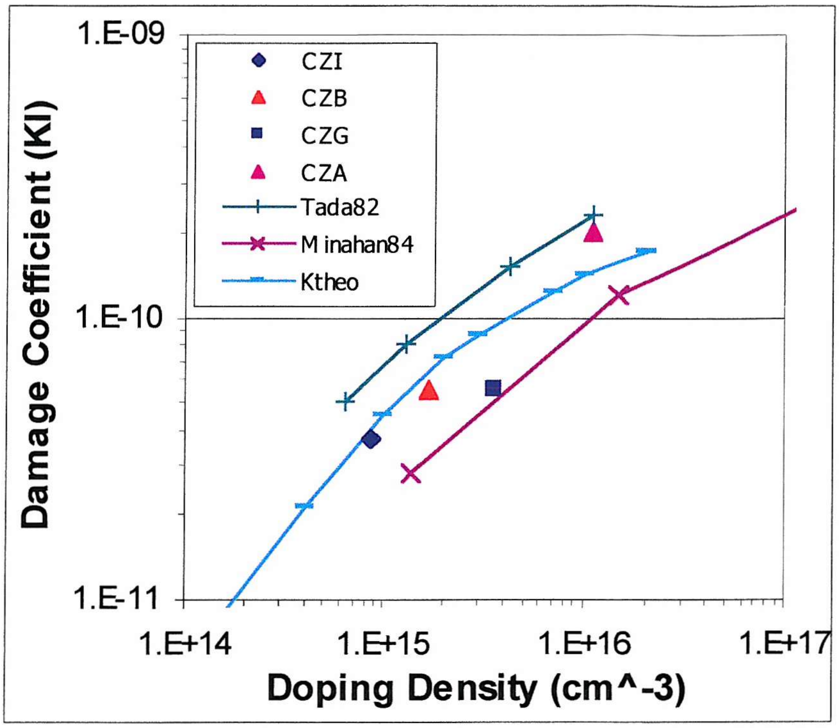

CHAPTER NINE

CONCLUSIONS AND FUTURE WORK

9.1 Conclusions

All of the high efficiency PERL/PERT cells studied in this report degrade severely when exposed to 1MeV electron irradiation. The IV characteristics were measured before and after three different fluence levels of electron irradiation and the n-type cells were shown to degrade more than the p-type cells as expected. The spectral response of each cell type was measured and the reduction in diffusion length caused by the radiation damage was determined by comparison with two different theoretical models. It was also predicted that the PERL/PERT cells with a fill factor of 0.80 would be 10% efficient after 1×10^{15} 1MeV electrons/cm^2 and further improvements are possible by using a shallow junction thin-film type of cell.

DLTS, FBDLTS and MCTS measurements were performed on all of the PERL/PERT cells as well as standard BSF/BSR czochralski and float-zone cells. The approximate energy levels and capture cross-sections were then determined and most of the observed defects were identified by comparison with the literature. It was also shown for the first time that the so called "photon effect" occurs in both the FZB and MCZ cells. The efficiency of these cells was further reduced after irradiation by AM0 illumination and this is because of the appearance of a new defect H(0.27) that acts as a recombination centre in these cells.

A new technique (FBRDLTS) has been developed to enable the determination of the minority-carrier capture-cross section of the divacancy (VV$^{+/0}$). This method is conceptually simple although it relies on an accurate determination of the electron concentration under forward bias conditions that is difficult to achieve. Analysis of the dark IV characteristics at varying temperatures however when combined with a solar cell model such as PC1D can be used to determine this concentration.

Once the electron concentration was calculated the electron capture cross-section of the divacancy (VV$^{+/0}$) was then determined for the first time to be at least 1×10^{-13} cm^2 at 125K. This was then shown to be close to the value predicted by theoretical arguments for an attractive "Coulomb" centre. The SRH lifetime model was then used to show that the divacancy ($VV^{+/0}$) is the dominant recombination centre under low injection conditions in the CZG cells. The A centre is also likely to determine the lifetime under high injection conditions, although the exact relationship is difficult to determine because the concentration of this defect in the CZG cells can only be estimated.

The relationship between doping density and radiation tolerance observed in p-type silicon solar cells was then examined and it was shown that the divacancy level ($VV^{+/0}$) is likely to be responsible for this effect. The recombination efficiency of this defect level increases significantly with increasing doping density because of the changing position of the Fermi level and hence as the doping density increases, the divacancy will become a more efficient recombination centre and reduce the minority carrier lifetime accordingly.

The damage coefficients were then determined for all of the cells examined in this study and they were compared to the literature data. It was then shown that the commonly observed relationship between the doping density and damage coefficient in p-type silicon solar cells can be explained simply in terms of the divacancies ($VV^{+/0}$) capture cross-section, introduction rate, and its probability of occupation. This relationship holds true for the gallium, indium, and boron-doped czochralski cells. The aluminium-doped cells however contain two additional aluminium-related defects that may effect the minority-carrier lifetime.

The most promising cells for future space use are therefore the CZG cells because they have a slightly lower damage coefficient in relation to their doping density (shown in Figure 8.37). The CZG cells have also been shown in other studies to be more tolerant to radiation damage at higher fluence levels[1,2] and they do not degrade when initially illuminated unlike the standard CZB cells[3,4,5]. The CZI cells are also worth considering as an alternative to the CZB cells although more research is required to study their resistance to radiation damage at higher fluence levels.

9.2 Future Work

This investigation can be extended in many areas. For example the new FBRDLTS technique could be used to determine the minority-carrier capture cross-section of some of the other defects, such as the A centre, the aluminium-related defect levels and the "photon effect" level at H(0.27). The A centre however occurs at the low temperature limit of the liquid nitrogen cryostat so to conduct this experiment the helium cryostat would have to be used. The SRH model could also be extended to consider the defects in the n-type cells to obtain the identification of the dominant defect in these cells.

The A centre concentration cannot be determined in the p-type cells using DLTS so another technique such as electron paramagnetic resonance (EPR) could be used. An accurate determination of the A centre's concentration in the p-type cells would then enable the SRH lifetime model to be completed and the defect responsible for lifetime at higher injection levels could be determined. These results could then be compared to the experimental results from a measurement technique such as the open-circuit carrier decay method (OCCD) to conclude with certainty the exact relationship at high injection levels.

9.3 References

---

[1] Khan, A., et al, 16th Photov. Solar Energy Conf., Glasgow, UK, (2000).

[2] Yamaguchi, M. *et al*, J. Appl. Phys. 86, p.217, (1999).

[3] Fischer, H., and Pschunder, W., Proc. 10th IEEE Photovoltaic Spec. Conf., Palo Alto, California, USA, p.404, (1973).

[4] Schmidt, J., et al, Proc. 26th IEEE Photovoltaic Spec. Conf., Anaheim, California, USA, p.13, (1997).

[5] Rein, S., et al, 16th European Photov. Spec. Conf., Glasgow, UK, 1-5 May (2000).

APPENDIX ONE

PHYSICAL CONSTANTS

A1.1 Physical Constants[1]

Permittivity in a vacuum	E_o	8.85418E-14	F/cm
Electron Volt	eV	1.60218E-19	J
Elementary Charge	q	1.60218E-19	C
Boltzmann Constant	k	1.38066E-23	J/K
Boltzmann Constant	k	8.61738E-05	eV/K
Thermal Voltage	kT/q	0.025852	V
Planck Constant	h	6.62617E-34	Js
Speed of Light	c	2.99792E+08	m/s
Dielectric Constant	E_s/E_0	11.9	
Semiconductor Permittivity	E_s	1.05365E-12	F/cm
Electron rest mass	m_0	9.11E-31	Kg

A1.2 Temperature Dependant Physical Constants[2]

T (K)	n_i (cm^{-3})	E_G (eV)	m_{dc}/m_0	m_{dv}/m_0	m_{tc}/m_0	m_{tv}/m_0	N_c (cm^{-3})	N_v (cm^{-3})	ν_n (cm/s)	ν_p (cm/s)
4.2	3.14E-686	1.1700	1.06	0.59	0.27	0.37	4.55E+16	1.87E+16	2.45E+06	2.09E+06
50	1.64E-41	1.1690	1.06	0.69	0.27	0.39	1.87E+18	9.78E+17	8.45E+06	7.03E+06
100	1.95E-11	1.1649	1.06	0.83	0.27	0.41	5.31E+18	3.66E+18	1.20E+07	9.70E+06
150	3.16E-01	1.1579	1.07	0.95	0.27	0.42	9.81E+18	8.16E+18	1.46E+07	1.17E+07
200	5.03E+04	1.1483	1.08	1.03	0.27	0.41	1.52E+19	1.43E+19	1.69E+07	1.37E+07
250	7.59E+07	1.1367	1.08	1.10	0.27	0.41	2.15E+19	2.20E+19	1.89E+07	1.53E+07
300	1.07E+10	1.1242	1.09	1.15	0.28	0.41	2.86E+19	3.10E+19	2.03E+07	1.68E+07
350	3.92E+11	1.1104	1.10	1.19	0.28	0.40	3.65E+19	4.13E+19	2.20E+07	1.84E+07
400	6.00E+12	1.0968	1.11	1.23	0.28	0.40	4.51E+19	5.26E+19	2.35E+07	1.96E+07
450	5.11E+13	1.0832	1.12	1.29	0.28	0.40	5.43E+19	6.49E+19	2.49E+07	2.08E+07
500	2.89E+14	1.0695	1.13	1.29	0.28	0.39	6.46E+19	7.81E+19	2.63E+07	2.22E+07

---

[1] Sze, S.M., Physics of Semiconductor Devices, Second Edition, John Wiley and Sons Inc., (1981).

[2] Green, M.A., Intrinsic Concentration, Effective Densities of States, and Effective Mass in Silicon, J. Appl. Phys., 67, 6, (1990).

GLOSSARY OF TERMS

σ_n = Electron capture-cross section
σ_p = Hole capture-cross section
τ = Lifetime
τ_n = Lifetime of electrons
τ_p = Lifetime of holes
τ_0 = Minority-carrier lifetime before particle irradiation
τ_f = Trap characteristic filling time
ν_n = Thermal velocity of electrons
ν_p = Thermal velocity of holes
$\alpha(\lambda)$ = Absorption coefficient at wavelength λ
β = q/kT
ε_S = Semiconductor permittivity
ε_S = Electric field strength
λ = Wavelength
μ_n = Electron mobility
μ_p = Hole mobility
η = Efficiency
$\bar{\nu}$ = Average number of displacements per primary displacement
θ = Scattering angle of the displaced atom
Φ = Radiation fluence (particles/cm^2)
κ = Dielectric constant
σ_d = Displacement cross-section
1-F = Proportion of empty traps
A = Cross-sectional area
a = Screening radius
a_0 = Bohr radius of hydrogen ($\approx 5.3*10^{-9}$ cm)
C = Capacitance
c = Velocity of light in a vacuum
c_n = Capture rate of electrons
c_p = Capture rate of holes
d_l = Depth of antireflection layer
D_n = Diffusion coefficient electrons
D_p = Diffusion coefficient holes
e = Magnitude of electronic charge
E_A = Critical energy
E_C, E_V = Energies of conduction and valence band edges
E_d = Displacement energy
E_D = Ionisation energy
E_F = Fermi energy level
E_f-E_{in} = Change in Fermi level in n-type
E_G = Forbidden energy gap
E_i = Intrinsic Fermi level
E_{ip}-E_f = Change in Fermi level in p-type
E_m = Photon energy at maximum power point
e_n = Emission rate of electrons

Eo = Permittivity in a vacuum
e_p = Emission rate of holes
E_{ph} = Photon energy
E_R = Rydberg energy $(= q^2/2a_0 \approx 13.6 \text{ eV})$
Es = Semiconductor permittivity
Es/Eo = Dielectric constant
E_t = Defect energy level in the bandgap
F = $N_{T(tp)}/N_{T(tpmax)}$
$F(\lambda)$ = Photon density at wavelength λ
F(E) = Density of free electrons
f_c = Collection probability of light generated carriers
FF = Solar cell fill factor
g = Degeneracy
$G(\lambda)$ = Generation rate of electron-hole pairs at wavelength λ
h = Planck's constant
H = Total cell thickness
H = Total cell thickness
H' = Depth of the edge of the depletion layer
I_1 = Diffusion current
I_2 = Generation-recombination current
I_L = Light generated current
I_m = Current at maximum power point
I_{ri} = Introduction rate of the ith recombination centre by irradiation
I_S = Dark saturation current
I_{sc} = Short-circuit current
I_{SH} = Shunt resistance current
J_d = Depletion region current density
J_n = Electron current density
J_p = Hole current density
J_S = Dark saturation current density
J_t = Total current density
k = Boltzmann's constant
k = Extinction coefficient
K_τ = Damage coefficient (lifetime)
K_L = Damage coefficient (diffusion length)
kT/q = Thermal voltage
L_ϕ Diffusion length after particle irradiation
L_0 = Diffusion length before particle irradiation
L_n = Electron diffusion length
L_p = Hole diffusion length
m = Electron mass (1/1823 in atomic mass units)
m_0 = Electronic rest mass
M_1 = Mass of the incident particle
M_2 = Mass of the struck particle
M_2 = Atomic weight of target atoms (69.72 for Ga, 28 for Si)
mc^2 = Mass-energy equivalence of the electron (0.511 MeV)
m_{dc} = Density of states effective mass conduction band

m_{dv} = Density of states effective mass valence band
m_e^* = Effective mass of electrons
m_h^* = Effective mass of holes
m_{tc} = Thermal velocity effective mass conduction band
m_{tv} = Thermal velocity effective mass valence band
n = Electron concentration
N = Refractive index of silicon
$n^{\wedge}$ = Real part of refractive index
n_0 = Refractive index of the uppermost layer
n_1 = Refractive index of the antireflection layer
n_2 = Refractive index of silicon
n_a = Number of atoms per unit volume of absorber
N_A, N_D = Densities of acceptors, donors
N_C, N_V = Effective density of states in conduction, valence bands
$n_c^{\wedge}$ = Refractive index
N_d = Number of displacements per unit volume
n_i = Intrinsic carrier concentration
n_{no}, n_{po} = Thermal equilibrium concentration of electrons in n, p-type materials
N_t = Deep level concentration
n_t = Unoccupied deep level concentration
$N_{T(tp)}$ = Trap concentration due to a particular pulse width
$N_{T(tpmax)}$ = Trap concentration for a saturating pulse width
P = Power
p = Hole concentration; crystal momentum
P = Total light intensity arriving at cell
P_0 = Total intensity arriving at back surface reflector
P_1 = Total intensity arriving for second reflection
P_2 = Total intensity arriving for third reflection
P_{in} = Intensity of light inside front surface
P_m = Power at maximum power point
p_{no}, p_{po} = Thermal equilibrium concentration of holes in n, p-type materials
q = Elementary charge
QE_{ext} = External quantum efficiency
QE_{int} = Internal quantum efficiency
R = Reflectance
r = Atomic separation
R_b = Reflection coefficient of back surface reflector
R_f = Reflection coefficient of front surface
R_S = Series resistance
R_{SH} = Shunt resistance
S_n = Surface recombination velocity electrons
S_p = Surface recombination velocity holes
SR = Spectral response
T = Absolute temperature
T_m = Maximum energy transfer
t_p = Fill pulse width
U = Net recombination rate

Un = Electron Mobility in p-type material
$V(r)$ = Coulomb potential energy
V_{bi} = Built-in voltage
V_m = Voltage at maximum power point
V_{oc} = Open-circuit voltage
W = Depletion width
W_n = Depletion width in n-type region
W_p = Depletion width in p-type region
x_j = Junction depth
Z_1 = Atomic number of moving particle
Z_2 = Atomic number of stationary particle